Escola de Engenharia • Universidade do Minho

experimental and numerical analysis of blocky masonry structures under cyclic loading

análise experimental e numérica de estruturas de alvenaria de blocos sob acções cíclicas

Thesis submitted in fulfilment of the requirements for the degree of Doctor of Philosophy in Civil Engineering

Tese apresentada para obtenção do grau de Doutor em Engenharia Civil

Daniel Vitorino de Castro Oliveira • Janeiro de 2003

EXPERIMENTAL AND NUMERICAL ANALYSIS OF BLOCKY MASONRY STRUCTURES UNDER CYCLIC LOADING

ANÁLISE EXPERIMENTAL E NUMÉRICA DE ESTRUTURAS DE ALVENARIA DE BLOCOS SOB ACÇÕES CÍCLICAS

Tese apresentada à Universidade do Minho

para obtenção do grau de Doutor em Engenharia Civil

por

DANIEL VITORINO DE CASTRO OLIVEIRA

Orientadores:

Prof. Paulo Barbosa Lourenço (Universidade do Minho)

Prof. Pere Roca (Universidade Politécnica da Catalunha)

As nozes têm bom gosto, mas é preciso quebra-las.

ACKNOWLEDGEMENTS

The present work was developed at both the Civil Engineering Department of Universidade do Minho, Portugal, and the Structural Technology Laboratory of Universitat Politècnica de Catalunya, Spain. This research was carried out under the joint supervision of Prof. Paulo Lourenço and Prof. Pere Roca. To Prof. Paulo Lourenço I would like to thank for his carefully advice, suggestions and incitement along all the research. I also would like to express my gratitude to Prof. Pere Roca for his care and for making my stay at Universitat Politècnica de Catalunya possible.

The experimental research performed at Universitat Politècnica de Catalunya would not have been successful without the assistance of the laboratory technicians, to whom I am grateful. I also would like to thank Dr. Ravindra Gettu, head of the laboratory, for his interest and advice. Likewise, the help of Victor Vásquez, Alexander Popa and Bogdan Tutoveanu during the construction and testing of the dry stone masonry walls is also appreciated.

To Luís Ramos, whom carried out the experimental work performed at Universidade do Minho and for the interesting discussions, I express my thanks, as well as to the other colleagues from the Civil Engineering Department, for their support and friendship. Thanks are also extended to the laboratory staff of Universidade do Minho, for their care and friendship.

The financial support provided by the Portuguese Science and Technology Foundation (program PRAXIS /C/ECM/13247/1998 and PRAXIS XXI BD/16168/98 grant) is gratefully acknowledged.

I am also very grateful to all my friends that always encouraged and supported me during the execution of this work.

Finally, I would like to thank my family for their love and unconditional support.

ABSTRACT

The work presented in this thesis was developed at both the Civil Engineering Department of Universidade do Minho and at the Structural Technology Laboratory of Universitat Politècnica de Catalunya, Spain. This study is composed of both an experimental part and a numerical part, aimed at contributing to a better knowledge of the behaviour of blocky masonry structures under cyclic loading.

Uniaxial monotonic and cyclic deformation-controlled tests were performed on stone and brick specimens as well as prisms, aiming at a complete characterization of the cyclic behaviour of these materials. Complementary to these tests, seven dry stone masonry walls were constructed and tested under combined compressive and shear loading. The main objective of this experimental work was to provide adequate data concerning the mechanical behaviour of historical masonry components and structures, capable of being used for numerical purposes, both for calibration of constitutive models and for validation of numerical results.

The micro-modelling strategy was adopted for the numerical analysis of the cyclic behaviour of masonry structures. Starting from an existing monotonic constitutive model developed for interface elements, fully based on the plasticity theory, a new constitutive model able to describe the cyclic loading of interface elements is proposed. This new model is also entirely founded on the incremental theory of plasticity. Elastic unloading is assumed only for the shear component. The normal component is described in a non-linear fashion. Thus, for unloading/reloading, two new auxiliary yield surfaces, termed unloading surfaces, similar to the monotonic ones, are introduced. The motion of the unloading surfaces is controlled by a mixed hardening law. The proposed constitutive model has been implemented in a pilot version of the DIANA finite element code.

Afterwards, some experiments available in the literature are simulated using the developed model. A good agreement between numerical and experimental results has been found.

RESUMO

O trabalho apresentado nesta Tese foi desenvolvido no Departamento de Engenharia Civil da Universidade do Minho e no Laboratório de Tecnologia de Estruturas da Universidade Politécnica da Catalunha, Espanha. Este trabalho, composto por uma parte experimental e por uma parte numérica, pretende contribuir para uma melhor compreensão do comportamento das estruturas de alvenaria de blocos sob acções cíclicas.

Foram realizados ensaios uniaxiais monotónicos e cíclicos, sob controlo de deslocamento, em provetes e prismas de pedra e tijolo, tendo em vista a caracterização do comportamento cíclico destes materiais. Complementarmente, foram ensaiados sete muros de alvenaria de pedra de junta seca, sob a acção combinada de forças normais e de corte. O principal objectivo deste trabalho experimental relaciona-se com a obtenção de um conjunto adequado de resultados sobre o comportamento mecânico de alvenaria histórica, susceptíveis de serem usados tanto na calibração de modelos constitutivos como na validação de resultados numéricos.

Para a análise numérica do comportamento cíclico de estruturas de alvenaria, foi adoptada a estratégia da micro-modelação. Com base num modelo constitutivo de elemento de junta existente, baseado na teoria da plasticidade e desenvolvido para carregamento monotónico, propõe-se neste trabalho uma extensão desse modelo para a inclusão do comportamento cíclico de elementos de junta. Este novo modelo é também totalmente baseado na teoria da plasticidade. O comportamento elástico em descarga é considerado apenas para a componente de corte. Para a componente normal, a descarga é regida por leis não lineares. Assim, os casos de descarga/recarga são considerados através da introdução de duas novas superfícies de cedência auxiliares, ditas de descarga, para compressão e para tracção, semelhantes às superfícies de cedência monotónicas. O movimento das superfícies de descarga é controlado por leis de endurecimento misto. O modelo constitutivo proposto foi implementado numa versão piloto do código de elementos finitos DIANA.

No final deste trabalho apresentam-se vários exemplos de aplicação do modelo numérico desenvolvido a ensaios experimentais de referência, evidenciando-se a capacidade do modelo em simular devidamente os resultados experimentais.

CONTENTS

1. INTRODUCTION

Masonry is the oldest building material that is still currently used in the building industry. The placing of stone or brick units on top of each other, laid dry or bonded with mortar has revealed itself as a successful technique during thousands of years, which is mainly justified by its simplicity and the durability of the constructions. In spite of the simplicity associated with building in masonry, the analysis of the mechanical behaviour of masonry constructions remains a true challenge. Masonry is a material that exhibits distinct directional properties due to the mortar joints, which act as planes of weakness. Consequently, masonry structures display a complex mechanical behaviour, essentially non-linear.

Structures may be classified as historical when they become part of our built heritage. Naturally this status is not conflicting with a useful function other than simply monumental. Historical buildings carry their cultural significance attached not only to their formal architectural language but also to their specific structural features, applied materials and building techniques and, by being old, they have also been a part of Human life. Therefore, engineers have to put their knowledge at the service of culture, in order to respect the historical value of the architectural heritage and to guarantee appropriate safety levels, changing the original design as little as possible.

The analysis of historical masonry structures presents an even bigger challenge, when compared to regular modern masonry structures. Simple aspects as geometry data or characterization of the mechanical properties of the materials used are, most of the times, inexistent. Associated to the characterization of the mechanical properties, a large variability is usually found, due to workmanship and use of natural materials, as well as to the existence of unknown damage in the structure. In addition, existing standard regulations and codes are non-applicable to the assessment of safety factors in historical masonry structures.

Research in the area of historical masonry buildings is, therefore, essential to understand their specificities, how they behave and how to define reliable and consistent philosophies to assess their safety level and to design potential retrofitting measures. To achieve these purposes, researchers have been trying to convert the highly indeterminate and non-linear behaviour of historical masonry constructions into something that can be understood with an acceptable

degree of mathematical certainty. The fulfilment of this objective is quite complex and burdensome, demanding a considerable effort centered on integrated research programs, able to combine experimental research with the development of consistent constitutive models.

1.1 Objectives

This study is concerned with the experimental and numerical analysis of masonry structures submitted to cyclic loading, with emphasis on their non-linear behaviour. Both experimental and numerical studies have been carried out, focusing on the in-plane structural behaviour of masonry.

From the previous paragraphs, the need for a consistent approach to the study of historical masonry structures became evident. Numerical studies should, whenever possible, be complemented with appropriate experimental programs, which provide appropriate material data necessary to calibrate advanced nonlinear numerical models. The objectives of this study are:

- To obtain an adequate set of experimental data concerning historical masonry components and structures, capable of being used for numerical purposes. This material characterization should include a complete stress-strain behaviour description with emphasis on the cyclic behaviour, a characterization of the failure modes, stiffness degradation and energy dissipation;
- To extend an existing constitutive monotonic multi-surface model in order to incorporate the main features that characterize cyclic behaviour of interfaces;
- To verify the adequacy of the developed model by comparing the predicted numerical response with the behaviour measured in reliable experiments. In spite of the wide scatter that characterizes masonry tests, the developed model should be able to provide a good agreement in terms of ultimate load, global behaviour and failure mode with experimental results.

These three objectives are directly related, since the performance of the numerical model depends on the existence of reliable and appropriate experimental data concerning inelastic and cyclic behaviour. On the other hand, the use of a numerical tool beforehand may allow enhancing the definition of experimental testing programs.

1.2 Outline of the thesis

In Chapter 2, a general overview about the experimental and numerical analysis of masonry structures is given. The most important achievements concerning the evolution of the structural form of masonry constructions and its implications on architecture are revised together with a presentation of relevant masonry buildings. The need for the combined use of experimental, both laboratorial and in situ, and numerical techniques, when dealing with historical constructions, is highlighted. Thus, the necessary laboratory displacement-controlled tests for a comprehensive description of masonry are described. This data must be complemented with information derived from in situ tests (non-destructive, slightly destructive and destructive techniques), which are briefly described. Modelling issues concerning the idealization of material behaviour are presented and related to the different levels of accuracy attained. The different modelling strategies for the study of masonry are also discussed, enlightening the main advantages and disadvantages of each approach.

In Chapter 3, the results from a comprehensive experimental program are presented. This experimental program aims at characterizing the non-linear behaviour of masonry components as well as masonry specimens, with an emphasis on the structural behaviour under cyclic loading. Tests concerning uniaxial compressive loading, as well as direct shear loading of stone specimens, are also presented. The adopted procedure for testing is described and the experimental results are discussed in detail. In addition, the results of four stone masonry prisms, tested under compression, are also presented and the comparison between the results obtained from specimen and prism tests is established. Afterwards, experimental uniaxial compressive tests on brick specimens are presented, with the results discussed in detail, followed by tests performed on brick masonry prisms and tests concerning cement mortar specimens from different mixes. Four stacked bonded prisms were constructed and tested under cyclic loading. Finally, the most important conclusions concerning the experimental research are summarized and the main difficulties are pointed out.

In Chapter 4, experimental results concerning the structural behaviour of dry stone masonry walls are presented. Seven walls made of sandstone blocks, built without any interposition material, were tested under compressive and shear loading. The most relevant results concerning their structural behaviour are discussed, including ultimate loads and failure modes. Complementary, an existing constitutive model based on the plasticity theory is used to simulate

and better understand the structural response of the walls. The model is calibrated with data collected from the experimental tests as well as from uniaxial experiments.

In Chapter 5, a brief reference to solution procedures used in non-linear finite element formulation is presented. The incremental plasticity theory is revised, and subsequent improvements of the classical theory are briefly described. Afterwards, an existing monotonic constitutive multi-surface model for interface elements is succinctly described. From this model, an extension to include cyclic loading is proposed. This new model is fully developed within the standard plasticity framework and formulated in modern plasticity concepts, including an implicit Euler backward algorithm and consistent tangent operators. Finally, selected uniaxial experiments available in the literature are simulated using the developed model.

In Chapter 6, applications of the developed numerical model are presented. The modelling and analysis of three different groups of masonry structures, under monotonic and cyclic loading, are discussed in detail. The first group concerns the analysis of two stacked bond prisms, whose experimental results are presented in Chapter 3. The second group is related with the analysis of a masonry shear wall tested at Eindhoven University of Technology. Finally, the last example concerns the analysis of two masonry shear walls, tested at the Joint Research Centre, under an international research program. The most relevant results concerning monotonic and cyclic analyses are presented and interpreted and the principal conclusions derived from the numerical study are pointed out.

Finally, in Chapter 7, an extended summary and final conclusions, which can be drawn out from this research, are given. Moreover, suggestions for future work are also pointed out.

2. HISTORICAL MASONRY STRUCTURES: AN OVERVIEW

Historical masonry constructions inevitably suffer damage with time. Earthquakes, soil settlements, material degradation and lack of maintenance are the main reasons for structural damage to these constructions (Macchi, 1998). Therefore, careful periodic inspections are necessary in order to evaluate their actual structural safety levels. However, performing the structural analysis of a historical masonry construction is, in general, a very complex and difficult task, since structural engineering is only one of the disciplines of a multidisciplinary group that should be constituted when a consistent plan of intervention for a given historical construction is intended to be drawn. Indeed, all the components of a historical construction must be taken into account when dealing with the design of an intervention. A given historical construction can be seen as a complex entity, where the structural skeleton together with the visual image and the architectural style are significant parts of it. Another important part that also carries important cultural significance is its age, which means that historically, these constructions have been a part of human lives. Therefore, besides the expected structural strengthening, it is required that both image and substance of historical constructions be preserved after any structural intervention (Langenbach, 1994).

Research in the area of unreinforced masonry is, thus, definitely necessary. This research should include appropriate laboratorial experiments, the development of reliable constitutive models, in situ testing and continuous monitoring. A historical analysis is also of great importance in obtaining the construction's historical information.

An outline of the remaining content of this Chapter can be summarized as follows. Initially, a brief review of the development of masonry structures from earliest times, in Europe and Middle East, is given, comprising both the use and evolution of masonry materials and structural forms. Afterwards, specific experimental tests capable of providing a comprehensive description of masonry, both in uniaxial and biaxial behaviour, are introduced. A brief review of the most common in situ tests is given, the importance of both laboratorial and in situ tests for successful experimental characterisation of ancient constructions being stressed. Finally, the different idealizations of the structural behaviour employed to study masonry structures are described. According to the level of accuracy and simplicity desired, the different modelling strategies for

the study of masonry are presented and their respective advantages and drawbacks are elucidated. The most relevant constitutive models derived for the analysis of masonry are also referred to.

2.1 Masonry structures through time

There are two fundamental structural problems when building with masonry: how to achieve height and how to span an opening, i.e. how to span vertical and horizontal spaces (Drysdale *et al.*, 1999). Spanning vertically is done by using columns, walls and towers, and spanning horizontally is done by using lintels, beams and arches. In addition, some structural elements such as vaults and domes can simultaneously span vertically and horizontally.

Along with timber, masonry is the oldest building material that is still commonly used nowadays. The placing of stone or brick units on top of each other, laid dry or bonded with mortar has revealed itself to be a very successful technique, which is mainly justified by its simplicity and the durability of the constructions. Most likely, the first masonry was a simple stack of selected natural stones and mortar, if any, was earth packed between the stones. As tools became available and skills developed, stone units were shaped in regular forms. The first bricks were made of mud or clay, shaped to form bricks and dried by the sun. The bricks were then laid with mud mortar into walls. This simple process has been widely used for millennia to construct dwellings, particularly in the valleys of the Nile and Mesopotamia (Croci, 1998). The practice of burning brick represented a natural evolution and the first prefabricated component. This process increased the strength and the durability of the bricks but at the same time demanded a supply of fuel, which was not always available.

Being the strongest and most durable material, stone was more difficult to shape and, due to its weight, it was difficult to transport. This limited its use to the most valuable constructions. On the other hand, brick was easy to produce and to mould, which when associated with its durability, made brick masonry the main building material until the 19th century.

Archaeological excavations have revealed masonry houses near Lake Hullen, Israel (9000-8000 B.C.), where dry-stone huts, circular and semi-subterranean were found, as one of the oldest building constructions (Lourenço, 1996). Another earliest example of building construction are the Walls of Jericho (8000 B.C.). These structures were built as a military defence and were

made from roughly worked limestone, whose joints were simply filled with earth (Croci, 1998). In the same area, archaeological surveys have found more recent walls (3000 B.C.) made from sun-dried bricks and mortar.

Due to environmental degradation, religious structures, built with better materials and skill than dwellings, supplied the oldest preserved constructions. In this way, the structural form of the pyramids, which represents one of the most stable structural shapes, was the logical development of the initial stone piles. Apart from possible settlements, their structural behaviour does not present any particular problem, as the inner space is limited and the stresses are low and perfectly compatible with the material strength. The most famous pyramids are undoubtedly the Egyptian pyramids at Giza, see Figure 2.1, which are the only survivors of the Seven Wonders of the World and remained the tallest structure (≈140 m) in the world until the 20th century.

Figure 2.1 – Egyptian pyramids (2800-2000 B.C.).

With time, the structural behaviour started to play a more important role in the construction of temples. The use of stone lintels to support the masonry above openings in walls, as the one used to build the Lion Gate at Mycenae, Greece (13th century B.C.), which spanned about 3 m and weighed between 25 and 30 tons, shows the beginning of the arched behaviour that would dominate the following millennium, see Figure 2.2.

During the classical period, columns and the corresponding capitals rose as their most distinctive elements. The reduced distance between the columns was mostly a structural need. Spanning large distances could not be achieved because it was difficult to transport large stone blocks and at the same time stone has a rather low tensile strength.

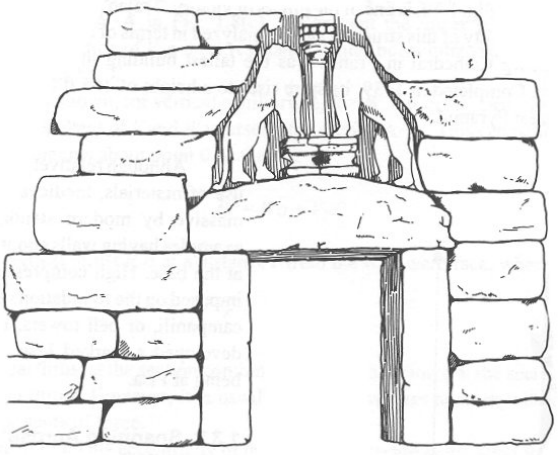

Figure 2.2 – Lion Gate at Mycenae (Drysdale *et al.*, 1999).

Greek architecture in general, and temples in particular, were aesthetically perfect and based on strict rules of proportion and symmetry between the different elements, which represented an important milestone in the history of buildings. Limestone was usually the stone used to build structural elements as walls, columns and beams. The Parthenon (5th century B.C.) represents the most famous construction of the Greek architecture, see Figure 2.3.

Figure 2.3 – The Parthenon at Athens.

The Romans, with a strong and centralized empire, provided one of the most important steps in the construction of buildings. Contrasting with the Greeks, their architecture was not only concerned with temples and amphitheatres, but also with roads, bridges, aqueducts and harbours. They introduced many innovations directly related to materials, structural concepts and construction processes.

Together with an improvement of the quality of bricks, the brick size became more standardized and different shapes were produced for special purposes. Apart from that, the production of concrete, made of rubble, lime and special volcanic sand (pozzolana) revolutionized building construction. During the Roman period, innovative techniques were introduced in the construction of walls, using bricks or stones as facing, finely finished, and filling the inner space with concrete, as shown in Figure 2.4.

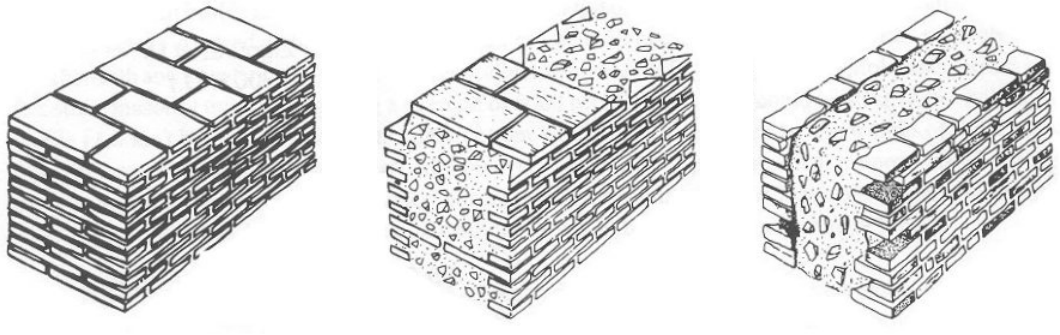

(a) (b) (c)

Figure 2.4 – Roman masonry walls: (a) bonded brick wall; (b) brick faced wall with header courses; (c) brick faced wall (Drysdale *et al.*, 1999).

The technique of dry stone block was also greatly improved and remarkable structures were built, such as the Colosseum (1st century A.D.) and Segovia's aqueduct (1st century A.D.), represented in Figure 2.5.

(a) (b)

Figure 2.5 – Dry stone constructions: (a) the Colosseum; (b) the Segovia's aqueduct.

Another significant structural advance was the change from linear to arched or curved structures, i.e. arches and vaults. The development of the arch allowed the replacement of cumbersome stone and vulnerable timber lintels in walls, with stone or brick masonry, spanning wider openings. In curved elements, it is common to find only compressive stresses in a given section, therefore no tensile resistant materials are needed. Structures made from units which simply touch each other could be built safely. Additionally, its cross-sectional area is large enough to avoid buckling instability or change of form, which can be improved when the arch is inserted in a wall. The resistive and adaptive capacity of arches against deformation or movement is enormous, as shown in Figure 2.6, and only a dramatic loss of the thrust at the springers leads to collapse.

(a) (b)

Figure 2.6 – The remarkable capacities of arches: (a) (Drysdale *et al.*, 1999); (b) (Croci, 1998).

Exploiting the structural form of the arch, the Romans constructed magnificent bridges and aqueducts all over their empire. One of the most outstanding examples is the Pont du Gard, see Figure 2.7, an enormous aqueduct formed of three tiers of arches and, except the top tier, made from dry stone masonry.

Figure 2.7 – The long aqueduct Pont du Gard, Nîmes, France.

Vaults can be seen as the three-dimensional extension of the arch in space. In the same way, domes can be regarded as the shape formed by rotation of an arch about its vertical axis. Barrel vaults and domes allowed the construction of large-span, durable, fire-resistant roofs. Great ingenuity was often shown and intricate and daring arrangements of vaults and domes were attempted. An excellent example is Hagia Sophia in Istanbul (6th century A.D.), see Figure 2.8. All these buildings generated from vaults and domes, though elegant in geometry, were massive in construction. They were essentially plate structures, with large thickness necessary to accommodate the thrust lines within the plates (Drysdale *et al.*, 1999).

Figure 2.8 – Hagia Sophia in Istanbul.

The fall of the Roman Empire caused an anonymous period in western architecture and it is only from the 11th century on that structural advances were made with the use of semicircular arches and barrel vaults. Churches and other buildings were marked by the presence of masonry towers. Another interesting structural form was represented by castles, which rapidly spread from Europe to the Middle East.

Gothic architecture, which originated in the 13th century, followed Roman architecture and represented a step forward where both architectural and structural functions were extraordinarily integrated together. Three major developments take place in order to convert the heaviness of Roman constructions to the lightness and openness of the later Gothic buildings. First, arch ribs were incorporated into roof structures, allowing the reduction of the thickness of the masonry spanning between the ribs. Second, the substitution of the semicircular arch by a pointed arch allowed a further reduction in weight, because the structure could follow the thrust lines more closely. The pointed arch provided architectural flexibility, since its shape helped solve the

complicated geometrical problems of lines formed by the intersection of different vaults of the same height but of different spans. Third, heavy supporting walls running across the thrust lines were substituted by flying buttresses and towers more aligned with the thrusts. These three major developments led to masonry-framed structures based on linear elements working in compression. The framing elements (rectilinear and curvilinear) were the columns, the arch ribs, the flying buttresses and the buttress wall or tower. Two of the most famous examples of Gothic architecture are illustrated in Figure 2.9, the Cathedrals of Amiens (13^{th} century) and Beauvais (13^{th} century).

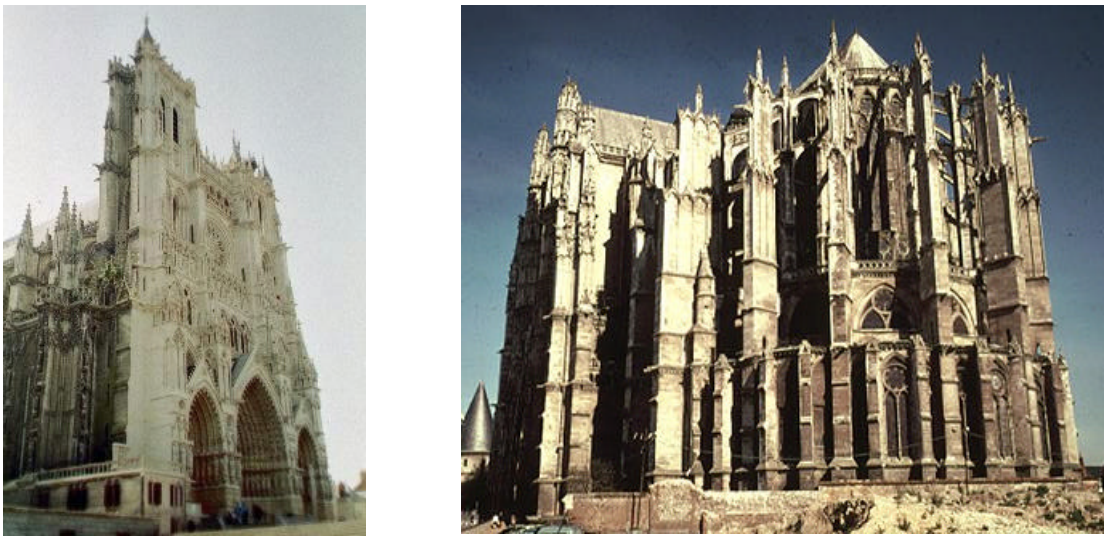

(a) (b)

Figure 2.9 – Famous Gothic structures: (a) Amiens Cathedral; (b) Beauvais Cathedral.

Based on innovative concepts and exceptional structural performance, the history of Gothic architecture is also marked by failures, cracks and permanent deformations, which represent the price to pay for abandoning traditional construction techniques.

Following Gothic architecture, Renaissance architecture, which born in Florence, brought new concepts of form and proportions, where buildings were characterized by regular forms and geometrical symmetry in plan and elevation. Churches, and in particular domes, are of great structural interest. Among them, two of the most interesting are undoubtedly the church of St. Maria del Fiore in Florence (15^{th} century) and the church of St. Peter in Rome (16^{th} century), see Figure 2.10. Their domes are characterized by the use of main ribs and by the construction of two shells, connected between them by these ribs. This arrangement reduces the weight during construction and allows a better solution for changing the inner and outer shape of the dome.

(a) (b)

Figure 2.10 – Famous Renaissance church domes: (a) St. Maria del Fiore in Florence; (b) St. Peter in Rome (Drysdale *et al.*, 1999).

During the Baroque period, no relevant or innovative solutions concerning the structural conception were developed. In fact, structural concepts were influenced more by the search of new forms of expression than by the refinement of the structural function (Croci, 1998). Important examples in Europe are St. Paul's Cathedral in London (17th century) and the Panthéon in Paris (18th century).

The English industrial revolution of the 18th and 19th centuries represents another important milestone in the history of the building industry. It was the advent of new building materials such as steel and reinforced concrete and led to a radical evolution in building techniques. The most characteristic structures of this period are probably the large steel bridges, such as the Firth of Forth Bridge in Scotland.

Nowadays, in Portugal, the use of masonry has become less important due to the progressive adoption of other structural materials, particularly concrete and steel. Its use has been reduced mainly to non-structural elements, such as cladding systems or infill panels. However, in several developed countries, especially in the USA, Canada, England, Germany and the Netherlands, the significant improvements in masonry materials and manufacturing, design methods and construction techniques have decisively contributed to the growth of masonry as a competitive building material (Drysdale *et al.*, 1999).

2.2 Experimental research on masonry structures

In spite of the need for reliable numerical analysis of historical masonry structures, only recently have researchers shown interest in developing and applying advanced constitutive models. Two main reasons may be referred to justify this situation: the higher complexity of masonry behaviour, when compared to other materials such as concrete or steel, and the absence of a comprehensive experimental description of the material, necessary to calibrate the numerical models. However, it has been shown that a complete set of displacement-controlled tests can be realistically carried out, with the purpose of properly describing the structural response of masonry and its components and thus obtaining the necessary properties for the use of advanced numerical models, see CUR (1997) and Lourenço (1998).

Masonry is a heterogeneous material composed of units of natural or artificial origin jointed by dry or mortar joints. Irregular stones, ashlars, adobes, bricks and blocks have been used as units. The units can be joined together using mortar (commonly clay, lime or cement based mortar) or just by simple superposition. With these two components, a large number of arrangements can be accomplished, generated from the different combinations of units and joints. A possible classification of stone masonry is shown in Figure 2.11. For brick masonry, the most used combinations are illustrated in Figure 2.12.

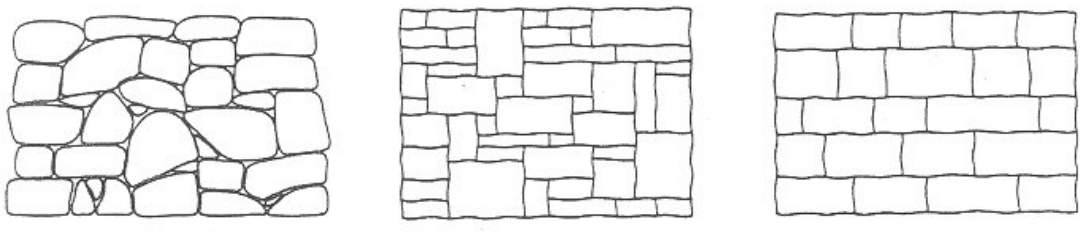

(a) (b) (c)

Figure 2.11 – Different kinds of stone masonry: (a) rubble masonry; (b) ashlar masonry; (c) coursed ashlar masonry (Lourenço, 1998).

However, the mechanical behaviour of the different types of masonry generally exhibits a common feature: a very low tensile strength. This property is so important that it has determined the structural form of historical constructions.

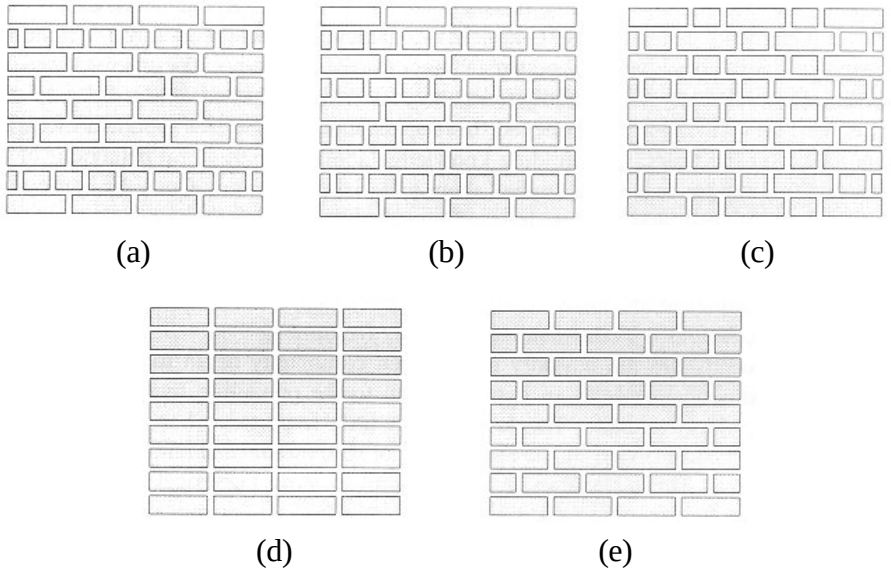

Figure 2.12 – Different arrangements for brick masonry: (a) American (or common) bond; (b) English (or cross) bond; (c) Flemish bond; (d) stack bond; (e) stretcher bond (Lourenço, 1998).

Achieving good characterization of ancient structures and materials, detailed enough in order to be used by advanced numerical models, is, most of the times, a very demanding task, both in time and cost. On the one hand, the possibility of performing non-destructive and minor destructive tests is very interesting since it allows one to obtain valuable data. Unfortunately it does not provide enough information about the characterization of the structural material required by advanced modelling. On the other hand, the feasibility of performing destructive tests on ancient constructions, either in-situ or by removing samples large enough to be representative, may be seen almost as an idealistic hypothesis since it is most of the times not possible. So, usually, the option is to carry out laboratory tests on masonry specimens representative of real constructions. However, this possibility turns out to be very complicated due to the enormous variations of masonry and to the impossibility of reproducing all its features in a specimen. Consequently, most of the effort devoted to experimental research in masonry has been directed towards brick and block masonry and its relevance for design. Nevertheless, most of what will be described henceforth in this Chapter can be applied to any type of masonry, in which bonding, cohesion and friction between units form the basic mechanical actions.

2.2.1 Uniaxial behaviour

The uniaxial behaviour, obtained under displacement-controlled tests, is usually characterized by the establishment of a stress-displacement diagram, in which the most important features that

characterize the behaviour of the material should be included, namely the complete pre-peak branch, the peak load and significant part of the post peak branch. In the case of cyclic experiments, features such as strength and stiffness degradation as well as energy dissipation should be also adequately characterized. An important feature, common to all frictional materials, is the occurrence of softening after peak, which is defined as a progressive decrease of the mechanical strength under continuous imposed displacement. Softening behaviour is experimentally observed in uniaxial compressive, tensile and shear failure.

Compressive testing

Compressive strength experiments on masonry prisms are rather easy to carry out. Until a few years ago, importance was only given to the evaluation of the ultimate load and, due to that, post-peak behaviour of the masonry is practically non-existent. This gap in knowledge was an encouragement to the execution of uniaxial cyclic compressive tests in both masonry prisms and unit specimens, including the characterization of the post-peak behaviour, which are described in detail in Chapter 3.

Stacked bond prisms or wallets, such as the RILEM test specimen (RILEM, 1994b), are frequently used to assess the uniaxial compressive strength of masonry. In a stacked bond prism loaded in uniaxial compression, the mortar tends to expand laterally more than the brick, due to their different elastic properties (softer mortar behaviour). The continuity between bricks and mortar, assured by cohesion and friction, creates a lateral confinement to the mortar. As a result, shear stresses develop at the mortar-brick interface, producing a triaxial compressive stress state in the mortar and bilateral tension coupled with uniaxial compression in the brick. Consequently, failure generally occurs by the development of cracks in the bricks, parallel to the loading direction.

Following the pioneer study of Hilsdorf (1969), many researchers (e.g. Hendry *et al.*, 1981; CEN, 1995) have tried to derive a relation between the compressive strength of masonry and the compressive strength of its single components, units and mortar. However, regarding advanced numerical modelling, these procedures are not very interesting since they do not provide any other information besides the initial stiffness and compressive strength of masonry. Therefore, masonry prisms have to be tested under displacement-controlled experiments.

It has been shown that the behaviour of masonry prisms under uniaxial compressive loading is clearly influenced by both the size of the specimen and the boundary conditions (Vermeltfoort, 1997). Both strength and cracking behaviour are influenced by the boundary conditions. Top and bottom bricks remain undamaged when typical steel plates are used, due to the confinement effect produced. On the other hand, when teflon is placed as an interposition material, the end bricks crack. This effect was already demonstrated for concrete specimens, e.g. Vonk (1992), who showed that under compressive loading due to cracking localization, the softening behaviour is dependent on the specimen's size and on the boundary conditions. Nevertheless, in spite of the boundary conditions, if an appropriate slenderness ratio is adopted (Neville, 1995), it is at least possible to ensure a uniaxial behaviour in the center of the specimen.

With respect to the mechanical behaviour of dry joint masonry under compression, almost nothing is known. Roca *et al.* (2001) performed a series of uniaxial compressive tests on dry joint stone masonry and mortar joint stone masonry, where it was observed that dry joint specimens show a lower compressive strength than those built with mortar joints. This can be explained by the lack of interlayer material, which promoted stress concentrations in a few discrete contact points, leading to the formation of vertical cracks in the stones. In addition, significant scale effects were identified, which strongly affected the compressive strength of the specimens. However, more research is clearly needed in order to fully understand the behaviour of dry joint masonry.

The most relevant material properties concerning modelling are the compressive strength and the fracture energy (mode III), which, by definition, is equal to the area under the compressive stress-displacement diagram. When dealing with cyclic loading, aspects such as strength degradation between cycles, stiffness degradation and energy dissipation must also be properly characterized.

Tensile testing

The tensile bond strength of the unit-mortar interface is a very important mechanical property of masonry constructions, in both historical and new structures, since most of the times non-linear behaviour is originated by cracking in the mortar joints. It should be noted that the non-linear behaviour of the joints is controlled by the unit-mortar interface.

Different types of tests have been used to evaluate the tensile strength, but no clear consensus has been obtained about the best test set-up to be used. Basically, tensile bond strength tests can

be divided into two main categories (Jukes and Riddinton, 1998): direct tensile bond strength tests and flexural bond strength tests, see Figure 2.13 for a schematic representation.

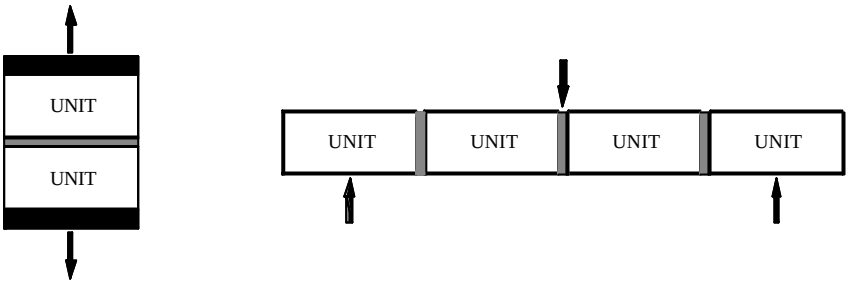

Figure 2.13 – Possible bond strength tests: (a) direct tensile bond strength test; (b) flexural bond strength test.

In the direct tensile test, it is required that the testing apparatus should be able to apply a uniform stress distribution at the unit-mortar interface, which is not easy to ensure. Flexural tests can also be used to obtain tensile bond strength data. The principle of this approach is to impose bending onto a masonry wallet until failure is achieved. In this way, flexural tests measure the bond strength at the edge of the mortar joint, but the strength at that point may not be representative of the strength of the all joint. Therefore, in the study of in-plane behaviour, direct tests should be preferred. Also, for the purpose of numerical modelling, the direct tensile bond strength test is the most interesting as it allows one to obtain the complete tensile stress-displacement diagram as well as the correct tensile strength. Tensile strength values derived from flexural tests need to be adjusted by a correction factor.

Van der Pluijm (1997) carried out monotonic direct tensile tests on masonry specimens of solid clay and calcium-silicate units under displacement control, whose results are illustrated in Figure 2.14(a), in terms of an envelope diagram. It was observed that the cracked specimens exhibited a bond area smaller than the cross sectional area of the specimen, see Figure 2.14(b). This net bond area seems to be concentrated in the inner part of the specimen, which can be attributed to a combined effect of setting of the mortar in its plastic phase and of shrinkage.

The most important material parameters concerning modelling are the tensile strength and the fracture energy (mode I), defined as the energy necessary to create a unitary area of a crack along the unit-mortar interface (area under the tensile stress-displacement diagram).

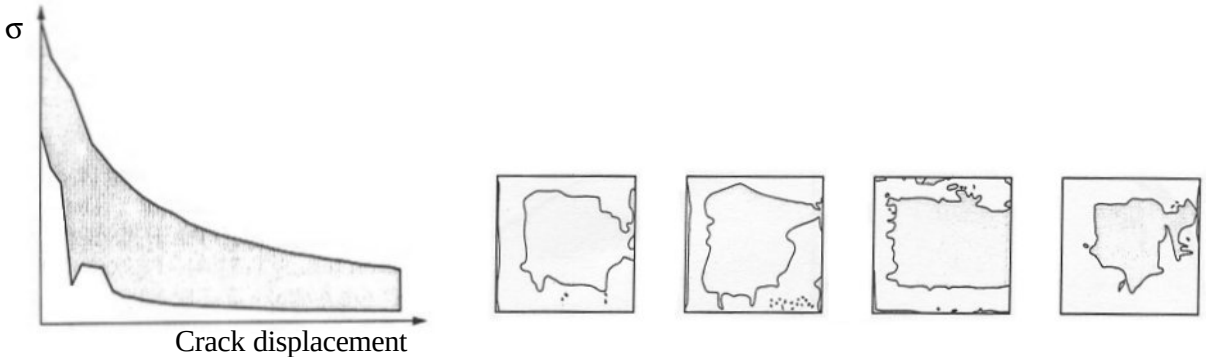

Figure 2.14 – Direct tensile tests: (a) typical experimental tensile stress-crack displacement diagrams represented in the form of an envelope curve; (b) typical tensile net bond areas (van der Pluijm, 1997).

Due to its great difficulty, cyclic, direct tensile tests on masonry specimens are practically absent from literature. In order to provide experimental data for the calibration of a numerical model, Jefferson and Mills (1998) carried out some cyclic flexural tests on notched concrete cylinders with mortar joints. However, more research concerning cyclic tensile tests has to be done, since knowledge on the cyclic tensile behaviour of masonry joints is absolutely fundamental, when dealing with cyclic numerical analyses, in order to fully characterise the opening-closing of the joints.

Shear testing

Shear has been identified as the governing mode of failure in masonry constructions subjected to lateral loads like wind and earthquakes, see e.g. Mann and Müller (1982). A certain degree of confinement present in the masonry walls is associ0061ted to these shear actions. Thus, pure shear mode is altered to shear-compression mode. This issue must be considered in testing, where direct shear loading applied to the joint has to be accompanied by normal loading. Direct shear tests are very demanding experiments because the test set-up, to be used idealistically, should generate a uniform state of stress on the joint. Moreover, this stress state should be kept constant during testing. These requisites are very difficult to attain since most of the time the shear load cannot be applied in line with the joint, originating, in consequence, an undesirable overturning moment for the joint, which creates a non-uniform normal stress state.

Different test methods have been proposed, see Jukes and Riddinton (1997) for a detailed description, but none has revealed to promote uniform stress distributions. The most common test configurations are the direct shear test, or couplet test (two units and one joint), and the triplet test (three units and two joints), see Figure 2.15.

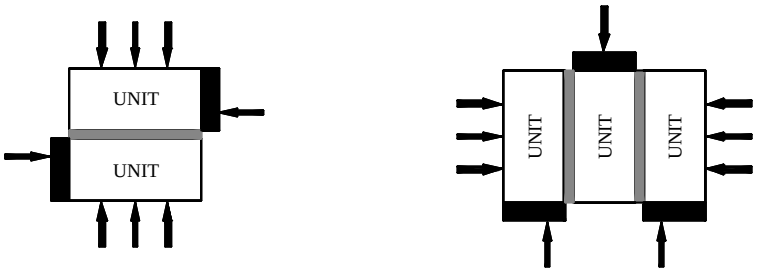

Figure 2.15 – Test set-ups for shear-compression loading: (a) couplet test; (b) triplet test.

Different arrangements have been developed in order to minimize the overturning moment applied to the joint. Van der Pluijm (1993) developed the couplet testing arrangement illustrated in Figure 2.16, which permits a constant compressive stress upon shearing. For this purpose, it is required that the specimen be rigidly attached to the steel loading elements.

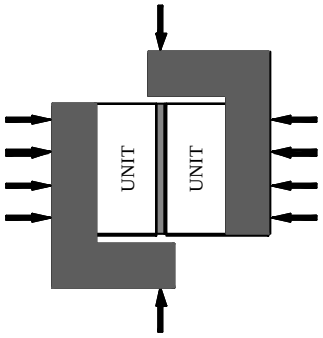

Figure 2.16 – Test set-up developed by van der Pluijm (1993).

Using the couplet testing arrangement shown above, van der Pluijm (1993) carried out the most complete characterization of masonry shear behaviour, for solid clay and calcium-silicate units, under monotonic loading, see Figure 2.17 for a schematic representation of the results. Besides the strength of mortar, the influence of joint thickness was experimentally detected on the shear strength and failure mechanisms at the unit-mortar interface. Binda *et al.* (1996b) demonstrated that the shear strength of the specimens decreases with the increase of the joint thickness.

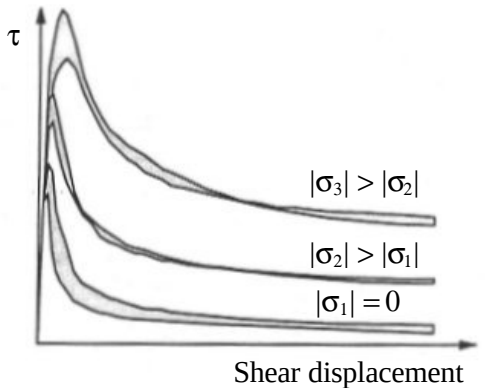

Figure 2.17 – Typical experimental shear stress-displacement diagrams (van der Pluijm, 1993).

For lower compressive stresses normal to the joint s, typically lower than 2 N/mm^2 (Jukes and Riddinton, 1997), the shear strength of the joint t is derived from a combination of bond shear strength (or cohesion) c and friction between the unit and the mortar, being expressed by the Coulomb friction law:

$$t = c - s \tan f \tag{2.1}$$

where f is the friction angle of the joint. Naturally, for dry joint masonry, the cohesion is equal to zero. Another important parameter concerning the structural behaviour of joints, especially when dealing with numerical modelling, is the dilatancy angle y. The ratio between the relative normal displacement and the relative tangential displacement along the joint is given by tan$y$. From displacement-controlled tests on ordinary masonry joints, it was observed that f and y are not equal and, additionally, y decreases when the normal compressive stress increases (van der Pluijm, 1993). For practical applications, zero dilatancy is recommended (Lourenço, 1996).

Experimental results concerning shear testing under cyclic loading are relatively scarce. The tests carried out by Atkinson *et al.* (1989) and Binda *et al.* (1996b), which used brick masonry specimens and a shear box testing apparatus, are the most relevant. This scarceness of experimental data becomes even more evident when dealing with dry joint masonry. In fact, cyclic shear tests performed on dry joint masonry are practically absent from literature. As such, the importance of such results to the calibration of advanced numerical models, has led Universidade do Minho to include cyclic shear testing on dry stone masonry into a wider research program concerning the mechanical behaviour of historical masonry structures. The novel results regarding cyclic shear experiments are presented in Chapter 3.

The most relevant properties for the modelling of shear behaviour are cohesion, friction angle, dilatancy angle and fracture energy (mode II), which is numerically equal to the area defined by the shear stress-displacement diagram and the residual dry friction shear level. When dealing with cyclic loading, an additional parameter to be evaluated is stiffness degradation. However, previous tests (Atkinson *et al.*, 1989; Binda *et al.*, 1996b) and tests to be described in Chapter 3 have shown that no relevant stiffness degradation takes place under cyclic shear loading.

2.2.2 Biaxial behaviour

Masonry can be regarded as a discontinuous material. Bed and head joints are responsible for its discontinuous nature. This feature becomes evident when considering dry joint masonry. By acting as planes of weakness, the joints induce an anisotropic behaviour in both elastic and plastic domains. Therefore, the strength of masonry is highly dependent on the orientation of the principal stresses with respect to the material axes (bed and head joints). Moreover, this anisotropic behaviour is further marked if the units exhibit anisotropic strength properties. Therefore, constitutive behaviour of masonry under biaxial stress states cannot be completely described from the constitutive behaviour under uniaxial loading conditions (Lourenço, 1996). Due to its anisotropic nature, the biaxial strength envelope of masonry is described by a three-dimensional surface, either in terms of the full stress vector in a fixed set of material axes or in terms of the two principal stresses and the rotation angle between the principal stresses and the material axes.

Only few attempts were performed to obtain the complete experimental in-plane strength envelope for masonry. The most complete experimental research concerning the characterization of biaxial behaviour of masonry was done by Page (1981, 1983), see Figure 2.18. The tests were performed on half scale brickwork panels, made of solid clay units, submitted to proportional biaxial loading. Both the orientation of the principal stresses relative to the material axes and the principal stress ratio had a great influence in the strength and failure modes. The different failure modes are shown in Figure 2.19. In all uniaxial loading cases, failure was brittle and occurred in planes normal to the panel, by cracking either the mortar joints alone or in a combined mechanism involving both brick and joints. In biaxial compression, failure occurred by splitting of the specimen at mid-thickness, in a plane parallel to its free surface, independent of the

orientation of the principal stresses. Due to testing complexities, experimental results in the biaxial tension range were not performed.

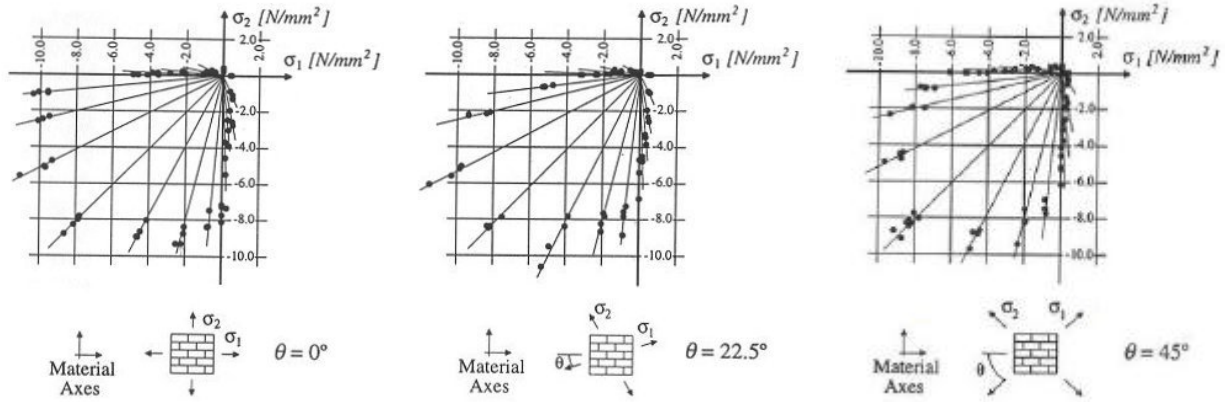

Figure 2.18 – Biaxial strength of solid clay brickwork panels (Page, 1981, 1983).

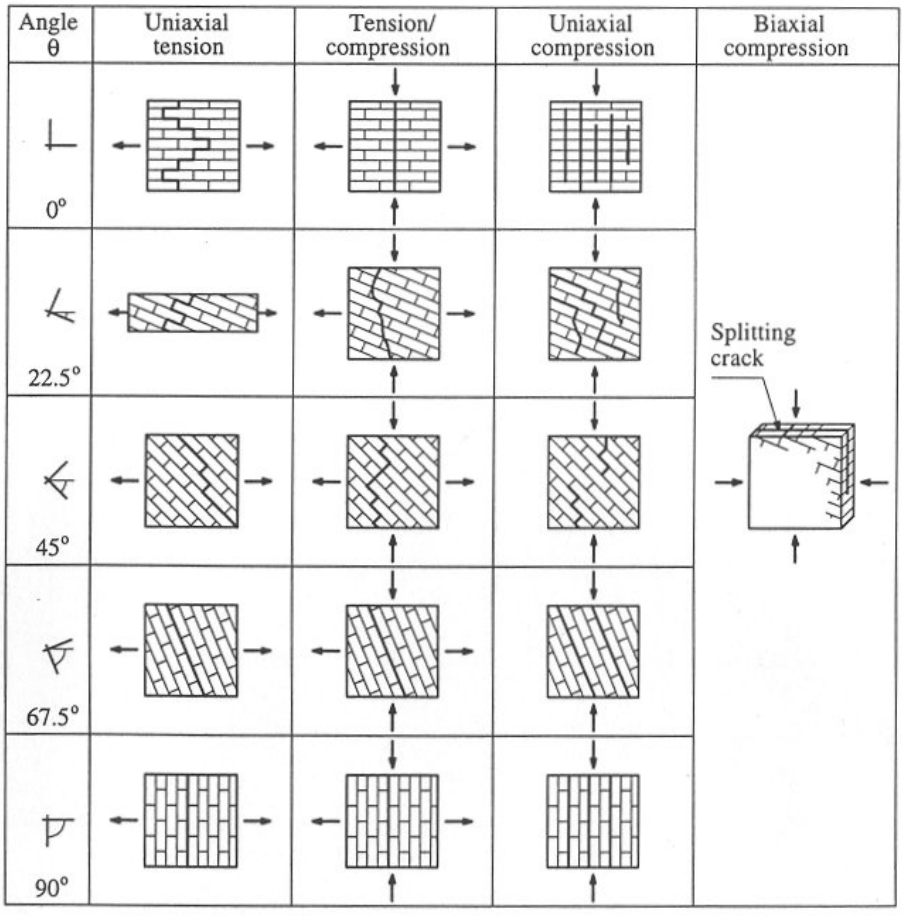

Figure 2.19 – Different modes of failure of solid clay brickwork panels under biaxial loading (Dhanasekar *et al.*, 1985).

In addition, it is noted that the biaxial strength envelope obtained by Page (1981, 1983) is of limited applicability for other types of masonry. Most likely, different biaxial strength envelopes and different failure modes may be obtained for different materials, shapes and geometry. Biaxial strength envelopes are rather useful to understand the biaxial behaviour of masonry, but for the development of advanced numerical models, a characterization based on the definition of the complete load-displacement diagrams is fundamental, necessarily including the softening behaviour.

2.2.3 In situ testing and monitoring

In addition to the laboratory tests described above, in situ testing can provide important information concerning the characterization of historical structures. In fact, issues such as the existing damage level in the structure or the composition of inner cores, can only be assessed by resorting to in situ tests. This means that, for most existing historical masonry constructions, the complete knowledge of the mechanical characteristics of their components, when available, does not necessarily assure a suitable understanding about the structural strength capacity. For such structures, complementary in situ tests are then required. Experimental data provided by in situ tests is, therefore, of great interest when used together with laboratory data for correct calibration of numerical models and evaluation of the analysis results. Therefore, for a given structure, once the constitutive model is properly calibrated against experimental results, numerical simulations of actions, such as earthquake loading, can be reliably carried out, which generally are impossible to perform on the existing structure.

Prior to any in situ testing, a preliminary investigation is needed in order to provide a wide knowledge of the structure under analysis (Rossi, 1997). In first place, an accurate geometrical survey must be carried out, in order to characterize the geometry of the structure as well as to identify possible geometrical irregularities. Afterwards, a crack pattern investigation should be performed. A detailed survey of the existing cracks as well as that of their width allows an early assessment of equilibrium and the establishment of possible instability causes. In addition, an analysis of the construction history is necessary to identify the structural building phases, the construction techniques used and possible strengthening interventions performed in the past.

Non-destructive and minor destructive tests

Non-destructive and minor destructive tests are used to evaluate the mechanical characteristics of ancient masonry structures. Non-destructive tests can be distinguished from minor destructive

tests because they do not exert a direct action on the masonry. Many times, diagnostic investigations on a given structure are performed using non-destructive testing techniques, such as sonic methods or radar techniques. Sonic methods consist in the generation of sonic or ultrasonic impulses at a point on the structure. The time the impulse takes to cover the section of material between the generator and the receiver is then qualitatively correlated with some masonry characteristics, such as its homogeneity. The radar technique uses high frequency waves and can be used to determine the location of the internal defects in masonry. Non-destructive testing equipment is, in general, not very expensive and testing is relatively simple to perform (Rossi, 1997). However, the results concerning non-destructive tests have a qualitative nature and only give a preliminary evaluation of the mechanical characteristics of masonry.

For some materials, as masonry, it is possible to obtain experimental data about their mechanical properties by using techniques that only slightly and damage temporarily the structure, which is easily repaired after testing. Usually, these techniques are denoted as minor destructive tests (Rossi, 1997). This class of tests allows a quantitative determination of the parameters that influence the mechanical behaviour of masonry, e.g. Young's modulus. Due to the minor damage induced onto the structures, slightly destructive testing techniques are especially convenient when testing valuable historical buildings. From the several testing methods included in this class, only the most well known will be briefly mentioned. For a comprehensive introduction the reader is referred to Bøving (1989) and Suprenant and Shuller (1994). In the case of masonry composed of multi-layers, the coring technique is often used. This method consists in the coring of small diameter boreholes and taking samples in the most representative sections, which can be mechanically tested. The boreholes can be used later for video survey, which can provide valuable information about the existence of internal cavities and cracks. Another common minor destructive technique is the flat-jack test. First used in the field of rock mechanics, flat-jack testing was later adapted by Rossi (1982) to be used on masonry structures. Nowadays, the flat-jack technique is used in the following tests:

- Evaluation of the compressive stress state of masonry;
- Evaluation of the compressive deformability properties of masonry;
- Evaluation of the shear strength along the mortar joints.

The compressive stress state is evaluated using a single flat-jack placed inside a cut mortar bed joint. To evaluate the deformability characteristics of masonry, a cut parallel to the first one is

made and a second flat-jack is inserted in this second cut. Therefore, the uniaxial compressive deformability properties of the masonry sample between the two parallel horizontal cuts can be assessed, including loading-unloading behaviour. The flat-jack method also allows the measurement of the shear strength along a mortar joint, although this technique is seldom used. This test implies the removal of a brick from the center of the masonry sample delimited by the two flat-jacks. A hydraulic jack is then put in the place of the removed brick and shear load is applied. This test allows one to obtain the peak and residual shear strength of the mortar joints. By performing this test on other places on the structure with different compressive stress states, it is possible to compute the friction angle and the cohesion of the mortar joints. All these evaluations can be done with minimum disruption to the masonry, since flat-jack testing requires only the removal of a portion of mortar joints and some individual bricks, which can be easily repaired to its original condition.

An important and promising technique of the non-destructive kind is dynamic identification (Fanelli and Pavese, 1993; Doebling *et al.*, 1996). This method is based on the measurement of the vibration response, in terms of amplitude and frequency content, of the structure to a given excitation and can be used to monitor the structure both locally (identification of properties of a single part) and globally (characterization of its overall properties). This method is based on the fact that the dynamic response of the structure to natural excitations of the environment (e.g. wind) or to artificial excitations (e.g. railroad traffic, vibrodyne), characterized by its dynamic parameters (natural frequencies, modal shapes and damping ratios), is a function of the stiffness, the mass, the damping and the boundary conditions. The knowledge of these parameters allows the numerical computation of the structural response to any known dynamic action as well as the localization of possible damaged zones in the structure. On the other hand, dynamic identification tests repeated over a length of time allow the assessment of damage evolution, since changes in the physical properties of the structure will cause detectable changes in the modal parameters.

Destructive tests

The analysis of a historical masonry construction can rarely be based on destructive tests on the original material. In cases of reconstructions or demolitions and when representative samples of masonry can be removed to be tested in laboratory, valuable data concerning the strength and deformability properties of masonry can then be obtained. This experimental data may further be extended to similar masonry structures, which had been built with similar materials and the same

building techniques. As an example, extensive series of destructive tests were performed on masonry samples of the Civic Tower of Pavia, which collapsed in 1989 (Machi, 1992).

Monitoring

Diagnostic investigations of historical buildings are often accompanied by the installation of instrumentation for the monitoring of deformational behaviour of the structure with time. Monitoring systems have been widely used to observe and control the movements of cracks (opening and sliding), vibrations and other deformations (Bartoli *et al.*, 1996), in order to follow the structural behaviour in time. After defining the purpose of the measurement system, the details regarding the specific type of instruments to be employed, the nature of data acquisition system and the method of data interpretation can then be reasonably identified (Rossi and Rossi, 1998).

If the sensors measuring the effects (e.g. settlements, displacements, tiltings, opening of cracks) are complemented by sensors measuring the possible causes (e.g. temperature, wind), then numerical models can be calibrated through the simulation of the measured causes and effects. In this way, the acquisition of data via monitoring systems contributes to a better understanding of the structural behaviour of ancient constructions and constitutes a reliable method to the assessment of the static condition of the structures (Rossi, 1997). Large monitoring systems are currently being used on the Florence Cathedral, the Pavia Cathedral, the Pisa Tower and the Mexico City Cathedral (Macchi, 1997).

2.3 Numerical modelling of masonry structures

Due to the high complexity of masonry behaviour, the approach towards the numerical simulation of its structural behaviour has led researchers to develop several constitutive models characterized by different levels of complexity. From the solutions based on the classical plastic methods (Heyman, 1995) to the most advanced computational formulations, a wide series of numerical methods is available nowadays. The definition of the most suitable method depends on, among other factors, the structure under analysis, the available input data and the analyst's experience and qualifications (Lourenço, 2002). It is possible that different methods lead to different results, depending on the adequacy of the numerical tool to the sought information. The best method might be defined as the method that provides the sought information in a reliable manner, i.e. within an acceptable error, with the least cost.

2.3.1 Idealization of structural behaviour

In order to solve a given structural problem, several idealizations of material behaviour can be established, each of them being necessarily associated with different degrees of complexity. Naturally, different types of constitutive models (i.e. different descriptions of the material behaviour, associated with different idealizations of the geometry, such as two- or three-dimensional description), originate a sequence, or hierarchy, of models, which allow the analysis to include more complex response effects as well as more costly solutions.

When dealing with masonry structures, the most common idealizations of material behaviour are elastic behaviour, plastic behaviour and non-linear behaviour. These different idealizations are schematically represented in Figure 2.20, where each idealization is represented by a typical general load-displacement diagram.

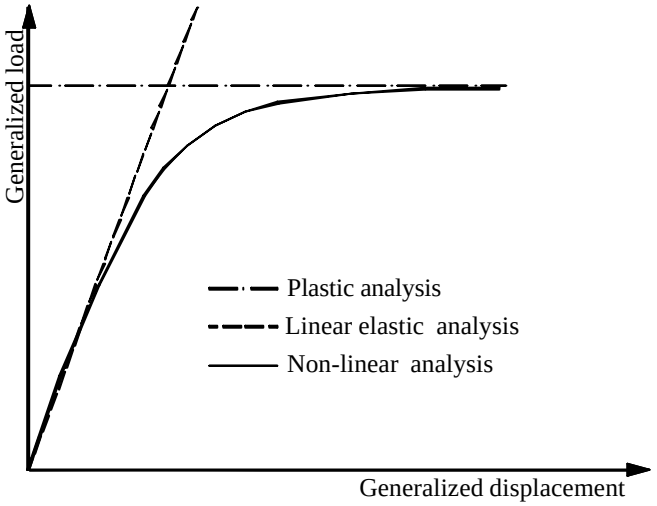

Figure 2.20 – General load-displacement diagrams of a structural analysis.

By adopting a non-linear analysis instead of a linear analysis, a more comprehensive insight into the structural response can be obtained, with a higher cost, both in terms of necessary input data and required knowledge of the analyst. In the following, a brief description concerning the three idealizations referred to above is given and the most relevant issues are discussed. Emphasis is given to non-linear behaviour, since the development of a non-linear constitutive material model able to perform cyclic analyses is one of the objectives of this study.

Linear elastic behaviour

The linear elastic analysis is the procedure usually followed in structural analysis, where the material is considered to exhibit an infinite linear elastic behaviour, both in compression and tension. In the case of masonry structures, where joints possess relatively low tensile strength, or even no-tensile strength in the case of dry joints, cracks arise at low stress levels and, therefore, the assumption of elastic behaviour is quite debatable.

In general, linear elastic analyses are not appropriate for ancient constructions (Macchi, 1997). However, in a first stage of analysis, the hypothesis of linear elastic behaviour can be of great help to the analyst. Linear analysis requires little input data, being less demanding, in terms of computer resources and engineering time used, when compared with non-linear methods. Moreover, for materials with tensile strength, linear analysis can provide a reasonable description of the process leading to the crack pattern.

Plastic behaviour

Plastic analysis, or limit analysis, is concerned with the evaluation of the maximum load that a structure can sustain (limit load). The assumption of plastic behaviour implies that, on one hand, the maximum load is obtained at failure and, on the other hand, the material should possess a ductile behaviour. Apparently, this last requirement seems to be unrealizable since the plastic deformations may exceed the ductility of the masonry. However, the limited ductility in compression does not play a relevant role as collapses, except in the case of columns, are generally related to the low tensile strength (Croci, 1998). Thus, the assumption of a zero tensile strength renders the method of plastic analysis as adequate for the analysis of masonry structures.

The plastic analysis is either based on the lower bound (static) method or on the upper bound (kinematic) method. The objective of both methods is to determine the multiplier of a pre-established load distribution on the structure that leads to failure. The static method uses the equations of equilibrium, and the multiplier (calculated by equilibrium conditions) forms a lower bound for the limit load. In the kinematic method, the structure is transformed into a mechanism by introducing plastic hinges or yield lines. Then, by applying the principle of virtual displacements, each mechanism is associated with a load multiplier. This multiplier forms an upper bound for the limit load. These two methods are often used in the analysis of masonry structures. Thrust line analysis is an example of the static method whereas the yield hinges

method for arches, where a collapse mechanism can be reliably identified, is an example of the kinematic method, see Figure 2.21.

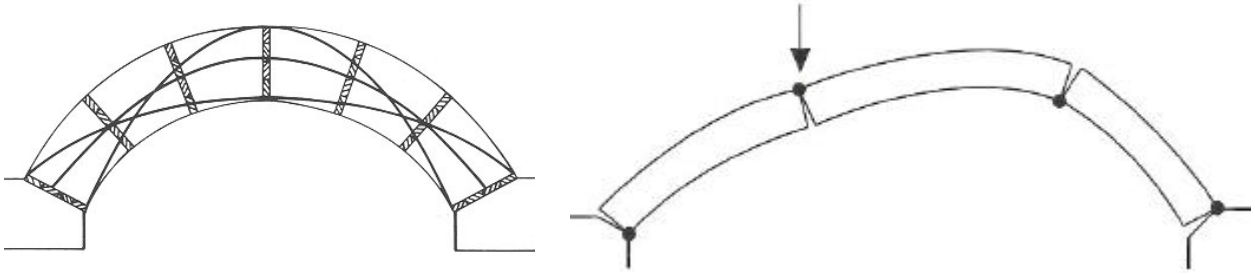

(a) (b)

Figure 2.21 – Plastic analysis of masonry structures: (a) alternative thrust lines in an arch - static method (Heyman, 1998); (b) four-hinge failure mechanism in an arch - kinematic method (Melbourne and Gilbert, 2001).

Non-linear behaviour

Non-linear analysis is the most powerful method of analysis, the only one able to trace the complete structural response of a structure from the elastic range, through cracking and crushing, up to failure. On the other hand, the existence of mortar or dry joints, generally the weakest link in a masonry assemblage and characterized by a marked non-linear behaviour, induces a non-linear response on masonry structures, even for moderate loads, e.g. serviceability loads. Therefore, non-linear behaviour, being the most complete method of numerical analysis, appears as the most adequate approach to be used in numerical simulations of masonry structures. But, as stated before, its use depends on which objectives are required from the analysis. If the sought information can be attained using a simpler method, which turns out to be less expensive or more in agreement with the expertise of the analyst, then its use is advised.

Several non-linear constitutive models have been developed for the analysis of masonry structures. The most popular theories used to formulate consistent constitutive models are plasticity and continuum damage mechanics, generally based on a phenomenological approach, i.e. the constitutive model is directly based on the observed features from experimental tests.

The first approach addressed here is the theory of plasticity. The first scientific work concerning plasticity goes back to Tresca's memoir in 1864 on the maximum shear stress criterion, see Lemaitre and Caboche (1985). Basically, the plasticity theory attempts to replicate the

dislocations of the material, being the plastic material behaviour characterized by the occurrence of permanent deformations. Initially developed for ductile materials, nowadays plasticity is extensively used for other materials such as soils, concrete and masonry. A number of non-linear models based on the plasticity theory aiming at the study of masonry structures have been developed in recent years, both for continuum and discontinuum approaches (Dhanasekar *et al.*, 1985; Stankowski *et al.*, 1993; Lofti and Shing, 1994; Pegon and Pinto, 1996; Lourenço and Rots, 1997; Lourenço *et al.*, 1998). The clarification of continuum and discontinuum approaches is given below. However, most of these constitutive models are unable to deal properly with cyclic loading since the plasticity theory, in its classical form, is only suitable for the modelling of monotonic loading conditions. To surpass this drawback, some enhancements have been introduced in the classical theory of plasticity, in order to incorporate, in a proper form, the most important features that characterize cyclic loading, such as stiffness degradation and hysteretic energy dissipation, see Chapter 5 for details. As an example, the model proposed by Pegon and Pinto (1996) is based on the plasticity theory and incorporates cyclic degradation in compression for continuum elements.

The plasticity framework is adopted in this study for the development of a phenomenological constitutive model for interface elements, according to the objectives presented in Chapter 1. Starting from a monotonic constitutive model formulated within the framework of the plasticity theory (Lourenço and Rots, 1997), an extension is proposed for the development of a constitutive model for interface elements, able to properly handle cyclic loading. For a comprehensive discussion, the reader is referred to Chapter 5.

The second approach to be considered is damage mechanics. A central issue in damage mechanics is the concept of damage itself. Damage is seen as the decrease in elasticity property as a consequence of a decrease of the area that transmits internal forces, through the appearance and subsequent propagation and coalescence of microcracks. As a result, in a damage process, the elasticity modulus is decreased (Maugin, 1992). Firstly introduced by Kachanov (1958) for creep-related problems, continuum damage mechanics has been further elaborated by several researchers (Lemaitre and Caboche, 1985; Kachanov, 1986; Mazars and Pijauduer-Cabot, 1989). In recent years, some damage models towards the analysis of masonry structures have been proposed, again both for continuum and discontinuum approaches (Papa, 1996; Gambarotta and Lagomarsino, 1997a, 1997b; Berto *et al.*, 2002).

In an engineering analysis, it is good practice that a non-linear analysis of a problem should always be preceded by a linear analysis. Based on the linear solution, the analyst is able to predict which parts of the structure will be more affected by non-linearities (e.g. low tensile strength) and, therefore, that should be studied more accurately, taking into account non-linear material models. When a non-linear analysis is preceded by a linear analysis, the effects of non-linearity are easily interpreted by comparison with linear results, and more confidence in the results can be established. In addition, physical non-linearity can be combined with geometrical non-linearity (the point of application of loads changes with the increase of actions) or with contact non-linearity (addition or removal of supports, or changes of contact between bodies with the increase of actions).

2.3.2 Modelling techniques for masonry structures

In the analysis of masonry structures, the existence of (mortar) joints is the major source of weakness and material non-linearities. Different levels of refinement have been used for the structural analysis. Depending on the degree of accuracy and the simplicity desired, the following modelling strategies can be used (Lourenço, 1996), see also Figure 2.22:

- Detailed micro-modelling: both units and mortar are discretized and modeled with continuum elements whereas the unit-mortar interface is represented by discontinuum elements;
- Simplified micro-modelling: expanded units are modeled with continuum elements, while the behaviour of the mortar joints and unit-mortar interface is lumped in discontinuum line interface elements;
- Macro-modelling: units, mortar joints and unit-mortar interface are smeared out in a homogeneous anisotropic continuum.

In the first approach, Young's modulus, Poisson's ratio and constitutive laws for both units and mortar are considered (Rots, 1991). Any analysis with this level of refinement is computationally very burdensome and only suitable for the detailed analysis of small specimens. In the second approach, masonry is considered as a set of elastic units bonded together by potential fracture/slip lines at the joints. Accuracy is lost since Poisson's effect on the mortar cannot be included (Lofti and Shing, 1994; Gambarotta and Lagomarsino, 1997a; Lourenço and Rots, 1997). Again, the large computational effort required even by simplified micro-modelling

strategies limits their applicability to the analysis of small structures. Additionally, micro-modelling can be accurately used for the calibration of the mechanical parameters of macro-models. In the third approach, masonry is considered a homogeneous anisotropic composite, where the behaviour of the composite is described in terms of average stresses and strains, assuming different elastic and inelastic properties along the material axes (Lourenço *et al.*, 1998; Berto *et al.*, 2002). Although this approach is very attractive for the analysis of large-scale masonry structures, it is not adequate for detailed studies and for capturing failure mechanisms in small masonry structures.

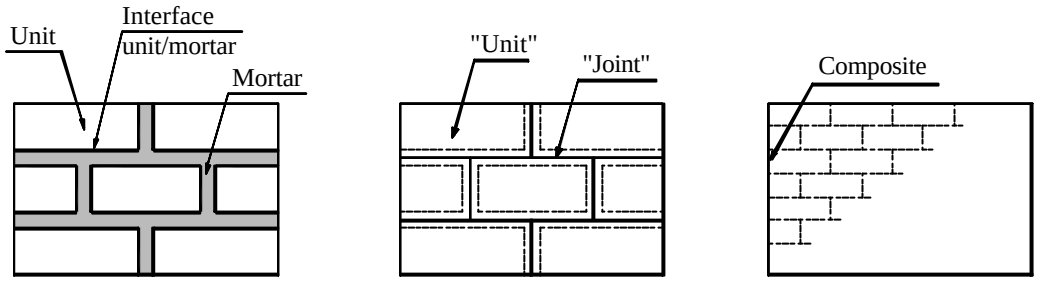

Figure 2.22 – Modelling strategies for masonry structures: (a) detailed micro-modelling; (b) simplified micro-modelling; (c) macro-modelling (Lourenço, 1996).

Following the description given above, it is clear that micro- and macro-modelling have different fields of application and one modelling strategy cannot be preferred over the other. The choice of the modelling strategy to be used, as well as the degree of refinement and accuracy, depends basically on the objectives of the study and the sought information. Moreover, this choice is constrained by the existing experimental data, required by numerical modelling.

In the following, the most important numerical modelling techniques concerning the analysis of masonry structures are presented. Particular emphasis is devoted to discontinuum finite element modeling since this approach will be amply used in the analysis of masonry structures in Chapter 4 and Chapter 5.

Structural elements and macro-elements

The simplest approach to the modelling of historical masonry constructions is based on the use of the standard techniques of structural analysis, where a structure is discretized in terms of a combination of structural elements, such as truss, beam, plate or shell elements. Generally, linear

elastic behaviour is assumed, but accurate non-linear analysis can also be carried out using structural elements. Molins and Roca (1997), based on the use of curved three-dimensional members of variable cross-section, analyzed skeletal structures considering elasto-plastic behaviour in compression and elastic-brittle response in tension, see Figure 2.23. The dependency of shear strength upon the applied compression was considered by means of the Coulomb failure criterion.

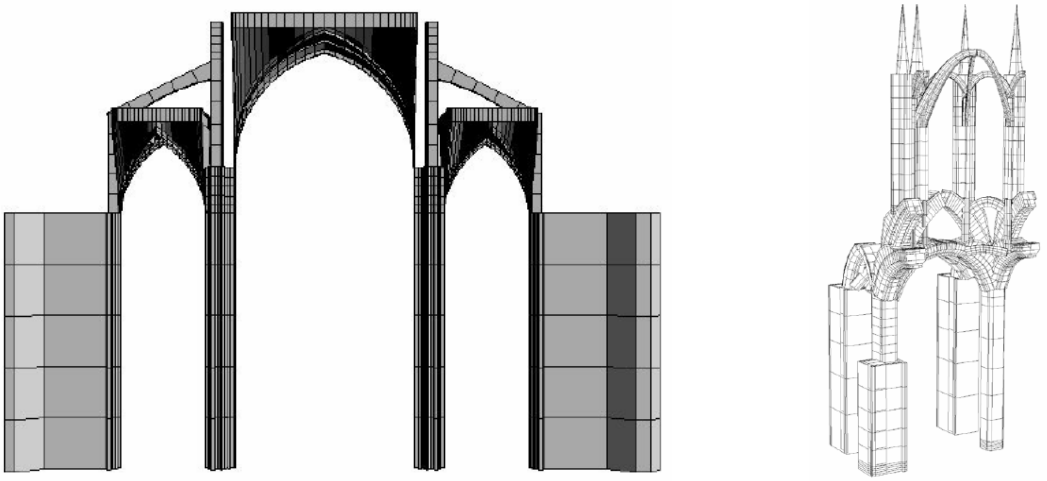

(a) (b)

Figure 2.23 – Beam models elaborated for the analysis of the Barcelona Cathedral: (a) plane model and (b) three-dimensional model with typical bay of the nave (Roca *et al.*, 1998).

For the study of buildings, important research efforts have been devoted to the development of (panel) macro-elements. Rigid and deformable macro-elements have been used for modelling walls and wall panels, resulting in a global model with a modest number of degrees of freedom. Diverse formulations have been proposed, e.g. either using rectangular damageable rigid macro-elements for incremental in-plane loading (Brencich and Lagomarsino, 1997), or using rigid blocks of variable form adopted for kinematic analysis (Giuffrè, 1993).

Continuum finite element models

The difficulty of achieving a suitable representation of historical construction components (e.g. piers and buttresses) through a discretization in terms of structural elements has led to the use of two- and three-dimensional continuum finite elements. In this approach, masonry is simulated as a homogeneous continuum. This higher level of refinement, involving a considerable number of degrees of freedom, implies an increase in computational effort that advises the use of the

continuum finite element approach for the analysis of partial or detailed models. However, quite large continuum finite element meshes are practicable with the actual computational resources. Figure 2.24 illustrates two well-known examples: the St. Mark's Basilica in Venice (Mola and Vitaliani, 1997) and the entire façade of S. Peter's Basilica in Rome (Macchi, 2001).

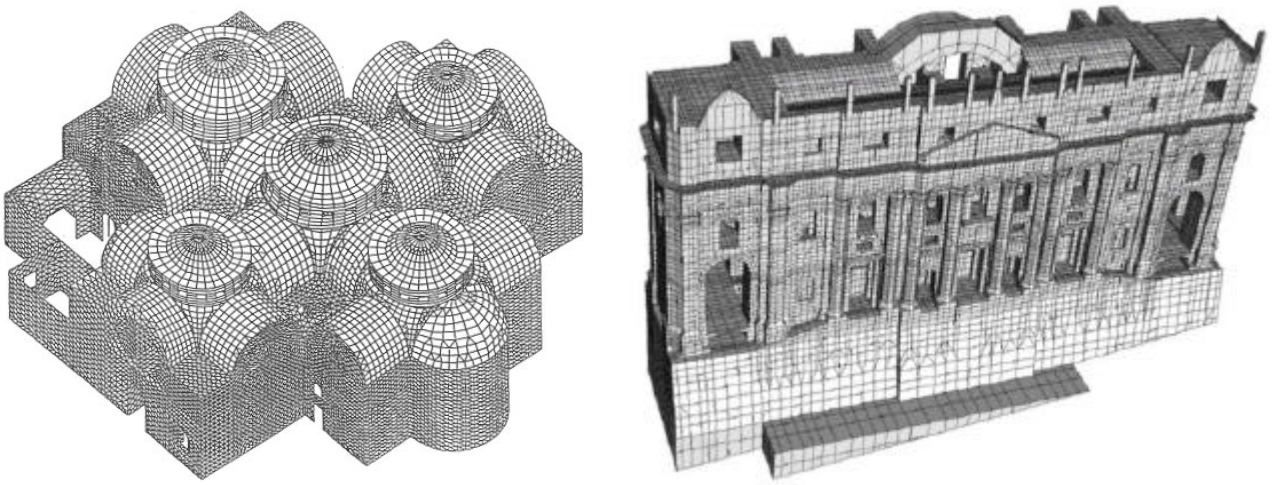

(a) (b)

Figure 2.24 – Finite element models: (a) St. Mark's Basilica in Venice (Mola and Vitaliani, 1997); (b) entire façade of S. Peter's Basilica in Rome (Macchi, 2001).

In such large finite element meshes, the most costly task is the generation of the mesh itself, which might represent several months of work. Considering the actual computational resources, structural analysis using simple non-linear models (as no-tension or ideal plastic models), that do not require much experimental data, are feasible. Assuming that a linear analysis can be carried out in one day and that a non-linear analysis can be performed in a week, the difference of cost between linear and non-linear analysis is not significant. The really costly task is the construction of the finite element model. Therefore, even a non-linear analysis based in a simple non-linear model should be preferable to a linear analysis.

However, the complexity associated with both the conception and implementation of consistent constitutive models and the analysis and interpretation of the results, have led, in many situations, to the adoption of linear elastic models. Many researchers have conducted linear analysis on historical constructions. Using an elastic finite element model, Mola and Vitaliani (1997) studied the St. Mark's Basilica in Venice, shown in Figure 2.24(a). The geometrical discretization of the structure was performed following the results derived from a photogrammetrical analysis and the model was calibrated using data obtained from previous monitoring and experimental tests. The

existing cracks were simulated using two distinct approaches: either by adopting a lower Young's modulus in the regions where diffuse micro-cracking were located or by introducing explicitly a physical separation between adjacent finite elements. The model was employed for the evaluation of the stress state in the various structural members and the related displacements produced by dead load, temperature and imposed displacements to the foundation. Adopting a global elastic finite element model, Croci (1997) analyzed the behaviour of the Colosseum in Rome under the effect of seismic actions, taking into account the different characteristics of the soil. This procedure allowed the identification of critical situations. Based on a critical analysis of the numerical data, preliminary criteria of intervention were indicated.

Several numerical studies on historical masonry structures have been performed at Universidade do Minho, using continuum finite element models and considering non-linear constitutive models. As an example, in Figure 2.25 is represented a three-dimensional finite element model adopted for a non-linear static analysis of a historical building complex located in Lisbon (Ramos, 2002).

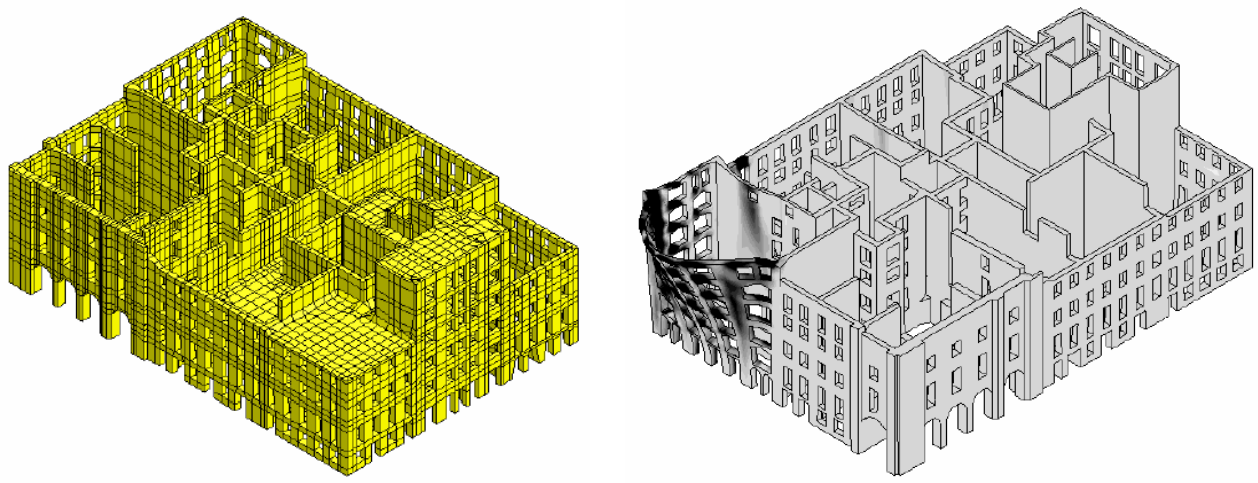

(a) (b)

Figure 2.25 – Finite element model of a block compound in Lisbon: (a) finite element mesh with 200.000 degrees-of-freedom; (b) results for seismic analysis using equivalent static loading, shading indicates damage levels (Ramos, 2002).

Modelling the behaviour of regular masonry assemblages may be addressed also by homogenization techniques. Basically, three different approaches might be considered (Zucchini and Lourenço, 2002). The first, very powerful, approach is to handle the brickwork structure of masonry by considering the salient features of the discontinuum within the framework of a generalized/Cosserat continuum theory (Mühlhaus, 1993). The second approach is related with

the rigorously application of the homogenization theory for periodic media to the basic cell, i.e. to perform a single step homogenization, with adequate boundary conditions and exact geometry (Anthoine, 1997). The third, and most used, approach aims at substituting the complex geometry of the basic cell by a simplified geometry so that a close-form solution of the homogenization problem is possible (Pande *et al.*, 1989; Zucchini and Lourenço, 2002). However, the regularity of masonry, required by homogenization techniques is rarely found in historical constructions, thus the phenomenological approach, based on experimental tests, has been followed towards the development of continuum constitutive models, able to describe masonry as an homogeneous material. Based on the phenomenological approach, various constitutive models have been proposed, as addressed in Section 2.3.1.

Discontinuum finite element models

By adopting a simplified micro-modelling strategy, the explicit representation of the joints introduces a discontinuity in the displacement field. Due to the higher computational effort required, discontinuum finite element models are especially adequate for the analysis of small masonry structures submitted to heterogeneous states of stress and strain. Discontinuities are generally introduced using interface elements, for which the constitutive model establishes a direct relation between the stress vector and the relative displacement vector along the interface, see Chapter 5 for further details.

Interface elements were initially used in the area of concrete by Ngo and Scordelis (1967), in the domain of rock mechanics by Goodman *et al.* (1968) and in the area of masonry by Page (1978), being used since then in a great variety of problems. Within the micro-modelling strategy, generally the units are assumed to behave elastically, whereas the overall non-linear behaviour is concentrated in the interface elements. Thus, for an accurate simulation of the masonry behaviour, it is essential to develop a constitutive model for the interface elements able to capture all the failure mechanisms of masonry, as cracking of the joints, cracking of the units, sliding over the joints and crushing of masonry.

Various constitutive models for interface elements have been developed. Lourenço (1996) developed a constitutive model for the monotonic analysis of interface elements (micro-modeling strategy) within the incremental theory of plasticity. The model has been checked

against experimental data, in which has shown great accuracy in reproducing experimental results, see Figure 2.26.

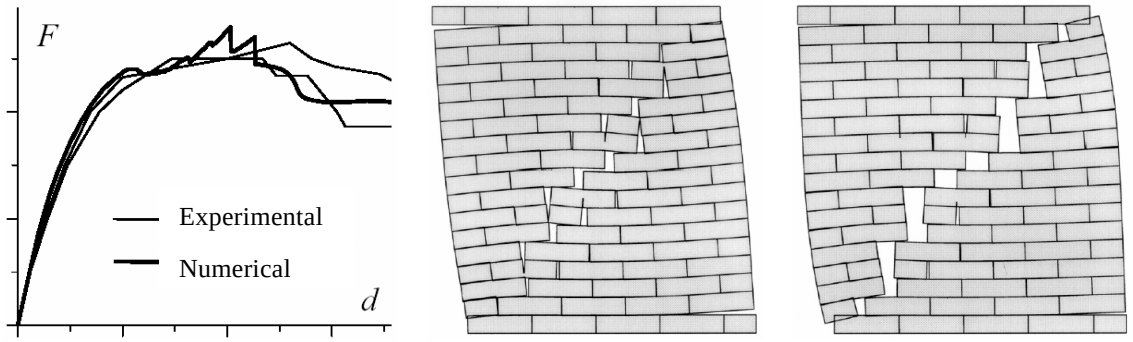

(a) (b) (c)

Figure 2.26 – Analysis of a masonry shear wall: (a) load-displacement diagrams; (b) deformed mesh at peak load; (c) deformed mesh at ultimate load (Lourenço, 1996).

Pegon and Pinto (1996) used a discontinuum finite element model to study the pillar-arch stone structure of the S. Vicente de Fora Monastery in Lisbon, tested under pseudo dynamic loading, see Figure 2.27. Both the stone block and the masonry wall were considered as being isotropic linear elastic, whereas joints were modelled by means of interface elements ruled by an elasto-plastic Coulomb friction law with small dilatancy. Unloading from the monotonic envelope was considered in a non-linear fashion for the normal stress component.

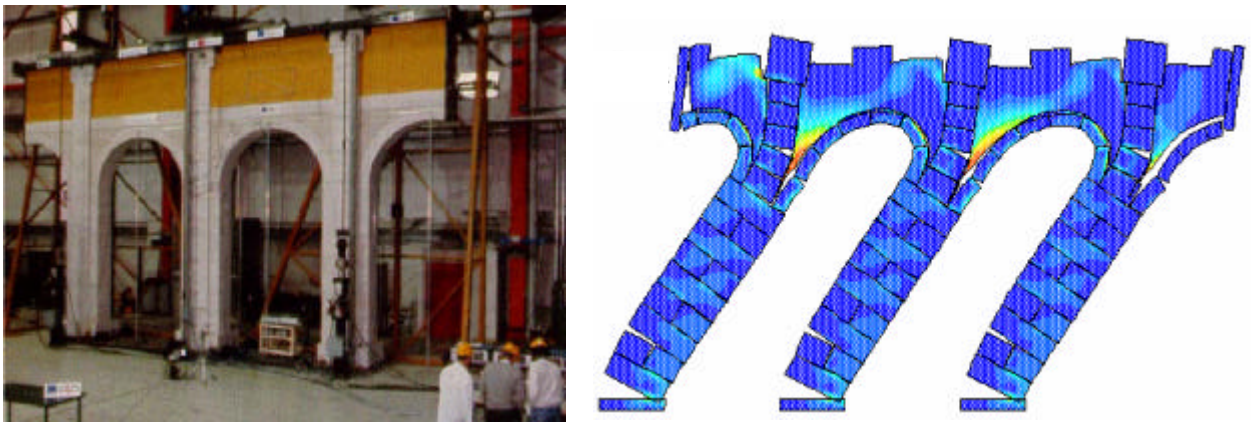

(a) (b)

Figure 2.27 – Monastery of S. Vicente de Fora, in Lisbon: (a) full-scale model of the façade; (b) deformed mesh and stress patterns using interface elements (Pegon and Pinto, 1996).

Gambarotta and Lagomarsino (1997a) developed a constitutive model for mortar joints within the damage framework. The damage of the joints is measured by an internal damage variable

associated with the strain energy release rate, to which the inelastic strain components, normal and shear strain, are related. The proposed model assumes that masonry consists of continuum elements that behave elastically until an appropriate failure criterion is activated, bonded together by interface elements that represent the mortar joints.

Almeida (2000) carried out a study on a historical masonry structure using interface elements. Initially, a linear elastic analysis under seismic loading was performed in order to characterize the overall dynamic response of the structure. Afterwards, the sub-structuring technique was used to analyze the structural elements where non-linear behaviour was most likely to occur. For those elements, a static analysis was performed, adopting the non-linear constitutive law proposed by Pegon and Pinto (1996) for the interface elements.

Discrete element models

The discrete, or distinct, element method was proposed by Cundall (1971) for the study of jointed rock, modeled as an assemblage of rigid blocks. Later, this approach was extended to others fields of engineering, where the detailed study of joints is required, e.g. soils and other granular materials (Ghaboussi and Barbosa, 1990). This numerical technique has also been used to the modeling of masonry structures, where good quality results have been achieved (Pagnoni, 1994; Lemos, 1998a; Sincraian, 2001), see also Figure 2.28.

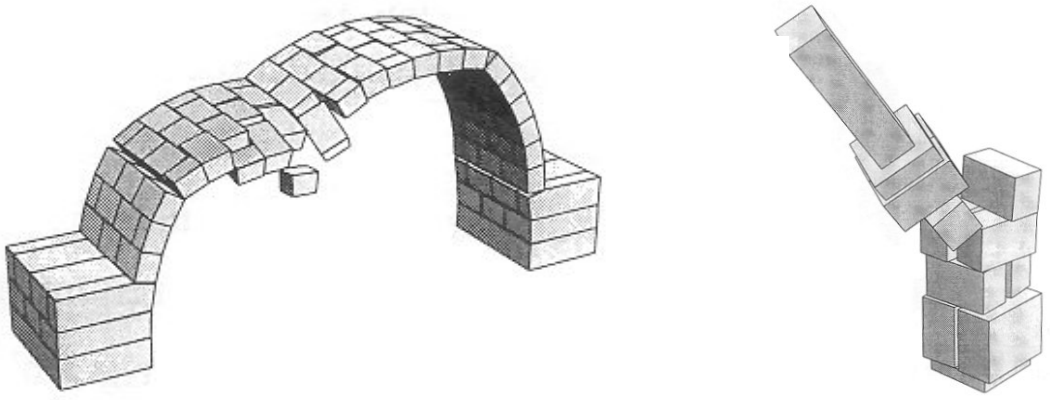

(a) (b)

Figure 2.28 – Analysis of masonry structures using the discrete element method: (a) masonry arch bridge (Lemos, 1995); (b) dry stone masonry pedestal sustaining a statue (Sincraian, 2001).

Within the discrete element method, blocks can be considered both rigid and deformable. For structures where relatively low stresses and deformations occur in the blocks, the hypothesis of undeformable blocks is rather realistic. On the other hand, the consideration of block deformability approaches discrete element method and discontinuous finite element method. Apart from solution techniques, the main difference between these two methods lies in the modelling of contact: discontinuous finite element models use interface elements and discrete element models are based on a point contact approach (Lemos, 1998b), i.e. at the interfaces the blocks are connected by means of contact points, since discrete element models are intended to simulate the large displacement range.

Limit analysis models

The applicability of limit analysis to masonry structures modeled as assemblages of rigid blocks connected through joints depends on some basic hypotheses (Orduña and Lourenço, 2002). The first hypothesis requires that the limit load occurs at small overall displacements, which is true for most cases. The second hypothesis is that masonry has zero tensile strength, which can be justified by the relatively low tensile strength. The third hypothesis requires that shear failure at the joints is perfectly plastic. This assumption is fully supported by experimental results. To end with, the fourth hypothesis is that the hinging failure mode at a joint occurs for a compressive load independent from the rotation. In the case of masonry crushing, this hypothesis might be questionable, but crushing behaviour (except for columns) seems to have minor importance in the response of masonry structures.

In many cases, the objective of the analysis is to estimate the maximum load that a structure can sustain prior to failure. In the analysis, the load distribution is known but the load magnitude that the structure can carry is unknown. Using limit analysis models, this load multiplier can be computed using either the static method or the kinematic method. Livesley (1978) was the first researcher to apply the limit analysis to rigid block arches, using the static method. Later, Gilbert and Melbourne (1994) applied the kinematic method to the same problem.

The limit analysis can be regarded as a practical computational tool, since it only requires a reduced number of material parameters and it can provide a good insight into the failure pattern and limit load. Current efforts have been done at Universidade do Minho aim at developing a design tool based on limit analysis, see Giuffrè (1993).

2.4 Summary

Our architectural heritage is mostly based on masonry constructions, from all of the historical periods that endured along the centuries. Due to damage accumulated with time, these structures require periodic inspections in order to assess their actual safety. To perform the structural assessment of a given structure, several idealizations of the material's behaviour can be established, each one of them necessarily associated to different degrees of complexity. Non-linear analysis is the most powerful method of analysis, and the only one able to trace the complete structural response of a masonry structure from the elastic range, through cracking and crushing, up to failure. Simpler constitutive models are easier to use and require fewer experimental data, but give less insight on the structural behaviour. On the other hand, advanced constitutive models demand a comprehensive description of material behaviour, are rather time consuming and require adequate knowledge of non-linear constitutive models by the analyst, but are fully able to describe the structural response. The choice regarding the adequacy of a given numerical tool depends on, among other factors, which objectives are required from the analysis. If the sought information can be achieved employing a simpler method, which turns out to be less expensive or more in agreement with the expertise of the analyst, then the usage of such a simpler method is advised. However, the lack of appropriate experimental data can restrain the use of advanced methods. This implies that, in parallel with the development of advanced numerical models, it is necessary to carry out comprehensive test programs, both at the micro- (specimens) and macro-level (structures) in order to supply data to the numerical models and also to validate numerical results against experimental results.

Concerning the modelling of in-plane behaviour of masonry structures, the material discontinuity introduced by the existence of the joints makes the use of interface elements within a finite element formulation a quite suitable option to model and understand such structures. This option has been followed in this study.

3. MECHANICAL TESTS ON STONE AND BRICK MASONRY

The use of natural stones and bricks as structural building materials has been known since ancient times. Over the centuries, their use has been improved and they have been applied in different forms all over the world, varying with culture and time. In fact, it can be observed that most of our historical constructions utilize stone and brick, laid dry or bonded with mortar, as a key building material. Historical constructions are defined here as buildings constructed before the advent of Portland cement, at the end of the 19th century. Nowadays, the role of these materials has become less important due to the progressive adoption of other structural materials, particularly concrete and steel, and therefore, their use has been limited mainly to non-structural elements.

In order to understand the mechanical behaviour of a given material or structure, it is fundamental to perform experimental tests. In this way, it is possible to characterize the material behaviour from the undamaged state through peak and also including the post-peak behaviour. But, if on one hand, it is almost impossible to carry out any kind of destructive test on elements belonging to historical constructions, on the other hand, the possibility of performing non-destructive tests, such as flat jacks, dynamic identification tests, impact echo or ultrasonic tests, e.g. Suprenant *et al.* (1994), is very interesting but does not provide enough information if a "complete" material description is needed. The word complete is used here in the sense that the description of the material includes the data necessary for advanced numerical models (Lourenço, 1998), obtained from complex deformation-controlled tests. Therefore, advanced material characterization has a huge importance when the use of accurate numerical models is intended. Numerical tools can only give reliable results if adequate experimental data are available. Consequently, the acquirement of material data necessary for advanced nonlinear numerical models is inevitably a key issue.

As referred in Chapter 1, the experimental research described in this study is a part of a comprehensive experimental program developed jointly by Universitat Politècnica de Catalunya (UPC), Barcelona, and Universidade do Minho (UM). With the exception of the direct shear tests, which have been carried out at UM, the remaining experiments described here were performed at UPC. Uniaxial monotonic and cyclic tests were performed in stone and brick specimens and prisms, aiming at a complete characterization of the cyclic behaviour of these

materials. Complementary to these tests, brick masonry walls and dry stone masonry walls were constructed and tested under combined compressive and shear loading. The experiments concerning dry stone masonry walls are fully described in Chapter 4 (where a numerical simulation is also included), while the tests concerning the brick masonry walls were performed outside the scope of this study. In both cases, if a numerical analysis of the structural behaviour of such structures is intended to be carried out, an appropriate experimental characterization of the constitutive materials is therefore required. Tests concerning this comprehensive material characterization were performed and are detailed described in this Chapter.

This Chapter is organized in six Sections. First, comprehensive tests concerning uniaxial compressive and direct shear behaviour of stone specimens are presented. The adopted procedure for testing is described in detail and the results are discussed. Then, results of four stone masonry prisms tested under compression are exhibited. Additionally, a comparison between the results obtained from specimens and prisms tests is established. Afterwards, uniaxial compressive tests on brick specimens are shown, being the results discussed with detail. Even using advanced control techniques, the compressive tests on stone and brick specimens were difficult to control, due to the brittleness of the tested materials. Therefore, only the successful results are reported in this study. Next, tests performed on brick masonry prisms are presented. Complementing the tests related to the brick specimens, tests concerning cement mortar specimens from different mixes are also presented. Four stacked bonded prisms made of five bricks each, were constructed and tested under cyclic loading. Finally, the most important conclusions are summarized and the main difficulties are pointed out.

3.1 Compressive tests on stone specimens

In order to fulfill the purposes initially set up in Chapter 1, the material chosen for the tests should be, as much as possible, similar to stones used for centuries in the construction of the monuments spread all over Catalonia. For this reason, a sandstone has been selected for all the tests concerning stones. It is a common and locally available stone, known as “Montjuic stone”. Initially, the stones were mechanically cut and delivered to the laboratory in small prismatic pieces ($20\times20\times10$ cm^3). Macroscopically, the stone presents a very homogeneous surface and a very small grain size. Also, it is impossible to define any kind of grain orientation or anisotropy, see Figure 3.1.

The complete load-displacement diagram for stones tested in unia xial compression has been obtained for decades, e.g. Cook (1965), and provide valuable information about its structural behaviour. During the initial development of the testing techniques, it became clear that, for some stones, it was impossible to obtain the full diagram without appropriate control techniques. As a matter of fact, for stone specimens that display a very brittle behaviour, the use of axial displacement as the control variable is not enough to ensure that post-peak behaviour can be obtained.

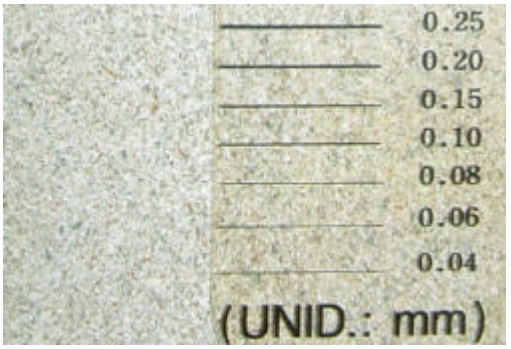

Figure 3.1 – Sandstone used for the tests (granulose texture with a very small grain size).

Two types of diagrams in terms of the characteristics of the post-peak region were identified by Wawersik (1968), see Figure 3.2. Class I diagrams are characterized by a monotonical increase in strain, where fracture propagation is stable in the sense that work must be done on the specimen for each incremental decrease in load-carrying ability (stable softening behaviour). In class II diagrams, fracture is unstable and the elastic strain energy absorbed in the material is sufficient to maintain fracture propagation until the specimen has lost all strength (unstable softening behaviour), as schematically illustrated in Figure 3.2.

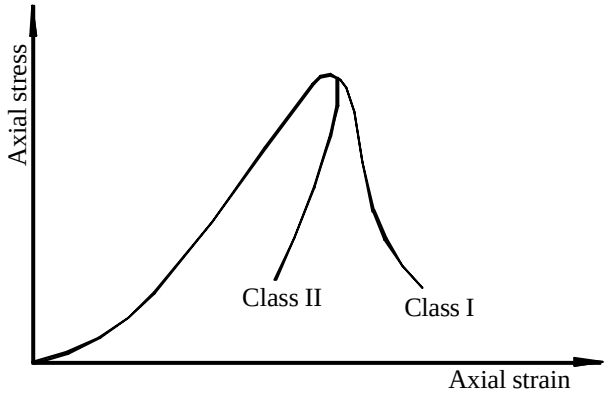

Figure 3.2 – Two classes of stress-strain behaviour observed in uniaxial compression tests of natural stones.

It is presently known that this response depends on the boundary conditions and on the size of the specimen, see Vonk (1992). In fact, compressive failure seems to exhibit local and non-local features.

3.1.1 Specimen preparation

The definition of specimen geometry depends on the type of test to be performed (e.g. compression, tension) and also on the control variable to be adopted. In order to ensure uniaxial loading, a height/diameter ratio (h/d) between two and three and a diameter preferably not less than 50 mm, are recommended if standard lateral deformations restraining steel plates are used, see Fairhurst *et al.* (1999), in order to secure a uniform stress distribution at least in the center of the specimen. The diameter of the specimen must be at least 20 times the largest grain in the stone microstructure. The h/d ratio highly influences the peak strength and the later decreases with the increase of the former, as showed by Neville (1995). The friction between the platen surface and the specimen, due to the higher platen stiffness value, creates a multiaxial stress state on the specimen extremities, which decreases with the distance from the platens. This confinement effect can be reduced if a low friction coefficient material is inserted between the specimen and the machine platens, like teflon, or by using steel brushes, see van Mier (1984) for a detailed approach. Here, it has chosen to adopt an h/d ratio such that a uniaxial stress state was ensured in the center of the specimen.

After grinding the top and bottom surfaces, cylindrical specimens (∅5×12 cm^3) were extracted from the prismatic stones by means of a drill, resulting in a h/d ratio equal to 2.4, see Figure 3.3. Using this ratio the confinement effect was expected to be absent and no additional provisions to eliminate this effect were taken.

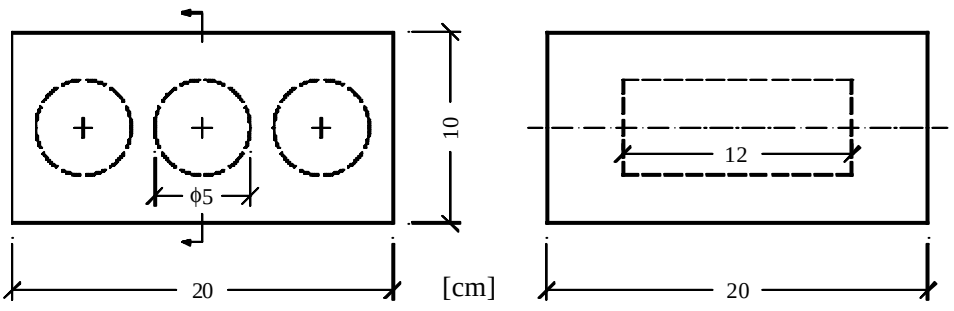

Figure 3.3 – Cutting scheme adopted for the stone specimens: front view and vertical cross-section.

The stone specimens (SS) will be denoted by the stone number and by the specimen number. Therefore, the reference SS2.3 represents the third specimen obtained from the prismatic stone nº2. In order to ensure correct sampling of the stones, the specimens were extracted randomly from different stone blocks. All the specimens were tested with their natural water content.

3.1.2 Test procedure

The closed-loop servo-controlled INSTRON testing machine used to test all the stone specimens has a 1000 kN load capacity and can work under several control techniques such as force, axial or circumferential displacement. The response time of the servo-valve was adjusted prior to the test, through the PID (Proportional-Integral-Derivative) feedback algorithm of the regulation system. For the stone specimens to be tested, a fast servo-system was needed, as for all materials exhibiting brittle response.

A circumferential linear variable differential transformer (LVDT) placed at the specimen mid-height and three axial LVDTs placed between the machine platens were used as displacement measurement transducers, see Figure 3.4. The applied force was measured by means of the machine load cell. Special attention was given to the transducers calibration and adopted testing procedures.

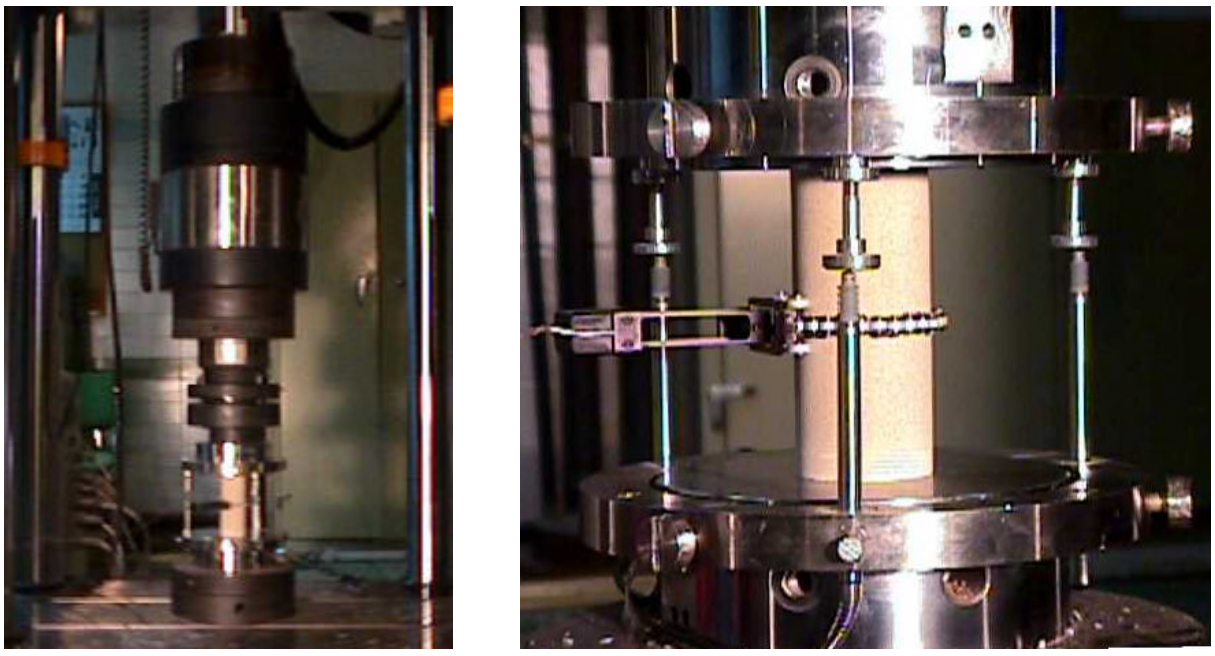

(a) (b)

Figure 3.4 – Testing set-up: (a) INSTRON machine; (b) measurement transducers arrangement.

Initially, the diameter and height of the specimen were measured and registered. Then, the specimen was put into the lower platen and carefully centered. Afterwards, a small preload was applied, in force control, in order to adjust the upper platen to the top surface of the specimen. This platen has a hinge to prevent any potential unfavourable effect due to non-parallelism between the specimen faces.

The following control variables were used for testing:

- Axial displacement control when the applied load was very small;
- Force control during unloading;
- Circumferential displacement control in general.

The displacement rate was kept about 5 μm/s and 1.5 μm/s in axial and circumferential control, respectively, and about 2 kN/s in load control. In this way, the peak load was reached in about 3 to 4 minutes and the complete test took from 70 to 90 minutes.

The axial displacement of each specimen tested was defined by the average value obtained from the three LVDTs placed between the machine platens. The axial strain was calculated by dividing the change in average measured axial length by the initial axial length of the specimen. The axial compressive stress was computed as the load divided by the initial cross-sectional area.

3.1.3 Monotonic tests

Preliminary monotonic tests

Just before starting with the procedure described above, a couple of specimens were tested under axial displacement control. The two specimens tested, SS1.1 and SS2.1 failed just after peak load, so post-peak behaviour could not be characterized, see Figure 3.5.

The displacement rate applied was kept constant at 5 μm/s. The results obtained confirmed that another control technique had to be used in order to obtain the full stress-strain diagram. It must be noted that, even if stones from the same delivery were used, different Young's modulus from the two specimens could be observed. In fact, this important feature will appear throughout the present experimental study for which appropriate comments will be made.

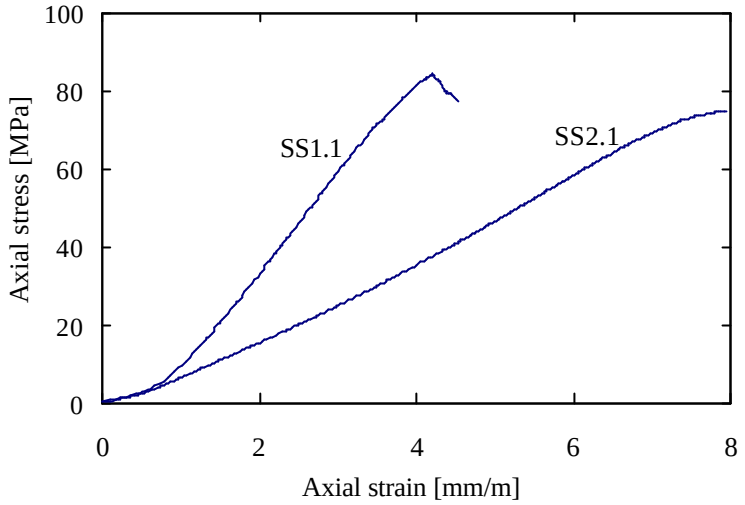

Figure 3.5 – Results from the monotonic compressive tests on stone specimens under axial displacement control.

Preliminary monotonic tests using axial and transversal extensometers

In order to compute the values of the Young's modulus and Poisson's ratio, two stone specimens (SS3.1 and SS4.1) were tested using three double electric resistance strain gauges rosettes, equally spaced around the perimeter and placed at mid-height of the specimen, see Figure 3.6.

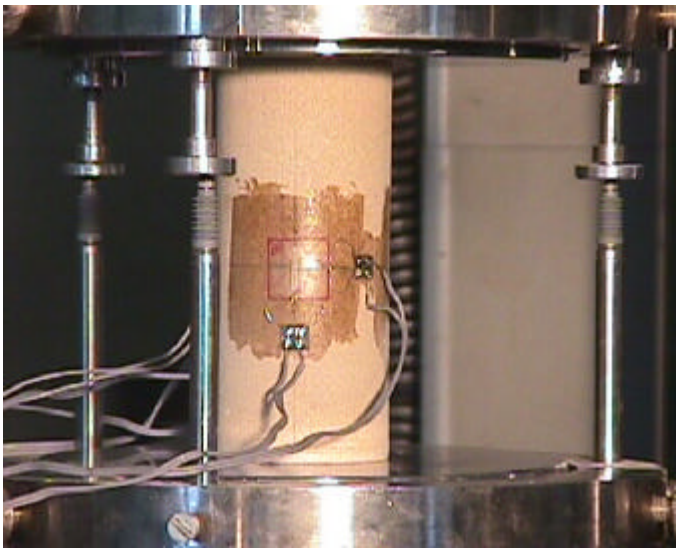

Figure 3.6 – Stone specimen and strain-gauge arrangement.

The specimens were tested in axial displacement control at a constant rate of 5µm/s. As expected, post-peak data could not be obtained because the specimens failed under axial

displacement control in an uncontrolled manner just after the peak load. The specimens SS3.1 and SS4.1 failed at 82.2 MPa and 94.8 MPa, respectively.

Measuring the axial displacements with the LVDTs on these specimens also allowed comparisons between the stress-strain diagrams obtained by the two available arrangements. Figure 3.7 shows the axial stress-strain and axial stress-circumferential strain diagrams for the specimens SS3.1 and SS4.1, respectively, where:

$e_{a,lvdt}$: axial strain measured using LVDTs (defined as positive in axial compression);

$e_{ea,sg}$: axial strain measured using the axial strain gauges;

e_c: circumferential strain measured by the horizontal strain gauges (defined as negative in axial compression).

In Figure 3.7 it can be observed that the axial stress-circumferential strain diagram exhibits high nonlinearities, even for lower stress levels, when compared with the axial stress-strain diagrams. The later show a much more linear behaviour, almost up to the peak load.

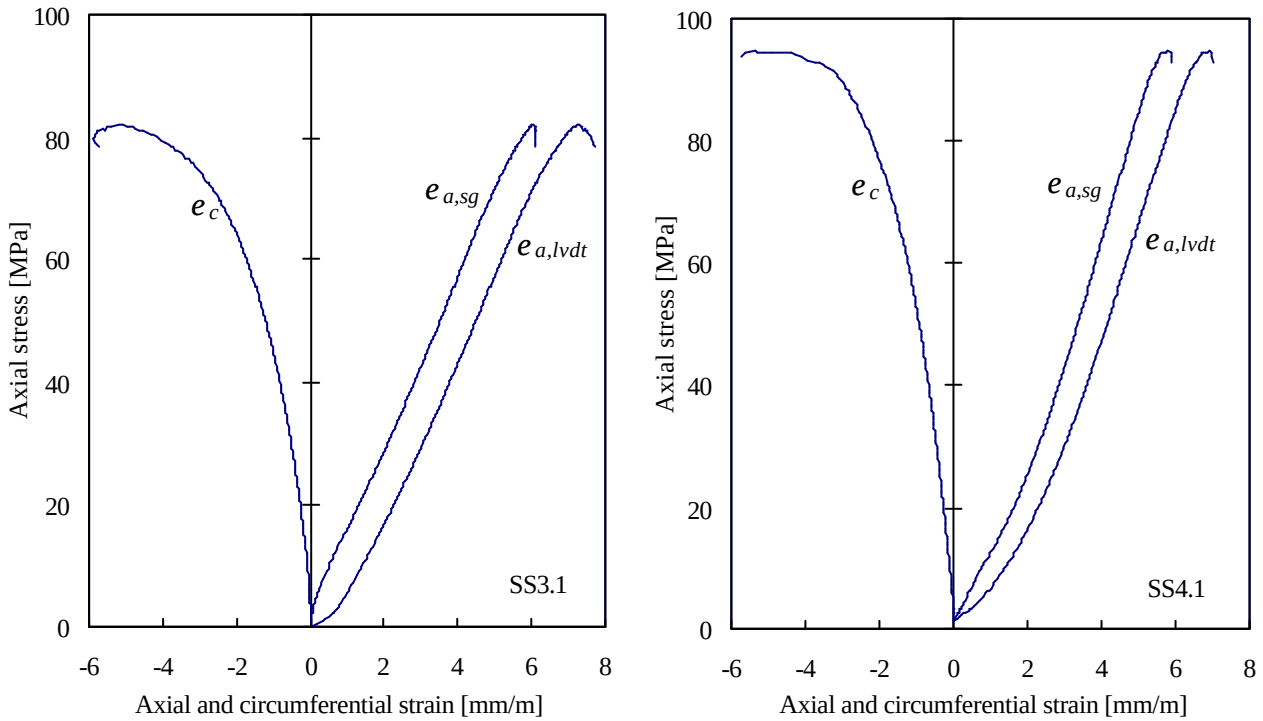

Figure 3.7 – Axial and circumferential strain versus axial stress for the stone specimens: (a) SS3.1; (b) SS4.1.

In order to fully characterize the specimens behaviour in terms of their elastic properties, the evolution of Young's modulus (E), Poisson's ratio (ν) and volumetric strain (e_{vol}) is presented in Figure 3.8 for the specimens SS3.1 and SS4.1. Here, E_{lvdt} and E_{sg} represent the computed Young's modulus using LVDT and strain gauges data, respectively.

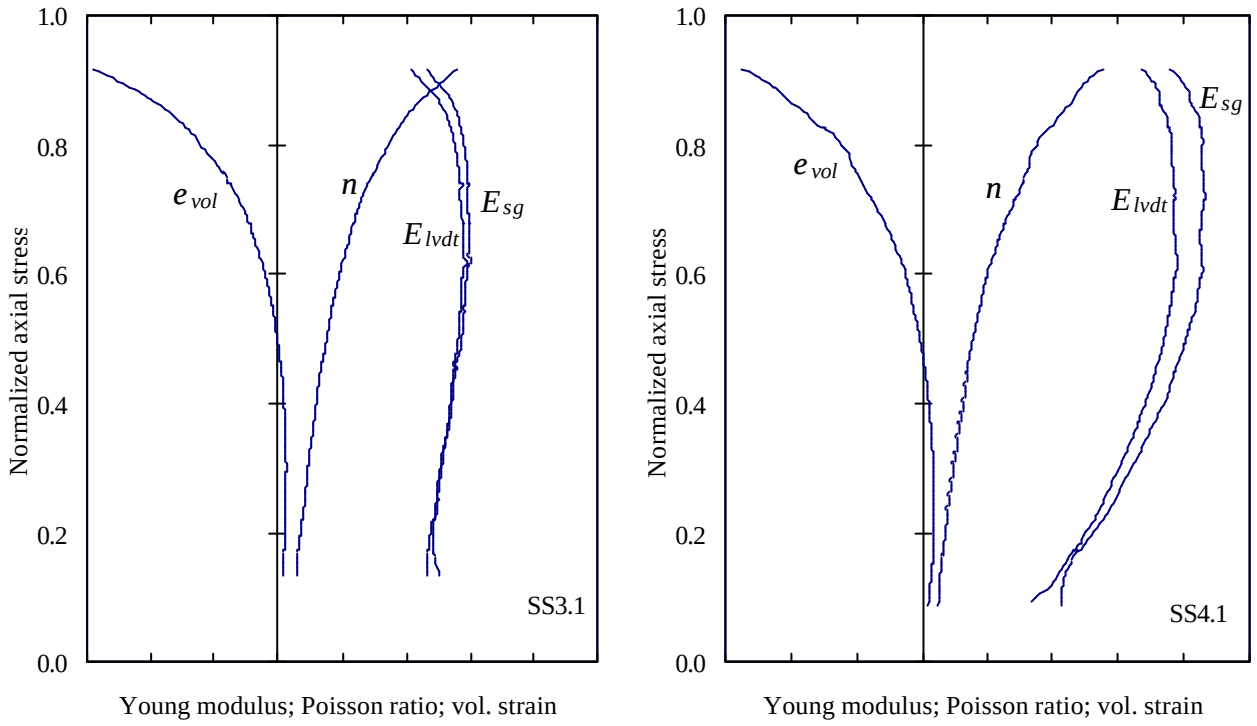

Figure 3.8 – Variation of Young's modulus, Poisson's ratio and volumetric strain for the stone specimens: (a) SS3.1; (b) SS4.1. The horizontal scale is normalized.

The Poisson's ratio ν and the volumetric strain e_{vol} were defined as follows:

$$n = \frac{e_c}{e_{a,sg}}$$

$$e_{vol} = e_{a,sg} + 2e_c = (1-2n)e_{a,sg} \tag{3.1}$$

The observed behaviour of the stone specimens can be summarized in the following:

– Initially an adjustment took place between the machine platens and the specimen. This happened in almost all the tests carried out and presented here.

- With an increase of the applied load, closure of existing microcracks and voids produced an increase of the Young's modulus. At higher stress levels, the Young's modulus (E) started to decrease due to the initiation of cracks. The Poisson's ratio (ν), defined as the ratio between the circumferential and axial strains, increased continually with the load increments. This behaviour can be explained by microcrack closure, for lower stress levels, and the initiation/propagation of cracks, for higher stress levels. In other words, the variations of E and ν are related to fracture of the specimen.
- Initially, a slight volume reduction took place, caused by the axial compression. An important volume increase, due to the crack formation followed this small reduction. It can be observed that for half of the peak load there was no volume variation. This means that crack formation took place for relative lower stresses.
- The very large positive volume variation for higher stresses (in compression) can be explained by splitting fracture. This phenomenon of positive volume variation in compression is known as dilatancy.
- When the applied load reached the last recordable level, the first macrocracks became visible. Due to this fact, the maximum load and failure mode could not be predicted during the execution of the test. From the observation of the collapsed specimen, failure may be attributed to disintegration along a shear band, formed by the coalescence of the major cracks. Tests using another control technique described latter in this report will make it possible to understand the collapse mode. The global behaviour described is well known in rock mechanics, e.g. Rocha (1981) and Li *et al.* (1998).

Figure 3.8 shows that E and ν were greatly affected by the nonlinearities in the stone's behaviour. Thus, it is difficult to define the elastic properties from the uniaxial test results. The procedure defined by ASTM (1999) allows the use of several methods employed in engineering practice, like tangent, secant or average modulus. This is clearly a consequence of the difficulties described above. In order to clarify some of these aspects, Tables 2.1 and 2.2 summarize the elastic properties, calculated for different stress levels using the tangent approach.

The elastic modulus calculated using strain gauges, E_{sg}, was always greater than the value obtained using the data from the LVDTs, but the differences are not significant (less than 12%). Therefore, the information obtained by means of LVDTs may be used to evaluate the Young's modulus in the specimens tested without strain gauges.

Table 3.1 – Elastic properties for the specimen SS3.1 (s_{peak} = 82.2 MPa)

Stress level	25%	50%	75%
E_{lvdt} [GPa]	12.34	14.04	14.09
E_{sg} [GPa]	12.47	14.31	14.73
ν	0.28	0.50	0.97

Table 3.2 – Elastic properties for the specimen SS4.1 (s_{peak} = 94.8 MPa)

Stress level	25%	50%	75%
E_{lvdt} [GPa]	13.87	18.57	19.20
E_{sg} [GPa]	14.69	20.22	21.47
ν	0.27	0.53	1.05

For a stress load near half of the ultimate load, the Poisson's ratio equals his theoretical maximum elastic value (0.50). This means that dilatancy has major importance in the behaviour of the specimen. Also, the previous results indicate that microcracking starts at relatively lower stress levels. As happened with the specimens SS1.1 and SS2.1, differences in Young moduli could also be found between SS3.1 and SS4.1.

Following the ASTM proposal, the Young's modulus can also be defined as the average slope of the linear portion of the stress-strain diagram. Taking into account that the straight-line portion is located in the [30%-60%] stress interval, the values of E obtained in this interval, using linear least square regression, are presented in Table 3.3.

Table 3.3 – Young's modulus defined in the [30%-60%] stress interval for the specimens SS3.1 and SS4.1.

Stress level	[30% – 60%]	
Specimen	SS3.1	SS4.1
E_{lvdt} [GPa]	13.68	17.71
E_{sg} [GPa]	13.86	19.20

Series of monotonic tests with complete results

Following the test procedure described above, four monotonic tests were performed in order to characterize the complete stress-strain diagram. Based on the data acquired via LVDTs, stress-strain graphics were obtained by normalizing the axial load applied and the change in measured axial length, respectively, by the initial cross-sectional area and by the axial length of specimen prior to loading, see ASTM (1999) and Fairhurst *et al.* (1999).

All the diagrams exhibited the common initial adjustment between the specimen and the machine platens (usually termed as “bedding down”). This means that the initial part of the stress-strain graphic presents a “curve” followed by a linear portion, see Figure 3.9.

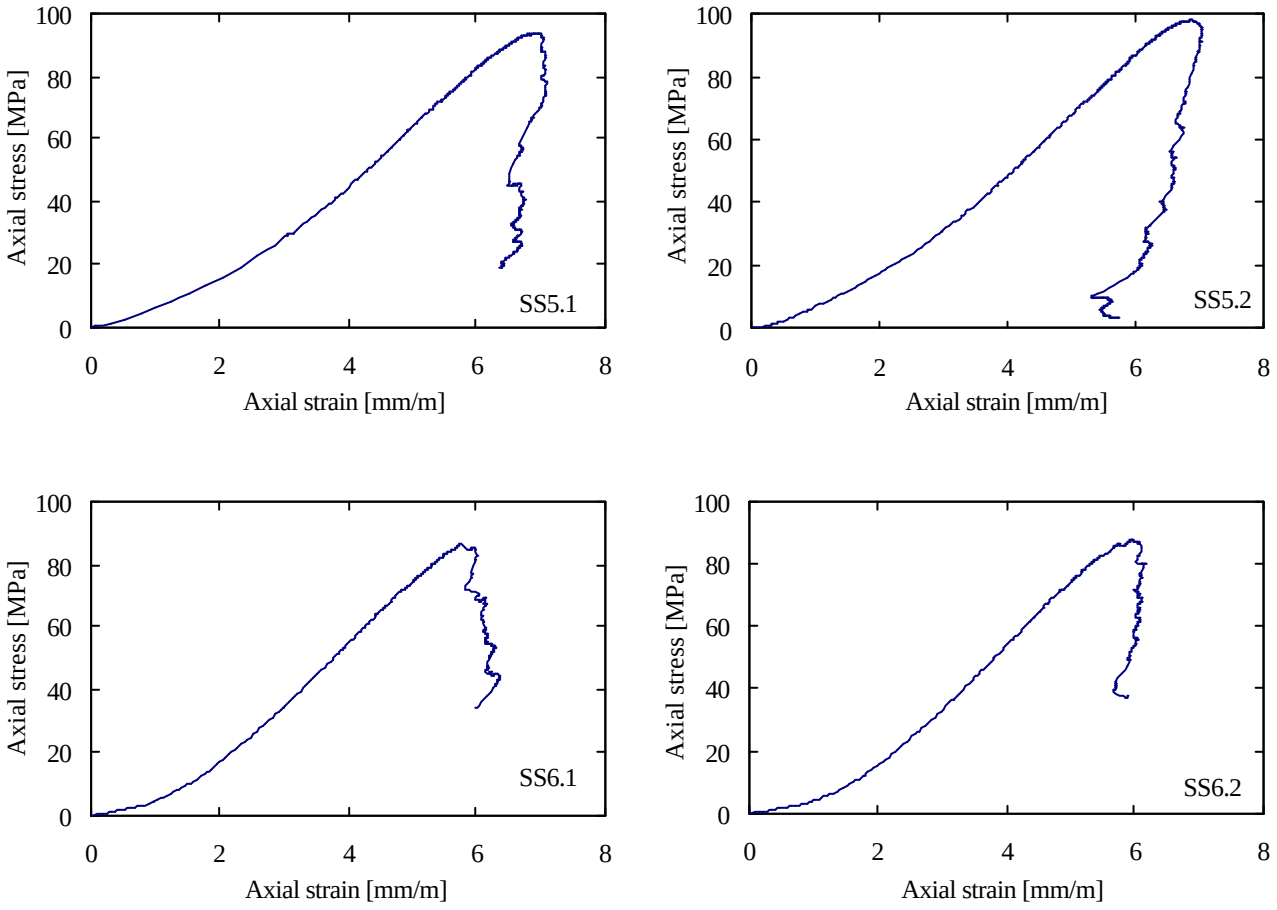

Figure 3.9 – Monotonic stress-strain diagrams for the four stone specimens tested.

The Young’s modulus of the four specimens was evaluated in the stress interval [30%-60%]. Table 3.4 summarizes the Young’s modulus and the ultimate compressive strength of the stone specimens (CV is the coefficient of variation).

Table 3.4 – Characterization of the monotonic tests on stone specimens.

Specimen	$E_{30\text{-}60}$ [GPa]	s_{peak} [MPa]
SS5.1	17.49	93.9
SS5.2	17.89	98.0
SS6.1	19.56	86.6
SS6.2	20.30	87.8
Average	18.81	91.6
CV	6.16 %	5.1 %

As expected, the pre-peak behaviour was very easy to follow. All the specimens showed a reasonable linear behaviour almost until the peak. Just after the peak load, the specimens exhibited very pronounced fragile behaviour. The initial macroscopical cracks were visible only for a load very close to the peak load. Macroscopic crack initiation took place at the extremities, progressing through the entire specimen. Some of the cracks had a sudden formation and, in some specimens, were accompanied by a clear sound. Figure 3.10 presents two specimens loaded in the post-peak regime where cracks are perfectly visible.

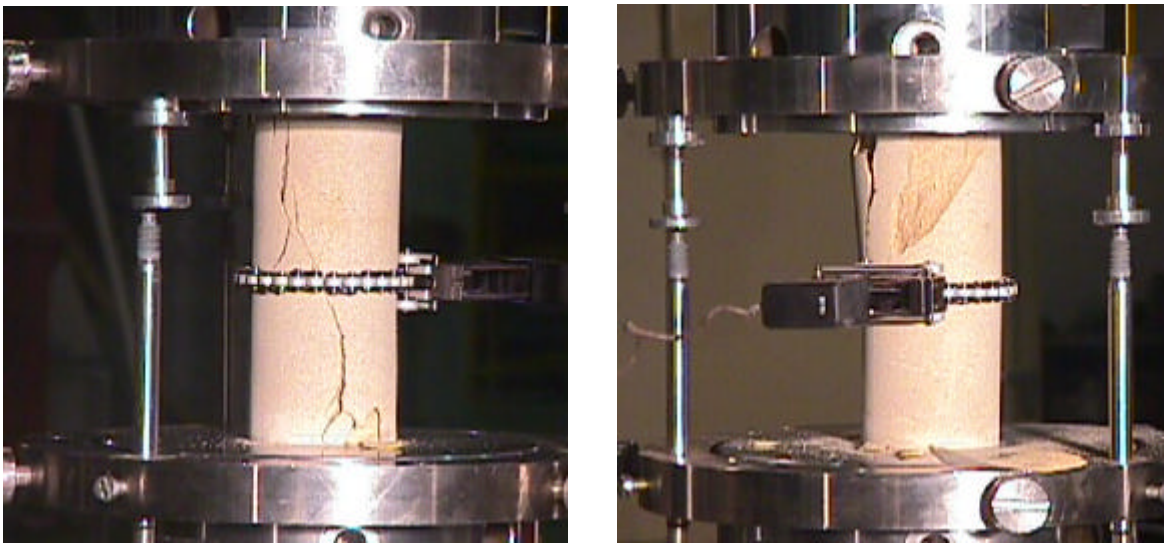

Figure 3.10 – Typical crack initiation for the stone specimens tested, around peak load.

In some specimens crack formation led to a sudden unloading on the load-displacement diagram, under circumferential displacement control. This unloading occurred very quickly, with increasing circumferential displacement and was followed generally by partial load recovery.

Apparently, the results concerning these four stone specimens show low scatter. However, this low scatter is due to the fact that the four specimens were extracted from only two different stone prisms. This low scatter is explained by the stone's nature. However, even if the stones were delivered in a single batch, it was not possible to ensure that all stones were submitted to the same conditions or even if they were extracted from the same place.

3.1.4 Cyclic tests

After monotonic compressive tests, a series of cyclic load tests were carried out to obtain data about the cyclic behaviour of the sandstone, with emphasis on the stiffness degradation evolution and energy dissipation. The general procedure adopted was the same as described before with the exception of the cyclic part. The unloading branch was always performed under force control until a fixed load value, serving as the lowest threshold. Figure 3.11 presents the stress-strain diagrams obtained in the cyclic tests. The general behaviour of these specimens was similar to the monotonic ones. On the one hand, the pre-peak behaviour was easily followed, but, on the other hand, the post-peak branch showed to be unstable and characterized only with great effort. It can be observed that in the post-peak branch the load decreased in a very non-smooth way. This clearly reflects the brittleness of sandstone.

Table 3.5 presents the Young's modulus and the ultimate compressive strength of the stone specimens tested under cyclic loading. Significant differences were found between the several specimens in terms of compressive strength and Young's modulus. Therefore, the intrinsic variability of the mechanical properties of stone is an important issue that should kept in mind when dealing with natural stone structures.

The coefficients of variation are higher in the cyclic tests, when compared to the monotonic tests. This is partially due to the specimens extracted from the stone piece number two (specimens SS2.2 and SS2.3) that present different elastic and mechanic properties (see also Figure 3.5). If new coefficients of variation are calculated without the contribution of these two specimens, less scatter is found (coefficients of variation of 15.95% and 10.9% for the elastic modulus and peak strength, respectively). Another reason for higher coefficients of variation in the cyclic tests had to do with the number of stones rather than the number of specimens. In the monotonic tests only two stones were used whereas in the cyclic tests five different stones were used.

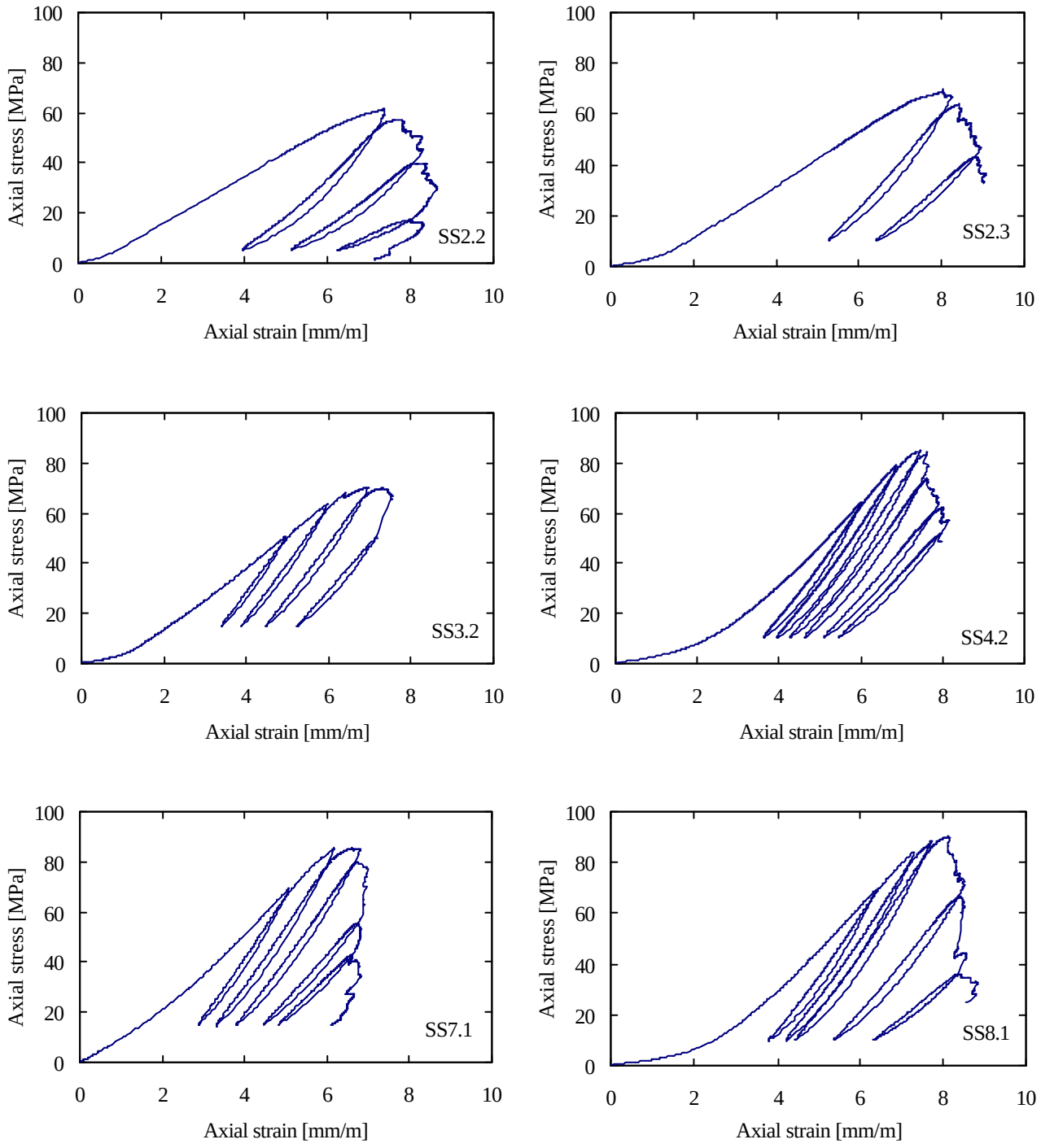

Figure 3.11 – Stress-strain diagrams of the stone specimens tested under cyclic loading.

In the post-peak region, the specimens had to be unloaded from defined post-peak locations and then reloaded in order to generate new stress-strain curves. The unloading points were chosen in a way that stiffness degradation, also called damage, could easily be followed. The local post-peak Young's modulus is then the positive slope of the ascending (reloading) portion of these new curves and it has been calculated using the same method adopted for the elastic Young's

modulus (linear least square regression in an interval). The evolution of the Young's modulus can be considered as a measure of the damage in the material.

Table 3.5 – Characterization of the cyclic tests on stone specimens.

Specimen	$E_{30\text{-}60}$ [GPa]	s_{peak} [MPa]
SS2.2	9.50	61.1
SS2.3	10.46	68.6
SS3.2	12.64	70.4
SS4.2	15.54	84.5
SS7.1	15.62	85.4
SS8.1	16.49	90.2
Average	13.38	76.7
C.V.	20.13 %	13.8 %

The unloading-reloading cycles were done in the pre-peak and post-peak regions. The Young's modulus was calculated for the initial [30%-60%] interval (see Table 3.5) and for all the reloading branches as being the slope obtained by linear least square regression, as used before. Table 3.6 shows the Young's modulus computed for all the reloading branches exhibit in Figure 3.11 ("rb" denotes reloading branch).

Table 3.6 – Young's modulus of the reloading branches obtained by linear least square regression (stone specimens).

Specimen	E [GPa]					
	rb1	rb2	rb3	rb4	rb5	rb6
SS2.2	15.15	12.07	7.47	——	——	——
SS2.3	18.38	14.30	——	——	——	——
SS3.2	22.05	22.38	21.85	18.44	——	——
SS4.2	21.97	22.92	23.28	21.80	18.88	17.09
SS7.1	24.00	23.86	22.79	18.28	16.03	——
SS8.1	22.66	23.27	23.43	19.43	13.15	——

In the pre-peak region, a slight increase of the Young's modulus can be observed (e.g. specimens SS3.2 and SS4.2). This result is in agreement with the results obtained from the tests using strain gauges. On the other hand, a monotonic decrease of the Young's modulus in the post-peak region can be observed (see specimens SS2.2 and SS7.1). This decrease is related to the progressive damage growth suffered by the specimen.

In the stress-strain diagrams presented, a different number of unloading-reloading cycles were performed for each specimen. Since the testing machine procedure had to be completely defined before the beginning of the test, the uncertain behaviour of the stone specimens produced major differences in the stress-strain diagrams for a same adopted procedure. Therefore, prior to each test, the testing machine procedure had to be adapted as a function of the stone behaviour. A simple stress-strain envelope diagram can give a visual idea about the scattering in the results. Figure 3.12 presents the envelope (shaded area) of the monotonic and cyclic stress-strain diagrams exhibit in Figure 3.9 and Figure 3.11. It can be observed that the pre-peak portion presents a smaller scattering, when compared with the post-peak branches. In the peak zone, the cyclic envelope presents a wide scatter, see also Table 3.5, but this can be associated with differences in the number of stones selected for monotonic and cyclic tests.

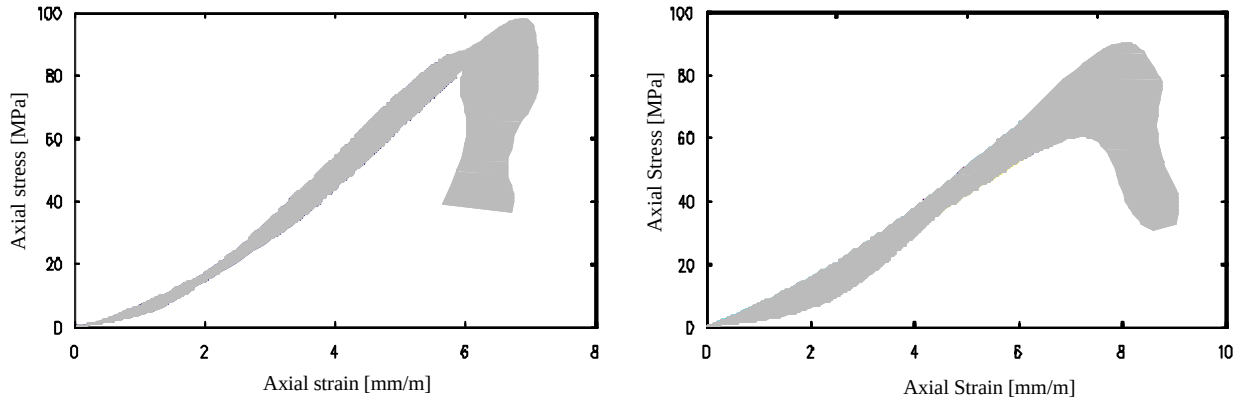

Figure 3.12 – Envelope of the stress-strain diagrams considering: (a) monotonic tests; (b) cyclic tests.

3.1.5 Failure modes

The analysis and observation of the obtained failure modes allow understanding the behaviour of the stone specimens tested. Typical failure modes obtained are shown in Figure 3.13. Due to the

confinement effect caused by the machine platens, the top and bottom surfaces did not generally present any visible cracks. On the other hand, when specimen rupture took place, the formation of circular cone pieces was visible. In all the specimens tested the formation of multiple shear bands took place when post-peak region was reached. Its development seemed to be the cause of specimen failure and it was associated with large volume increase of the specimen.

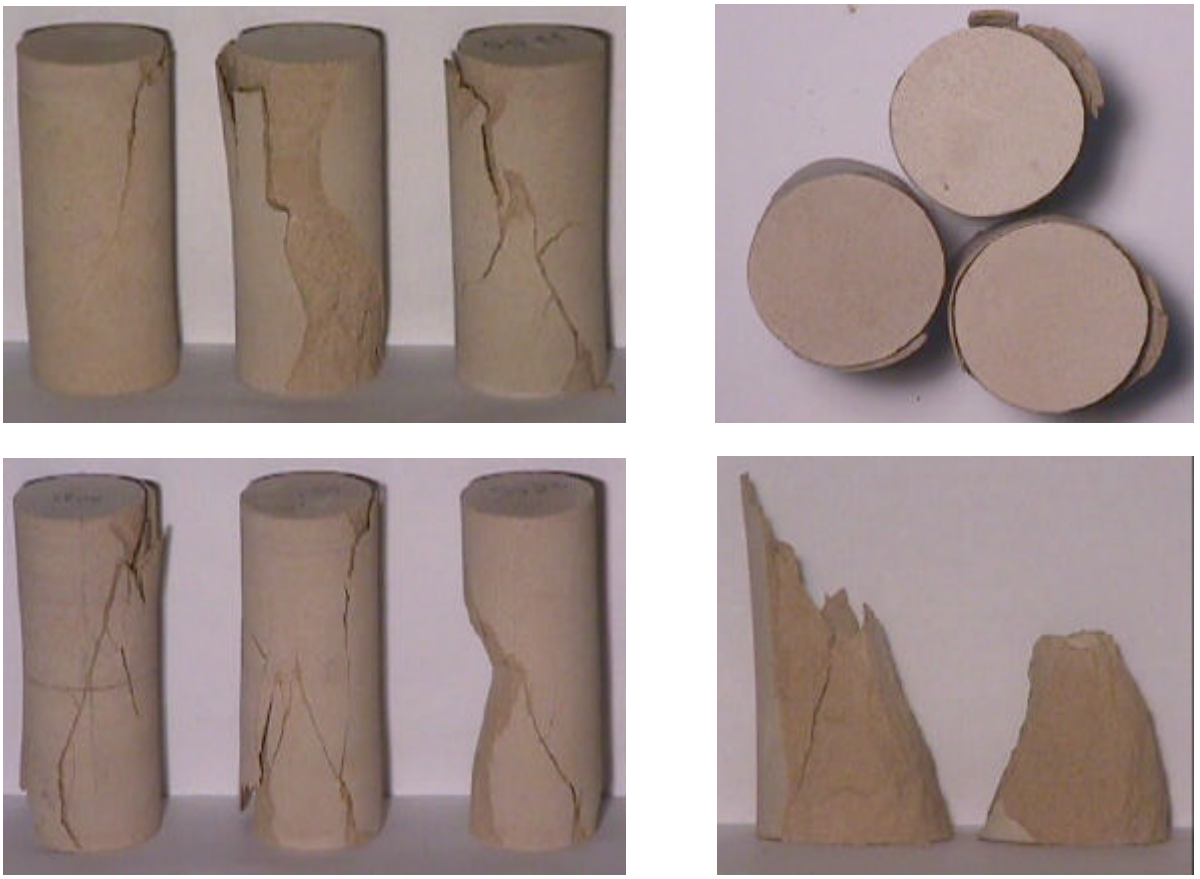

Figure 3.13 – Failure modes of the tested stone specimens.

3.1.6 Tests using specimens with different geometry

In order to check the influence of the confinement effect and slenderness ratio, it was decided to perform some tests on specimens with slightly different geometry. All the specimens tested up to then had a geometry of $\varnothing 5 \times 12$ cm^3. Thus, two cylindrical specimens of $\varnothing 5 \times 10$ cm^3 (h/d = 2.0) were tested under monotonic compression. Table 3.7 shows the results obtained for the two specimens tested, in terms of Young's modulus and ultimate strength. It must be noted that results presented in Table 3.7 do not have statistical meaning due to the reduced number of specimens tested.

Table 3.7 – Characterization of the monotonic tests on stone specimens with h = 10 cm.

Specimen	$E_{30\text{-}60}$ [GPa]	s_{peak} [MPa]
SS11.1	20.63	91.6
SS12.1	14.85	93.1
Average	17.74	92.4

Figure 3.14 illustrates the stress-strain diagram for the specimens described above. With such decrease in the specimen's height (about 17 %) no significant differences were found when comparing the peak strength. With respect to the elastic modulus, it turned out to be very difficult to extract any conclusions because this property seems to show a wide scatter.

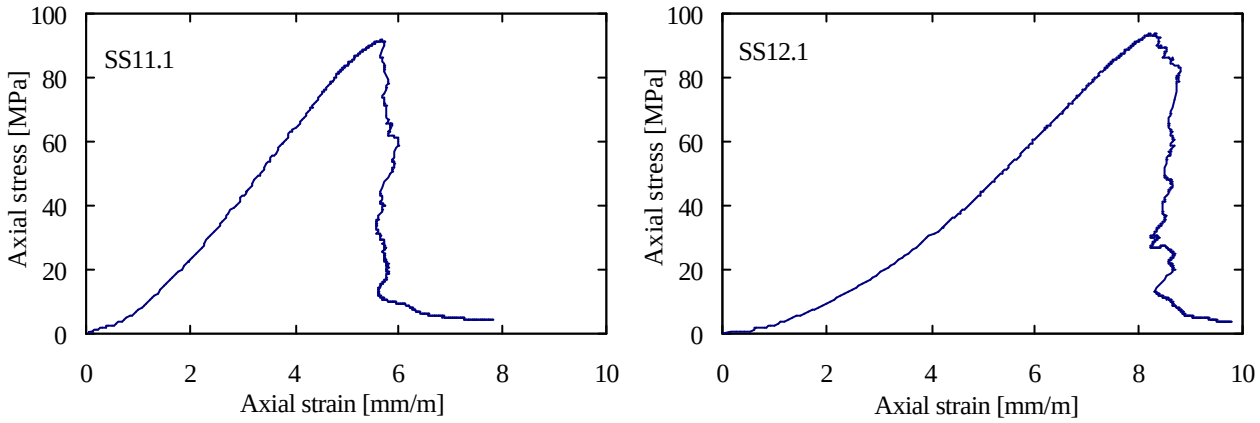

(a) (b)

Figure 3.14 – Monotonic compressive stress-strain diagrams for two specimens 10 cm height: (a) SS11.1; (b) SS12.1.

However, if a comparison between the post-peak branches is made, it can be observed that the smaller height is associated with a better stability until complete loss of strength capacity, see Figure 3.14. It can be observed that a quasi-linear path forms the last part of the curve and, for a very small load decrease, large decrease in axial length is found. This last branch could be obtained because the specimen exhibited a stable post-peak behaviour. Experiments have demonstrated that the post-peak behaviour becomes more ductile when the confining pressure is increased (Wawersik *et al.*, 1970). So, it is believable that a smaller slenderness factor (from 2.4 to 2.0) provides a less brittle behaviour, probably due to an increasing confinement effect. The reasons why this ratio was not used are given later.

In order to illustrate the great importance of an appropriate choice of the control technique, the relation between variations in measured axial and circumferential lengths obtained for the specimen SS11.1 is shown in Figure 3.15. As it can be observed, pre-peak is characterized by a remarkable variation in axial length when compared with the circumferential one. As a result, this branch can be obtained under common axial displacement control.

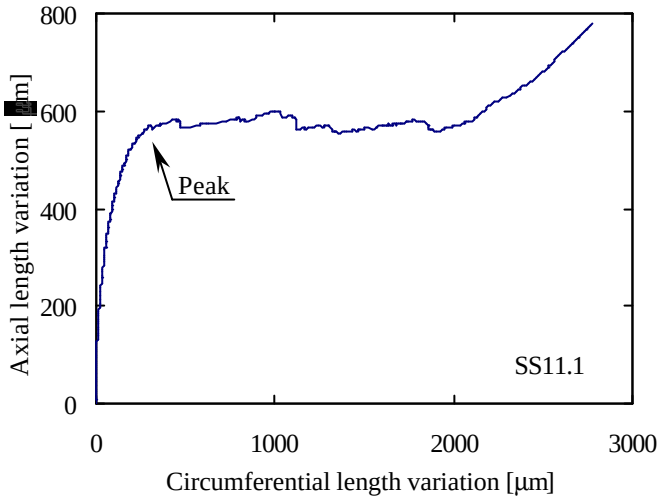

Figure 3.15 – Relation between the axial and circumferential length variation for the stone specimen SS11.1.

Figure 3.15 also shows that the post-peak behaviour cannot be described for this particular material if axial displacement control is used, due to the plateau obtained. This control must be substituted by a monotonic increasing signal in order to obtain the complete stress-strain diagram. A possible control seems to be the adopted circumferential displacement control.

3.2 Direct shear tests on stone specimens

Shear failure is a very common failure mode observed in most masonry walls when subjected to in-plane loading. As a consequence, the structural behaviour of masonry joints has been carefully studied, see Atkinson *et al.* (1989) and van der Pluijm (1993) for a comprehensive analysis. However, little is known about the shear behaviour of dry masonry joints, particularly under cyclic loading. Therefore, an experimental program aiming at the mechanical characterization of the behaviour of dry jointed stone masonry under cyclic shear loading was carried out. The first results are presented and discussed in this Section. The main purposes of these tests were the assessment of the friction angle f and the dilatancy angle y as well as the characterization of the

complete stress-displacement diagram under cyclic shear loading. A discussion of the complete experimental program can be found elsewhere (Ramos, 2002). These results are needed for the numerical analysis of dry jointed stone masonry walls to be presented in Chapter 4 and for the calibration of the constitutive model to be developed in Chapter 5.

3.2.1 Equipment and specimen preparation

Several test configurations have been used to determine the cohesion (when it exists) and the friction and dilatancy angles. A comprehensive review of this subject is given by Jukes and Riddington (1997), where available test configurations are detailed discussed. The most critical point involved in these tests is to guarantee that the test set-up ensures a stress distribution as uniform as possible in the bed joint.

In this study the direct shear tests where performed with a servo-controlled testing machine, existing at the roadway laboratory, specially conceived to carry out fatigue tests on asphalt specimens. This machine is equipped with two opposite platens, each one controlled by an independent loading actuator, with a load capacity of 20 kN. Each loading actuator is equipped with a load cell and is able to work under load or displacement control.

Due to geometric restrictions related to the maximum distance allowed between machine platens, the maximum specimen height was limited to 8,5 cm. Therefore, specimens were composed by two equal stone units, each one measuring 4×5×8 cm^3, as shown in Figure 3.16.

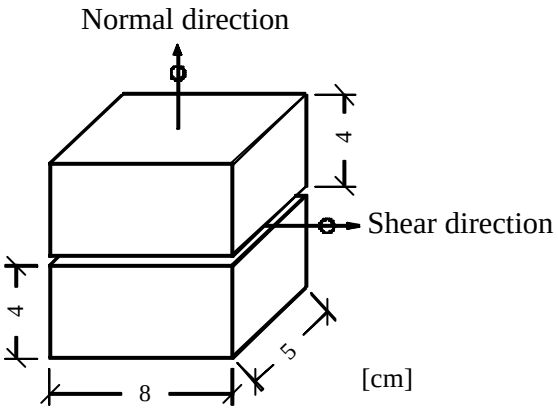

Figure 3.16 – Adopted geometry of the stone units tested under shear loading.

The units were obtained by mechanical cut of the prismatic sandstones pieces described in the previous Section. The surface of the units in direct contact during the shear tests presented the same smoothness as the stones used to build the stone masonry walls to be described in Chapter 4. It is important to emphasize this feature since some of the stone characteristics to be estimated here will be used later in modeling.

The specimens were instrumented with three LVDTs, placed according to Figure 3.17. Two LVDTs measured the relative vertical displacement whereas the third LVDT measured the relative horizontal displacement along the dry joint. The compressive and shear forces were measured by means of two built-in load cells, each one associated to a loading actuator. The machine platens were modified by adding lateral steel bars, fastened with screws, to prevent any relative horizontal movement between the unit and the platen. In addition, a pre-compressive load was applied to the steel bars in order to avoid any relative sliding between the unit and the platen during shear loading reversal.

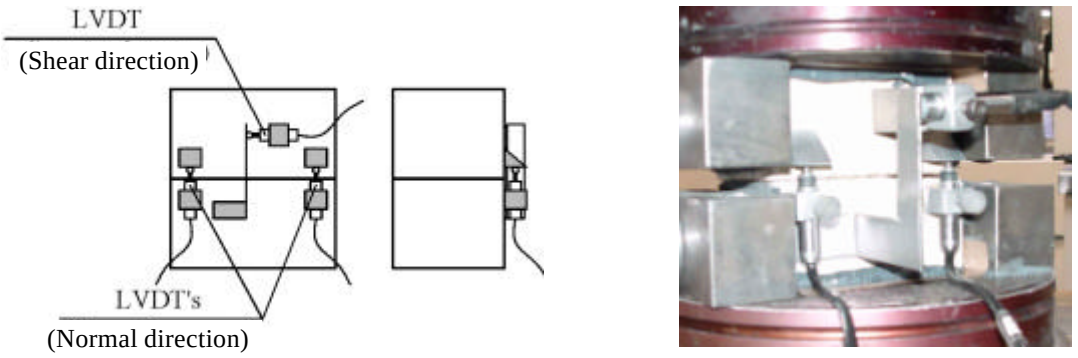

(a) (b)

Figure 3.17 – LVDTs arrangement: (a) schematic representation; (b) picture taken during testing.

In order to minimize the overturning moment applied to the joint by the shear load, the contact between the unit and the lateral steel bar was located as close to the joint as possible by placing a small neoprene sheet between them, see Figure 3.18. Furthermore, two greasy teflon sheets were placed between the unit and the platen. Fixing the unit to the base of the platen would increase considerably the overturning moment.

Taking into consideration that the reliability of the results depends greatly on the capacity of the test method to assure an appropriate stress distribution down the dry joint, a numerical assessment was carried out (Ramos, 2002). In this way, the loading arrangement idealized in Figure 3.18(b) was validated by means of a non-linear finite element analysis.

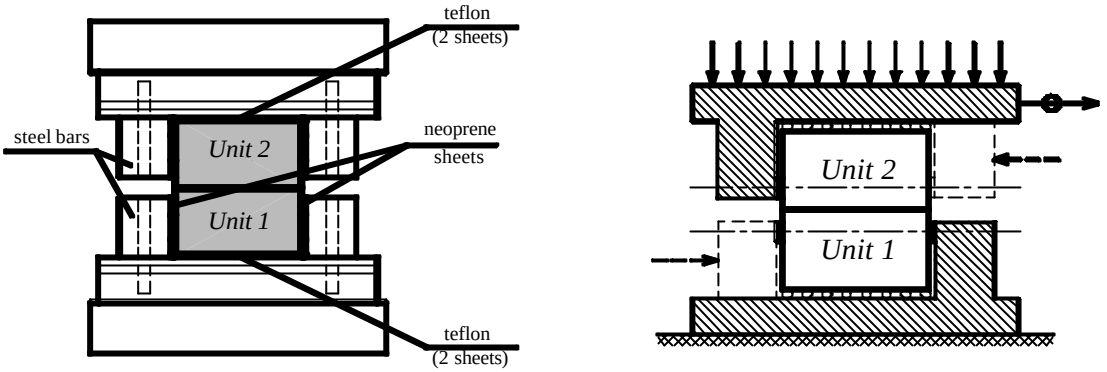

Figure 3.18 – Test configuration: (a) specimen arrangement; (b) idealized loading arrangement.

The procedure is the same as used for testing, which is described in the following Section. First a vertical compressive stress of 1.5 MPa was applied to the specimen. Then, a monotonic increasing horizontal displacement was imposed to the dry joint until complete yielding was achieved. It was found that just before the occurrence of yielding in the joint, see Figure 3.19, the average normal stress in the joint was very close to the imposed compressive stress (1.5 MPa) and that shear stresses presented an acceptable profile stress distribution, quite uniform in a great extension of the central part of the joint.

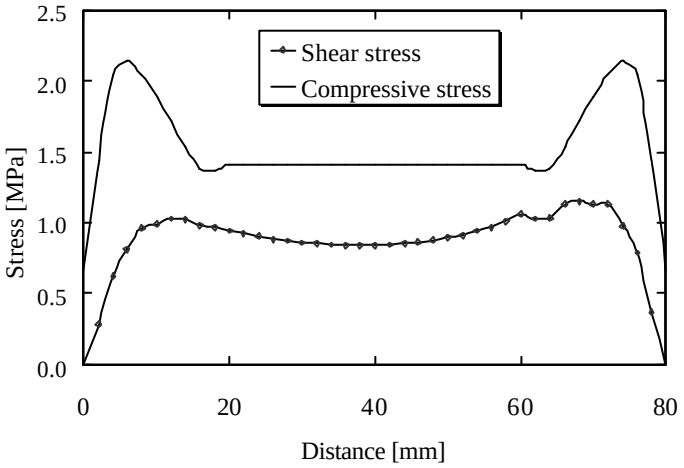

Figure 3.19 – Normal and shear stress distribution along the joint just before the occurrence of yielding.

The numerical results have shown that the adopted loading arrangement can lead to a uniform stress distribution in a great extension of the joint, which is the main demand that any shear test should attain. Therefore, it seems that the proposed testing set-up is able to generate reliable results.

3.2.2 Testing procedure

Initially, the units were measured and registered. Then, both units were put into the platens. Any potential non-parallelism between the specimen's faces was corrected by placing a thin layer of epoxy resin between the platens and the greasy teflon sheets. This procedure guaranteed a very good contact between the two units and between the units and the platens. Special attention was devoted to the adjustment of the steel bars and to the setting of the neoprene sheets. Afterwards, the three LVDTs were placed in the units, according to Figure 3.17(a). Since only three LVDTs were available, only one face was instrumented. However, no rotation along the shear direction was expected.

The test was started by imposing a compressive stress state to the specimen, under force control. Three compressive stress levels of 0.5 MPa, 1.0 MPa and 1.5 MPa were defined and for each stress level, three specimens were tested cyclically. Afterwards, a cyclic displacement law was imposed to the LVDT 3, at a constant rate of 2.5 μm/s. Four cycles of increasing amplitude, varying from 0.1 mm to 0.4 mm, were carried out, as shown in Figure 3.20. Their amplitude and number were based on preliminary tests. The objective was to stop the test when variations between cycles were not visible.

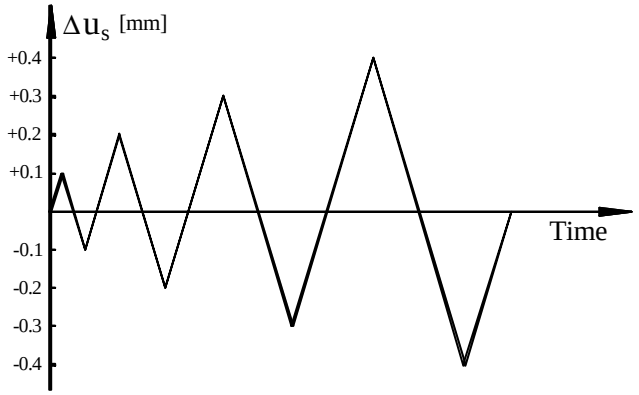

Figure 3.20 – Imposed displacement law under cyclic direct shear loading.

3.2.3 Results

Typical obtained cyclic shear load-relative shear displacement diagrams are shown in Figure 3.21, for the three compressive stress levels adopted in this study. As expected, the maximum shear load increased with the compressive stress level. It was observed that, for each

stress level, a very close behaviour was found. During loading and reloading shear load grew in a non-linear way whereas unloading was almost linear elastic. Moreover, practically no stiffness degradation between cycles was observed and no hardening behaviour was found.

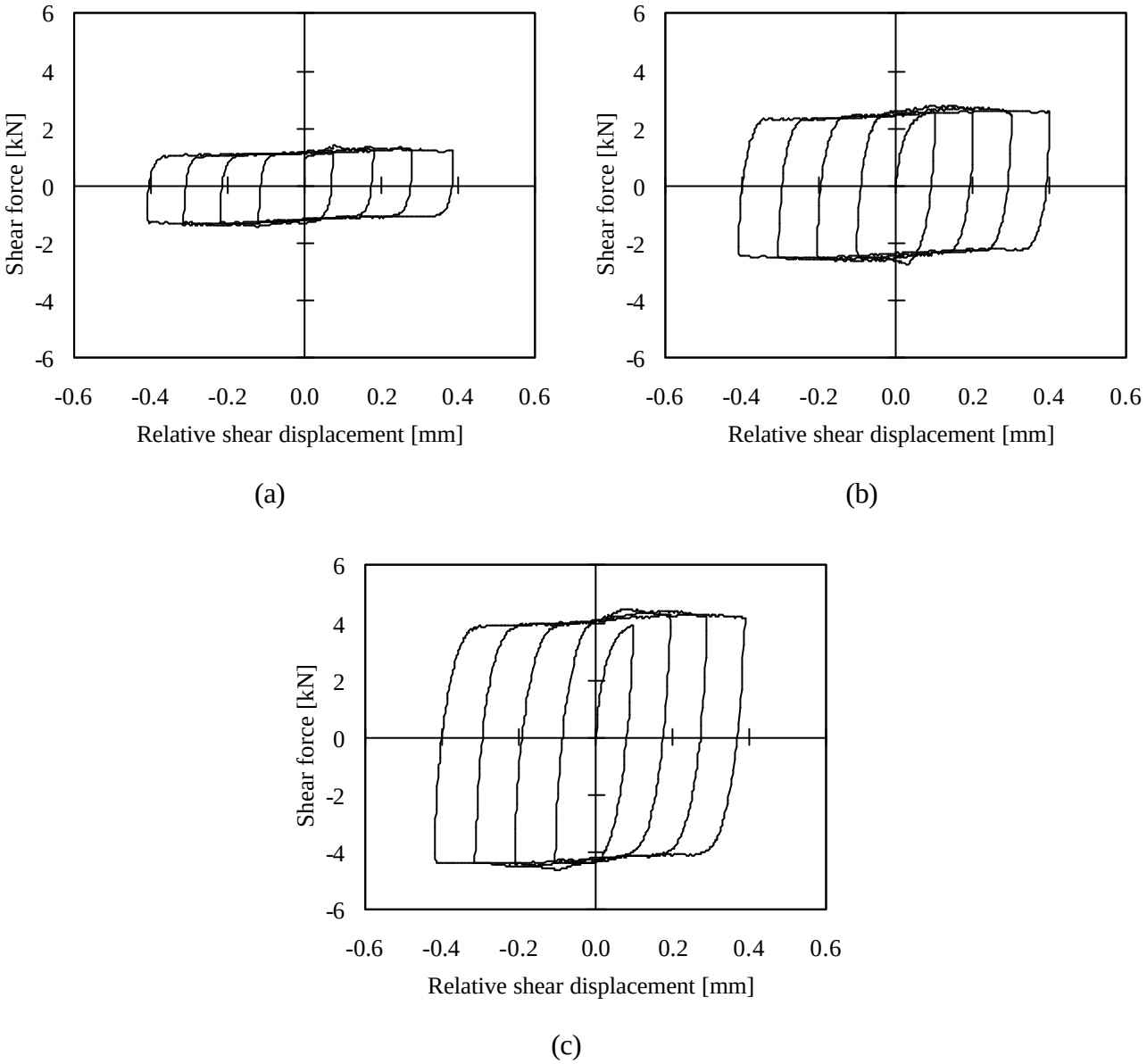

Figure 3.21 – Shear load-relative shear displacement for a compressive stress level of: (a) 0.5 MPa; (b) 1.0 MPa; (c) 1.5 MPa.

Table 3.8 presents the statistical values of the stiffness computed from the unloading branches, using linear least square regressions. It was observed that, for specimens tested under a same compressive stress level, unloading stiffness did not present important variations between cycles.

However, the increase of the compressive stress applied to the specimens originated a linear increase of both unloading and reloading stiffness.

Table 3.8 – Unloading stiffness (average value and coefficient of variation).

Stress level	0.5 MPa	1.0 MPa	1.5 MPa
Average [N/mm^3]	149952	176320	220924
CV (%)	7.7	16.2	16.9

By performing linear least square regressions in all the specimens, it was found that the value of tan$f$ assumes an average value of 0.62 and tan$y$ is equal to 0.05. For practical purposes, tan$y$ can be considered equal to zero. Finally, Figure 3.22 shows the appearance of the unit's surface after testing. In spite of all the care put in the specimens preparation, the contact between the units was not totally uniform.

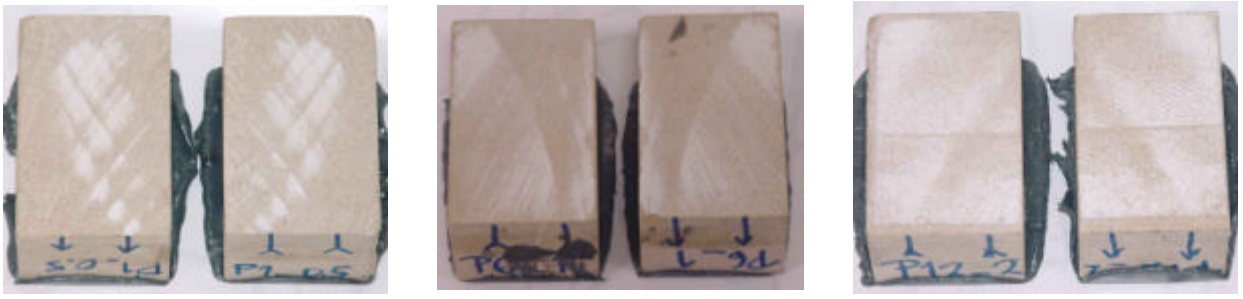

(a) (b) (c)

Figure 3.22 – Dry joint surface after testing: compressive stress levels of (a) 0.5 MPa; (a) 1.0 MPa; (b) 1.5 MPa.

3.3 Compressive tests on stone prisms

Along with the tests on stone specimens, uniaxial compressive tests were also performed on stone masonry prisms. The stones were laid dry to replicate dry (mortarless) masonry. The stones used in these tests were taken from the batch delivered for the tests described in the previous Sections.

3.3.1 Prism preparation

It was decided to perform monotonic uniaxial compressive tests on two different geometries, with different slenderness ratios. Therefore, according to available stones, two prisms made of three 10×20×10 cm^3 pieces and other two prisms made of four 20×20×10 cm^3 pieces were built and tested. The slenderness ratios obtained (h/d) were three and two, respectively, where h is the height and d is the lowest base dimension of the prism. A schematic representation of the prisms is shown in Figure 3.23. The adopted h/d ratios allowed a uniaxial compressive behaviour at least at the center of the prisms.

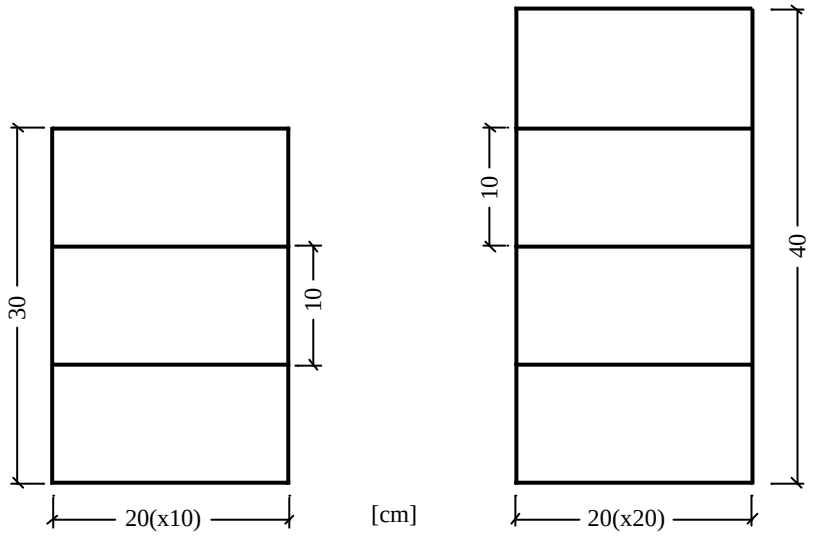

Figure 3.23 – Geometry of the two different stone prisms tested (front view).

The prisms were built just by superposition of the stone prismatic pieces and no additional surface treatment was made on those pieces. Once again, no material was placed between the stones. Stone pieces that presented clearly visible defect were removed and were not used in these or in any other tests performed using stones.

The prisms were denoted by the letters SP (stone prism) and by an order number. SP1 and SP2 were prisms made of three pieces each and the prisms made of four pieces were denoted by SP3 and SP4. All the specimens were tested with their natural water content.

3.3.2 Test procedure

The stone prisms were tested in a SUZPECAR testing machine controlled by a MTS 458 system. This machine has a 5000 kN load capacity and can work under force or axial displacement control. Three axial LVDTs placed between the machine platens, see Figure 3.24, were used as displacement measurement transducers. The LVDTs, equally spaced, were attached to a thick steel plate (40×32 cm^2) placed on the lower machine platen. The applied load was measured by means of the machine load cell. Special attention was given to transducers calibration and to the adopted testing procedures described, next.

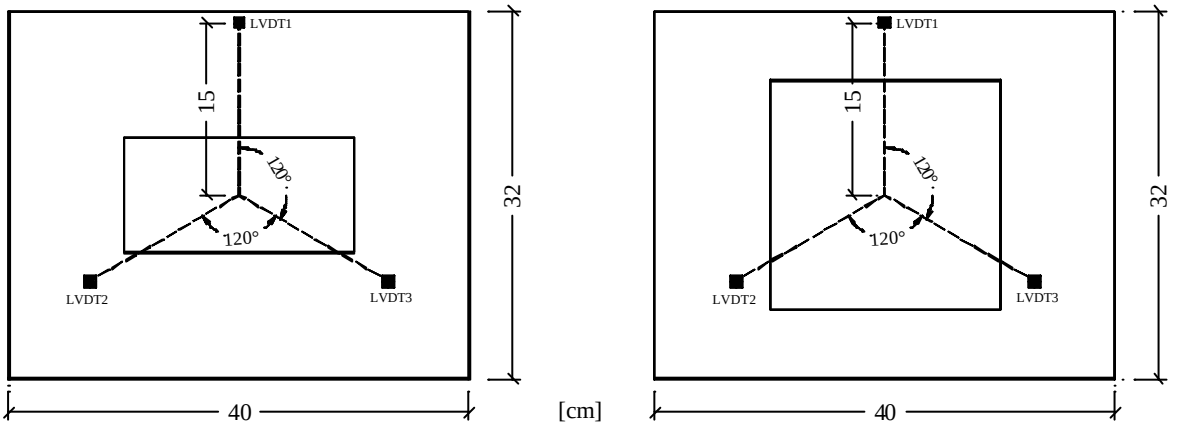

Figure 3.24 – Measurement transducers arrangement for the two prism geometries tested (top view).

Initially, the stone pieces were carefully aligned and the cross-sectional area and height of the prism were measured and registered. Then, the prism was put into the lower platen and centered. Afterwards, a small preload was applied, in force control, in order to adjust the upper platen to the top surface of the specimen. This platen has a hinge in order to avoid any unfavourable effect due to non-parallelism between the prism faces.

The four tests were performed under axial displacement control and force control. The displacement rate was kept about 3 μm/s and the unloading branches were performed at a rate of 10kN/s. The axial displacement of each tested prism was defined by the average value obtained from the three LVDTs placed between the machine platens. The axial strain was calculated by dividing the change in average measured axial length by the initial axial length of the prism. The axial compressive stress was computed as the load divided by the initial cross-sectional area, as done before.

3.3.3 Test results

Due to high load values and the brittleness of the stones, careful safety measures were adopted. Therefore, the four tests were performed by placing a cylindrical metallic box around the machine platens. Thus, due to these safety measures, it was not possible to observe the prisms being tested.

Figure 3.25 presents the stress-strain diagrams of the four tested stone prisms. In all the curves the common initial adjustment between the prism and the machine platens is visible. Again, the pre-peak behaviour was easy to follow. All the specimens showed a reasonable linear behaviour almost until the peak. All the prisms failed just after the peak load, exhibiting a very pronounced fragile behaviour. Therefore, post-peak could not be characterized.

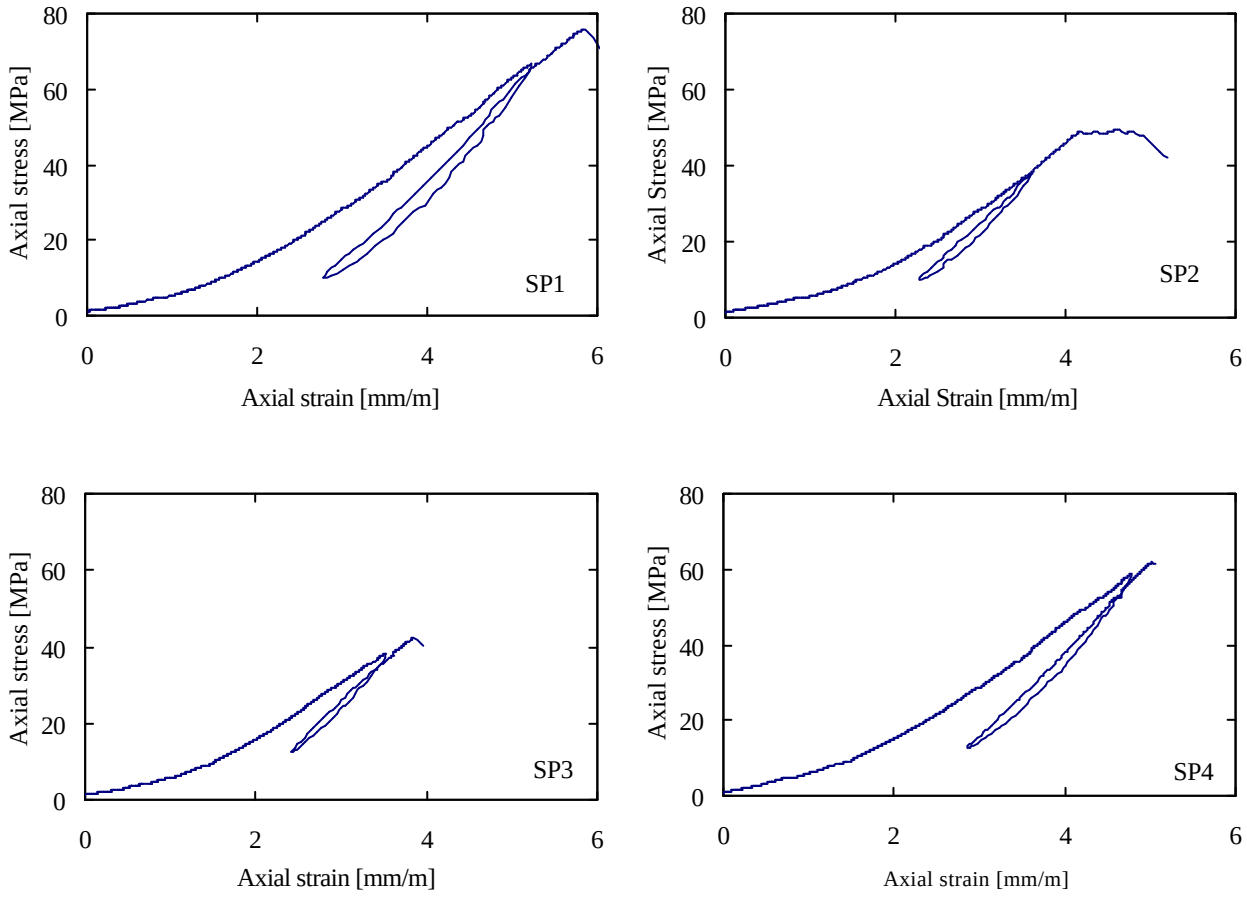

Figure 3.25 – Stress-strain diagrams of the four stone prisms tested.

As done in Section 3.1, the Young's modulus of the four prisms was evaluated in the [30%-60%] stress interval. Table 3.9 summarizes the Young's modulus and the compressive strength values

of the four stone prisms. Again, it can be seen that a wide scatter is present in the results due to the fact that prisms were made of various pieces that could have distinct properties.

If a comparison between these results and the results presented in Section 3.1 is established, no significant differences respecting the Young's modulus are found. However, important differences with respect to the peak strength are found.

Table 3.9 – Initial Young's modulus and peak strength of the stone prisms.

Specimen	$E_{30\text{-}60}$ [GPa]	s_{peak} [MPa]
SP1	16.21	75.2
SP2	14.27	49.3
SP3	13.75	42.1
SP4	14.96	61.9

The use of several stone pieces in one prism associated with the wide scattering is an important factor that can originate lower maximum strength values when a comparison with the stone specimens is done. In fact, if only one of the stone pieces presents lower mechanical strength with respect to the others, the peak strength of the prism will be naturally reduced. Thus, the use of stone pieces associated together may have increased the scatter of the results.

However, an interpretation purely based on statistics, Mosteller *et al.* (1973), cannot explain completely such decrease in strength. Being the compression failure controlled by mode I behaviour, the discontinuity between the stone pieces (horizontal joints) is likely to result in stress concentrations in a few contact points that probably originated failure for a load lower than the values achieved with the stone specimens.

The peak load and consequent failure were preceded by crack formation detected only by the clear sounds produced. Figure 3.26 shows the failure modes of the two different kinds of prisms used, at the end of the tests. From Figure 3.26, the failure may be attributed to relative displacements along shear bands, for both prism types.

(a) (b)

Figure 3.26 – Failure modes observed: (a) three pieces prisms; (b) four pieces prism.

3.4 Compressive tests on brick specimens

Parallel to the research on the mechanical behaviour of natural stone specimens, this Section introduces a complementary experimental work carried out on brick units and brick masonry. The main reason for adopting traditional masonry is that the more ductile behaviour of such masonry under compression provides adequate mechanical characterization under cyclic loading.

The brick adopted for this study is presently used mostly in facade elements, solely for aesthetic reasons. Nevertheless, in the past, this type of brick was widely used as a structural material. The bricks, produced in Barcelona by the Almar S.A. company, exhibit red colour and present the average dimensions of 28.5×13×5 cm^3, see Figure 3.27. No data concerning the mechanical characterization of the bricks was available previously to the current work.

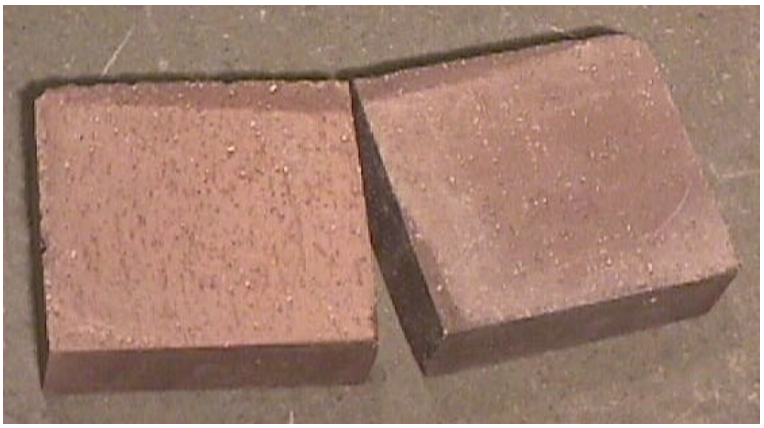

Figure 3.27 – Two half bricks used in the present testing program.

It is known that due to the production process, bricks can exhibit different mechanical properties for the vertical and horizontal directions. The vertical and horizontal directions are defined as the head joint direction (flatwise) and bed joint direction (lenthwise), respectively. Moreover, the microstructure of the brick is highly influenced by the firing temperature. Therefore, it was decided to perform preliminary compressive tests on prismatic specimens, testing them in the flatwise (5 cm) and lengthwise (28.5 cm) directions, see Figure 3.28. No tests were performed on the widthwise direction (13 cm) because it was not possible to extract specimens with the same height as the lengthwise direction in one single piece. Considering that masonry structures are generally submitted to uniaxial or biaxial plane stress, the flatwise and lengthwise directions are clearly the most important to be studied. All the brick specimens tested were randomly extracted from brick units, which were previously delivered in a single batch.

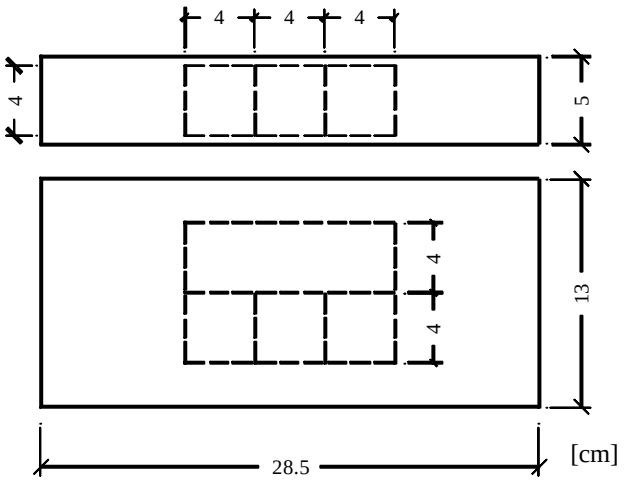

Figure 3.28 – Cutting scheme adopted for the prismatic brick specimens.

3.4.1 Monotonic tests on prismatic specimens

The problem of adopting an appropriate slenderness ratio for the specimens has been already presented and discussed in Section 3.1. To ensure a suitable height/width ratio, prisms of $4\times4\times12$ cm^3 were selected (height/width ratio equal to 3.0). Due to the low height of the brick, it was impossible to cut prisms perpendicularly to the flatwise direction unless they had a very small dimension, not representative of the material.

The grinding process, applied on both faces of the brick, reduced its thickness from 5 cm to 4 cm. Afterwards, specimens representing the flatwise and lengthwise directions were cut. The

vertical prisms (flatwise direction) were made of three aligned cubes of $4\times4\times4$ cm^3 with no material between the cubes, according to RILEM (1994a), and the horizontal prisms (lengthwise direction) were cut in one single piece, as shown Figure 3.29. A machine with a diamond covered circular blade was used for cutting. After cutting, surfaces that made contact with the platens and with each other were carefully polished.

The prismatic brick specimens were denoted by the specimen number preceded by a reference to the direction. Therefore, VPBS1 and HPBS3 indicate, respectively, the vertical prismatic brick specimen nº1 and the horizontal prismatic brick specimen nº3.

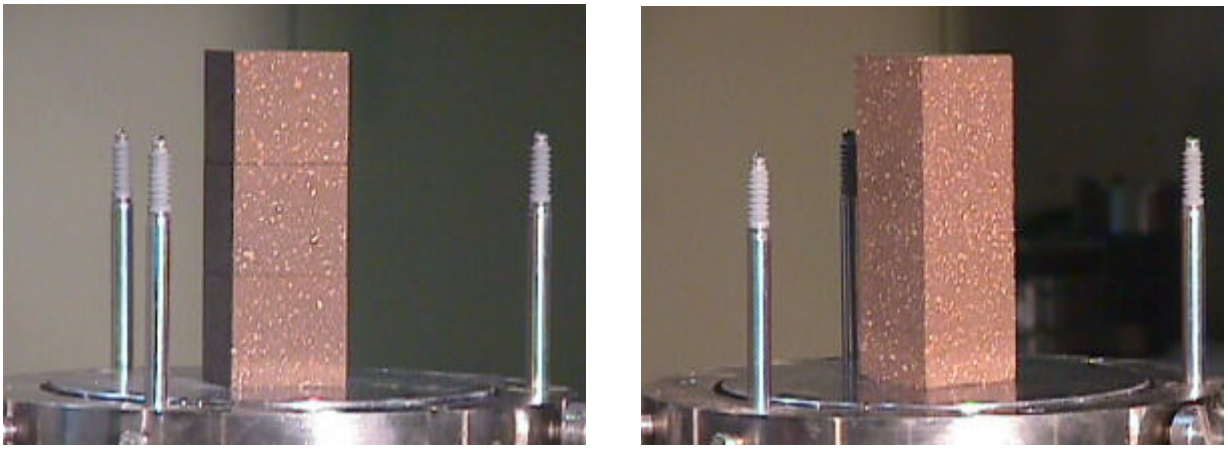

(a) (b)

Figure 3.29 – Prismatic brick specimens representative of: (a) vertical direction; (b) horizontal direction.

The day before testing, the specimens were immersed in water with free access to all surfaces. The specimens were removed from the water just before the beginning of the test, according to the RILEM standard (1994a).

The prismatic specimens were tested using the INSTRON testing machine described in Section 3.1. The aim of this test was to obtain the Young's modulus and the peak strength for each direction. In order to calculate those parameters only the effective displacements of the specimen should be taken into account. Therefore, three axial LVDTs were placed between the machine platens to measure the relative displacement under the two platens, see Figure 3.29.

As mentioned previously in Section 3.1 and Section 3.3, the specimens were placed into the lower platen and carefully aligned with the center of the platen. Afterwards, the upper platen was

moved, under force control, to the top surface of the brick specimen. This platen had a hinge to prevent any unfavourable effect due to non-parallelism between the specimen faces. No interposition material between machine platens and specimen was used.

All the prismatic specimens were tested monotonically under axial displacement control. The displacement rate was changed from 10 μm/s at the beginning up to 2 μm/s near the peak load. Following the described procedure, four specimens were tested for each direction. Figure 3.30 presents four typical stress-strain diagrams obtained. Again, it can be seen that the post-peak branch could not be obtained using axial displacement control.

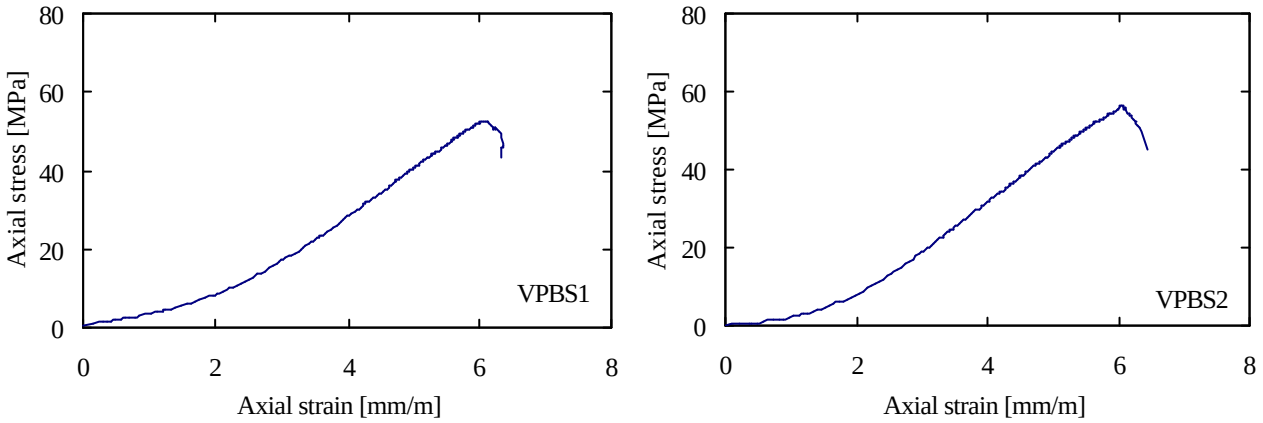

(a)

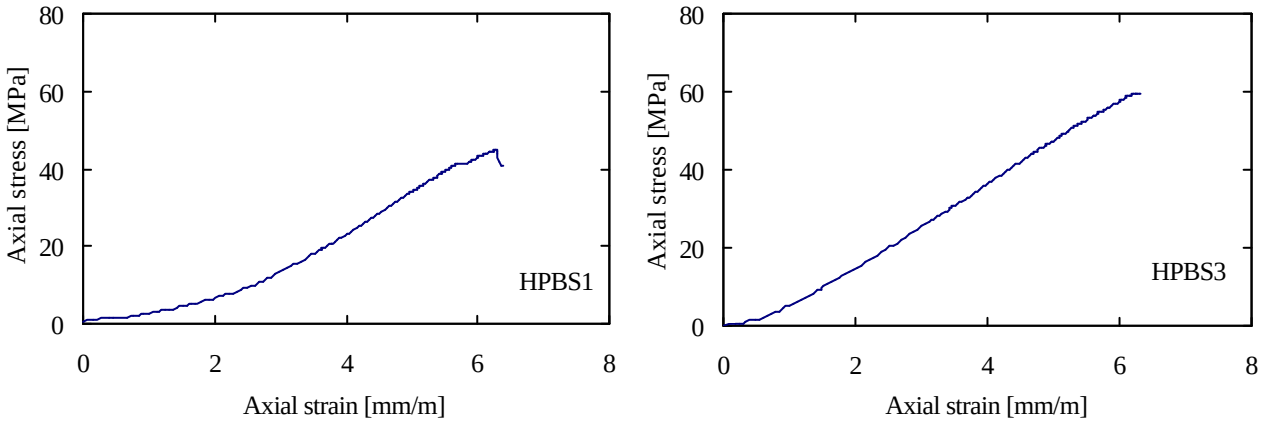

(b)

Figure 3.30 – Stress-strain graphics for four prismatic brick specimens tested under axial displacement control: (a) vertical direction (VPBS1, VPBS2) and (b) horizontal direction (HPBS1, HPBS3).

Table 3.10 and Table 3.11 summarize the obtained results. The Young's modulus was calculated in the [30%-70%] stress interval of the peak load because the stress-strain diagrams exhibited linear behaviour within this region.

Table 3.10 – Young's modulus, ultimate strength and statistical characterization of the vertical prismatic brick specimens.

Specimen	$E_{30\text{-}60}$ [GPa]	s_{peak} [MPa]
VPBS1	11.86	52.7
VPBS2	12.84	56.2
VPBS3	12.86	62.7
VPBS4	13.43	55.7
Average	12.75	56.8
C.V.	4.43 %	6.4 %

Table 3.11 – Young's modulus, ultimate strength and statistical characterization of the horizontal prismatic brick specimens.

Specimen	$E_{30\text{-}60}$ [GPa]	s_{peak} [MPa]
HPBS1	10.51	44.8
HPBS2	10.94	59.5
HPBS3	10.47	54.1
HPBS4	9.89	45.5
Average	10.45	51.0
C.V.	3.57 %	12.0 %

In terms of average values, the specimens representative of the vertical direction exhibit a higher elastic modulus (an increase of 22% when compared to the horizontal direction). A small coefficient of variation was found for both directions (about 4%). With respect to the peak strength, it can be observed that the vertical strength is, on average, 11% higher than the horizontal strength due to extruding anisotropy. However, for the peak strength higher coefficients of variation were found (6% for the vertical direction and 12% for the horizontal direction). These values seem to indicate a wide scatter in the peak strength values of the horizontal direction, probably due to the alignment of the shrinkage or firing cracks.

3.4.2 Monotonic tests on cylindrical specimens

It became evident after the previous tests that to obtain a post-peak material characterization another control technique had to be adopted. The acquired experience using circumferential displacement control technique and the encouraging results from the stone specimens tests, recommended the use of the same solution for the brick specimens. Only vertical cylindrical brick specimens were tested because this is the normal loading direction of masonry walls. Moreover, the diameter of the drill used (∅5 cm) did not enable the extraction of complete specimens from the available bricks (height = 5.0 cm). Figure 3.31 shows the cutting scheme adopted.

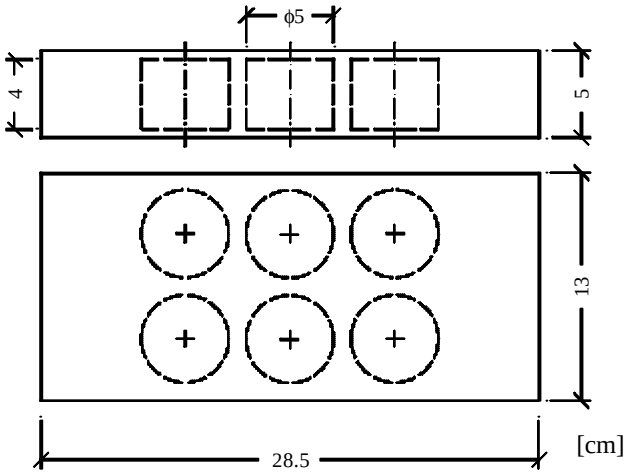

Figure 3.31 – Cutting scheme adopted for the cylindrical brick specimens.

Specimen preparation

An appropriate height/diameter ratio was adopted in order to obtain uniform stress distribution at the central region of the specimen. After grinding the top and bottom surfaces of the bricks, cylindrical specimens (∅5×4 cm^3) were extracted by means of a drill. As in the previous tests with cubes, vertical brick specimens were formed by three aligned cylindrical pieces, see Figure 3.32.

Test procedure

The adopted notation for the specimens was VCBSn, where VCBS denotes the vertical cylindrical brick specimen and n represents the specimen number. All the brick specimens were immersed in water with free access to all surfaces for a minimum period of 24 hours. Afterwards, the brick disks were removed from the water and carefully aligned. The diameter

and height were measured and registered. Then, the three-piece specimen was put on the lower platen and centered. In order to adjust the upper platen to the top surface of the specimen a preload was applied, under force control. The upper platen had a hinge to avoid any unfavourable effect due to non-parallelism between the specimen faces. No interposition material was placed between the specimen and the machine platens. A circumferential LVDT placed at the specimen mid-height and three axial LVDTs placed between the machine platens were used as displacement measurement transducers, see Figure 3.32. The applied force was measured by means of the machine load cell.

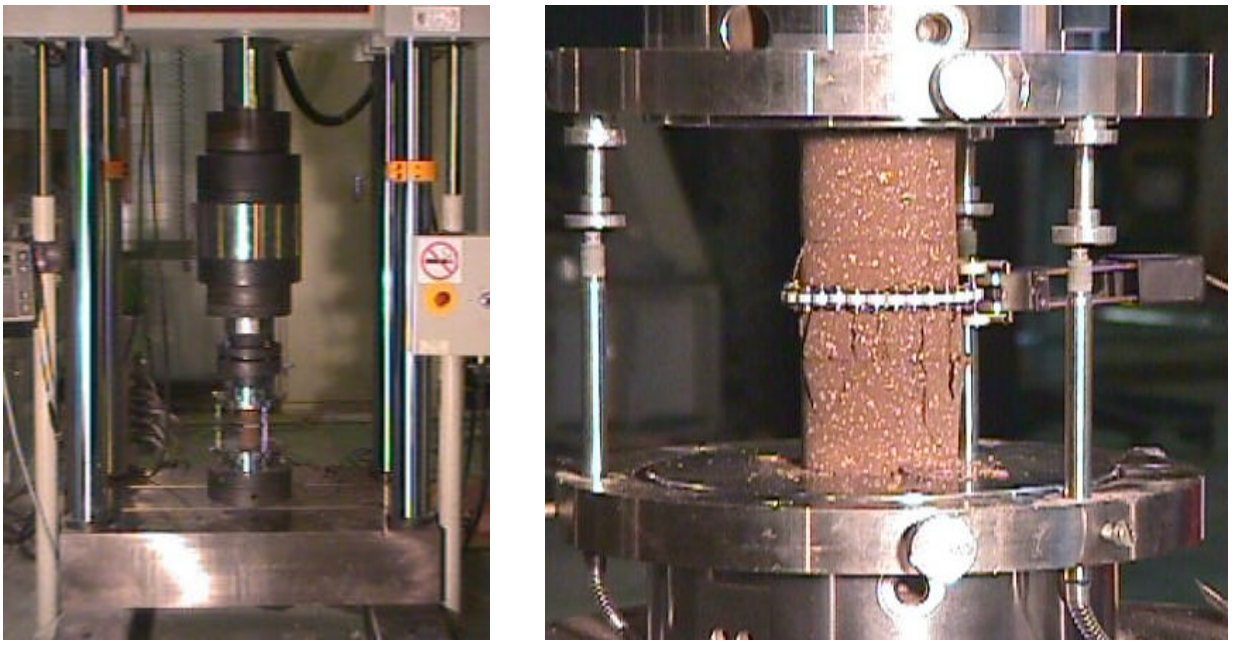

(a) (b)

Figure 3.32 – Testing set-up: (a) machine; (b) cylindrical brick specimen under testing conditions.

The following control variables were used:

- Axial displacement control for lower load levels;
- Force control during unloading;
- Circumferential displacement control in general.

The displacement rate was kept at about 5μm/s in circumferential control, 1.5 μm/s in axial displacement control and 2 kN/s during load control.

Monotonic tests using axial and transversal extensometers

As with the stones, a study concerning the rigorous computation of the brick elastic properties was fundamental. Hence, two brick specimens (VCBS1 and VCBS2) were tested using three double electric resistance strain gauges rosettes, equally spaced around the perimeter and placed at mid-height of the specimen, as shown in Figure 3.33. The simultaneous use of the axial LVDTs on these specimens, as done before, allowed comparisons between the two computed stress-strain diagrams.

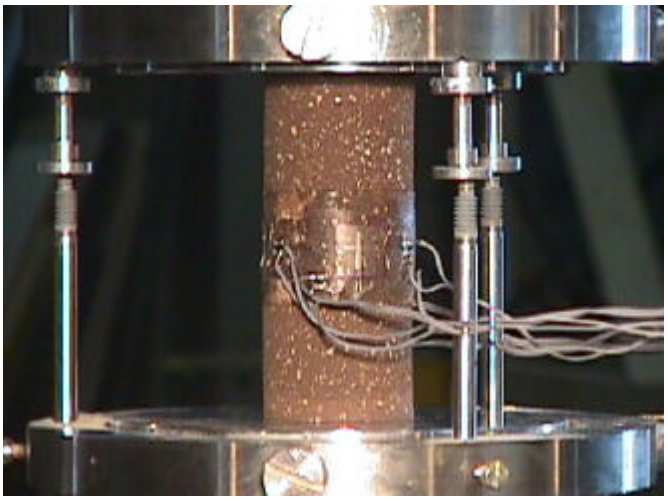

Figure 3.33 – Strain-gauge arrangement for the cylindrical brick specimens.

These two specimens were tested under axial displacement control at a constant rate of 5 μm/s. Therefore the load was applied in a continuous manner. Figure 3.34 presents the axial stress-strain and axial stress-circumferential strain diagrams for the specimens VCBS1 and VCBS2. Both specimens failed just after the peak load, so post-peak behaviour could not be chracterized.

The evolution of the tangent values of Young's modulus (E), Poisson's ratio (ν) and volumetric strain (e_{vol}) is shown in Figure 3.35, for the brick specimens VCBS1 and VCBS2. The Young's modulus was calculated using both LVDT (E_{lvdt}) and strain-gauge data (E_{sg}).

From the results presented above, the following conclusions can be derived:

- The typical adjustment between the machine plates and the specimen is again visible in the initial branch of the stress-strain diagram. In the diagrams computed with strain-gauge data, such accommodation does not exist.

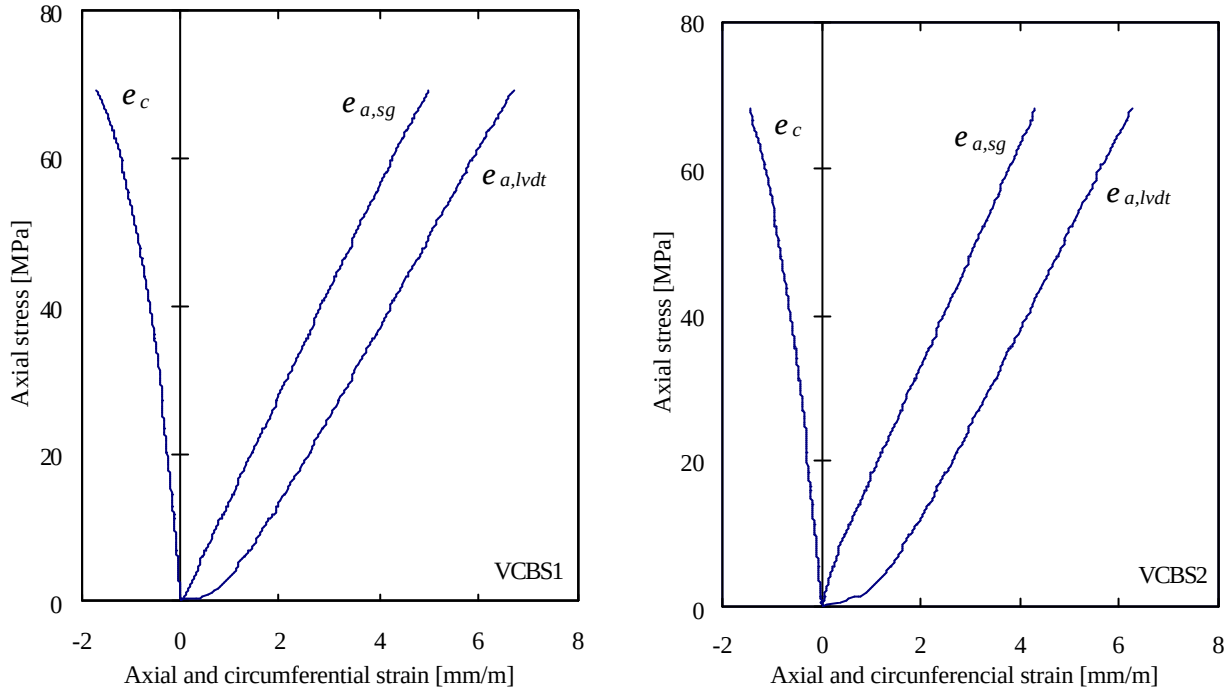

Figure 3.34 – Axial and circumferential strain versus axial stress for the brick specimens: (a) VCBS1; (b) VCBS2.

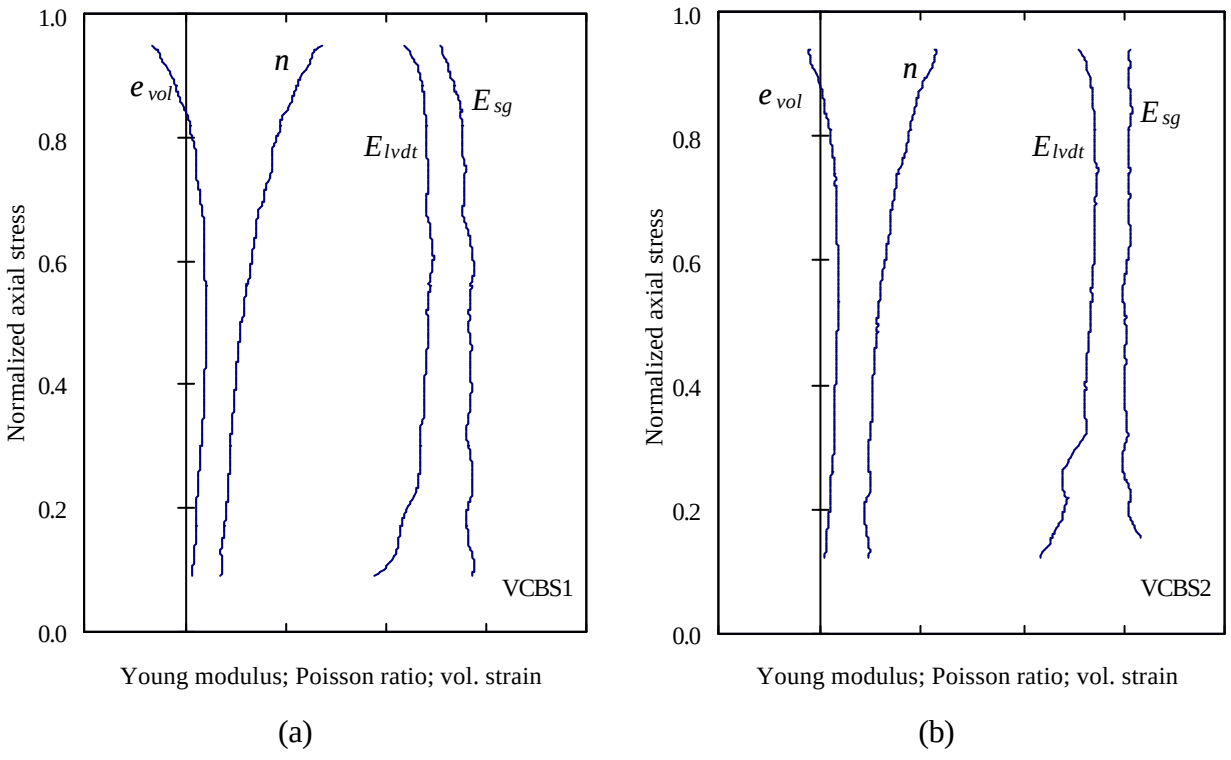

Figure 3.35 – Young's modulus, Poisson's ratio and volumetric strain for the brick specimens: (a) VCBS1; (b) VCBS2 (the horizontal scale is normalized).

- The Young's modulus remains more or less constant under load increase, especially for the specimen VCBS2. For both specimens, the Young's modulus presents higher values if calculated with the strain-gauge data, probably due to the introduction of the artificial joints. Therefore, the elastic modulus based on the LVDTs measurements seems to be slightly underestimated.
- Poisson's ratio increases continuously with the applied load. The increase is particularly slow up to 50% of the peak load, but grows from there up to the peak and equals 0.5 for a very high load (between 80% and 90% of the ultimate load). A Poisson's ratio equal to 0.5 corresponds to a volumetric strain equal to zero.
- Due to axial compression, a volume reduction occurs up to approximately 50% of the peak load. Afterwards, due to the dilation process, a volume increase takes place. The initial volume is retrieved for a very high stress.

Table 3.12 and Table 3.13 condense the elastic properties of the two brick specimens tested with strain gauges along the load path. This information helps to understand the diagrams presented above.

Table 3.12 – Elastic properties for the specimen VCBS1 (s_{peak} = 69.2 MPa).

Stress level	25%	50%	75%
E_{lvdt} [GPa]	11.60	12.10	12.15
E_{sg} [GPa]	14.29	14.16	14.02
ν	0.21	0.29	0.43

Table 3.13 – Elastic properties for the specimen VCBS2 (s_{peak} = 68.2 MPa).

Stress level	25%	50%	75%
E_{lvdt} [GPa]	11.98	13.30	13.63
E_{sg} [GPa]	15.05	15.05	15.22
ν	0.24	0.28	0.39

The tangent values of E and ν exhibit limited variations for different load increments but an important difference between the two available ways of computing the Young's modulus (strain

gauges and LVDTs) can be detected. A possible reason has to do with the stiffness of the glue used to fix the strain gauges. Tests done on bricks have shown that the stiffness, measured with strain gauges, increased due to glue penetration into the brick, see Binda *et al.* (1996a). For porous and less stiff materials, the glue had a considerable local influence and such influence increased with the porosity of the materials to be tested. On the other hand, the introduction of the artificial joints in the brick specimens might have influenced the measurement of the Young's modulus by means of LVDTs, leading to a lower value. Hence, if accurate elastic parameters are to be achieved, special care should be put into the computation and definition of these parameters. No remarkable differences are found if a comparison between the two specimens is made. So, it can be accepted that the results obtained offer a reasonable degree of confidence.

Considering that the Young's modulus can also be computed in the approximately linear region of the stress-strain diagram, Table 3.14 presents the values of E computed in the [30%-70%] stress interval, by linear least square regression. These values can be considered accurate enough for the purpose of numerical calculations.

Table 3.14 – Young's modulus defined in the [30%-70%] stress interval for the specimens VCBS1 and VCBS2.

Stress level	[30% – 70%]	
Specimen	VCBS1	VCBS2
E_{lvdt} [GPa]	12.11	13.29
E_{sg} [GPa]	14.24	15.07

Series of monotonic tests with complete results

In order to acquire knowledge with regard to the post-peak behaviour, it was decided to perform some monotonic tests on brick specimens. Due to the promising results concerning stone specimens, the option for circumferential displacement control was made. From the results concerning the prismatic specimens, a very strong brittle post-peak behaviour was expected. According to the procedure described before, three brick specimens were tested monotonically. Two of the obtained stress-strain diagrams are illustrated in Figure 3.36.

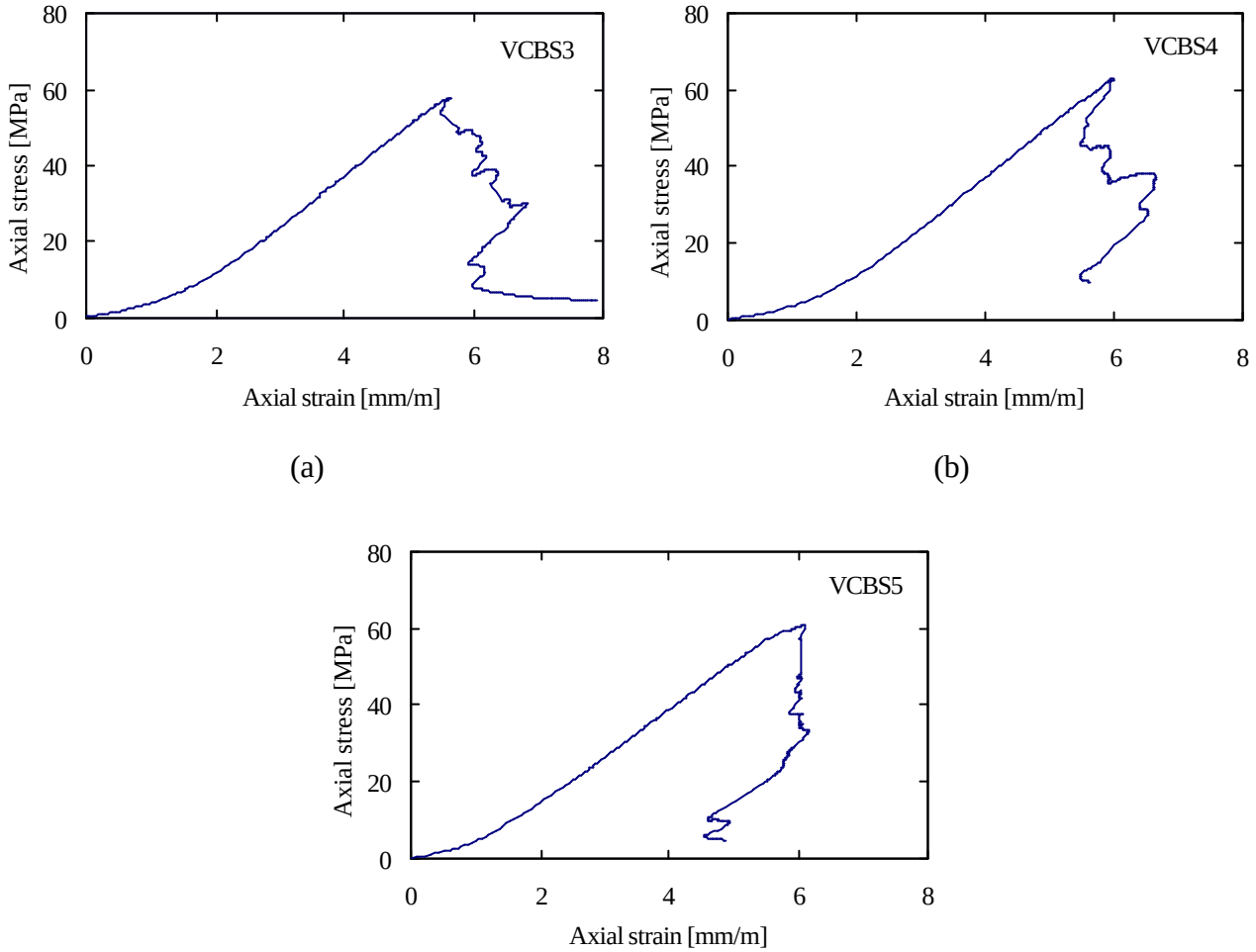

Figure 3.36 – Stress-strain diagrams of two cylindrical brick specimens tested monotonically: (a) VCBS3; (b) VCBS4; (c) VCBS5.

The diagrams are characterized by an initial curve (typical adjustment between the specimen and the machine platens), a linear and stable pre-peak branch and an unstable post-peak region. The pre-peak portion is quite similar in both specimens presented and easy to follow. Near the peak load the first macroscopic cracks became visible. Visible crack initiation took place in the brick cylinders close to the platens, see Figure 3.37. When peak load was reached, the test turned very unstable showing all the brittleness of the material. In this way, post-peak behaviour became extremely difficult to characterize.

The three specimens achieved resembling ultimate loads. Table 3.15 presents the Young's modulus computed in the [30%-70%] stress interval, the peak strength for the three specimens

and the main statistical quantities. It can be observed that no important differences regarding either the Young's modulus or the ultimate strength were found.

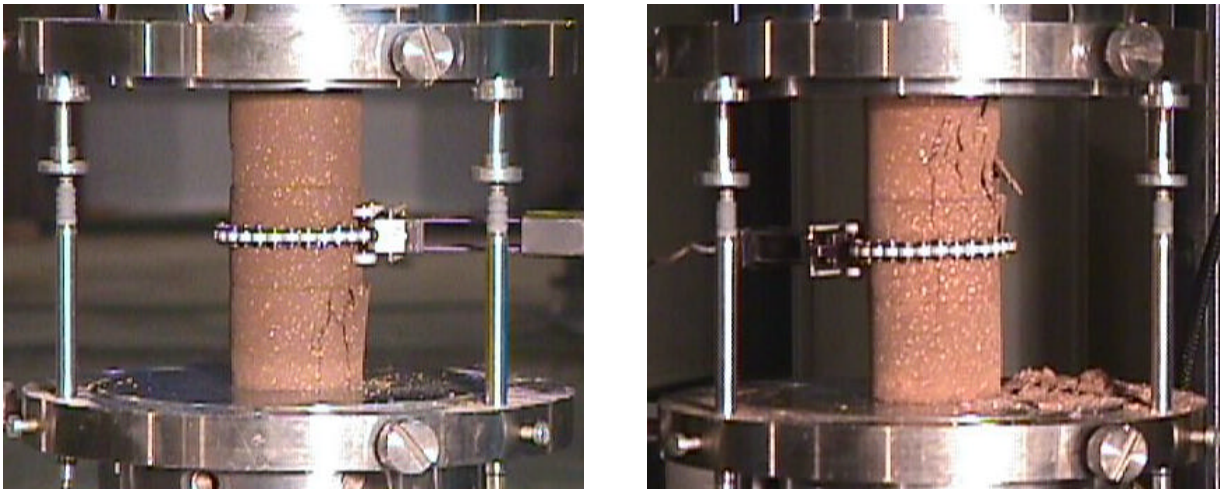

Figure 3.37 – Typical crack initiation and progressive evolution.

Table 3.15 – Characterization of the monotonic tests performed on brick specimens.

Specimen	$E_{30\text{-}70}$ [GPa]	s_{peak} [MPa]
VCBS3	13.04	57.8
VCBS4	13.36	63.1
VCBS5	12.09	60.9
Average	12.83	60.6
C.V.	4.20 %	3.6 %

3.4.3 Cyclic tests on cylindrical specimens

In this Section, the tests carried out under cyclic loading are presented and discussed. A series of unloading-reloading cycles were performed, particularly in post-peak, to acquire data about stiffness degradation and energy dissipation, as done before with stones specimens. This knowledge is especially important if numerical models on cyclic behaviour are intended to be used. The general procedure was similar to the monotonic tests. The unloading branches were performed under force control at a constant rate of 2 kN/s (≈1 MPa/s).

The stress-strain diagrams of the four brick specimens are illustrated in Figure 3.38. The diagrams were very difficult to obtain, due to the material's brittleness. The control in post-peak was quite difficult to maintain and some specimens were lost during testing.

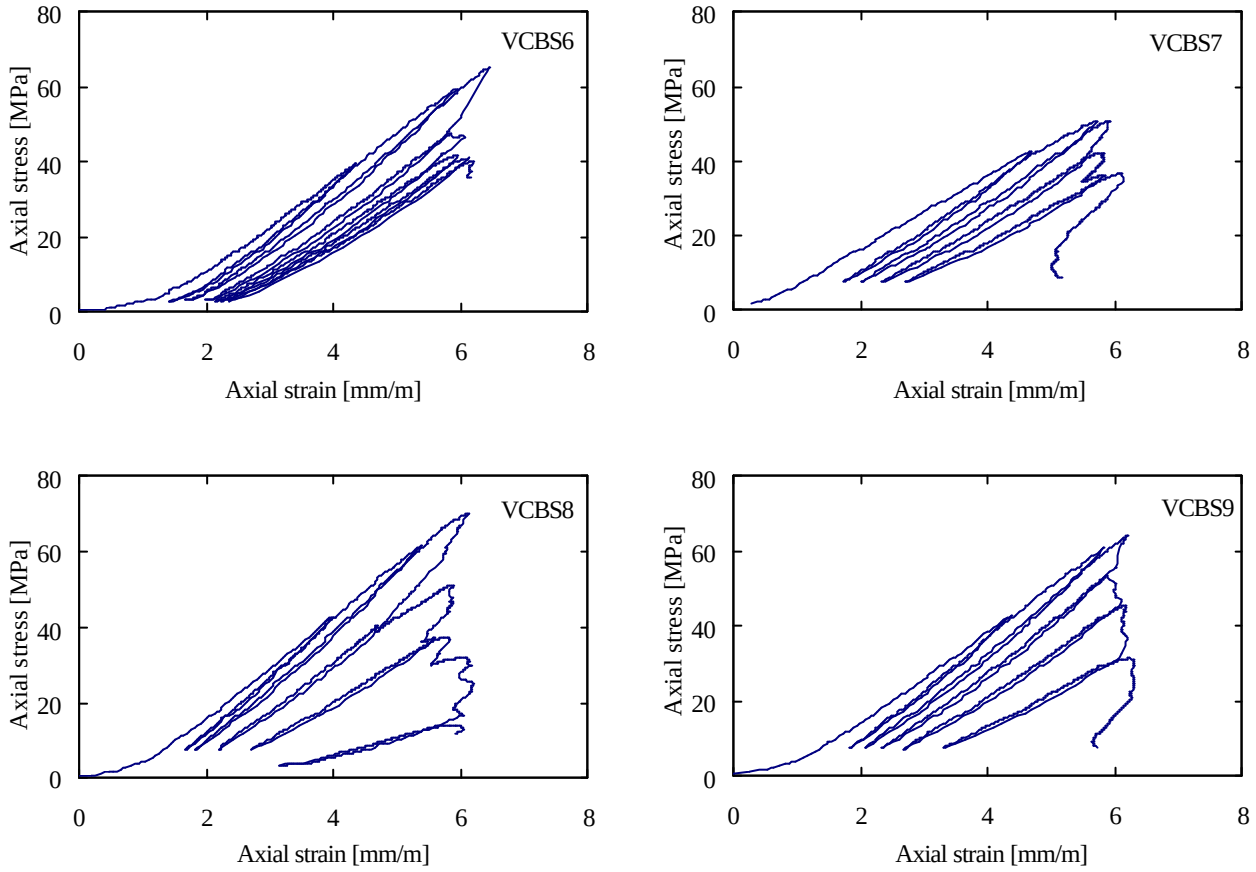

Figure 3.38 – Stress-strain diagrams of the cylindrical brick specimens tested cyclically.

The average Young's modulus, defined in the [30%-70%] stress interval, the peak strength, their average quantities and coefficients of variation are presented in Table 3.16.

Table 3.16 – Characterization of the cyclic tests performed on brick specimens.

Specimen	$E_{30\text{-}70}$ [GPa]	s_{peak} [MPa]
VCBS6	12.61	65.0
VCBS7	9.84	50.8
VCBS8	13.76	70.5
VCBS9	12.27	63.9
Average	12.12	62.6
C.V.	11.78 %	11.6 %

The specimen VCBS7 exhibited lower values than the other three. Possibly, this specimen could have been damaged during preparation. Another possibility has to do with the material nature. Due to the firing temperature and chemical composition it is possible to obtain different mechanical strengths inside the same brick. So, some differences in the obtained strengths and Young's modulus may have been related with the different parts of the bricks used to build the specimens.

The Young's modulus (E) was computed for all the reloading branches showed in Figure 3.38. The values obtained by linear least square regression are represented in Table 3.17, where "rb" means the reloading branch for which E has been computed.

Table 3.17 – Young's modulus of the reloading branches obtained by linear least square regression (brick specimens).

Specimen	E [GPa]					
	rb1	rb2	rb3	rb4	rb5	rb6
VCBS6	13.07	13.45	11.88	10.61	10.43	10.29
VCBS7	11.55	11.27	10.34	8.99	——	——
VCBS8	14.98	15.05	12.96	10.20	5.51	——
VCBS9	13.76	13.97	13.14	11.35	8.90	——

A very slight increase of the Young's modulus the can be detected in the pre-peak portion (see specimens VCB6 and VCB9). However, for higher stress levels and during the entire post-peak, an important and monotonic decrease on the Young's modulus occurred for all specimens. This reduction is associated with damage growth in the material.

3.4.4 Failure modes

The failure modes showed in Figure 3.39 help to understand the behaviour of the brick specimens. Although three aligned cylinders formed the vertical specimens, they behaved as solid prisms, as happened with other authors, e.g. Binda *et al.* (1996a). The cracks ran through the cylinders with continuity. The existence of shear bands was perfectly visible. The specimens presented a diagonal crack, from the bottom to the top, and, usually, the failure through this shear band was the cause of specimen collapse.

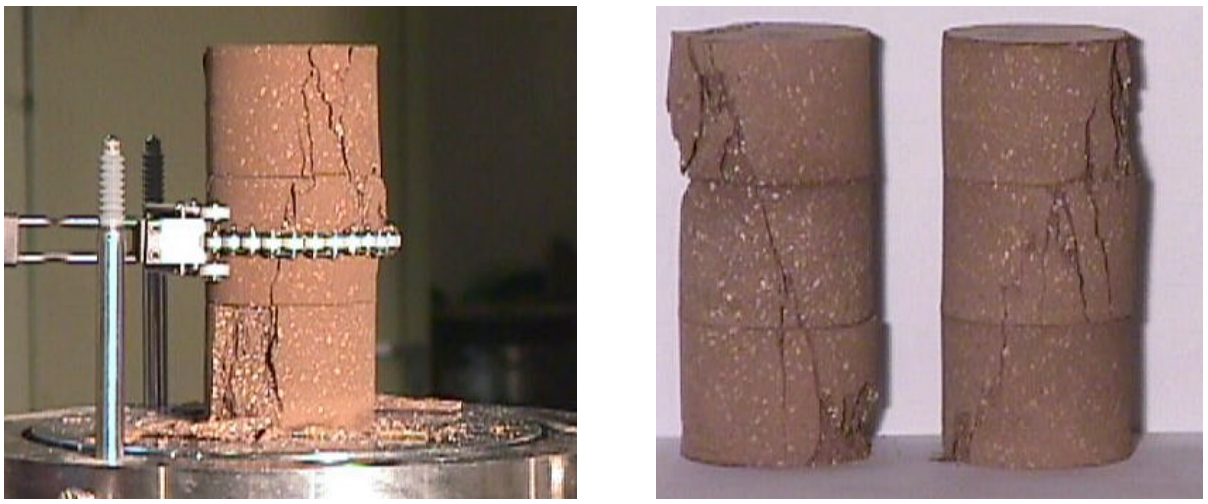

Figure 3.39 – Failure mechanism of the cylindrical vertical brick specimens.

3.5 Compressive tests on brick prisms

In order to characterize the behaviour of masonry under cyclic loading, four stacked bond prisms of five bricks each, were constructed and tested. The main purpose was to examine the effects of brick and mortar properties on the strength and deformation characteristics of the masonry prisms.

Brick masonry is composed of two materials with different mechanical properties: mortar and bricks. Usually, mortar presents a softer behaviour whereas clay brick exhibits a stiffer behaviour. The mechanical properties of masonry depend on the characteristics of the component materials and on the construction conditions. In fact, workmanship effects can have a large influence on the mechanical properties of masonry.

It is known that, under uniaxial compressive loading, mortar tends to expand laterally more than the brick, because it has weaker mechanical properties. Due to the continuity between bricks and mortar, ensured by cohesion and friction, mortar is confined laterally by the bricks. Thus, shear stresses, developed at the mortar-brick interface, produce a triaxial compressive stress state in the mortar and bilateral horizontal tension coupled with vertical compression in the brick, see Figure 3.40 for a schematic illustration. In this way, failure usually occurs by the development of cracks in the bricks, parallel to the loading direction.

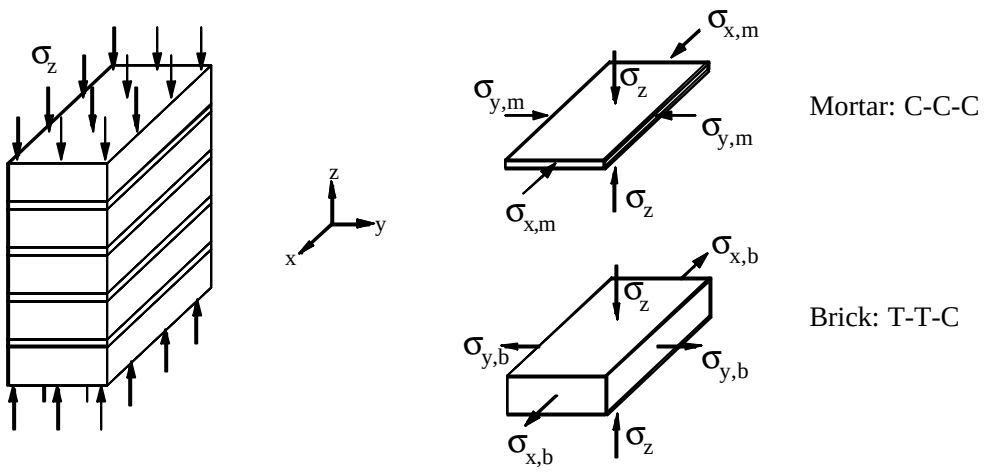

Figure 3.40 – Masonry prism under compressive loading normal to bed joints and stress states for brick and mortar elements (C denotes compression and T denotes tension).

3.5.1 Prism preparation

The bricks used in this study are from the same batch as those that were used in Section 3.4. They are currently produced in Barcelona and have the average dimensions of 28,5×13×5 cm^3. The stacked bond prisms were built in accordance to code LUM B1, see RILEM (1994b) and Figure 3.41.

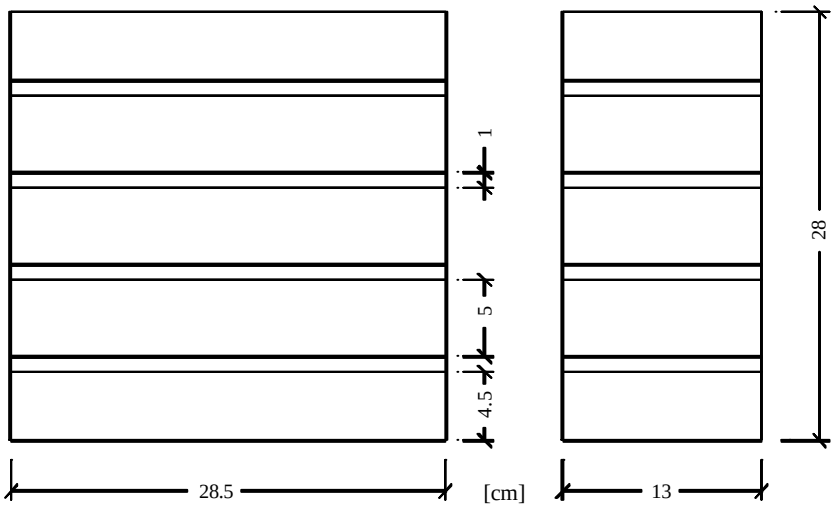

Figure 3.41 – Geometry established for the brick masonry prisms, based on the RILEM recommendations.

The joints were kept at a uniform thickness of about 1 cm and filled with mortar. The top and bottom bricks were carefully grounded for a better surface planarity and parallelism between the prism faces. The grinding process, applied on one face of the bricks, reduced their thickness from 5 cm to 4,5 cm. Then, the bricks used to build the prisms were immersed in water with free access to all surfaces, at least for one hour. Using pre-mixed cement mortar, four prisms of five bricks high were built, resulting in prisms of $28.5 \times 13 \times 28\ cm^3$ with a slenderness ratio of 2.15 (see Figure 3.41 for a schematic presentation). This ratio allows a uniaxial compressive behaviour at the center of the prisms. In spite of the care put into the construction of the prisms, not all of them were built precisely with the same height. Table 3.18 shows the measured height of each prism. In this study, the brick masonry prisms were designated by the name BP (brick prism) followed by an order number.

Table 3.18 – Relative brick and mortar heights computed for the four prisms.

Prism	h_{total} [cm]	h_{mortar} / h_{total}	h_{brick} / h_{total}
BP1	28.1	15 %	85 %
BP2	27.7	14 %	86 %
BP3	27.3	14 %	86 %
BP4	27.3	15 %	85 %

The maximum error was about 2.5% with respect to the prism height as it was initially defined. Also, the mortar thickness was kept almost equal to the value established (14.3% of the prism height). The stacked bonded prisms were not stored and cured at controlled temperature and humidity, as RILEM code specifies. Instead, they were cured outside of the laboratory in order to simulate practical curing conditions, close to the brick masonry walls. During the first days following construction, the prisms were wetted to prevent from drying out.

3.5.2 Mortar specimens

Some results performed on mortar specimens are presented in this section. However, it must be noted that the conditions of mortar curing inside the prism and inside the mould are necessarily different. Nevertheless, the data obtained in this way provides an indication about the mortar

properties. The mortar used was made from a pre-mix, based on Portland cement and fine aggregates (0-2 mm).

During the construction of the brick prisms, three cylindrical mortar specimens of $\varnothing 10 \times 20$ cm^3 were made, at the same time and with the same mortar used to build the brick prisms. The specimens were made of mortar from three different mixes. The specimens were left outside together with the stacked bond prisms and submitted to the same atmospheric conditions.

The specimens were then tested under axial displacement control, at a constant rate of 2 µm/s. The tests were done in the closed-loop servo-controlled INSTRON testing machine, described in Section 3.1. The axial displacements were measured by using three axial LVDTs placed between the machine platens and the applied force was measured by means of the machine load cell. The axial strains and stresses were computed by dividing the average axial displacement and load by the initial axial length of the specimen and the initial cross-sectional area, respectively. The diagrams obtained in this way are presented in Figure 3.42. Unfortunately, the specimen M1 was seriously damaged just before testing, so only results concerning specimens M2 and M3 are available.

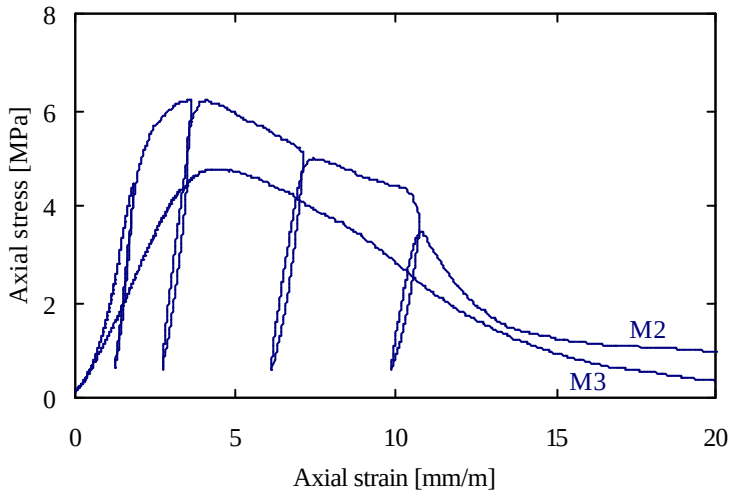

Figure 3.42 – Stress-strain diagrams obtained for the cement mortar specimens M2 and M3, used to build the brick masonry prisms.

Table 3.19 exhibits the results in terms of Young's modulus and ultimate strength. As it can be observed, the specimens were tested at an age higher than the standard 28 days. Also, the stacked bond prisms were tested at similar age.

Table 3.19 – Cement mortar specimens: age of testing, Young's modulus and peak strength.

Specimen	Age (days)	E_0 [GPa]	s_{peak} [MPa]
M1	——	——	——
M2	78	4.19	6.2
M3	76	1.57	4.8

The Young's modulus was defined based on the higher linear least square regression coefficient computed in the [0% -50%] stress interval. The cyclic test performed on specimen M2 showed that no remarkable stiffness degradation was found when the slopes of the reloading branches were analyzed.

3.5.3 Test procedure

The brick masonry prisms were tested in the SUZPERCAR testing machine, presented in Section 3.3, due to its high load capacity (5 MN). The ages of testing as well as the mortar type used are referred to in Table 3.20, for each prism.

Table 3.20 – Brick prisms: age of testing and mortar type used.

Prism	Age (days)	Mortar type
BP1	63	M1
BP2	63	M1
BP3	61	M2
BP4	59	M3

Three axial LVDTs were placed between the machine platens, equally spaced and attached to a thick steel plate (40×32 cm^2) located on the lower machine platen, see Figure 3.43 for a schematic representation. The applied load was measured by means of the machine load cell. After making all the measurements necessary for an appropriate geometric characterisation, the prism was placed into the lower platen and carefully centered. Then, the lower platen was moved under force control until a pre-compression was applied to the prism. The hinge located in the

upper platen was used to prevent any adverse effect due to any potential non-parallelism between the prism faces. No interposition material was used between the machine platens and the prim.

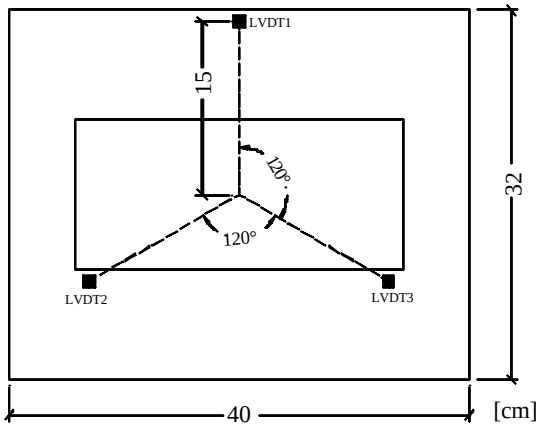

Figure 3.43 – Measurement transducers arrangement used for the brick masonry tests (top view).

For testing, the following control variables were used:

- Axial displacement control for loading and reloading;
- Force control during unloading.

The axial displacement rate was kept about 3 μm/s and unloading was done at an approximate rate of 10 kN/s. It was decided to perform unloading-reloading branches in order to check the properties related to cyclic behaviour, such as stiffness degradation and hysteretic energy dissipation.

3.5.4 Test results

The stress-strain diagrams of the four masonry prisms are presented in Figure 3.44. The axial displacement of each prism was defined by the average value computed from the three axial LVDTs used. Then, the axial strain was calculated by dividing the average axial displacement by the initial axial length of the prism. In the same manner, the axial compressive stress was computed as the axial load divided by the initial cross-sectional area.

Apart from the initial adjustment between the prism and the machine platens, stress-strain curves exhibited a pre-peak bilinear behaviour. An initial linear branch was followed by another branch up to near the peak, with lower stiffness and greater development. Transition between these two

different slopes was located from 6 MPa to 10 MPa (between 21% and 35% of the peak load) and defined the beginning of the nonlinear behaviour of the masonry prisms. The beginning of brick cracking and mortar nonlinearities are likely to originate this behaviour. The ultimate strength of each prism is displayed in Table 3.21. All prisms presented very close strength values.

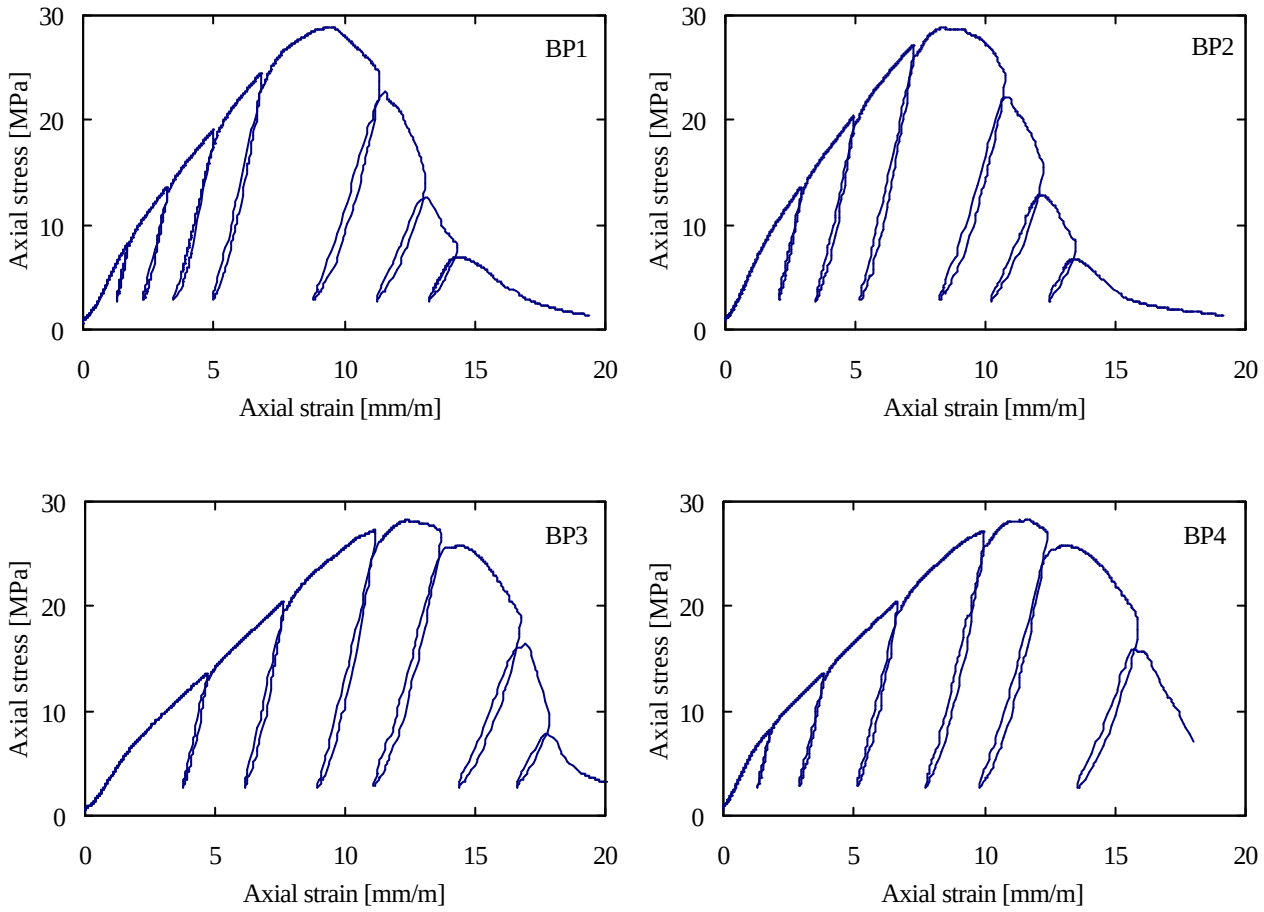

Figure 3.44 – Stress-strain diagrams obtained for the brick masonry prisms under cyclic loading.

Table 3.21 – Ultimate strength of the masonry prisms

Prism	s_{peak} [MPa]
BP1	28.9
BP2	28.8
BP3	28.2
BP4	28.3
Average	28.6
CV	1.1 %

Two other relevant aspects are clearly visible from the analysis of Figure 3.44. The average strength value of the masonry prisms is much higher than the mortar strength presented in Section 3.5.2. This is mainly due to two factors. On one hand the mortar joint between bricks was subjected to a triaxial compressive stress state. Results from triaxial tests have shown that mortar behaviour is dependent on confining pressure as well as on mortar type, and that axial stress increases along with confining pressure, McNary and Abrams (1985). On the other hand, the different conditions of cure of the mortar inside the prism and inside the mould may have changed significantly its mechanic properties.

A second aspect has to do with the ductility presented by the diagrams showed in Figure 3.44, when compared to the stress-strain curves exhibited in Section 3.3 of the brick specimens (very fragile structural behaviour). From this comparison, it can be concluded that mortar has a preponderant influence on the prism deformation. A comparison made with brick specimens showed that a reduction of the peak strength was compensated by a stable post-peak behaviour. As reported by Binda *et al.* (1996b), it can be concluded that the compressive strength of the masonry is highly influenced by the characteristics of the single components.

With the purpose of investigating the magnitude of stiffness degradation, the slope of all reloading branches was computed by linear least square regression and it is shown in Table 3.22. The graphical representation of the elastic modulus of the reloading branches (values in Table 3.22) as a function of the axial stress is illustrated in Figure 3.45.

Table 3.22 – Elastic modulus of the reloading branches calculated by linear least square regression.

Brick prism	*E* [GPa]						
	rb1	rb2	rb3	rb4	rb5	rb6	rb7
BP1	10.58	10.82	10.13	10.83	7.86	6.68	4.16
BP2	10.84	11.16	11.07	7.91	5.66	4.40	——
BP3	10.72	10.95	10.50	8.85	6.10	4.34	——
BP4	10.50	10.59	10.72	10.12	8.78	6.14	——

Even for the distinct values of the secant Young's modulus, visible in the stress-strain envelope of Figure 3.46, Table 3.22 shows that stiffness of the reloading branches, computed via linear least

square regression, present values relatively close for a same strain level. In the pre-peak portion of the stress-strain curves, the stiffness of the reloading branches remained relatively constant. On the other hand, in post-peak the slope of the reloading branches suffered an important decrease. Figure 3.44 shows also that energy dissipation increased with the strain level.

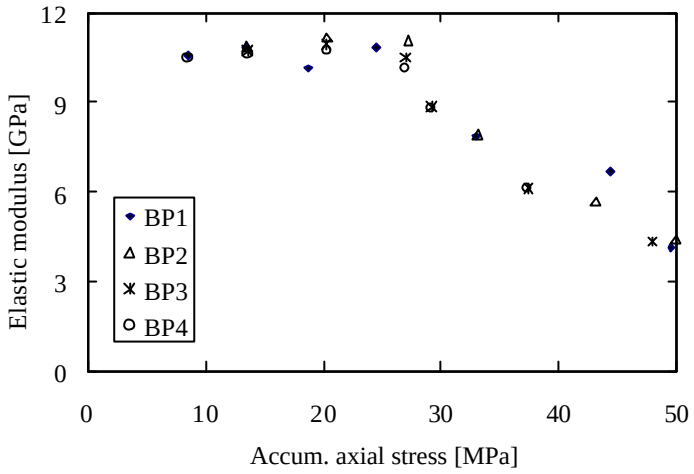

Figure 3.45 – Graphical representation of the elastic modulus of the reloading branches as a function of the accumulative axial stress, for each brick prism.

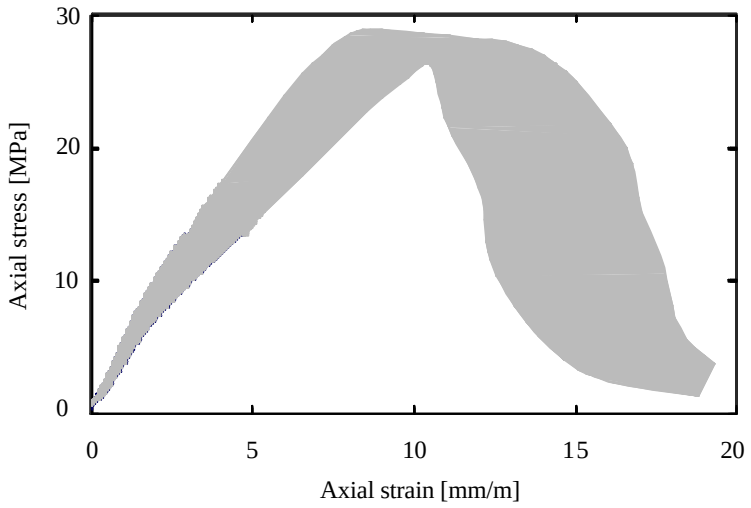

Figure 3.46 – Stress-strain envelope diagram of the four diagrams present in Figure 3.44.

3.5.5 Failure modes

The failure modes obtained from testing the stacked bond prisms are shown in Figure 3.47. The pictures were obtained at the end of each test, corresponding to the final part of the post-peak

branch of the stress-strain diagrams. In these tests, the post-peak branch was easy to follow and a satisfactory stable behaviour was found.

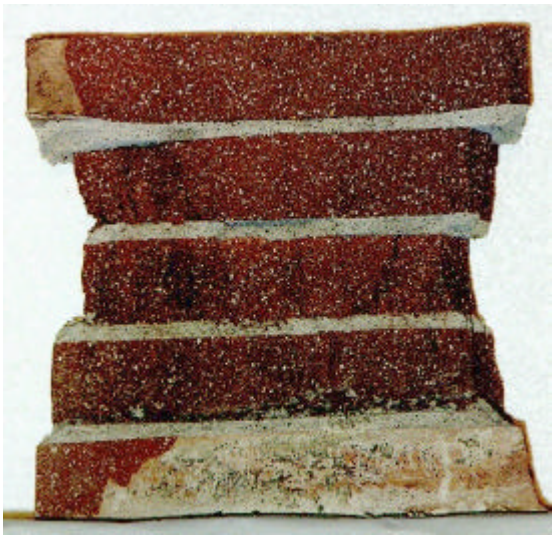

(a)

(b)

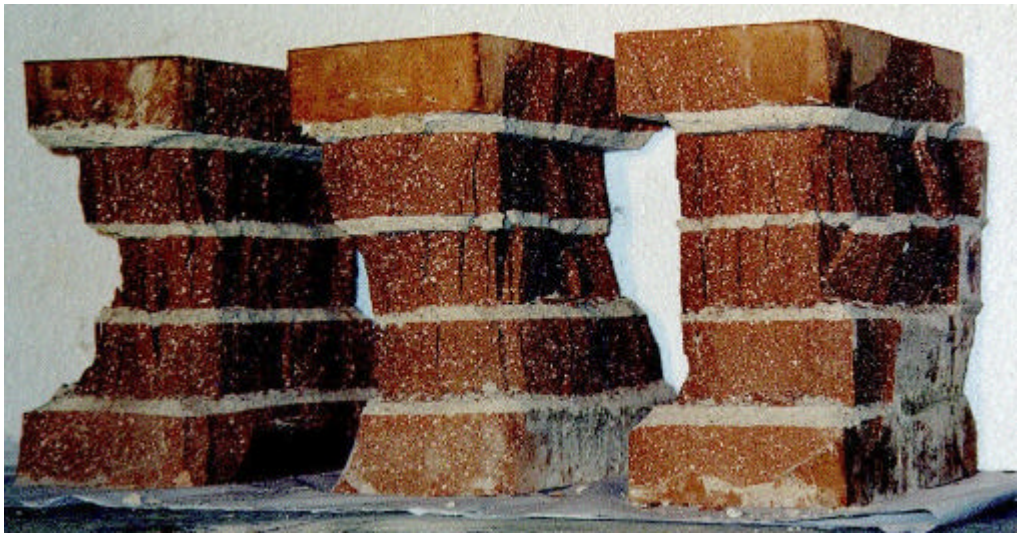

(c)

Figure 3.47 – Failure modes of the brick masonry prisms: (a) frontal view; (b) lateral view; (c) perspective of three tested prisms.

3.6 Summary

This Chapter presents an experimental study inserted in a wider experimental research program aiming at the mechanical characterization of historic building materials, e.g. Ramos (2002) and Almeida (2002). Within this experimental program, a sandstone was fully characterized in tension

(Ramos, 2002), shear and compression. The experimental tests described in this study were performed at Universitat Politècnica de Catalunya and at Universidade do Minho, consisting of several specimens and masonry prisms made of stone and bricks tested under monotonic and cyclic compressive and shear loading, allowing obtaining valuable experimental data.

The stone specimens tested under compressive loading were characterized by high ultimate strength values and a very pronounced fragile behaviour after peak load. The cyclic tests indicate that stiffness degradation occurred especially during post-peak domain. Moreover, the small difference between LVDTs measurements and strain gauges measurements enables the assessment of the Young's modulus by means of axial LVDTs. A comparison between the results discussed in Sections 3.1 and 3.3 allowed concluding that the Young's modulus computed for the cylindrical stone specimens and for the stone prisms presented very similar average values. However, the scatter concerning the mechanical properties constitutes an important issue in the sense that a significant decrease of resistance took place when shifting from stone specimens to masonry (in terms of average values). Thus, this subject should be further studied since existing design codes, e.g. EC6 (CEN, 1995), do not take stacked dry-stone masonry into consideration.

The direct shear tests performed on dry stone joints showed a typical elasto-plastic behaviour for the shear stress-relative shear displacement diagrams. During the cyclic loading neither stiffness degradation nor hardening behaviour between cycles was observed. It was found that $\tan\phi$ equals 0.62 and that $\tan\psi$ is equal to zero.

Afterwards, sets of brick specimens were tested in uniaxial compression. The results showed a brittle behaviour. Even if the brick specimens were made of three aligned cylinders, they behaved as whole specimens, where cracks ran continuously through the cylinders. In addition, no significant differences were found between prismatic and cylindrical specimens, in terms of Young's modulus and peak strength values (considering average values). Complementary, four stacked bond prisms made of five bricks each, were constructed and tested under cyclic loading. The average strength value of the prisms was much higher when compared to the mortar specimens, but less than the average strength of the bricks tested separately. Mortar had a very large influence on prism deformation. A reduction on the peak strength was compensated by stable post-peak behaviour. The compressive strength of masonry was highly influenced by the characteristics of the single components, brick and mortar.

The brittle behaviour exhibited both by stone and brick specimens, where a same height/diameter ratio (h/d=2.4) was used, has evidenced that the post-peak regime cannot be followed even using an axial displacement control. A more advanced control technique, as circumferential control, has to be used. Subsequent tests on stone specimens, where the height/diameter ratio was reduced from 2.4 to 2.0, have shown a better stability until complete loss of strength capacity, i.e. a more stable post-peak behaviour, without significant variation of the peak strength.

Finally, the results described in this Chapter show undoubtedly that when dealing with historical building materials, the intrinsic variability of the mechanical properties of natural stone and clay brick masonry is an important issue that should be kept in mind.

4. DRY STONE MASONRY WALLS UNDER COMPRESSIVE AND SHEAR LOADING

Although not as common as mortar jointed masonry, structures made of stones laid without mortar between them represent nowadays an important legacy when dealing with historic constructions. Moreover, in the Northern part of Portugal, it is common to find dry stone masonry historical constructions due to the lack of lime in ancient times. Understanding and preserving constructions made of dry joints, either related to structural assessment or repair, inevitably demands adequate knowledge of their mechanical behaviour, which can be extremely complex. If out-of-plane failure is prevented by appropriate construction techniques, the research concerning these structures can focus on their in-plane structural behaviour. In spite of that, research on this particular type of masonry structures is almost inexistent and therefore little is known about the mechanical behaviour of masonry structures with dry joints. Since the possibility of performing destructive tests on historical constructions, either in-situ or by removing samples large enough to be representative is most of the times impossible (Macchi, 1992), the key is to carry out laboratory tests. In these tests, careful attention should be paid to the geometric definition and to the adopted materials in order to assure a representation of the existing constructions.

In an equal manner, the numerical analysis of this particular type of masonry structures constitutes a great challenge nowadays, even for the most sophisticated numerical tools available. The material discontinuity introduced by the joints makes the use of interface elements within a finite element formulation an appropriate option to model such structures. Another attractive tool is the discrete element method, e.g. Cundall and Hart (1992), Lemos (1998a), briefly discussed in Chapter 2. Independently of the numerical tools adopted to perform such analyses, it is necessary to introduce appropriate experimental data concerning inelastic and cyclic behaviour, which most of the times is not available.

In this Chapter an experimental research concerning the structural behaviour of dry stone masonry is presented. Seven walls made of sandstone blocks, built without any interposition material, were tested under combined compressive and shear loads. The most relevant results concerning the behaviour of the shear walls are described, including ultimate loads and failure modes, and the main conclusions are discussed. For the latter purpose, an existing numerical

plasticity model based on the micro-modelling strategy was used to simulate the structural response of the walls. The model was calibrated with data collected from the tests as well as from uniaxial testing. The computational model appropriate for each wall is also discussed.

4.1 Experimental research

In order to contribute to improving the knowledge of dry jointed masonry, an experimental research program was developed at the Structural Technology Laboratory of Universitat Politècnica de Catalunya, in cooperation with Universidade do Minho, concerning the structural behaviour of dry jointed masonry stone walls submitted to combined vertical and horizontal loads. In total, seven walls were built and successfully tested. These tests were planed and performed aiming at two main complementary objectives, namely:

- To contribute to the enlightenment of the mechanics of dry jointed masonry made of stone blocks, subjected simultaneously to compressive and shear loading (typical of a seismic action). This knowledge is essential for assessing the structural behaviour of ancient stone masonry constructions, when existing mortar exhibits lower mechanical strength due to weathering, the use of weak raw materials, or even those originally made without any kind of interposition material between the stone pieces. This type of construction was very common in Ancient Greece and in the North of Portugal.
- To make available adequate data aiming at the calibration of numerical models, especially those based on the micro-modelling strategy. In fact, the numerical model of the walls presented in this Chapter was calibrated with data obtained directly from the tests.

It must be noted that these tests a characterized the structural response of a specific type of stone and geometry to the given loading conditions. Therefore, extrapolating these results for other contexts might be erroneous.

All the tests were carried out under monotonic loading due to equipment restrictions. It is, however, of great interest to perform such tests in a cyclic fashion, in order to obtain experimental data about cyclic behaviour, which is almost unavailable, but essential to evaluate the safety level of historical constructions in seismic areas (e.g. South of Europe).

4.1.1 Materials and geometry

Using the same type of stones referred to in Chapter 2 for uniaxial compressive and shear tests, seven dry jointed stone masonry walls were built, according to the geometry shown in Figure 4.1. All the stones used were mechanically cut and showed a smooth surface.

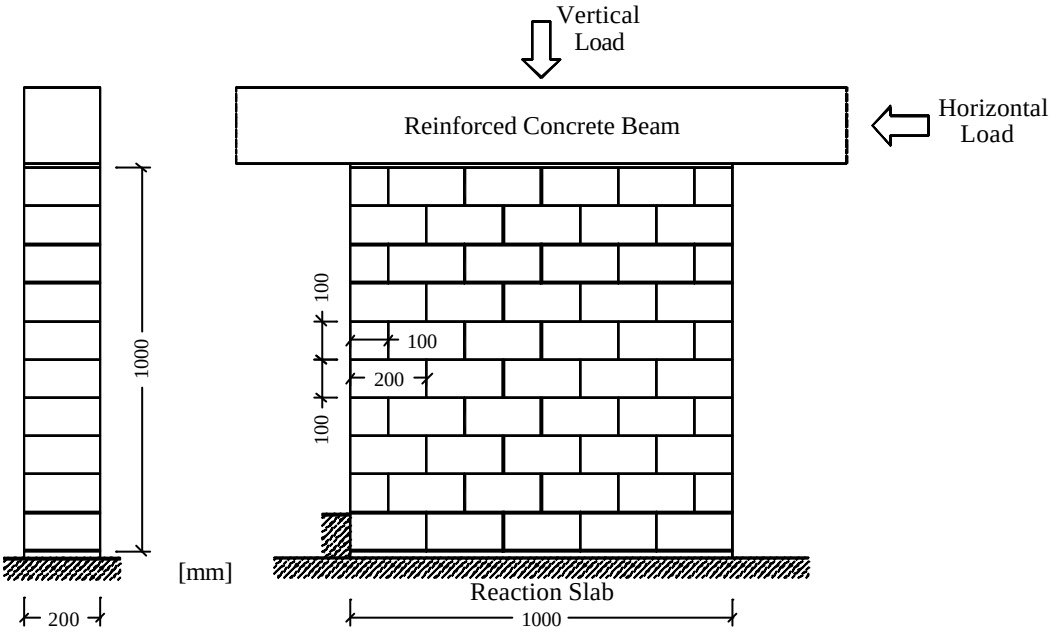

Figure 4.1 – Adopted geometry for the dry stone masonry walls and schematic loading arrangement.

The terminology adopted to designate the walls, based on the value of the vertical load applied, is given in Table 4.1.

Table 4.1 – Wall notation according to the applied vertical load.

Wall designation	Vertical load [kN]
SW.30.1	30
SW.30.2	30
SW.100.1	100
SW.100.2	100
SW.200.1	200
SW.200.2	200
SW.250.1	250

Considering that historical structures are usually submitted to low compressive stress states and taking into account the laboratory facilities, the walls were tested for vertical loads of 30, 100, 200, and 250 kN, which resulted in compressive stresses of 0.15, 0.50, 1.00 and 1.25 MPa, respectively. For the higher vertical loads (200 and 250 kN), the risk of lateral buckling was real. In fact, a test not described here failed prematurely by lateral buckling. All the walls were built inside the laboratory, directly under the load frame, since the absence of any adhesive material between the stones would make extremely difficult the transport of the walls to their testing place. The several phases necessary to carry out the manual construction are briefly described in the following:

- First, a thin layer of self-levelling mortar was laid on the floor in order to correct any potential roughness of the reaction slab. The mortar used was a high strength (≈50 MPa) and rapid hardening mortar (≈1 day);
- Then, the wall construction was initiated. The stones were carefully placed in order to preserve verticality and alignment, see Figure 4.2(a). During the building process, no interposition material was used. The stones with clearly visible defects were rejected;
- After laying the ten courses of stones, totalling a height of 1.0 m, a thin layer of self-levelling mortar was laid on the top of the wall. This layer had the aim of linking the last stone course and of enabling a good contact between the top of the wall and the top reinforced concrete beam, where vertical load was applied;
- Finally, the wall was instrumented with eight LVDTs, see Figure 4.2(b), in order to measure relative displacements between stone pieces during horizontal loading.

(a) (b)

Figure 4.2 – Wall construction: (a) stone laying and (b) LVDTs arrangement (side A).

4.1.2 Equipment and test procedure

The walls were tested one day after their construction, which was made possible due to the rapid mortar strength development. The main steps of the adopted procedure for testing are described as follows:

- Initially, a vertical compressive load was applied by means of a hydraulic actuator of 1000 kN capacity, under force control at a rate of 1kN/s, until the desirable load was totally applied to the wall. Subsequently, the hydraulic actuator was kept under force control, resulting in an applied constant vertical load, e.g. Figure 4.3. Consequently, the beam was allowed to move in vertical and horizontal directions;
- Afterwards, the horizontal load was applied by imposing small displacement increments. For this purpose, a hydraulic actuator was horizontally fixed and the load was applied against the reinforced concrete beam;
- During the test, the main events, as opening of the joints and appearance of cracks, were registered by means of photographs (see Appendix A for detailed sequences). The total duration of the tests varied between 15 and 25 minutes, depending on the applied vertical load;
- The tests were stopped before complete collapse of the walls, in order to protect the equipment against possible damage. In some tests, failure happened suddenly, without any previous visible signs.

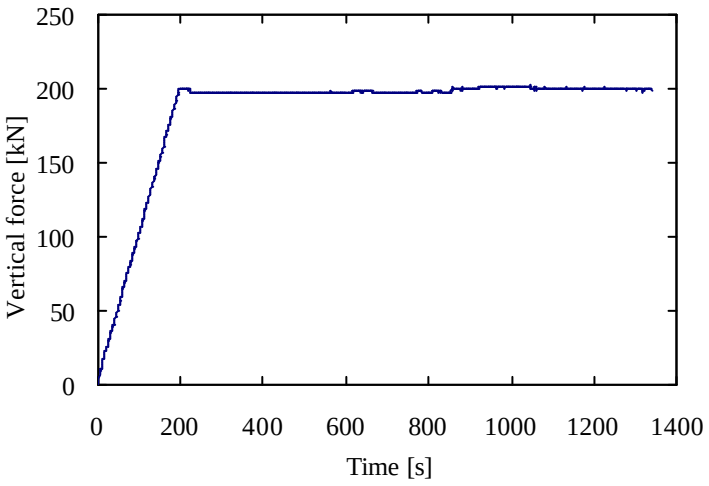

Figure 4.3 – Chronological history of the vertical load applied to SW.200.1 stone wall, under force control.

4.1.3 Load-displacement diagrams

Following the procedure described before, a large amount of experimental data was collected during the tests, ranging from applied loads to relative displacements between stone blocks. Clearly, one of the most important information is the relation between the horizontal load and the horizontal displacement, shown in Figure 4.4. The walls tested with the same compressive load are presented in the same diagram, for better comparison. The horizontal load was measured by using a load cell placed between the hydraulic actuator and the reinforced concrete beam. The horizontal displacement was computed as the difference between the horizontal displacement of the beam and the displacement measured at the bottom of the wall (which was verified to be irrelevant). Moreover, relative displacements between the reinforced concrete beam and the last level of stones did not occur.

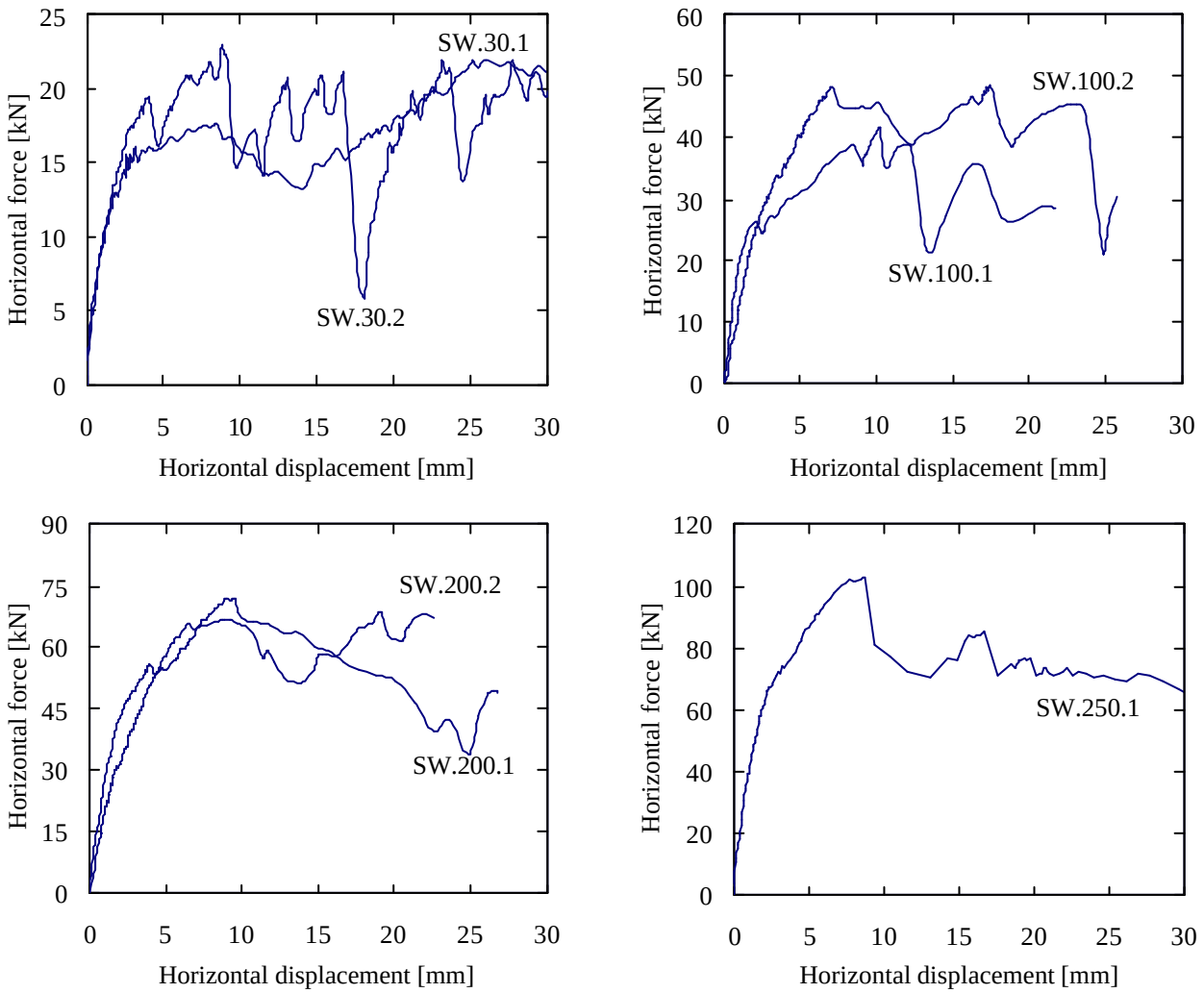

Figure 4.4 – Horizontal load-displacement diagrams of the seven tested walls, sorted by equal applied vertical load.

The horizontal load-displacements diagrams are characterized by two distinct main behaviours, see Figure 4.5. Initially, the curves exhibited great stiffness. Elastic behaviour was observed at almost 30% of the respective peak load. Then, continuous stiffness degradation took place under increasing horizontal displacement. The second part of the diagrams is characterized by an oscillation of the horizontal load in all the diagrams shown. Sudden relative stone movements originated these oscillations, due to the absence of an interlayer material. For successive displacement increments, a load growth occurred until the next load dropping took place. This process was repeated several times during testing.

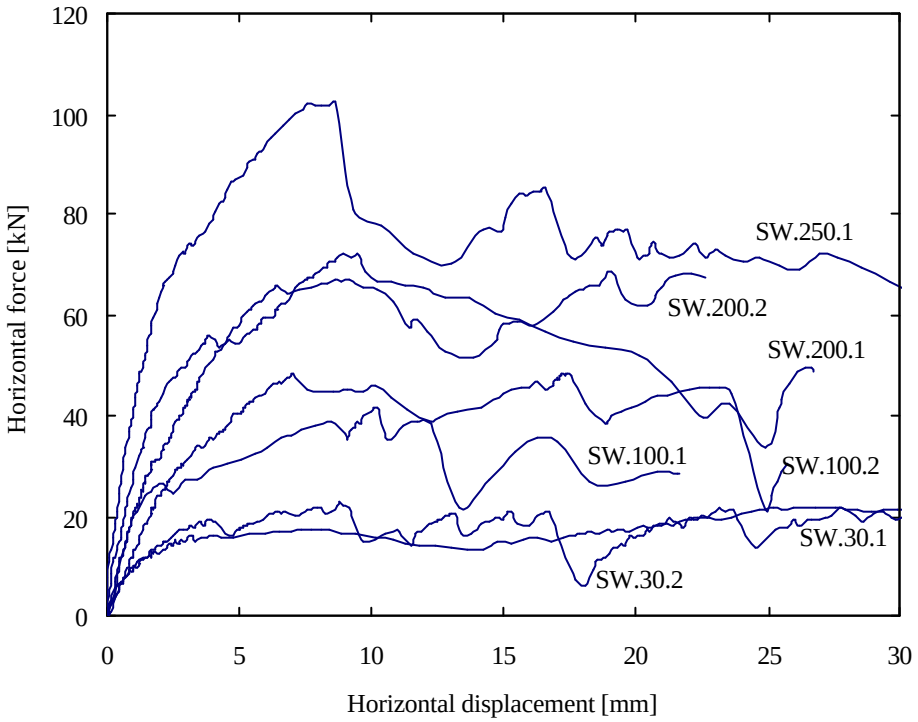

Figure 4.5 – Horizontal load–displacement diagrams grouped together.

4.1.4 Failure modes

The failure pattern of each wall is shown in Figure 4.6 and Figure 4.7. The complete cracking evolution is given in Appendix A, for all walls. The pictures show that the failure mode is linked with the level of vertical load applied to the wall. This result is already well known for regular masonry, e.g. Page *et al.* (1980) and Mann and Müller (1982), who have shown that the level of compression controls the failure mode of shear walls.

For lower stress levels, failure occurred by simple rotation of the upper part of the wall and sliding along the bed joints, leading to a stepped diagonal crack, without visible cracking in the stones, see Figure 4.6. For higher vertical loads, this kind of rigid body movement of the stones was gradually prevented from occur. Cracking in the stones started to become noticeable, being the stepped diagonal crack partially replaced by a diagonal cracking band, with several cracks running through the stones, where visible damage was localized, see Figure 4.7.

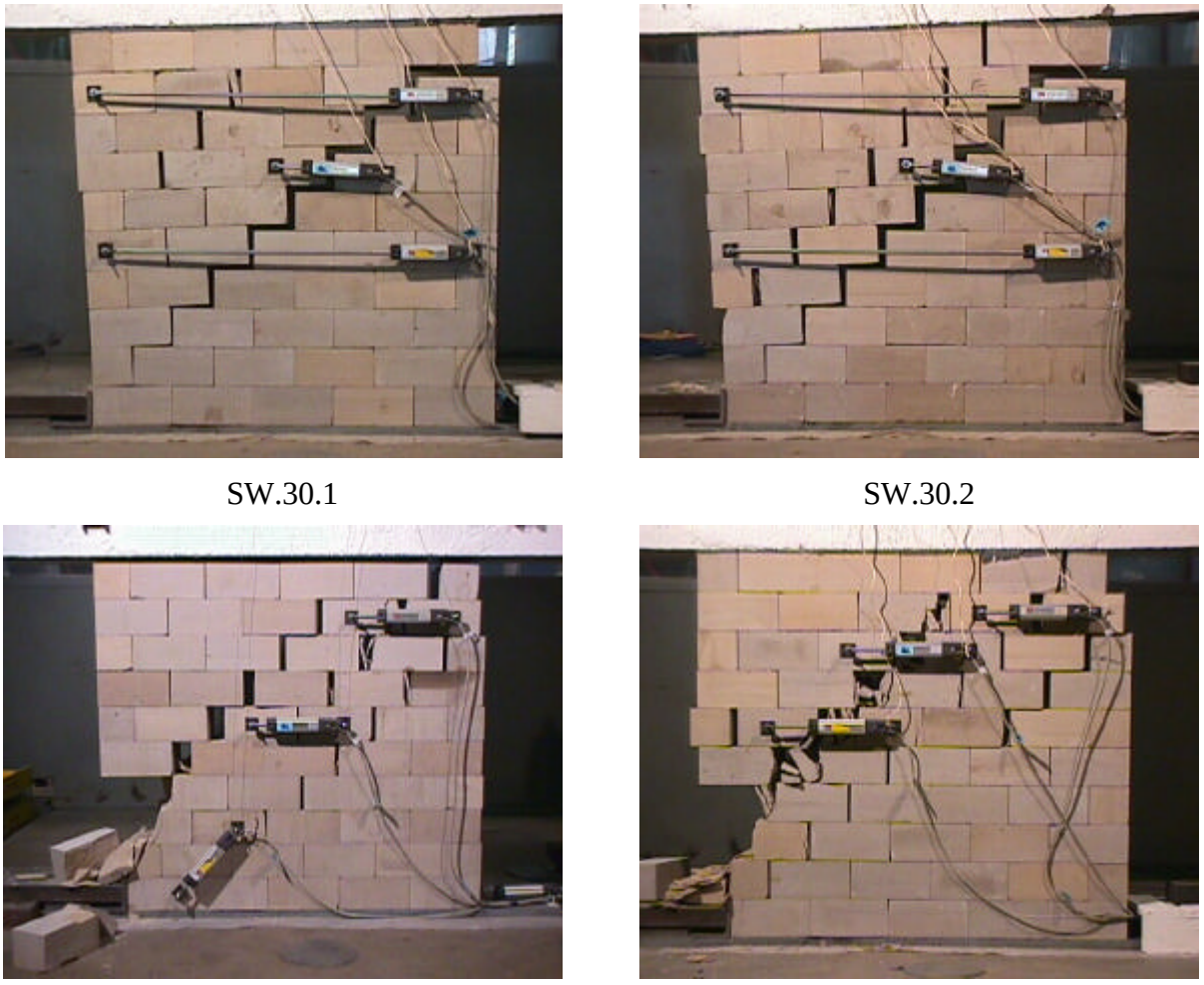

SW.30.1 SW.30.2

SW.100.1 SW.100.2

Figure 4.6 – Failure modes observed (vertical load equal to 30 and 100 kN).

From simple friction failure along bed joints, the failure pattern has successively become characterized by the occurrence of cracking of the stones. This means that for an increasing vertical load, failure of the units under combined loading is likely to occur prior to friction failure along the bed joints. Naturally, this phenomenon is highly dependent on the tensile strength of the stones, which appears to be rather low when compared to the compressive strength.

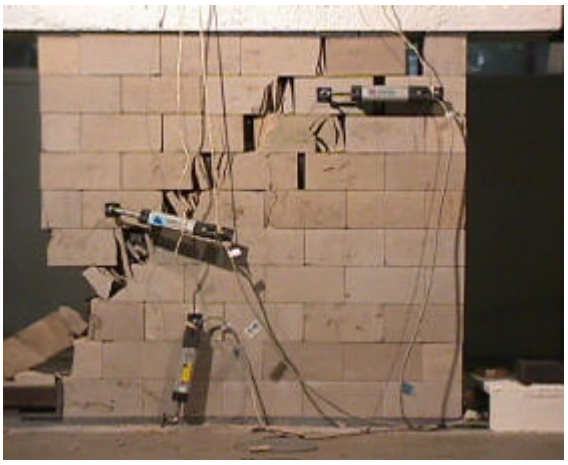

SW.200.1

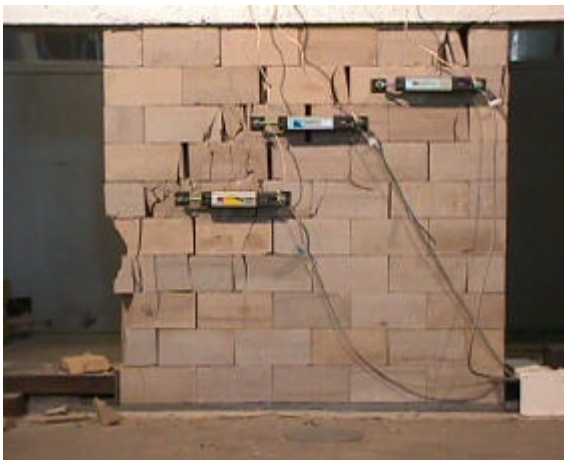

SW.200.2

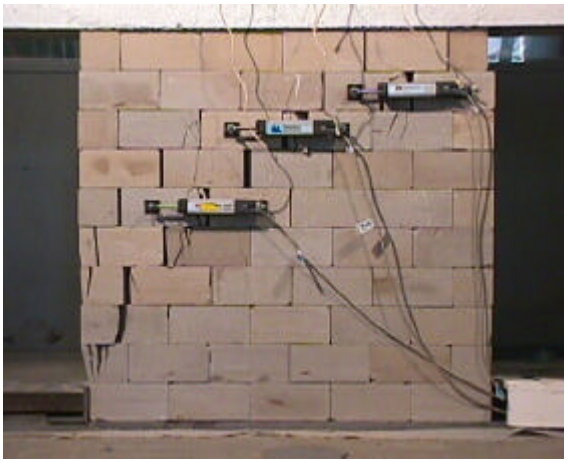

SW.250.1

SW.250.1

Figure 4.7 – Failure modes observed (vertical load equal to 200 and 250 kN).

From the pictures it can be observed that all walls exhibited diagonal failure, with increasing stone damage level according to increasing compressive stress levels. In all walls, the lack of an interlayer material (e.g. mortar) induced stress concentrations in the contact points, leading to premature vertical cracking of the stones. Naturally, this cracking process was much more relevant for higher vertical loads.

4.1.5 Relation between normal and shear stresses

Usually, test results concerning in-plane testing of walls concerning compressive and shear loading, are presented in terms of a relation between the normal and shear stresses, at failure. However, this procedure does not account for local peak stresses that may influence failure. In spite of that, it was decided to investigate such a possible relation. Table 4.2 summarizes the values obtained for the vertical and maximum horizontal loads, for all tests.

Table 4.2 – Vertical and maximum horizontal loads measured.

Wall	Vert. load [kN]	Máx. horiz. load [kN]
SW.30.1	30	22
SW.30.2	30	23
SW.100.1	100	42
SW.100.2	100	49
SW.200.1	200	72
SW.200.2	200	69
SW.250.1	250	102

It can be observed that the maximum horizontal load increased with the vertical load applied, as expected. A graphic representation, in terms of stresses, is shown in Figure 4.8.

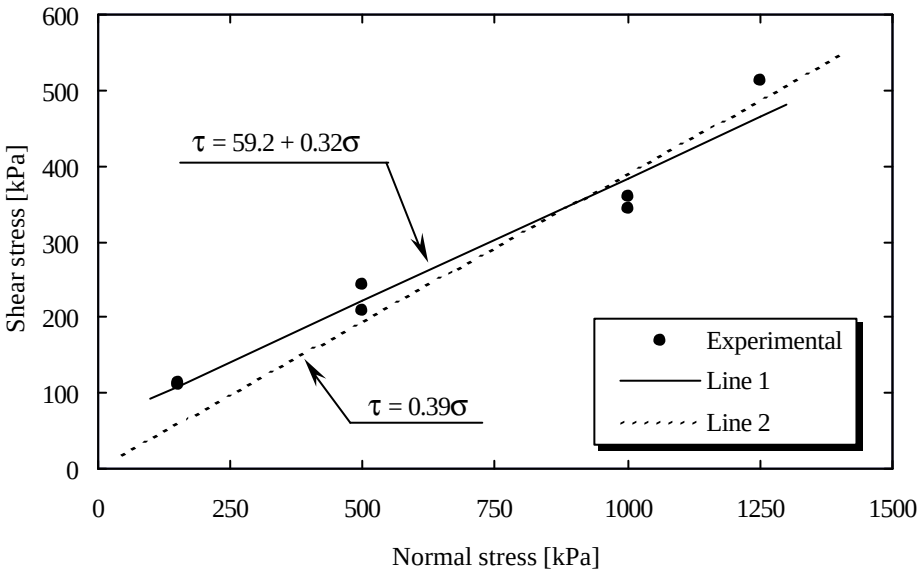

Figure 4.8 – Relation between normal and tangential stresses: experimental data and linear least square regressions.

The normal (s) and tangential (t) stresses were obtained by dividing the vertical and horizontal forces by the wall cross-sectional area (bed joint area), respectively. These stresses represent average values, since neither vertical stresses nor horizontal stresses are constant along the bed joint.

The linear least square regression computed for the seven walls showed a good approximation to the experimental data ($r^2 = 0.98$). However, this approximation implies cohesion different from zero. For a linear least square regression with zero cohesion, a slightly greater coefficient was

obtained, but the first two points (SW.30.1 and SW.30.2) are weakly approximated ($r^2 = 0.95$). In both cases, a linear relation between the average compressive stress and the average ultimate shear stress fits reasonably well the experimental data. Nevertheless, the obtained friction coefficient of the walls (0.32 and 0.39) is rather different from the tangent of the friction angle of the stone joints, $\tan\phi$, which was experimentally found to be equal to 0.62, see Chapter 3.

4.2 Numerical modelling

Complementary to the experimental research described above, see also Oliveira (2000), a numerical simulation of the tested stone walls is presented in this Section to further discuss and understand the experimental results. The simulations were carried out using the multisurface interface model proposed by Lourenço and Rots (1997). Complementarily, a brief description of the model is given in Section 5.3.

Basically, the model assumes that the stone units behave in an elastic fashion whereas inelastic behaviour is concentrated in the joints. In these simulations, the stones were modelled using eight-node continuum plane stress elements with Gauss integration and, for the joints, six-node zero-thickness line interface elements with Lobatto integration were used. The boundary conditions and the load application method were defined in accordance with the experimental arrangement.

4.2.1 Elastic parameters

Dry stone masonry exhibits a peculiar "elastic" behaviour under compressive loading. Young's modulus of the stones used to build the walls was characterized in Chapter 3, under uniaxial compression. The average value of 10 monotonic uniaxial compressive tests performed on cylindrical specimens reads 15500 N/mm^2. On the other hand, Young's modulus of stone prisms, built using four stacked stones, under uniaxial compression resulted in the slightly lower value of 14800 N/mm^2 (average of 4 prisms). Nevertheless, because of the large coefficients of variation found when testing natural stone, as found in Chapter 3, this difference has no statistical relevance. For this reason, for the micro-modelling strategy adopted here, Young's modulus of the stone will be assumed equal to 15500 N/mm^2. However, when building large walls, it was found that Young's modulus is considerably different from the values measured in small

specimens. This phenomenon was also reported by Lourenço (1996), when modelling masonry shear walls tested at the Eindhoven University of Technology. The reason for the difference in stiffness between large and small specimens is, most likely, related to the less uniform assembly of large specimens.

Here, the calculation of joint stiffness is based on the experimental data of the vertical displacements measured during the vertical load application. All walls, with the exception of the series with a 30 kN pre-compression load (SW.30.1 and SW.30.2), were instrumented with two LVDTs measuring relative vertical displacements of points separated by 0.9 m. The Young moduli, based on these measurements, and calculated as the normal stress divided by the average strain measured, are presented in Table 1. It is observed that:

- The values calculated in this way are in the range of only 3.5-7.5% of Young's modulus of the separately tested stone;
- Young's modulus of the walls increases with the vertical load.

Based on these values, a linear least square regression was performed and the calculated Young's moduli are presented both in Table 4.3 and Figure 4.9.

Table 4.3 – Vertical load test results.

Wall	Young's modulus [N/mm^2]		
	E_{test1}	E_{test2}	E_{calc}
SW.30	—	—	566
SW.100	824	688	768
SW.200	969	1302	1057
SW.250	1024	1353	1202

This peculiar dependency of the stiffness on the compressive loading is explained by the larger contact between stone blocks (or the closing of the joints) under higher normal stresses. This feature seems a clear indication of the complexity of the behaviour of dry jointed masonry structures and of the difficulty to model its structural behaviour adequately. Unfortunately, this characteristic can hardly be taken into account directly in FEM analyses. One possibility would be the consideration of a non-linear elastic behaviour that promoted a stiffness growth as a

function of the compressive load. Here, this feature is indirectly considered by modifying the joint stiffness in each model, as a function of the vertical load applied.

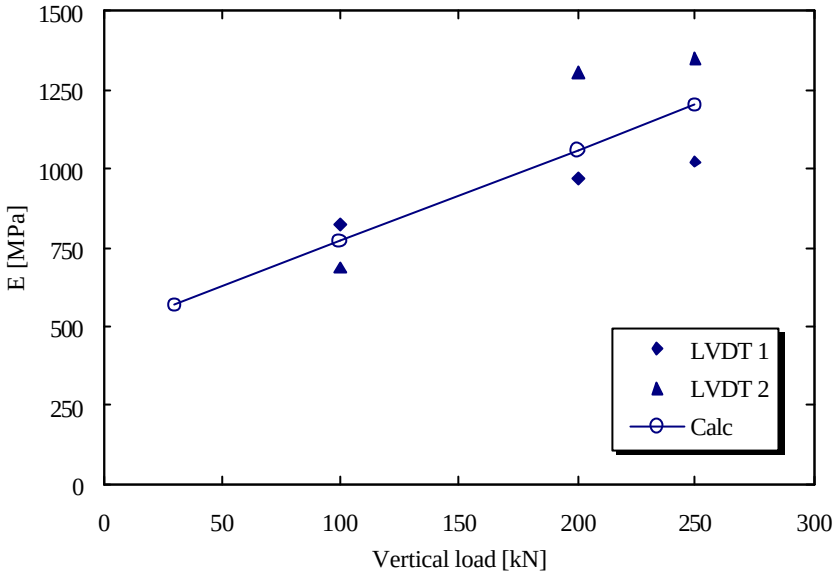

Figure 4.9 – Young's modulus vs. vertical load applied.

Normal joint stiffness $k_{n,joint}$ is calculated by considering the wall, in the vertical direction, as a series of two springs, one representing a stone block and the other representing a joint. This assumption leads to

$$k_{n,joint} = \frac{1}{h\left(\frac{1}{E_{wall}} - \frac{1}{E_{stone}}\right)} \tag{4.1}$$

where h is the height of the block (equal to 100 mm), E_{wall} is the Young's modulus of the wall (given in Table 4.3) and E_{stone} is the Young's modulus of the stone (assumed equal to 15500 N/mm^2). The tangential stiffness $k_{s,joint}$ is calculated directly from the normal stiffness, assuming that the theory of elasticity is applicable, as

$$k_{s,joint} = \frac{k_{n,joint}}{2(1+n)} \tag{4.2}$$

where ν is the Poisson's ratio (assumed equal to 0.2). With these assumptions, the stiffness of the joints is given in Table 4.4.

Table 4.4 – Stiffness calculated for the joints.

Walls	k_n [N/mm^3]	k_t [N/mm^3]
SW.30	5.87	2.45
SW.100	8.08	3.37
SW.200	11.4	4.73
SW.250	13.0	5.43

4.2.2 Inelastic parameters

In the particular case of dry stone masonry joints, the tensile strength and cohesion are assumed to be equal to zero. Obviously, this renders the numerical analysis more demanding because almost all the joints will behave in a non-linear fashion. The tensile behaviour of the stone has been characterized by Ramos (2002), where a tensile strength of 3.7 N/mm^2 and a fracture energy of 0.11 Nmm/mm^2 were found. The shear behaviour of the stone joints has been characterized in Chapter 3, where a value of 0.62 was found for tan$f$ and a value of zero was found for tan$y$, being f and y the friction and dilatancy angles of the stone joints, respectively. The uniaxial compressive behaviour of the block assembly has been characterized in Chapter 3, with a compressive strength of 57 N/mm^2. The fracture energy in compression was assumed to be half of the value given by Model Code 90 (CEB-FIB, 1990) for concrete, due to the higher brittleness of stone.

4.2.3 Load-displacement diagrams

As discussed in the previous Section, the walls with a vertical load of 30 kN and 100 kN exhibited limited stone cracking. For this reason, the possibility of cracking through the stone blocks was not considered in the model of these walls. Quite on the contrary, potential cracks through the middle of the blocks were considered for the walls with a vertical load of 200 kN and 250 kN. Figure 4.10 illustrates the load-displacement diagrams from the tests and the numerical results, up to a displacement of 15 mm. Table 4.5 presents the differences between the numerical and experimental collapse loads, where the experimental collapse load represent the average of two tests, when applicable.

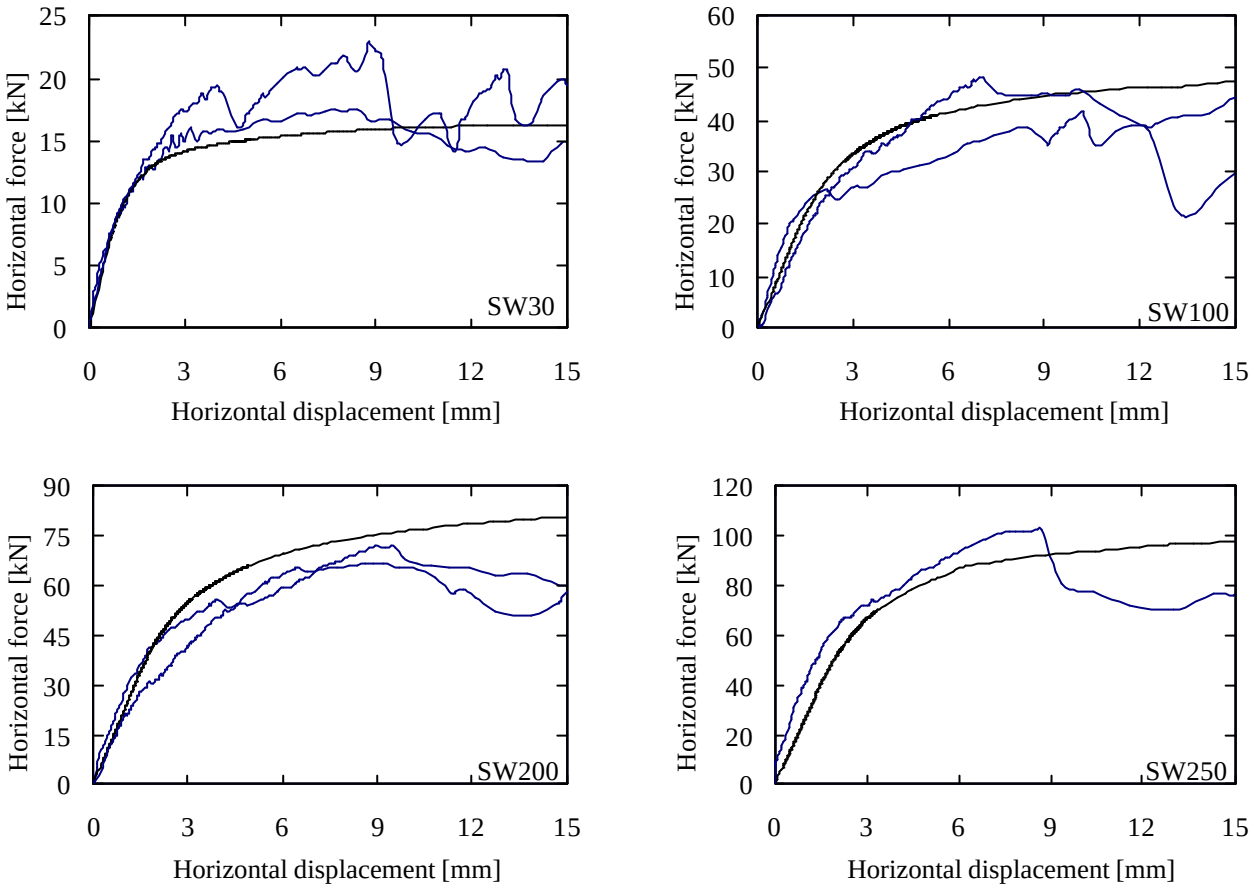

Figure 4.10 – Horizontal load-displacement diagrams for all walls (the thicker line indicates the numerical result).

Table 4.5 – Comparison of experimental and numerical collapse loads. The experimental value represents the average of two tests (except for SW.250).

Walls	Experimental [kN]	Numerical [kN]	Ratio [-]
SW.30	22.4	16.3	0.73
SW.100	45.0	47.5	1.06
SW.200	70.3	81.4	1.16
SW.250	102.7	98.0	0.95

The agreement between experimental and numerical responses can be considered satisfactory, taking into account that the experiments have been carried out with dry masonry and with natural stone.

4.2.4 Failure modes

Together with the global load-displacement response, a comparison in terms of the deformed mesh and failure pattern is necessary to appraise the quality of the numerical analyses. Figure 4.11 and Figure 4.12 show a representation of the minimum (compressive) principal stresses for the SW30 and SW200 models, on the incremental deformed mesh.

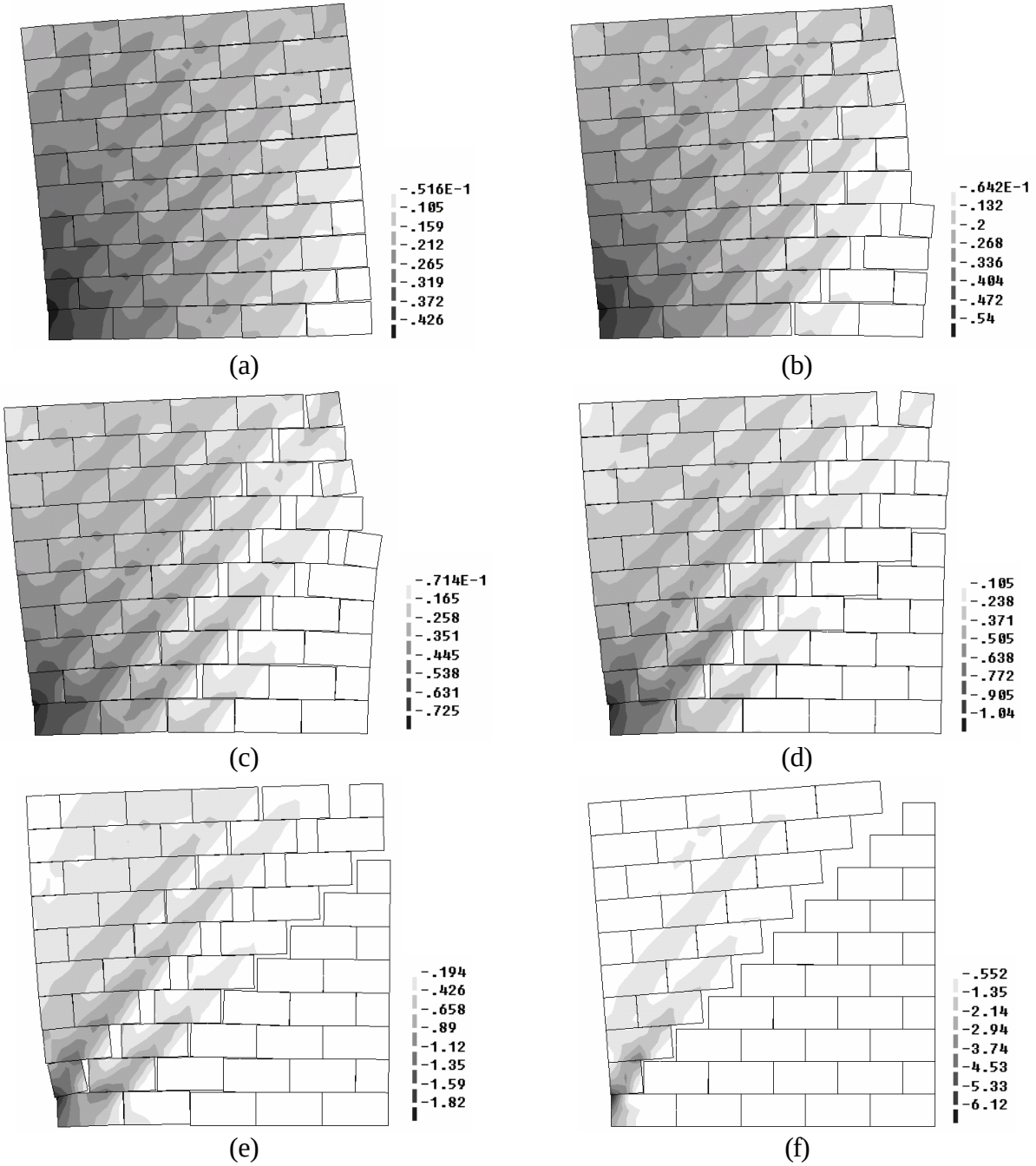

Figure 4.11 – SW.30. Principal compressive stresses [N/mm^2] depicted on the incremental deformed mesh for a horizontal displacement equal to [mm]: (a) 0.5; (b) 1.0; (c) 1.5; (d) 2.0; (e) 3.0; (f) 15.0.

For lower vertical loads, see Figure 4.11, it is possible to observe that separation of the blocks through diagonal cracks gradually progresses from the bottom courses to the top, while the number of active compressive struts decreases. Finally, an overturning failure mechanism is found with a complete diagonal crack through head and bed joints. It is noticed that, at this stage, the compressive stresses are still rather low, with respect to the peak compressive stress of the block assemblage.

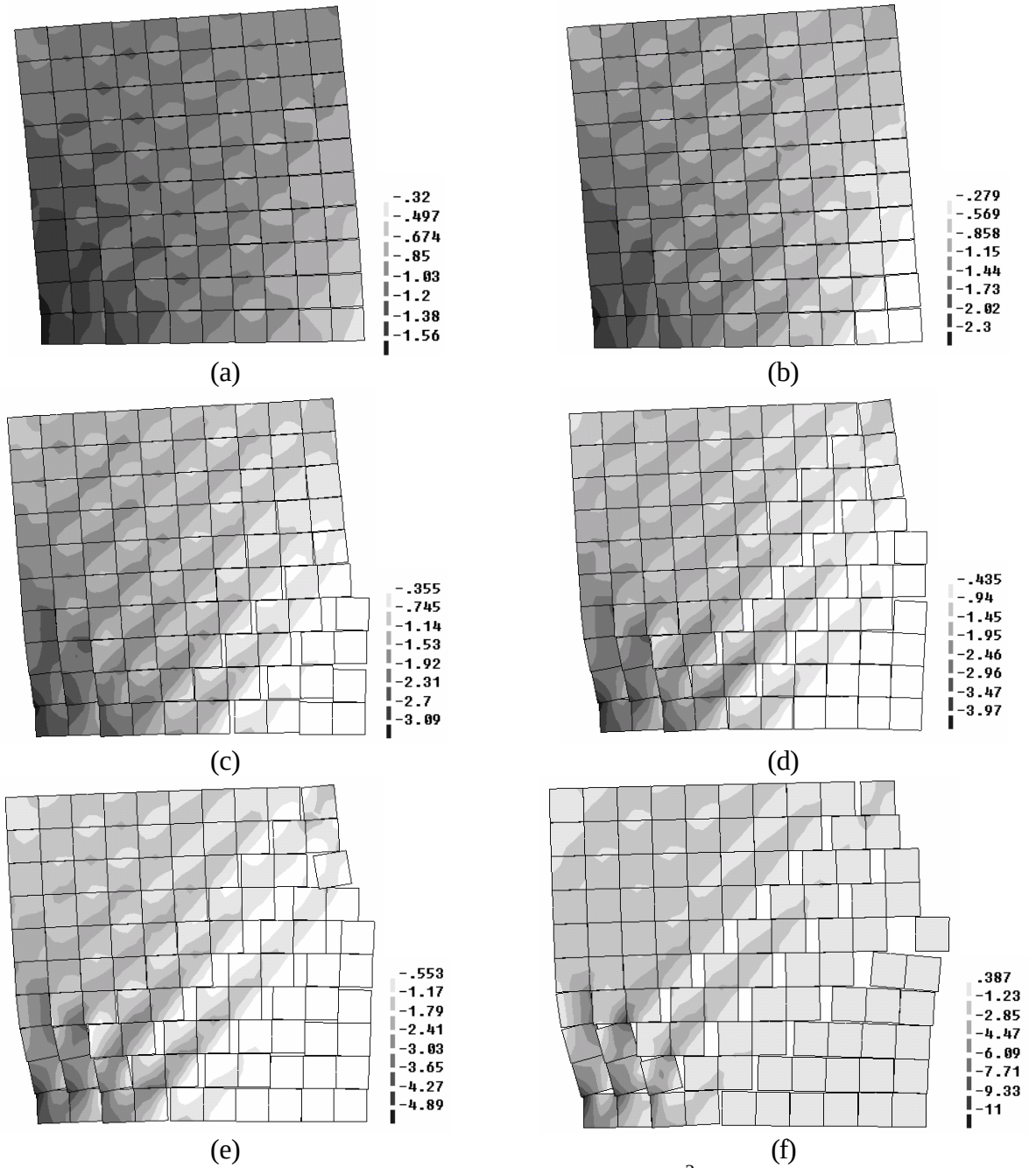

Figure 4.12 – SW.200. Principal compressive stresses [N/mm^2] depicted on the incremental deformed mesh for a horizontal displacement equal to [mm]: (a) 1.0; (b) 2.0; (c) 3.0; (d) 4.0; (e) 5.0; (f) 15.0.

For higher vertical loads, see Figure 4.12, the onset of diagonal cracking if delayed to great extent. Up to a horizontal displacement of 1 mm, no diagonal compressive struts are found and the complete wall is still structurally active. When diagonal cracking starts to occur, it seems that some shear is always transmitted to the lower part of the wall. A complete diagonal crack fails to propagate and the failure mode seems to be mostly controlled by shear, together with rocking of the cracked stone pieces in the compressed toe of the wall. Again, the compressive stresses are low in comparison with the peak compressive stress of the block assemblage. This seems to indicate that the "crushing" observed in the experiments results from a combination of shear and tensile failure of the stone. In fact, the smooth grain of the stone results in a very low dissipation of energy due to mode I failure. In the numerical analysis, in order to obtain reasonable agreement with the experiments, as shown in Figure 4.10, a full crack was assumed in the potential cracks in the middle of the blocks, once the peak tensile strength of the stone was reached. The use of the fracture energy measured by Ramos (2002) for the potential cracks in the middle of the blocks, resulted in overly high collapse load values. This, again, indicates that the peak stresses at the irregular contacts result in extremely rapid crack propagation in the stone blocks. It is expected that significant higher collapse loads would be found for walls SW.200 and SW.250 if bedding of the stones even with a very weak bonding agent, was present.

4.3 Summary

The results involving dry jointed stone masonry walls were presented and discussed. The walls were built without any kind of material between the stone blocks and combined vertical and horizontal loads were applied for different vertical compressive loads. A variable vertical stiffness of the walls was found. It was observed that vertical stiffness increased with the compressive stress. The horizontal load-displacement diagrams are characterized by two main features. Initially, the curves exhibited great stiffness and elastic behaviour was observed almost up to 30% of the peak load. Then, continuous stiffness degradation took place under increasing deformation. The second part of the diagrams was characterized by an oscillation of the horizontal load. The observed failure modes are clearly associated with the vertical load applied. For lower stress levels, failure happened by rotation and sliding of part of the wall, whereas for higher vertical loads cracking started to become noticeable. A linear relation between average compressive stresses and average ultimate shear stresses seems to be a good approximation to experiments.

The modelling performed on the same walls allowed to numerically follow the load history and to understand the main phenomena related with the behaviour of the walls. Besides the resemblance of the collapse loads, the evolution of the deformed meshes is in accordance with experimental loading. Numerical results have also shown rapid crack propagation under high compressive stresses. Bedding of the stones, even using a very weak mortar, would be convenient, since it would most likely lead to a more stable structural response.

5. MODELLING OF CYCLIC BEHAVIOUR OF MASONRY

It has been recognized that an advanced numerical analysis should not only be able to give the maximum load capacity but also to trace the structural response through post-peak behaviour and to outline the failure mode of the structure. In fact, numerical modelling has already been used in order to design experimental tests on representative structures to be tested in the laboratory (Pegon and Pinto, 1996). These "numerical experiments" allow the enhancement of experimental test programs (e.g. changing geometric configuration, localizing data acquisition equipment or even load levels). Nevertheless, numerical tests inevitably imply the use of proper modelling of inelastic constitutive behaviour that must be fed by advanced experimental testing.

A common feature to all mechanical analysis of structures is the need for constitutive models that relate the states of stress and strain in the material. Naturally, different constitutive models may be chosen depending on the engineering materials, as well as on the purpose and required precision of the model predictions. Constitutive models should be seen as mathematical simplifications that approximate complex physical behaviour under certain circumstances. Therefore, "exact" models do not exist because it is impossible to reproduce all the information present in nature. However, the choice of an appropriate constitutive model is crucial and completely determines the insight into the structural problem.

The two most popular classes of inelastic material constitutive theories used to derive consistent constitutive models are plasticity and continuum damage mechanics (Hansen and Schreyer, 1994). The theory of plasticity attempts to replicate the dislocations of the material, being the plastic material behaviour characterized by the occurrence of permanent deformations. In contrast, continuum damage mechanics is concerned with the description of progressive weakening of a material due to the development of microcracks and microvoids. Both theories are generally either based on a micromechanical or a phenomenological approach. In the micromechanical (or fundamental) approach, elementary constitutive relations are established for the microstructural behaviour (mechanical description). This kind of approach is still less developed, although important achievements have been attained, see Nemat-Nasser and Hori (1993). In contrast, the phenomenological approach establishes a model directly based on the observed features from experimental tests.

Constitutive models based on the standard plasticity framework according to a phenomenological approach (also known as the mathematical theory of plasticity), will be proposed in the present study. According to the objectives presented in Chapter 1, it is advantageous to develop constitutive relations that present numerical robustness and allow one to follow the entire response of the structure, even beyond the experimental failure load, rather than incorporate quite complex material models, which could result in unstable algorithms. It must be noted that, generally, numerical failure, at which the iterative solution procedure no longer converges, has no physical meaning with respect to the real structural failure (Crisfield, 1991; Feenstra, 1993).

In this Chapter, a brief description of the solution procedures used in non-linear finite element formulation is presented, followed by a revision of the incremental plasticity theory, and some subsequent improvements of the classical theory which are briefly described. Then, a succinct description of an existing constitutive model for interface elements is given, from which an extension to include cyclic loading, totally based on the plasticity theory and formulated in modern plasticity concepts, is proposed. Finally, illustrative examples of the behaviour of the developed model together with an assessment of the ability of the model to reproduce reputed experimental results available in the literature are given.

5.1 Non-linear finite element formulation

Modelling of a given structure consists of two tasks: (a) spatial discretization of the geometry into elements and, (b) representation of the physical behaviour of the materials from which the structure is made. In the present study, the finite element method based on the displacement method is adopted to simulate the observed structural behaviour. Then, the assembly of all elements in conjunction with applied loads and boundary conditions results in a system of equilibrium equations that has to be solved in order to obtain the unknown nodal displacements.

The application of a micro-modelling strategy to in-plane structures, previously described in Chapter 2, requires the use of continuum elements and line interface elements, as schematically shown in Figure 5.1. For each type of element, the respective constitutive model establishes a relation between generalized stress and strain vectors that is usually expressed as

$$\boldsymbol{s} = \mathbf{D}\,\boldsymbol{e} \tag{5.1}$$

where **D** represents the stiffness matrix. For plane continuum plane stress elements, the stress vector $\boldsymbol{s}$ and strain vector $\boldsymbol{e}$ are defined, respectively, as

$$\boldsymbol{s} = \begin{Bmatrix} \sigma_x \\ \sigma_y \\ \tau_{xy} \end{Bmatrix} \qquad \boldsymbol{e} = \begin{Bmatrix} \varepsilon_x \\ \varepsilon_y \\ \gamma_{xy} \end{Bmatrix} \tag{5.2}$$

These elements are integrated here using the standard reduced Gauss scheme (2x2-point Gauss quadrature).

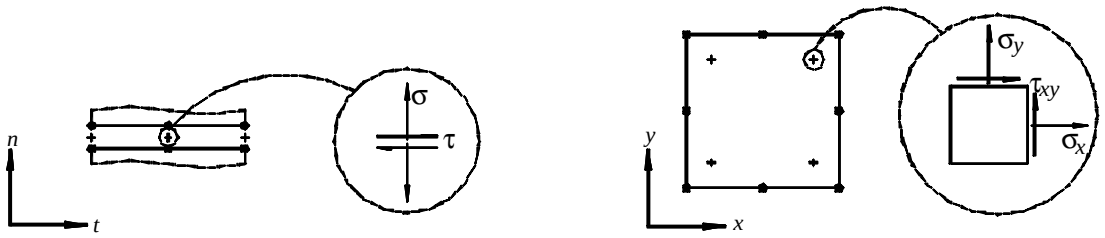

(a) (b)

Figure 5.1 – Types of finite elements employed in this study: (a) six-node zero-thickness line interface element with Lobatto integration; (b) eight-node continuum plane stress element with Gauss integration.

For zero-thickness line interface elements, the constitutive relation defined by eq. (5.1) expresses a direct relation between the traction vector $\boldsymbol{s}$ and the relative displacement vector $\boldsymbol{e}$ along the interface, which read

$$\boldsymbol{s} = \begin{Bmatrix} \sigma \\ \tau \end{Bmatrix} \qquad \boldsymbol{e} = \begin{Bmatrix} \Delta u_n \\ \Delta u_t \end{Bmatrix} \tag{5.3}$$

The option for zero-thickness line interfaces is related to the fact that physical thickness of an interface should only be modelled if strain gradients across the layer are expected and need to be resolved (Hohberg, 1992). This option is further encouraged by the fact that for the analyses performed along this study involving the use of interface elements, only the global effect of a displacement discontinuity needs to be modelled. The interface elements are integrated with a Lobatto scheme, for which the integration points match the nodal points (3-point Lobatto quadrature). This scheme has shown to be more stable than standard Gauss integration, see Hohberg (1992) and Schellekens and De Borst (1993) for a comprehensive analysis.

5.1.1 Solution procedures for non-linear problems

The adoption of complex constitutive relations leads generally to a non-linear relation between the internal force vector $\mathbf{f}_{int}$ and the nodal displacement vector $\mathbf{u}$, which implies that displacements often depend on the displacements at previous stages. In this study, the external force vector $\mathbf{f}_{ext}$ is assumed to be displacement independent, since non-linear geometrical behaviour is not considered.

The complete structural response is obtained using an incremental procedure where the load is applied into a finite number of increments. These increments can also be associated to time steps, for which a pseudo-time variable could be introduced to describe the loading progression. Hence, this pseudo-time variable would be used just to hierarchize the succession of events because time independent behaviour is considered along all of the study.

The problem is formulated by imposing equilibrium between internal and external forces. Starting from a converged load stage n (Zienkiewicz and Taylor, 1991),

$$\mathbf{u} = \mathbf{u}_n \qquad Y_n = 0 \qquad \mathbf{f}_{ext} = \mathbf{f}_{ext,n} \tag{5.4}$$

where Y represents the unbalanced force vector, a load increment is applied, at stage n+1

$$\mathbf{f}_{ext,n+1} = \mathbf{f}_{ext,n} + \Delta\mathbf{f}_{ext,n+1} \tag{5.5}$$

The equilibrium between internal and external forces is affected, being the system of equations to be solved expressed as

$$\mathbf{?}_{n+1} = \mathbf{?}(\mathbf{u}_{n+1}) = \mathbf{f}_{int}(\mathbf{u}_{n+1}) - \mathbf{f}_{ext,n+1} = 0 \tag{5.6}$$

The objective is to calculate the nodal displacement increment vector $\Delta\mathbf{u}_{n+1}$

$$\mathbf{u}_{n+1} = \mathbf{u}_n + \Delta\mathbf{u}_{n+1} \tag{5.7}$$

that equilibrates the internal and external forces. It is important that $\Delta\mathbf{f}_{ext,n+1}$ should be kept reasonably small so that path dependence can be followed.

The non-linear problem defined by eq. (5.6) is solved iteratively using a local quadratic Newton-Raphson procedure, which linearizes the non-linear equilibrium equations at each iteration. Eq. (5.6) is, then, approximated as

$$\mathbf{?}\,(\mathbf{u}_{n+1}^{i+1}) \approx \mathbf{?}\,(\mathbf{u}_{n+1}^{i}) + \left(\frac{\partial \mathbf{?}}{\partial \mathbf{u}}\right)_{n+1}^{i} \delta\mathbf{u}_{n+1}^{i} = 0 \tag{5.8}$$

being *i* the iteration counter starting from

$$\mathbf{u}_{n+1}^{0} = \mathbf{u}_{n} \tag{5.9}$$

and

$$\left(\frac{\partial \mathbf{?}}{\partial \mathbf{u}}\right)_{n+1}^{i} = \left(\frac{\partial \mathbf{f}_{int}}{\partial \mathbf{u}}\right)_{n+1}^{i} = (\mathbf{?}_{t})_{n+1}^{i} \tag{5.10}$$

where $\mathbf{?}_{t}$ is the tangential stiffness matrix. From eq. (5.8), the iterative displacement vector correction reads

$$\delta\mathbf{u}_{n+1}^{i+1} = -\left(\mathbf{K}_{t}^{-1}\right)_{n+1}^{i} \mathbf{?}\,(\mathbf{u}_{n+1}^{i}) \tag{5.11}$$

The sum of successive iterative increments $\delta\mathbf{u}_{n+1}^{i+1}$ gives

$$\mathbf{u}_{n+1}^{i+1} = \mathbf{u}_{n} + \Delta\mathbf{u}_{n+1}^{i+1} = \mathbf{u}_{n} + \sum_{k=1}^{i+1} \delta\mathbf{u}_{n+1}^{k} = \mathbf{u}_{n+1}^{i} + \delta\mathbf{u}_{n+1}^{i+1} \tag{5.12}$$

until appropriate convergence criteria are satisfied. Frequently the criteria used to stop the iteration process are based on norm ratios, defined in terms of force, displacement or energy.

For path dependent constitutive relations, which is the case of the plasticity theory, it is essential to use the total increment $\Delta\boldsymbol{u}_{n+1}^{i+1}$ to compute the stress changes $\Delta\boldsymbol{s}_{n+1}^{i+1}$. If not, the iterative increment changes $\delta\mathbf{u}_{n+1}^{i+1}$ may lead to spurious unloading during the iterations (Crisfield, 1991).

5.1.2 Advanced solution procedures

In addition to the Newton-Raphson method described above, some advanced solution procedures will be briefly presented. In order to improve the convergence of the iterative scheme and to pass

limit points, these techniques will be used actively in the analyses performed with the numerical model to be proposed later on in this Chapter. However, only a general approach will be presented just to introduce the issue. For detailed discussions the reader is referred to selected references.

Line search technique

One of the drawbacks of the iterative procedure described above has to do with the fact that convergence depends strongly on the starting solution. Indeed, a good starting point can lead to convergence where otherwise divergence would occur (Crisfield, 1991). When ordinary iteration schemes fail to converge, the application of line search techniques can be very useful to achieve convergence and also to accelerate the overall convergence of modified Newton-Raphson methods (Zienkiewicz and Taylor, 1991).

Basically, the line search technique can be regarded as a minimization of the total potential energy of the system, which is a function of the total displacements $\mathbf{u}$, in the direction of the iterative displacement increment vector $\delta\mathbf{u}_{n+1}^{i+1}$. The displacements are updated according to

$$\mathbf{u}_{n+1}^{i+1,\,j} = \mathbf{u}_{n+1}^{i} + h_{ij}\, d\mathbf{u}_{n+1}^{i+1} \tag{5.13}$$

in which j is the counter of the line searches. The line search factor h_{ij} scales the iterative displacement and is calculated making the projection of the unbalanced forces $\mathbf{?}(\mathbf{u}_{n+1}^{i+1})$ in the search direction $\delta\mathbf{u}_{n+1}^{i+1}$ equal to zero,

$$(\delta\mathbf{u}_{n+1}^{i+1})^{T}\ \mathbf{?}\ (\mathbf{u}_{n+1}^{i+1,\,j}) = 0 \tag{5.14}$$

For a detailed discussion related to the line search technique see Crisfield (1991) and Zienkiewicz and Taylor (1991).

Constrained Newton-Raphson method

An important aspect of the incremental-iterative method described above is that the load increment size applied has to be adapted to the structural response. If the load increment is chosen reasonably small, convergence is usually achieved in a small number of iterations and the convergence of the Newton-Raphson method is typically quadratic (Bathe, 1996).

The standard procedure where the load increment is kept constant during the necessary iterations to achieve equilibrium is not totally efficient and fails at limit points. This aspect is especially important for structures made of materials characterized by softening behaviour, as is the case of masonry structures. Figure 5.2 illustrates schematically the complex structural behaviour that can be found in engineering structures. To compute the response beyond maximum load points, as in Figure 5.2 (a) and (b), a special solution procedure that allows for a decrease in load and an increase in displacement must be used.

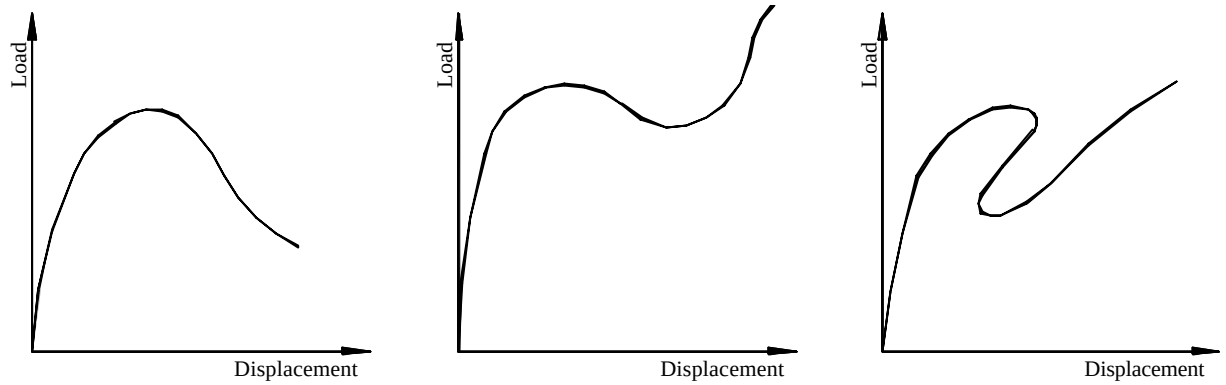

(a) (b) (c)

Figure 5.2 – Complex structural behaviour: (a) softening; (b) snap-through; (c) snap-back.

One possibility is to use direct displacement control by incrementing in a continuous fashion some degrees of freedom. However, this approach cannot be applied to all structural problems and is incapable of properly handling strong localizations, as shown in Figure 5.2 (c).

These difficulties can be surpassed by adding a constraint equation to the initial non-linear equilibrium equation system. The basic idea, due to Riks (1979) and developed by Crisfield (1981) and Ramm (1981), is to introduce the load multiplier as a new variable that increases or decreases the size of the load increment in order to pass limit points. The additional equation required for the solution expresses a constraint between the load multiplier $\Delta\lambda_{n+1}$ and the incremental displacement vector, of the form

$$f(\Delta\lambda_{n+1}, \Delta\mathbf{u}_{n+1}) = 0 \tag{5.15}$$

Different constraint equations have been proposed in literature, see Crisfield (1991) and Bathe (1996) for a comprehensive discussion. This constraint procedure is known as the arc-length method and has shown to be particularly effective near limit points (Bathe, 1996).

5.2 The incremental theory of plasticity

The plastic material behaviour is characterized by the occurrence of permanent deformations. Although the occurrence of these permanent deformations can be related to processes inside the material like slip in metals, the mathematical formulation of plasticity has been successfully extended to materials showing irreversible deformations, such as concrete (Chen, 1982), soil (Chen and Mizuno, 1990) or masonry (Lourenço, 1996). As stated before, the theory of plasticity should just be seen as a mathematical model that approximates the observed behaviour under certain circumstances.

In the following Sections, a brief review of the theory of plasticity will be presented. Recent books covering the plasticity theory are due to Lemaitre and Caboche (1985), Lubliner (1990) and Simo and Hughes (1998), among others, where a comprehensive study of the subject can be found.

5.2.1 Fundamentals

In the context of small strains, the total strain rate vector can be additively decomposed into an elastic part and an irreversible, or plastic part, respectively denoted by $\dot{\boldsymbol{e}}^e$ and $\dot{\boldsymbol{e}}^p$:

$$\dot{\boldsymbol{e}} = \dot{\boldsymbol{e}}^e + \dot{\boldsymbol{e}}^p \tag{5.16}$$

These and all the rate quantities presented along this Chapter are derivatives in order to the pseudo-time variable introduced above, because rate independent behaviour is assumed. The elastic strain rate vector is related with the stress rate vector $\dot{\boldsymbol{s}}$ through the elastic stiffness matrix **D**,

$$\dot{\boldsymbol{s}} = \mathbf{D}\dot{\boldsymbol{e}}^e = \mathbf{D}\left(\dot{\boldsymbol{e}} - \dot{\boldsymbol{e}}^p\right) \tag{5.17}$$

The essential elements of any constitutive model based on the classical plasticity theory are the yield criterion, the hardening rule and the flow rule (Koiter, 1960). The yield criterion defines a surface (hypersurface) in the stress space that bounds all possible stress states. In general, this surface is not fixed in stress space and its motion is controlled by the hardening rule. Inside the yield surface every material point exhibits elastic behaviour. Yield can only occur if the stress vector satisfies the yield function, which has the form

$$f(\boldsymbol{s}, \boldsymbol{a}, k) = 0 \tag{5.18}$$

where $\boldsymbol{a}$ and k are internal variables of the model. $\boldsymbol{a}$ is the back-stress vector that defines the centre of the yield surface, allowing for kinematic hardening behaviour, and k is a scalar hardening variable that controls the amount of hardening/softening.

During the incremental plastic deformation process the yield surface can change size, shape or location. These modifications are defined by the hardening rules. Based on experimental results, three main phenomenological hardening models were proposed to represent hardening behaviour: isotropic hardening (Odqvist, 1933), kinematic hardening (Prager, 1955) and mixed hardening (Hodge, 1957), see Figure 5.3 for a schematic representation.

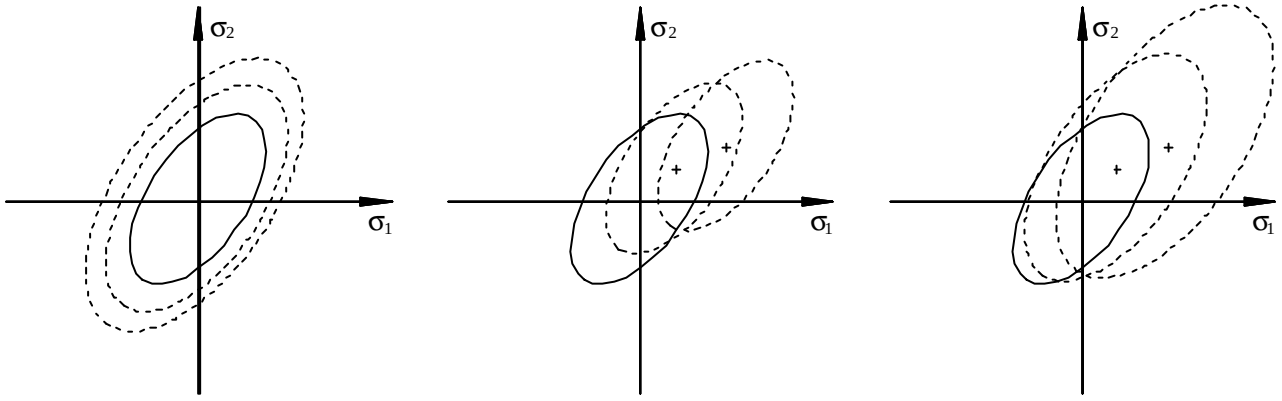

Figure 5.3 – Movement of the yield surface ruled by: (a) isotropic hardening; (b) kinematic hardening; (c) mixed hardening. σ_1 and σ_2 are the principal stresses.

Referring to eq. (5.18), $\boldsymbol{a}$ controls the location of the centre of the yield surface whereas k controls the size and shape of the yield surface. A simple example can be constructed assuming linear isotropic and kinematic hardening laws. Figure 5.4 represents the mechanical response of a one-dimensional model to the three hardening hypotheses mentioned above. The scalars I and K represent the isotropic hardening modulus and the kinematic hardening modulus, respectively. In Figure 5.4 both parameters are assumed to be constant.

The isotropic hardening law is the easiest one and good results can be achieved under monotonic loading conditions. However, the description of induced anisotropy or other features related to cyclic behaviour, e.g. the Bauschinger effect, cannot be suitably carried out using such a law and therefore more complex hardening laws are required.

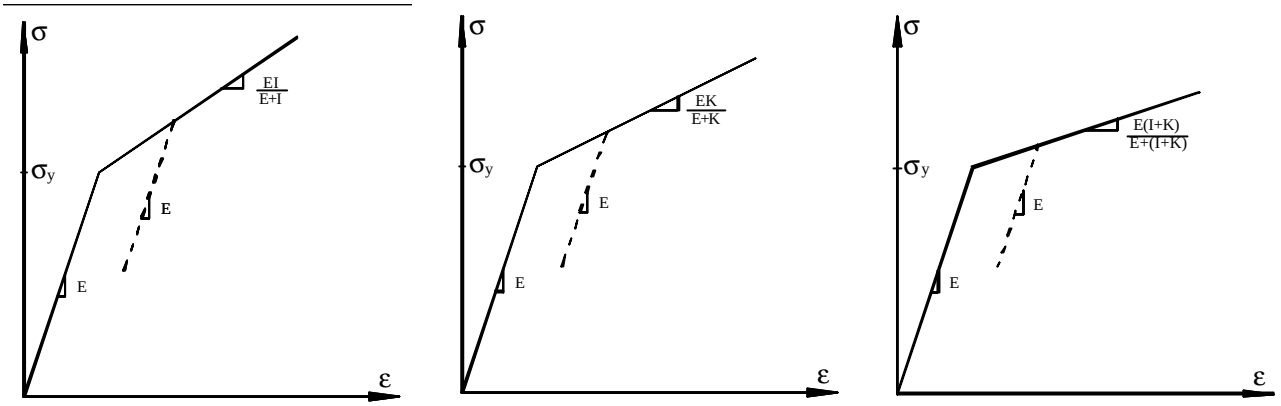

(a) (b) (c)

Figure 5.4 – Schematic representation of the mechanical response of a one-dimensional model to a: (a) isotropic hardening law; (b) kinematic hardening law; (c) mixed hardening law. The elastoplastic tangent modulus is specified for each case, including unloading.

The evolution of the plastic strain rate is given by the flow rule

$$\dot{\boldsymbol{e}}^{p} = \dot{l}\,\frac{\partial g}{\partial \boldsymbol{s}} \tag{5.19}$$

where λ is a non-negative scalar named plastic multiplier and g is the plastic potential function that describes a plastic potential surface in stress space. Generally g is expressed as a function of the stress vector and some internal variables (hardening variables). For the case of $g = f$, the flow rule is termed associated. Otherwise, a non-associated flow rule is obtained.

The plastic multiplier rate $\dot{\lambda}$ and the yield function have to fulfil the Kuhn-Tucker conditions:

$$\dot{l} \geq 0 \qquad f \leq 0 \qquad \dot{l}\, f = 0 \tag{5.20}$$

Suitable rules for the evolution of the hardening variables, in the rate form, have to be established. The scalar k is generally related with the equivalent plastic strain rate $\dot{e}^{eps}$ (strain hardening) or with the plastic work rate $\dot{W}^{p}$ (work hardening). For the former hypothesis, the equivalent plastic strain rate can be defined as

$$\dot{k} = \dot{e}^{eps} = \sqrt{(\dot{\boldsymbol{e}}^{p})^{T}\,\dot{\boldsymbol{e}}^{p}} \tag{5.21}$$

The equivalent plastic strain rate can also be derived from the plastic work per unit of volume, resulting

$$\dot{k} = \dot{e}^{eps} = \frac{\dot{W}^p}{\bar{s}} = \frac{\boldsymbol{s}^T \dot{\boldsymbol{e}}^p}{\bar{s}} \tag{5.22}$$

in which $\bar{s}$ is a scalar named effective stress, expressed as a function of the hardening variable k, defining the hardening law. Instead, here, if the hypothesis of work hardening is adopted, the rate variable $\dot{k}$ is defined as

$$\dot{k} = \dot{W}^p = \boldsymbol{s}^T \dot{\boldsymbol{e}}^p \tag{5.23}$$

Generally, the evolution of the back-stress vector is related with the flow direction, known as the Prager's hardening rule (Prager, 1955)

$$\dot{\boldsymbol{a}} = (1-g)\,\dot{l}\; K \frac{\partial g}{\partial \boldsymbol{s}} \tag{5.24}$$

or with the direction of the relative stress vector, Zigler's rule (Zigler, 1959), which reads

$$\dot{\boldsymbol{a}} = (1-g)\,\dot{l}\; K\,(\boldsymbol{s}-\boldsymbol{a}) \tag{5.25}$$

The scalar K represents the kinematic hardening modulus and g is an adimensional parameter that settles the proportion of isotropic and kinematic hardening. $g = 0$ implies full kinematic hardening while full isotropic hardening is obtained with $g = 1$.

5.2.2 Integration of the elastoplastic constitutive equations

The local integration of the non-linear rate equations over the finite step $(\cdot)_n \rightarrow (\cdot)_{n+1}$, or $(\cdot)_t \rightarrow (\cdot)_{t+1}$, and the subsequent solution of the resulting system of equations are the main problems in computational plasticity. With regard to the later, the reader is referred to Section 5.1, where the general solution procedure is described.

At the current increment n (or time t) all the basic variables $\boldsymbol{e}_n$, $\boldsymbol{e}_n^p$, $\boldsymbol{a}_n$ and k_n are known. The elastic strain and stress vectors are regarded as dependent variables because they are related with the basic variables through the equations

$$\boldsymbol{e}^e = \boldsymbol{e} - \boldsymbol{e}^p \qquad \boldsymbol{s} = \mathbf{D}\boldsymbol{e}^e \tag{5.26}$$

The integration of the rate equations is a strain driven process in which the total strain vector is the only independent variable,

$$\boldsymbol{e}_{n+1} = \boldsymbol{e}_n + \Delta\boldsymbol{e}_{n+1} \tag{5.27}$$

Then, it is just necessary to update the remaining basic variables. By applying the implicit Euler backward algorithm, the continuous constrained problem is transformed in a discrete problem for the variables $\boldsymbol{e}^p_{n+1}$, $\boldsymbol{a}_{n+1}$ and k_{n+1}, constrained by the discrete Kuhn-Tucker conditions

$$l_{n+1} \geq 0 \qquad f_{n+1} \leq 0 \qquad l_{n+1} f_{n+1} = 0 \tag{5.28}$$

as shown by Simo *et al.* (1988). The stability and accuracy of the implicit Euler backward has been exhaustively demonstrated, e.g. Ortiz and Popov (1985), De Borst and Feenstra (1990). Application of this algorithm results in the following discrete set of equations

$$\begin{aligned}
&\boldsymbol{s}_{n+1} = \mathbf{D}\left(\boldsymbol{e}_{n+1} - \boldsymbol{e}^p_{n+1}\right)\\
&\boldsymbol{e}^p_{n+1} = \boldsymbol{e}^p_n + \Delta l_{n+1} \left.\frac{\partial g}{\partial \boldsymbol{s}}\right|_{n+1}\\
&\boldsymbol{a}_{n+1} = \boldsymbol{a}_n + \Delta\boldsymbol{a}_{n+1}\left(\boldsymbol{s}_{n+1}, \boldsymbol{a}_{n+1}, \Delta l_{n+1}\right)\\
&k_{n+1} = k_n + \Delta k_{n+1}\left(\boldsymbol{s}_{n+1}, \boldsymbol{a}_{n+1}, \Delta l_{n+1}\right)\\
&f_{n+1}\left(\boldsymbol{s}_{n+1}, \boldsymbol{a}_{n+1}, k_{n+1}\right) = 0
\end{aligned} \tag{5.29}$$

The algorithm procedure consists of two phases, an elastic predictor and a plastic corrector. The elastic predictor step is obtained by freezing plastic flow during the finite step, which leads to an elastic trial state (auxiliary state)

$$\begin{aligned}
&\boldsymbol{s}^{trial}_{n+1} = \boldsymbol{s}_n + \mathbf{D}\Delta\boldsymbol{e}_{n+1}\\
&\boldsymbol{e}^{p,trial}_{n+1} = \boldsymbol{e}^p_n\\
&\boldsymbol{a}^{trial}_{n+1} = \boldsymbol{a}_n\\
&k^{trial}_{n+1} = k_n\\
&f^{trial}_{n+1} = f_{n+1}\left(\boldsymbol{s}^{trial}_{n+1}, \boldsymbol{a}^{trial}_{n+1}, k^{trial}_{n+1}\right)
\end{aligned} \tag{5.30}$$

If the elastic trial stress $\boldsymbol{s}_{n+1}^{trial}$ lies outside the yield surface, then the elastic state becomes inadmissible and plastic flow must occur. As a result, a plastic corrector, given by eq. (5.29), is used to find an admissible stress state consistent with eq. (5.28), which is named return mapping of the stress update.

Equations (5.29) are of general use and in some cases can be greatly simplified. In particular, for the hardening laws and the yield functions used in the model to be presented in Sections 5.3 and 5.4, the former system of equations can be reduced to a non-linear equation with only one unknown, see also Feenstra (1993) and Lourenço (1996), solved with a local Newton-Raphson method. This simplification will be conveniently detailed later on.

5.2.3 Evaluation of the consistent tangent operator

The application of the Newton-Raphson method to solve the incremental-iterative procedure described before guaranties a quadratic rate of asymptotic convergence while close enough to the solution provided that an appropriate tangent operator is used. Simo and Taylor (1985) referred that the use of a continuum tangent operator, derived from the rate elastoplastic equations (Owen and Hilton, 1980), was the main cause of the absence of quadratic convergence. Simo and Taylor (1985) also demonstrated that to preserve the quadratic rate of asymptotic convergence it is necessary to use a tangent operator obtained from the consistent linearization of the non-linear incremental constitutive equations resulting from the integration over a finite step. Thus, the consistent tangent stiffness matrix has to be derived from the update stress at the end of iteration *n+1*

$$\mathbf{D}^{ep} = \left.\frac{d\boldsymbol{s}}{d\boldsymbol{e}}\right|_{n+1} \tag{5.31}$$

The unknowns of the return mapping algorithm described above are the stress vector $\boldsymbol{s}_{n+1}$, the internal variables $\boldsymbol{a}_{n+1}$ and k_{n+1} and the plastic multiplier l_{n+1}, which are now grouped in a vector $\mathbf{q}_{n+1}$. The linearization of eq. (5.29), see Lourenço (1996), results in

$$[\mathbf{J}]\begin{Bmatrix} d\boldsymbol{s}_{n+1} \\ d\mathbf{q}_{n+1} \end{Bmatrix} = \begin{bmatrix} \mathbf{J}_{n_s \times n_s} & \mathbf{J}_{n_s \times n_q} \\ \mathbf{J}_{n_q \times n_s} & \mathbf{J}_{n_q \times n_q} \end{bmatrix} \begin{Bmatrix} d\boldsymbol{s}_{n+1} \\ d\mathbf{q}_{n+1} \end{Bmatrix} = \begin{Bmatrix} d\boldsymbol{e}_{n+1} \\ \mathbf{0} \end{Bmatrix} \tag{5.32}$$

in which **J** is the Jacobian computed to solve the return mapping, and n_s and n_q are, respectively, the dimensions of the vectors $\boldsymbol{s}$ and $\mathbf{q}$. By inversion of the Jacobian, the consistent tangent stiffness matrix becomes as

$$\mathbf{D}^{ep} = \left.\frac{d\boldsymbol{s}}{d\boldsymbol{e}}\right|_{n+1} = \left[\mathbf{J}_{n_s \times n_s}\right]^{-1} \tag{5.33}$$

Eq. (5.33) represents a general expression for the consistent tangent stiffness matrix. This expression will be opportunely detailed for the constitutive models to be used.

5.2.4 Extended formulations of classical plasticity theory

Although isotropic and kinematic hardening models have been extensively used in engineering modelling, they are not capable of adequately describing the structural cyclic behaviour of quasi-brittle materials. In order to surpass this deficiency, several improvements have been proposed to extend the classical plasticity formulation to include cyclic loading in an appropriate manner. In the following, some of these improvements are briefly introduced, namely nested yield surface models, bounding surface models and generalized plasticity models. These models can include classical plasticity as a particular case.

Nested yield surface models

In order to account for a more realistic prediction of cyclic behaviour, an extended formulation of the classical incremental theory of plasticity was proposed independently by Iwan (1967) and Mróz (1967). Instead of using a single yield surface, they proposed the use of a family of yield surfaces, in which each surface had an independent motion, ruled by a kinematic hardening law, see Figure 5.5 . The hardening rules are defined separately for each yield surface.

The movement of the stress point is performed in an elastic fashion until the yield surface f_1 is reached. Afterwards, plastic flow begins and the surface f_1 starts to move towards the surface f_2. When surface f_2 is reached, it becomes the active yield surface and f_1 is translated by the stress point, remaining tangent to surface f_2 on the stress path. Unloading and subsequent reloading processes have a similar treatment to loading.

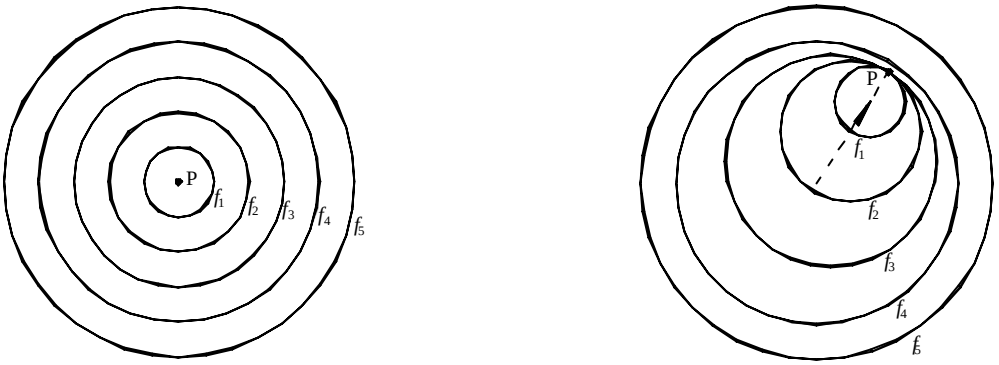

(a) (b)

Figure 5.5 – Schematic representation of a series of nested yield surfaces in stress space: (a) initial position; (b) motion.

This class of models may be very useful to overcome some limitations of the plasticity theory, but its use is made difficult by the need of a complete memorization of size and location of each yield surface, which may turn computer implementation hard and costly.

Bounding surface models

This class of models was initially introduced by Dafalias and Popov (1975) and Kreig (1975) separately. Two surfaces need to be defined in the stress space, an inner surface termed loading surface and an outer surface termed bounding surface. The inner surface encloses an elastic domain and moves with plastic deformation within the outer surface. The loading surface may contact the bounding surface but not intersect it. Both surfaces can move and deform according to isotropic and kinematic hardening rules, see Figure 5.6 .

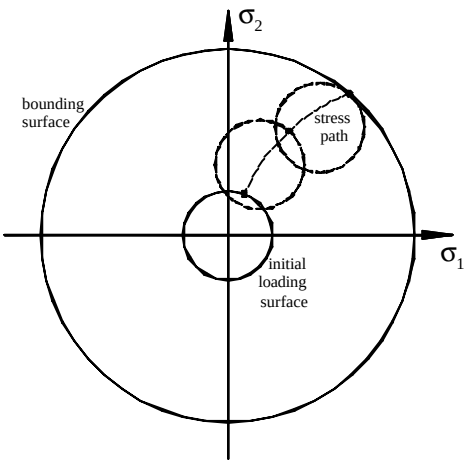

Figure 5.6 – Schematic representation of a bounding surface model.

The plastic modulus, at a given stress point, is specified as a function of the measure of the distance between the stress point and its image on the bounding surface, obtained from a mapping rule, see Dafalias (1986) for a detailed description. A special case is obtained by assuming that the loading surface coincides with the bounding surface, resulting in the classical plasticity theory. The bounding surface concept has been used by several authors to establish constitutive models for soils (Mróz *et al.*, 1978), concrete (Fardis *et al.*, 1983) and metals (Hashiguchi, 1989).

Generalized plasticity models

The generalized plasticity theory appeared as a natural enhancement of the classical plasticity theory to face complex loading conditions. An initial framework of generalized plasticity was proposed by Zienkiewicz and Mróz (1984), with applications to soil mechanics.

Irreversible (plastic) strains are produced without the need for specifying any yield surfaces, for explicitly defining plastic potentials, or for applying consistency rules. Furthermore, the constitutive matrix becomes dependent of the incremental stress direction.

A direction vector, defined in stress space, is used to discriminate between loading and unloading conditions, for which scalar functions are used to characterize plastic moduli. The reader is referred to the works of Zienkiewicz *et al.* (1985) and Pastor *et al.* (1990) for a detailed introduction. Naturally, classical plasticity and bounding surface theories can be obtained from particular cases of the generalized plasticity theory.

5.3 An existing constitutive interface model

The micro-modelling strategy, in which the units are discretized with continuum elements and the joints are discretized with interface elements, as discussed in detail in Chapter 2, is a very powerful tool to understand the behaviour of masonry, as shown by Lourenço (1996). Therefore, an appropriate simulation of the interface behaviour is a key aspect of masonry modelling in a micro-modelling approach.

Lourenço (1994) developed a constitutive model for the monotonic behaviour of interface elements within the incremental theory of plasticity, including all the modern concepts used in computational plasticity, such as the implicit return mapping and consistent tangent operators.

The model was closely checked against experimental data in which it showed great accuracy in reproducing experimental results. However, if a cyclic loading is intended to be performed, this model is unable to reproduce the main observed features, such as stiffness degradation, crack opening/closing and energy dissipation, as already examined in Chapter 2. The reader should keep in mind that classical plasticity is characterized by pure elastic behaviour during unloading from the yield surface, as illustrated in Figure 5.4 (page 130). Based on the framework of plasticity, the model developed by Lourenço (1994) will be extended in order to include in a proper fashion the main phenomenological aspects that characterize cyclic loading of masonry. This Section is devoted to the description of the existing model, being the reader referred to Lourenço (1994, 1996) for a comprehensive introduction.

5.3.1 Yield surfaces, hardening laws and flow rules

The rate independent interface model is defined by a convex composite yield criterion which consists of three individual yield functions, where softening behaviour has been included for all modes (tensile, shear and cap modes). The yield functions read

$$\begin{aligned}
&\text{Tension criterion:} && f_t(\boldsymbol{s},k_t) = s - \bar{s}_t(k_t) \\
&\text{Coulomb friction criterion:} && f_s(\boldsymbol{s},k_s) = |t| + s\,\tan\phi - \bar{s}_s(k_s) \\
&\text{Compressive cap criterion:} && f_c(\boldsymbol{s},k_c) = \tfrac{1}{2}\boldsymbol{s}^T\mathbf{P}\boldsymbol{s} - \left(\bar{s}_c(k_c)\right)^2
\end{aligned} \tag{5.34}$$

where ϕ represents the friction angle and $\mathbf{P}$ is a projection diagonal matrix, based on material parameters. $\bar{s}_t$, $\bar{s}_s$ and $\bar{s}_c$ are the isotropic effective stresses of each of the adopted yield functions, ruled by the scalar internal variables k_t, k_s and k_c, respectively. Figure 5.7 schematically represents the three individual yield surfaces that compose the multisurface interface model in stress space. The rate expressions for the evolution of the isotropic hardening variables were assumed to be given by

$$\begin{aligned}
\dot{k}_t &= \left|\Delta\dot{u}_n^p\right| = \left|[1\ 0]\,\dot{\boldsymbol{e}}^p\right| = \dot{l}_t \\
\dot{k}_s &= \left|\Delta\dot{u}_t^p\right| = \left|[0\ 1]\,\dot{\boldsymbol{e}}^p\right| = \dot{l}_s \\
\dot{k}_c &= \sqrt{\left(\dot{\boldsymbol{e}}^p\right)^T\dot{\boldsymbol{e}}^p} = \dot{l}_c\sqrt{\boldsymbol{s}^T\mathbf{P}\mathbf{P}\boldsymbol{s}}
\end{aligned} \tag{5.35}$$

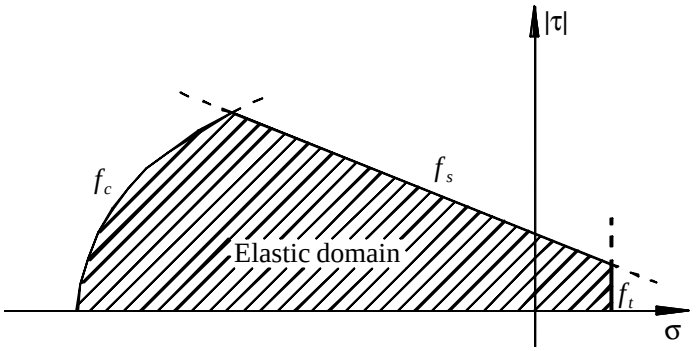

Figure 5.7 – Existing multisurface interface model (stress space).

For tensile and shear modes exponential softening laws were adopted according to available experimental data, whereas for compression a hardening/softening law was chosen. Based on these isotropic hardening laws, the uniaxial behaviour under tensile, compressive and shear loading, illustrated in Figure 5.8 , is easily reproduced. The elastic unloading is also exemplified.

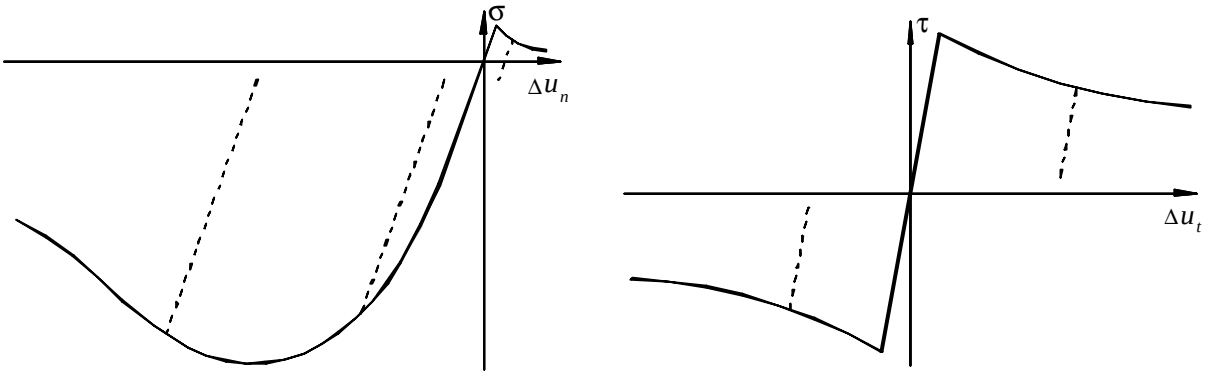

(a) (b)

Figure 5.8 – Monotonic behaviour under (a) uniaxial tensile and compressive loading; (b) direct shear loading.

Associated flow rules were assumed for tensile and cap modes and a non-associated plastic potential g_s was adopted for the shear mode with a dilatancy angle y and a cohesion c, given by

$$g_t = f_t$$

$$g_s = |t| - s \tan y - c \tag{5.36}$$

$$g_c = f_c$$

A non-associated flow rule for shear is necessary because friction and dilatancy angles are different, as shown by Van der Pluijm (1993).

5.3.2 Integration of the elastoplastic constitutive equations

From eqs. (5.29) and (5.30), the stress update for each individual yield surface is obtained according to

$$\boldsymbol{s}_{n+1} = \boldsymbol{s}_{n+1}\left(\Delta l_{n+1}\right) = \boldsymbol{s}_{n+1}^{trial} - \Delta l_{n+1}\,\mathbf{D}\left.\frac{\partial g}{\partial \boldsymbol{s}}\right|_{n+1} \tag{5.37}$$

Furthermore, since $\boldsymbol{s}_{n+1}$ and k_{n+1} can be expressed as functions of Δl_{n+1}, the yield function is transformed into a non-linear equation of one variable $f\left(\Delta l_{n+1}\right) = 0$, which is solved locally using the Newton-Raphson method. Considering that only one surface is active, the derivatives necessary to the iterative procedure read

$$\begin{aligned}
\left.\frac{\partial f_t}{\partial \Delta l_t}\right|_{n+1} &= -\left(\frac{\partial f_t}{\partial \boldsymbol{s}}\right)^T \mathbf{D}\frac{\partial g_t}{\partial \boldsymbol{s}} - h_t \\
\left.\frac{\partial f_s}{\partial \Delta l_s}\right|_{n+1} &= -\left(\frac{\partial f_s}{\partial \boldsymbol{s}}\right)^T \mathbf{D}\frac{\partial g_s}{\partial \boldsymbol{s}} - h_s \\
\left.\frac{\partial f_c}{\partial \Delta l_c}\right|_{n+1} &= \left(\frac{\partial f_c}{\partial \boldsymbol{s}} + \frac{\partial f_c}{\partial k_c}\frac{\partial k_c}{\partial \boldsymbol{s}}\right)^T \frac{\partial \boldsymbol{s}}{\partial \Delta l_c} - h_c
\end{aligned} \tag{5.38}$$

where

$$h_t = -\frac{\partial f_t}{\partial k_t} \qquad h_s = -\frac{\partial f_s}{\partial k_s} \qquad h_c = -\frac{\partial f_c}{\partial k_c}\frac{\partial k_c}{\partial \Delta l_c} \tag{5.39}$$

5.3.3 Consistent tangent operator

For the constitutive model described above, the consistent tangent stiffness matrix reads

$$\mathbf{D}^{ep} = \left.\frac{d\boldsymbol{s}}{d\boldsymbol{e}}\right|_{n+1} = \mathbf{H} - \frac{\mathbf{H}\dfrac{\partial g}{\partial \boldsymbol{s}}\boldsymbol{?}^T\mathbf{H}}{h + \boldsymbol{?}^T\mathbf{H}\dfrac{\partial g}{\partial \boldsymbol{s}}} \tag{5.40}$$

where $\mathbf{H}$, g and h are defined as

$$\mathbf{H} = \left[\mathbf{D}^{-1} + \Delta l_{n+1} \frac{\partial^2 g}{\partial \boldsymbol{s}^2} \right]^{-1}$$

$$\boldsymbol{?} = \frac{\partial f}{\partial \boldsymbol{s}} + \frac{\partial f}{\partial k} \frac{\partial k}{\partial \boldsymbol{s}} \bigg|_{n+1} \tag{5.41}$$

$$h = -\frac{\partial f}{\partial k} \frac{\partial k}{\partial \Delta l} \bigg|_{n+1}$$

5.3.4 Corner regime

In the described composite yield criterion, the intersection of the different yield surfaces defines two possible corners, see Figure 5.7 , composed by the tensile and shear modes or by the shear and cap modes, since intersection between cap and tensile modes is numerically prevented from occurring. Following Koiter's rule (Koiter, 1953), the plastic strain rate in a corner is given by a linear combination of the plastic strain rates of yield surfaces 1 and 2

$$\dot{\boldsymbol{e}}^p = \dot{\boldsymbol{e}}_1^p + \dot{\boldsymbol{e}}_2^p = \dot{l}_1 \frac{\partial g_1}{\partial \boldsymbol{s}} + \dot{l}_2 \frac{\partial g_2}{\partial \boldsymbol{s}} \tag{5.42}$$

In the model, tensile and shear softening are coupled because, physically, both phenomena are related with the degradation of bond between the unit and the mortar. At this corner, a quadratic combination for the hardening parameters rate was adopted, which read

$$\begin{aligned} \dot{k}_t^{cor} &= \sqrt{(\dot{l}_t)^2 + (a\, \dot{l}_s)^2} \\ \dot{k}_s^{cor} &= \sqrt{\left(\frac{\dot{l}_t}{a}\right)^2 + (\dot{l}_s)^2} \end{aligned} \tag{5.43}$$

where a is a scalar that depends on material parameters. Again by physical reasoning, shear and cap modes were assumed to be uncoupled, since phenomena that rule the hardening/softening of each mode seem to be only lightly related. Thus, eqs. $(5.35)_{2,3}$ remain unchanged. The stress update is then given by

$$\boldsymbol{s}_{n+1} = \boldsymbol{s}_{n+1}\left(\Delta l_{1,n+1}, \Delta l_{2,n+1}\right) = \boldsymbol{s}_{n+1}^{trial} - \Delta l_{1,n+1} \mathbf{D} \frac{\partial g_1}{\partial \boldsymbol{s}} \bigg|_{n+1} - \Delta l_{2,n+1} \mathbf{D} \frac{\partial g_2}{\partial \boldsymbol{s}} \bigg|_{n+1} \tag{5.44}$$

For the corner regime, the Euler backward algorithm can be simply expressed in a system of two nonlinear equations on the variables $\Delta l_{1,n+1}$ and $\Delta l_{2,n+1}$

$$\begin{cases} f_1\left(\Delta l_{1,n+1}, \Delta l_{2,n+1}\right) = 0 \\ f_2\left(\Delta l_{1,n+1}, \Delta l_{2,n+1}\right) = 0 \end{cases} \tag{5.45}$$

solved by a Newton-Raphson iterative procedure. The Jacobian matrix is given in Lourenço (1996). For multisurface plasticity an expression equivalent to eq. (5.40) can also be obtained. The reader is referred to Lourenço (1996), where such expression can be found.

5.4 Extension to cyclic loading

As discussed in Chapters 2 and 3, experimental work carried out to investigate the cyclic behaviour of interfaces allow one to recognize some important features, now summarized as:

- Stiffness degradation in tension;
- Residual relative displacements at zero stress;
- Absence of stiffness degradation in direct shear;
- Complete crack closing under compressive loading.

Based on the available experimental results concerning the cyclic behaviour of interfaces and masonry structures, the following will be assumed:

- Elastic behaviour constitutes a satisfactory approach for shear unloading/reloading inside the monotonic yield surface;
- Elastic unloading/reloading is not an appropriate hypothesis for tensile and compressive loading since observed experimental behaviour cannot be simulated accurately, namely stiffness degradation and crack closing/reopening which clearly exhibit nonlinear behaviour.

With these assumptions, it becomes clear that the classical formulation of the plasticity theory is unable to reproduce those particular features and therefore cannot be accepted for cyclic loading. This section is dedicated to the description of a new constitutive model, able to accurately reproduce the main features related to cyclic behaviour of interfaces and fully based on the plasticity theory.

5.4.1 Fundamentals

Previous to the extension of the existing model to account for cyclic loading, a change was made in the monotonic version. In order to obtain a simpler relation between k_c and l_c, the monotonic compressive cap criterion was rewritten in square root form

$$f_c(\boldsymbol{s}, k_c) = \left(\boldsymbol{s}^T \mathbf{P} \boldsymbol{s}\right)^{1/2} - \bar{s}_c(k_c) \tag{5.46}$$

in which the projection matrix $\mathbf{P}$ equals $diag\{1, C_{ss}\}$ with C_{ss} being a material parameter. Considering a strain hardening hypothesis, where the equivalent plastic strain rate is derived from the plastic work per unit of volume, eq. (5.22) gives

$$\dot{k}_c = \dot{e}^{eps} = \frac{\boldsymbol{s}^T \dot{\boldsymbol{e}}^p}{\bar{s}} = \dot{l}_c \tag{5.47}$$

and eq. $(5.38)_3$ is replaced by

$$\left.\frac{\partial f_c}{\partial \Delta l_c}\right|_{n+1} = -\left(\frac{\partial f_c}{\partial \boldsymbol{s}}\right)^T \mathbf{D} \frac{\partial g_c}{\partial \boldsymbol{s}} - h_c \tag{5.48}$$

where

$$h_c = -\frac{\partial f_c}{\partial k_c} \tag{5.49}$$

In addition, the consistent tangent operator can be rewritten as

$$\mathbf{D}^{ep} = \left.\frac{d\boldsymbol{s}}{d\boldsymbol{e}}\right|_{n+1} = \mathbf{H} - \frac{\mathbf{H}\frac{\partial g}{\partial \boldsymbol{s}}\left(\frac{\partial f}{\partial \boldsymbol{s}}\right)^T \mathbf{H}}{h + \left(\frac{\partial f}{\partial \boldsymbol{s}}\right)^T \mathbf{H}\frac{\partial g}{\partial \boldsymbol{s}}} \tag{5.50}$$

$\mathbf{H}$ is given by eq.$(5.41)_1$ and h is defined in eqs. $(5.39)_{1,2}$ and eq. (5.49).

In order to include unloading/reloading behaviour in an accurate fashion, an extension of the plasticity theory is proposed. Two new auxiliary yield surfaces (called unloading surfaces), similar to the monotonic ones, are introduced in the monotonic model, described in Section 5.3, to model unloading behaviour to tension and to compression. Each unloading surface can only move inside the admissible stress space and towards the similar monotonic yield surface. In

recent years, other researchers have used this concept of unloading surface in soils (Pan, 1991), masonry (Combescure and Pegon, 1996) and concrete (Cachim, 1999).

In the proposed model, the motion of the unloading surface is controlled by a mixed hardening law. By adopting appropriate evolution rules, it is possible to reproduce non-linear behavior during unloading from the monotonic surface. A new unloading surface must be activated each time a stress reversal takes place, being deactivated when the unloading surface reaches the monotonic envelope for which it moves to or when a subsequent stress reversal occurs. The developed model comprises six possibilities for unloading movements, as schematized in Figure 5.9. Two unloading cases from the monotonic envelope are considered: unloading to tension (CT) and unloading to compression (TC). In both cases, a stress reversal can occur even before the monotonic envelope has been reached, leading to reloading movements to compression (CTC) or to tension (TCT), respectively. These two cases may originate two new other movements if a reversal situation happens before stresses reach the monotonic envelope, respectively CTCT and TCTC. If a stress reversal takes place during a CTCT or TCTC movement, reloading movements CTC and TCT are assumed to occur, respectively.

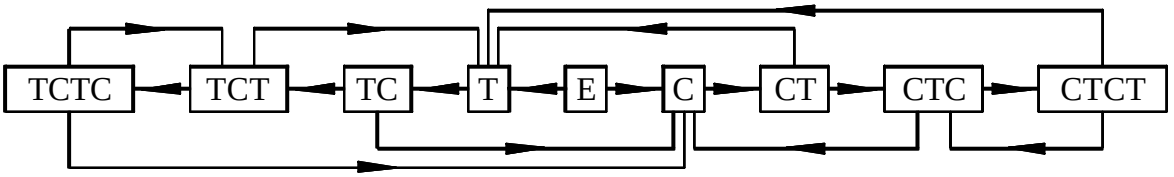

Figure 5.9 – Adopted hypotheses for cyclic behaviour (E for elastic, C for compression and T for tension).

The movements to tension (CT, TCT and CTCT) are carried out with the same unloading surface, but different hardening laws, which must be based on reliable experimental data. The same applies to movements to compression (TC, CTC and TCTC). The adopted hardening laws will be discussed in the next Sections. Both unloading surfaces are ruled by mixed hardening laws, for which a definition of a is necessary. The evolution of the back-stress vector is assumed to be given by (Feenstra, 1993; Cachim, 1999)

$$\dot{\boldsymbol{a}} = (1-g)\,\dot{l}_U K_t\,\boldsymbol{u}_a \tag{5.51}$$

where K_t is the kinematic tangential hardening modulus, $\dot{l}_U$ is the unloading plastic multiplier rate and $\boldsymbol{u}_a$ is the unitary vector of a. g is the parameter that controls the proportion of isotropic

and kinematic hardening. Associated flow rules are assumed during unloading to tension and to compression, leading to

$$g_U = f_U \tag{5.52}$$

5.4.2 Unloading to tension

Unloading to tension (CT, TCT and CTCT) can occur from any admissible stress state outside the tensile monotonic envelope. The yield function is given by

$$f_{Ut}(\boldsymbol{s},\boldsymbol{a},k_{Ut}) = \left(s - a_{(1)}\right) - \bar{s}_{i,Ut}(g\,k_{Ut}) \tag{5.53}$$

where the (1) subscript represents the first component of a. Or, introducing the relative (or reduced) stress vector x,

$$\boldsymbol{?} = \boldsymbol{s} - \boldsymbol{a} \tag{5.54}$$

eq. (5.53) can be rewritten as

$$f_{Ut}(\boldsymbol{s},\boldsymbol{a},k_{Ut}) = \boldsymbol{?}_{(1)} - \bar{s}_{i,Ut}(g\,k_{Ut}) \tag{5.55}$$

with $x_{(1)}$ the first component of x, $\bar{s}_{i,Ut}$ the isotropic effective stress and k_{Ut} is the tensile unloading hardening parameter. Figure 5.10 represents a hypothetical CT case, where the stress point initiates a stress reversal at point A and reaches the monotonic tensile envelope at point D, being deactivated afterwards.

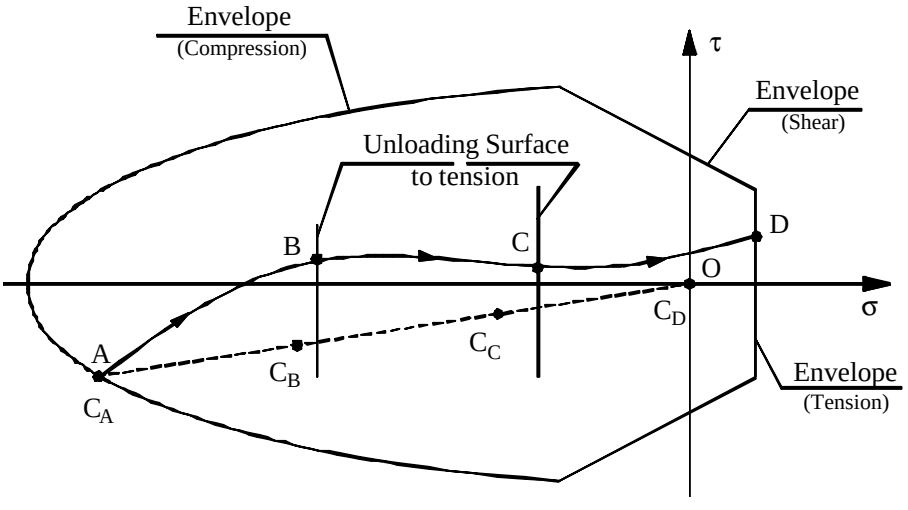

Figure 5.10 – Motion of the unloading surface f_{Ut} to tension.

The points B and C represent intermediary stages of the stress path. The points C_A, C_B, C_C, and C_D represent the centre of the unloading surface f_{Ut} when the stress point is at A, B, C and D, respectively.

Considering a strain hardening hypothesis and assuming that the hardening behaviour is controlled only by the normal plastic relative displacement, see eq. $(5.35)_1$, the evolution equation for the hardening parameter reads

$$\dot{k}_{Ut} = \left|\Delta \dot{u}_n^p\right| = \dot{l}_{Ut} \tag{5.56}$$

5.4.3 Unloading to compression

Considering eq. (5.54), the yield function used to describe unloading to compression (TC, CTC and TCTC) reads

$$f_{Uc}(\boldsymbol{s},\boldsymbol{a},k_{Uc}) = \left(\boldsymbol{?}^T \mathbf{P} \boldsymbol{?}\right)^{1/2} - \bar{s}_{i,Uc}(g\, k_{Uc}) \tag{5.57}$$

where $\bar{s}_{i,Uc}$ is the isotropic effective stress and k_{Uc} the compressive unloading hardening parameter. A possible TC case is exemplified in Figure 5.11. The unloading plastic process starts at point A, on the monotonic tensile surface, goes through points B and C and has its finish at point D, for which the stress point touches the monotonic compressive envelope. The points C_A, C_B, C_C, and C_D represent the centre of the unloading surface f_{Uc} when the stress point is at A, B, C and D, respectively.

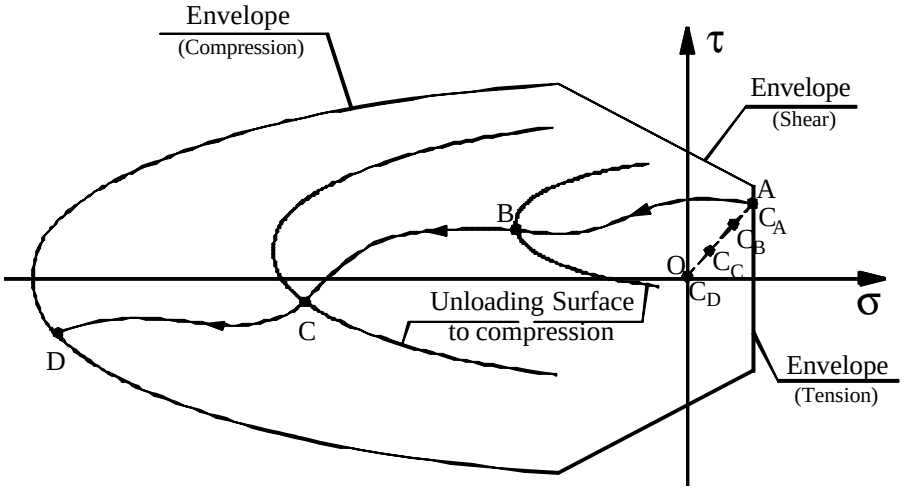

Figure 5.11 – Motion of the unloading surface f_{Uc} to compression.

By assuming a strain hardening hypothesis, eq. (5.22) results in

$$k_{Uc} = \frac{\boldsymbol{?}^T \dot{\boldsymbol{e}}^p}{\bar{s}_{i,Uc}} = \dot{l}_{Uc} \tag{5.58}$$

5.4.4 Adopted hardening laws

For each of the six hypotheses considered for unloading movements in Section 5.4.1, a curve that relates the unloading hardening parameter k_U and the unloading effective stress $\bar{s}_U$ must be defined. The characterization of its shape must be based on a phenomenological approach to existing experimental results. Subsequently, these relations are calibrated for the uniaxial case, as usual in classical plasticity. So, a complete material description based on adequate experimental data and focused on cyclic behaviour is essential for calibrating advanced numerical models, see Chapter 2 for details. Figure 5.12 shows schematically the three curves adopted to simulate unloading from compression (CT) and subsequent stress reversals before reaching the monotonic envelope (CTC and CTCT). Their mathematical characterization may be summarized as:

CT: This curve is based in three points and is described by two parabolas. Two points (0 and 2) belong to the monotonic envelopes and a third point (1) corresponds to the zero stress point in the $(s, \Delta u_n)$ uniaxial diagram. The hardening parameters are given through linear relations between the plastic strain at zero stress (1), the plastic strain at the tensile envelope (2) and the plastic strain at the compressive envelope.

CTC: This diagram is described by a parabola, defined by two points and a derivative: the reversal point and a point belonging to the compressive monotonic envelope, where the derivative is imposed according to the compressive plastic strain.

CTCT: This curve can either be similar to a CT curve or be represented by a parabola, depending on the stress reversal point. The former case occurs for a negative stress reversal value, being the point 1 defined as a function of the other two points and point 1 of Figure 5.12(a). The later situation is based in two points and a derivative: the reversal point and a point belonging to the tensile monotonic envelope, where the derivative is compelled according to the previous CT curve.

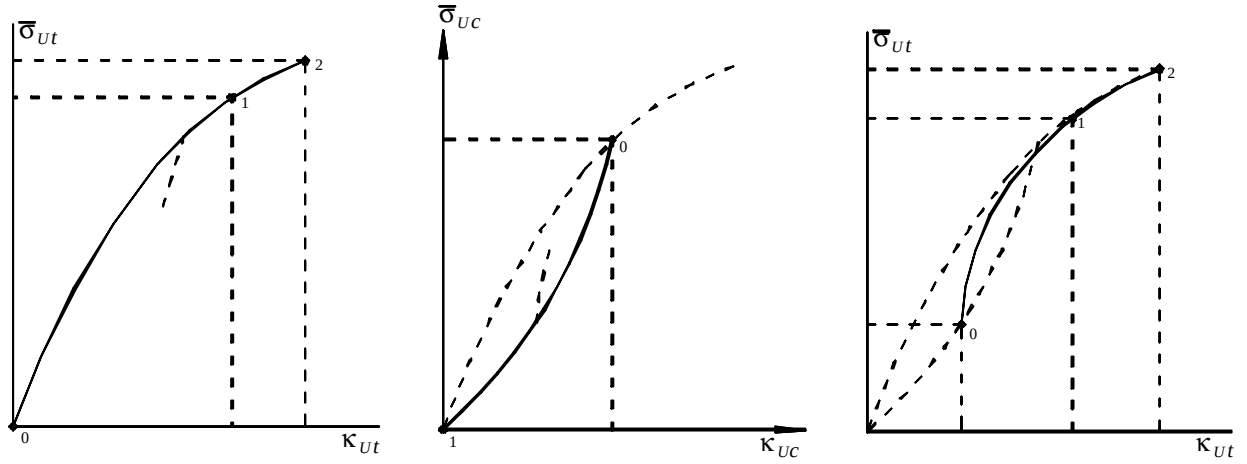

(a) (b) (c)

Figure 5.12 – Schematic hardening laws for: (a) CT, (b) CTC and (c) CTCT movements.

In the same way, an initial unloading from the tensile monotonic envelope can originate three different types of movement (TC, TCT and TCTC), as shown in Figure 5.13. The higher complexity of these curves with respect to the former ones is directly related to the phenomena of closing and reopening experienced by the interface, specially important in the context of cyclic behaviour of masonry structures using a micro-modelling strategy. The adopted curves can be synthesized as follow:

TC: This curve is based in four points, in which two of them belong to the monotonic envelopes. The full description is given by three different branches. First a linear branch takes place until stress changes signal. Point 1 is given through a linear relation between the plastic strain at zero stress and the plastic strain at the tensile envelope. Then, two parabolas are used to reproduce the variation of stiffness associated to the closing of the interface, being point 2 defined as a function of the other points;

TCT: This diagram is described by two parabolas, which are necessary to accurately describe the interface reopening. Their definition is based on three points. Point 1 is defined as a function of the reversal point and the point belonging to the tensile monotonic envelope. For a positive stress reversal value only one parabola is used;

TCTC: This curve can either be similar to a TC curve or be based only on two parabolas, depending on the stress reversal point. The former situation is used for a positive stress reversal value whereas the later case is triggered if a reversal from TCT occurs for a negative stress value;

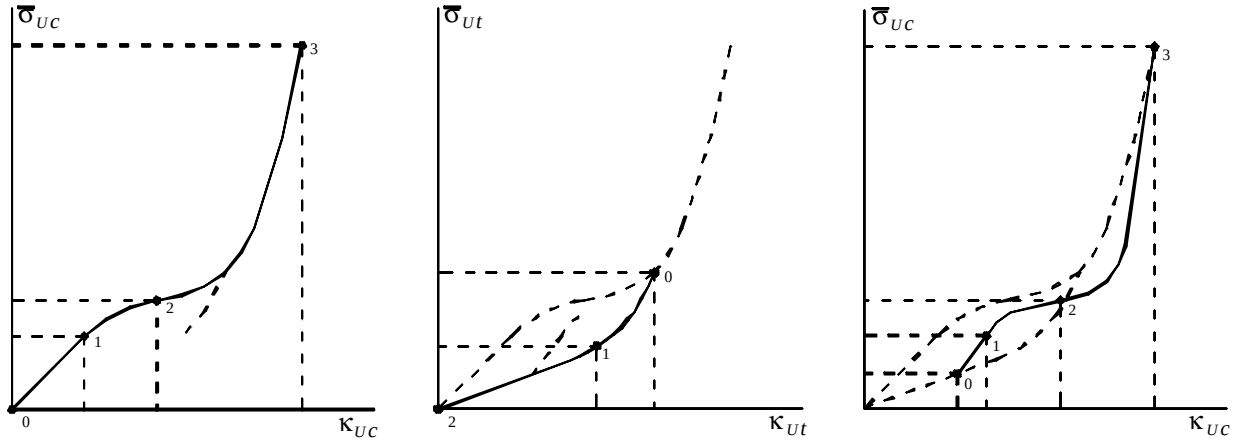

(a) (b) (c)

Figure 5.13 – Schematic hardening laws for: (a) TC, (b) TCT and (c) TCTC movements.

These six different curves characterized above will be used in the definition of the isotropic hardening laws and the kinematic hardening laws as well. Physical reasons force that C^1 continuity (continuous functions with continuous derivatives) must be imposed to all $(\bar{\sigma}_U, \kappa_U)$ curves. Also, all functions must originate positive effective stress values and their derivatives must always be non-negative. Within these restrictions, the mathematical parameters that characterize the hardening laws must be adequately chosen to fit experimental data, obtained from uniaxial tests.

5.4.5 Integration of the elastoplastic constitutive equations

By applying an implicit Euler backward integration scheme to the equations of evolution, the following discrete set of equations is obtained at $n+1$

$$
\begin{aligned}
&\boldsymbol{\sigma}_{n+1} = \mathbf{D}\left(\boldsymbol{\varepsilon}_{n+1} - \boldsymbol{\varepsilon}^{p}_{n+1}\right) \\
&\boldsymbol{\varepsilon}^{p}_{n+1} = \boldsymbol{\varepsilon}^{p}_{n} + \Delta\lambda_{U,n+1} \left.\frac{\partial g_U}{\partial \boldsymbol{\sigma}}\right|_{n+1} \\
&\boldsymbol{\alpha}_{n+1} = \boldsymbol{\alpha}_{n} + (1-\gamma)\,\Delta\lambda_{U,n+1} K_{k\sigma}\,\mathbf{u}_{\alpha,n+1} \\
&\kappa_{U,n+1} = \kappa_{U,n} + \Delta\lambda_{U,n+1} \\
&f_{U,n+1}\left(\boldsymbol{\sigma}_{n+1}, \boldsymbol{\alpha}_{n+1}, \kappa_{U,n+1}\right) = 0
\end{aligned}
\tag{5.59}
$$

where K_{ks} is the kinematic secant hardening modulus, defined as a function of the unloading hardening parameter and the kinematic effective stress (Feenstra and De Borst, 1992). The discrete Kuhn-Tucker conditions at step $n+1$ are expressed as

$$\lambda_{U,n+1} \geq 0\,, \quad f_{U,n+1}\left(\boldsymbol{\sigma}_{n+1}, \boldsymbol{\alpha}_{n+1}, k_{U,n+1}\right) \leq 0\,, \quad \lambda_{U,n+1}\, f_{U,n+1}\left(\boldsymbol{\sigma}_{n+1}, \boldsymbol{\alpha}_{n+1}, k_{U,n+1}\right) = 0 \tag{5.60}$$

Considering an auxiliary elastic trial state, where plastic flow is frozen during the finite step, eqs. (5.59) can be reformulated and read

$$\begin{aligned}
&\boldsymbol{\sigma}_{n+1}^{trial} = \boldsymbol{\sigma}_{n} + \mathbf{D}\Delta\boldsymbol{\varepsilon}_{n+1} \\
&\boldsymbol{\varepsilon}_{n+1}^{p,trial} = \boldsymbol{\varepsilon}_{n}^{p} \\
&\boldsymbol{\alpha}_{n+1}^{trial} = \boldsymbol{\alpha}_{n} \\
&k_{U,n+1}^{trial} = k_{U,n} \\
&f_{U,n+1}^{trial} = f_{U,n+1}\left(\boldsymbol{\sigma}_{n+1}^{trial}, \boldsymbol{\alpha}_{n+1}^{trial}, k_{U,n+1}^{trial}\right)
\end{aligned} \tag{5.61}$$

A stress reversal occurrence is based on the elastic trial state. After a plastic process (monotonic or cyclic), a stress reversal case is established under the condition of a negative unloading yield function value. Within the notation inserted before, unloading movements CT or TC must be started from the respective monotonic envelope whenever, after a converged load step where $f_n\left(\boldsymbol{\sigma}_n, k_n\right) = 0$, the following condition occurs

$$f_{n+1}^{trial} = f_{n+1}\left(\boldsymbol{\sigma}_{n+1}^{trial}, k_{n+1}^{trial}\right) < 0 \tag{5.62}$$

The remaining unloading hypotheses, see Figure 5.9, are trigged whenever, after a successful load step in which $f_{U,n}\left(\boldsymbol{\sigma}_n, \boldsymbol{\alpha}_n, k_{U,n}\right) = 0$, the following situation happens

$$f_{U,n+1}^{trial} = f_{U,n+1}\left(\boldsymbol{\sigma}_{n+1}^{trial}, \boldsymbol{\alpha}_{n+1}^{trial}, k_{U,n+1}^{trial}\right) < 0 \tag{5.63}$$

The system of non-linear equations expressed by eqs. (5.59) can be greatly simplified because the variables $\boldsymbol{\sigma}_{n+1}$, $\boldsymbol{\alpha}_{n+1}$ and $k_{U,n+1}$ can be expressed as functions of $\Delta\lambda_{U,n+1}$ and therefore eq. $(5.59)_5$ is transformed in a non-linear equation in one variable. The plastic corrector step

consists of computing an admissible value of $\Delta l_{U,n+1}$ that satisfies eqs. (5.60) using the Newton-Rapshon method. The derivative necessary reads

$$\left.\frac{\partial f_U}{\partial \Delta l_U}\right|_{n+1} = -\left(\frac{\partial f_U}{\partial \boldsymbol{s}}\right)^T \mathbf{H} \frac{\partial g_U}{\partial \boldsymbol{s}} - h_U \tag{5.64}$$

where

$$\begin{aligned} \mathbf{H} &= \left[\mathbf{D}^{-1} + \Delta l_{U,n+1} \frac{\partial^2 g_U}{\partial \boldsymbol{s}^2}\right]^{-1} \\ h_U &= (1-\gamma) K_t \left(\frac{\partial f_U}{\partial \boldsymbol{s}}\right)^T \boldsymbol{u}_{a,n+1} - \left.\frac{\partial f_U}{\partial k_U}\right|_{n+1} \end{aligned} \tag{5.65}$$

5.4.6 Consistent tangent operator

The consistent tangent stiffness matrix is obtained by consistent linearization of the stress update resulting from the return-mapping algorithm. The total derivative of s (single surface) at $n+1$ reads

$$d\boldsymbol{s} = \mathbf{D}\left(d\boldsymbol{e} - \frac{\partial g_U}{\partial \boldsymbol{s}} d l_U - \Delta l_U \frac{\partial^2 g_U}{\partial \boldsymbol{s}^2} d\boldsymbol{s}\right) \tag{5.66}$$

Imposing the consistency condition at $n+1$

$$d f_U = \left(\frac{\partial f_U}{\partial \boldsymbol{s}}\right)^T d\boldsymbol{s} + \left(\frac{\partial f_U}{\partial \boldsymbol{a}}\right)^T d\boldsymbol{a} + \frac{\partial f_U}{\partial k_U} d k_U = 0 \tag{5.67}$$

the consistent tangent stiffness matrix is obtained as

$$\mathbf{D}^{ep} = \left.\frac{d\boldsymbol{s}}{d\boldsymbol{e}}\right|_{n+1} = \mathbf{H} - \frac{\mathbf{H}\frac{\partial g_U}{\partial \boldsymbol{s}}\left(\frac{\partial f_U}{\partial \boldsymbol{s}}\right)^T \mathbf{H}}{h_U + \left(\frac{\partial f_U}{\partial \boldsymbol{s}}\right)^T \mathbf{H} \frac{\partial g_U}{\partial \boldsymbol{s}}} \tag{5.68}$$

Where the modified stiffness matrix $\mathbf{H}$ and h_U are given by eq. (5.65).

5.4.7 Unloading behaviour with active shear mode

From analysis of Figure 5.10 and Figure 5.11, it can be observed that a composite yield criterion, composed by an unloading/shear corner, may occur. These two modes are assumed to be uncoupled, resulting $k_U = \dot{l}_U$ and $k_s = \dot{l}_s$. Based on eqs. (5.29), (5.30), (5.59) and (5.61), the stress vector is updating according to

$$\boldsymbol{s}_{n+1} = \boldsymbol{s}_{n+1}\left(\Delta l_{U,n+1}, \Delta l_{s,n+1}\right) = \boldsymbol{s}_{n+1}^{trial} - \Delta l_{U,n+1}\mathbf{D}\left.\frac{\partial g_U}{\partial \boldsymbol{s}}\right|_{n+1} - \Delta l_{s,n+1}\mathbf{D}\left.\frac{\partial g_s}{\partial \boldsymbol{s}}\right|_{n+1} \tag{5.69}$$

Since all unknowns can be expressed as functions of $\Delta l_{U,n+1}$ and $\Delta l_{s,n+1}$, the system of non-linear equations to be solved can be reduced simply to

$$\begin{cases} f_s\left(\Delta l_{U,n+1}, \Delta l_{s,n+1}\right) = 0 \\ f_U\left(\Delta l_{U,n+1}, \Delta l_{s,n+1}\right) = 0 \end{cases} \tag{5.70}$$

and the components of the Jacobian necessary for the iterative Newton-Raphson procedure are computed from

$$\begin{aligned} \left.\frac{\partial f_U}{\partial \Delta l_U}\right|_{n+1} &= -\left(\frac{\partial f_U}{\partial \boldsymbol{s}}\right)^T \mathbf{H}\frac{\partial g_U}{\partial \boldsymbol{s}} - h_U & \left.\frac{\partial f_U}{\partial \Delta l_s}\right|_{n+1} &= -\left(\frac{\partial f_U}{\partial \boldsymbol{s}}\right)^T \mathbf{H}\frac{\partial g_s}{\partial \boldsymbol{s}} \\ \left.\frac{\partial f_s}{\partial \Delta l_U}\right|_{n+1} &= -\left(\frac{\partial f_s}{\partial \boldsymbol{s}}\right)^T \mathbf{H}\frac{\partial g_U}{\partial \boldsymbol{s}} & \left.\frac{\partial f_s}{\partial \Delta l_s}\right|_{n+1} &= -\left(\frac{\partial f_s}{\partial \boldsymbol{s}}\right)^T \mathbf{H}\frac{\partial g_s}{\partial \boldsymbol{s}} - h_s \end{aligned} \tag{5.71}$$

where

$$\mathbf{H} = \left[\mathbf{D}^{-1} + \Delta l_{U,n+1}\frac{\partial^2 g_U}{\partial \boldsymbol{s}^2} + \Delta l_{s,n+1}\frac{\partial^2 g_s}{\partial \boldsymbol{s}^2}\right]^{-1} \tag{5.72}$$

h_U is defined by eq. $(5.65)_2$ and h_s is given by eq.$(5.39)_2$. Following a procedure similar to the one described at Section 5.4.6, the consistent tangent stiffness matrix for corner mode is obtained as

$$\mathbf{D}^{ep} = \left.\frac{d\boldsymbol{s}}{d\boldsymbol{e}}\right|_{n+1} = \mathbf{H} - \mathbf{H}\mathbf{U}\left[\mathbf{E} + \mathbf{V}^T\mathbf{H}\mathbf{U}\right]^{-1}\mathbf{V}^T\mathbf{H} \tag{5.73}$$

where the modified stiffness matrix **H** is given by eq. (5.72) and the matrices **U** and **V** read

$$\mathbf{U} = \begin{bmatrix} \dfrac{\partial g_U}{\partial \boldsymbol{s}} & \dfrac{\partial g_s}{\partial \boldsymbol{s}} \end{bmatrix} \qquad \mathbf{V} = \begin{bmatrix} \dfrac{\partial f_U}{\partial \boldsymbol{s}} & \dfrac{\partial f_s}{\partial \boldsymbol{s}} \end{bmatrix} \tag{5.74}$$

and the hardening matrix reads

$$\mathbf{E} = \begin{bmatrix} h_U & 0 \\ 0 & h_s \end{bmatrix} \tag{5.75}$$

A remaining problem is how to identify which modes are active, because the location of the corner is unknown at the beginning of the load step and the trial stress cannot be used to predict accurately the number of active yield surfaces at the end of the increment. Several algorithms have been proposed to solve this question, e.g. Simo *et al.* (1988) and Feenstra (1993). Lourenço (1996) proposed an algorithm based on a trial and error procedure, which will be used here.

5.4.8 Sub-incremental procedure

A new unloading surface is activated each time a stress reversal takes place and it is deactivated when reaches the monotonic envelope for which it moves to. This means that yielding may occur on the unloading surface at the beginning of a given load step and on the monotonic surface at the end. Therefore, a sub-incremental procedure must be used in order to split such load increment in two sub-increments, each one corresponding to a different yield surface.

In a strain driven process, in which the total strain vector is the only independent variable, see Section 5.2.2, the problem consists in the computation of the scalar $0 < \beta < 1$

$$\boldsymbol{e}_{n+1} = \boldsymbol{e}_n + \beta\,\Delta\boldsymbol{e}_{n+1} + (1-\beta)\Delta\boldsymbol{e}_{n+1} \tag{5.76}$$

for which the use of the strain increment $\beta\,\Delta\boldsymbol{e}_{n+1}$ leads the unloading surface to touch the monotonic envelope. After the deactivation of the unloading surface, the remaining strain increment $(1-\beta)\Delta\boldsymbol{e}_{n+1}$ is used with the monotonic surface. In this study, β is computed through a mathematical iterative procedure, where the monotonic yield function is evaluated at each iteration.

5.5 Validation against experimental data

The numerical model has to be validated by comparisons with experimental results. However, available experimental results performed under cyclic loading in cementitious interfaces are scarce, especially experiments performed under tensile loading. Therefore, comparison will be done using masonry and concrete test results. It is important to note that the failure of the interface element under tensile loading is directly related with the failure of the mortar joint, but its failure under compressive loading is associated with the failure of the unit and mortar joint. The ability of the proposed constitutive model to simulate experimental results is next assessed by a comparison with reputed available experimental data obtained under several loading conditions.

5.5.1 Direct shear test

A direct shear test on mortar joints carried out by Atkinson *et al*. (1989) is used here to evaluate the ability of the model to predict cyclic shear loading assuming elastic unloading/reloading behaviour. The comparison between experimental data and numerical response is shown in Figure 5.14. The results were scaled by the experimental values at peak. A good agreement can be found between the experimental and the numerical results. As assumed at the formulation of the constitutive model, elastic behaviour for shear unloading/reloading showed to be a good approximation to experiments. The hypothesis of exponential softening seemed also to be appropriate for shear monotonic loading.

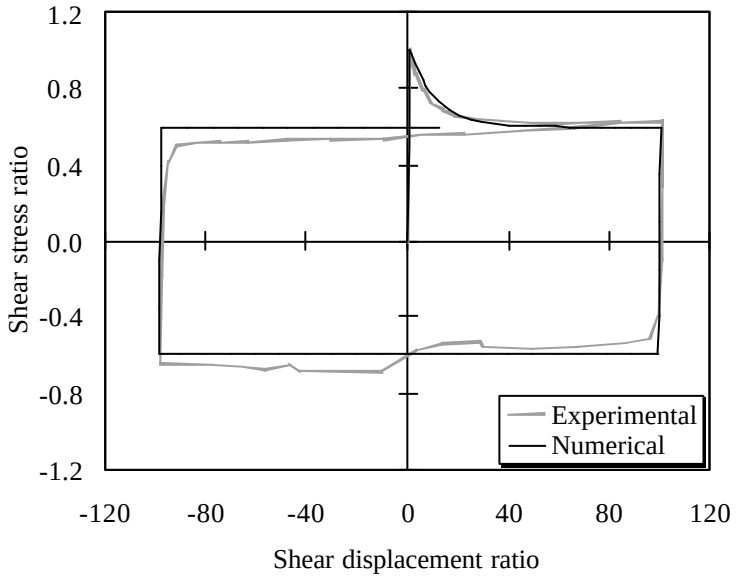

Figure 5.14 – Direct shear test under cyclic loading.

5.5.2 Uniaxial tensile test

The ability of the model to capture the main features related to cyclic tensile tests is checked against the experimental results of Gopalaratnam and Shah (1985) on concrete specimens. The comparison between experimental and numerical results is shown in Figure 5.15, in terms of (s-Δu) curve and total energy. The experimental data was modified in order to express a (s-Δu) relationship and then scaled by experimental values at peak. The numerical response is in a good agreement with the experimental results, namely in terms of stiffness degradation and dissipated energy. A better agreement could be found if monotonic exponential softening were replaced by a more suitable law, e.g. Hordijk (1991).

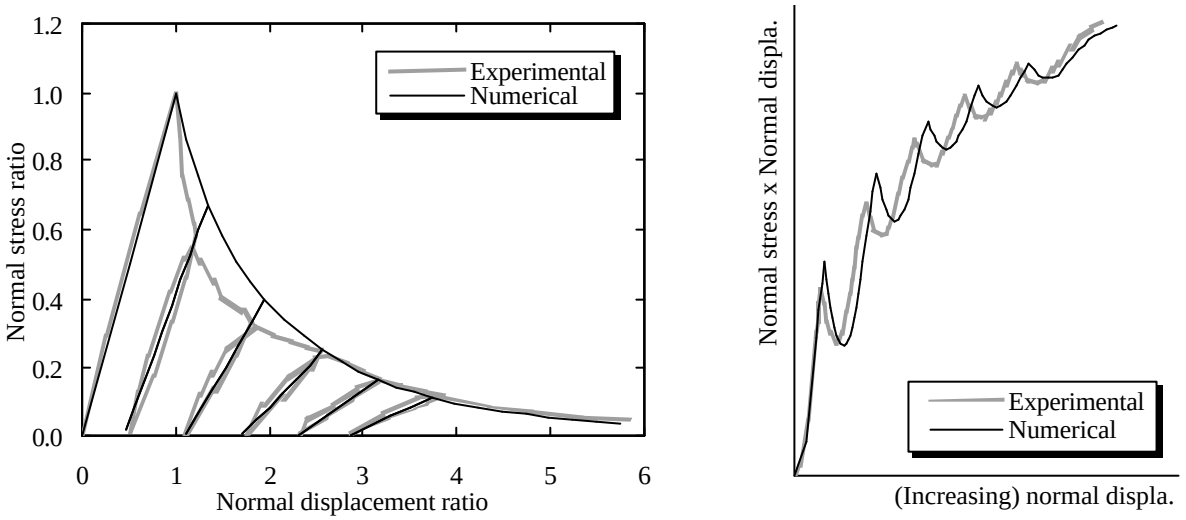

(a) (b)

Figure 5.15 – Uniaxial tensile test under cyclic loading: (a) scaled (s-Δu) curve and (b) total energy.

5.5.3 Uniaxial compressive test

The experiments carried out by Karsan and Jirsa (1969) under cyclic compressive loading are used here to appraise the ability of the proposed model to simulate cyclic compressive loading. The experimental and numerical results are compared in Figure 5.16. As done in the previous Section, the experimental results were modified in order to express a (s-Δu) relationship and then scaled by experimental values at peak. Characteristic features such as stiffness degradation during each unloading/reloading cycle and between cycles, as well as energy dissipation are simulated by the model in an appropriate fashion.

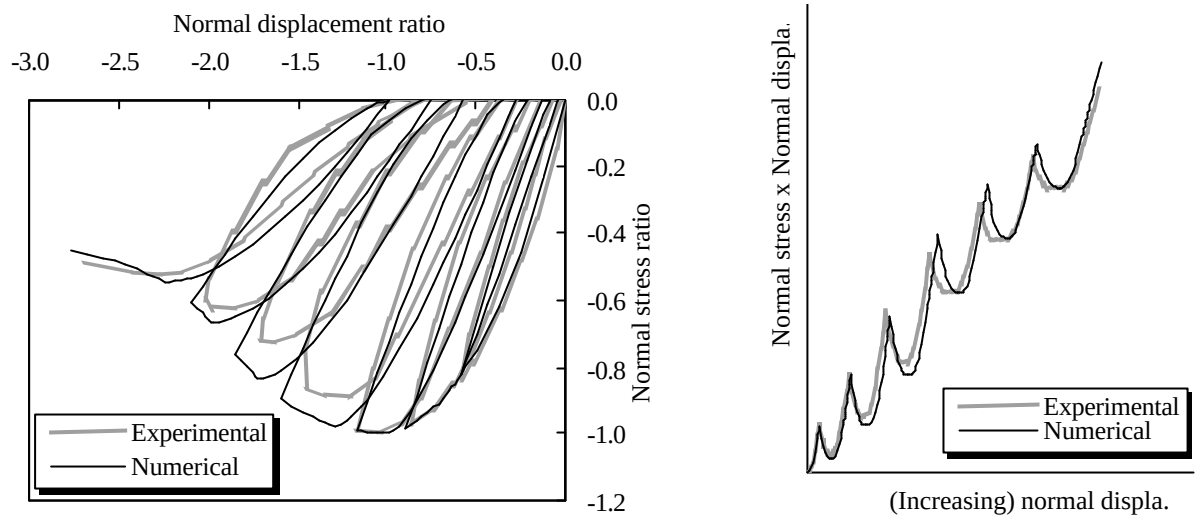

Figure 5.16 – Uniaxial compressive test under cyclic loading: (a) scaled (s-Δu) curve; (b) total energy.

5.5.4 Uniaxial tensile-compressive test

The last example presented here deals with a tensile-compressive loading test performed by Reinhardt (1984) on a concrete specimen. Only six loading cycles were simulated. The comparison between experimental and numerical results is shown in Figure 5.17.

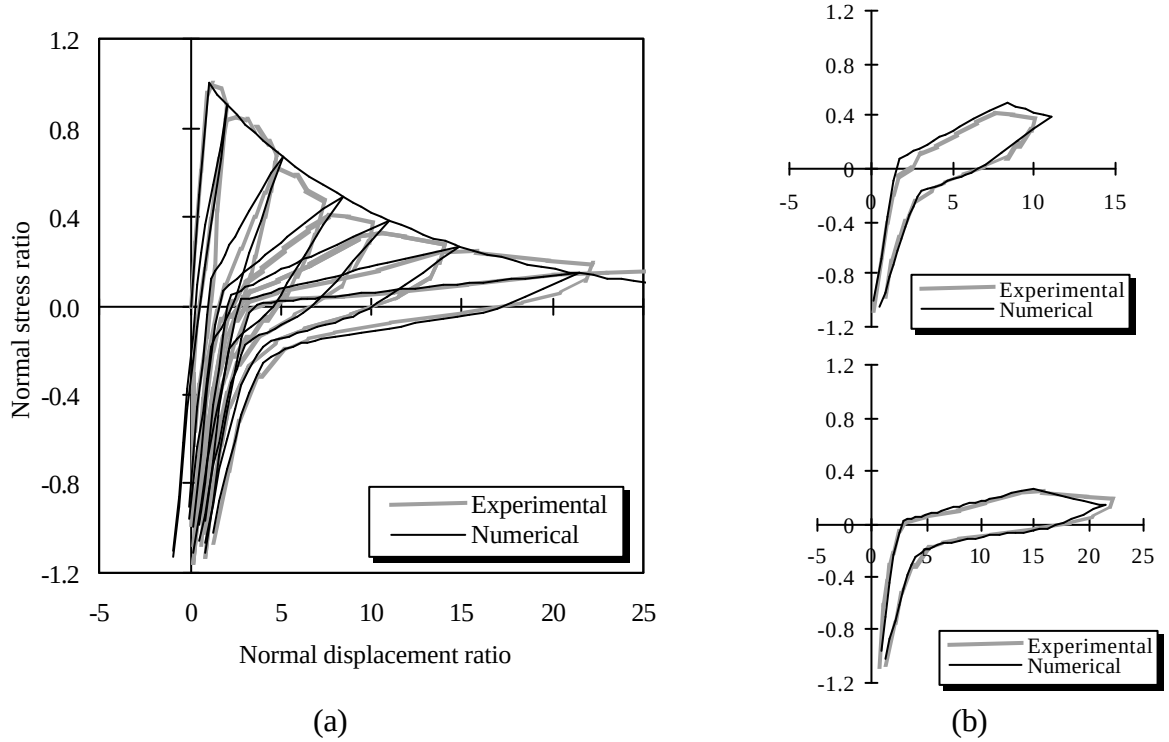

Figure 5.17 – Cyclic tensile-compressive loading test: (a) all cycles and (b) details of cycle 4 and cycle 6.

Once more, the results were normalized by experimental values at peak. In spite of the complex cyclic behaviour exhibited by the experimental result, particularly important stiffness changes associated with closing and reopening of cracks, the model showed to be able to describe accurately the experimental behaviour.

5.6 Reflections about the proposed model

The complete definition of the hardening laws presented in Section 5.4.4 requires the need of four new material parameters with respect to the monotonic version, which can be obtained from uniaxial cyclic experiments under tensile and compressive loading. These parameters define ratios between the plastic strain expected at some special points of the uniaxial (s-Δu_n) curve and the monotonic plastic strain. Some of these points are schematized in Figure 5.18, and are defined as:

- k_{1t}: plastic strain at zero stress when unloading from the monotonic tensile envelope, see Figure 5.18(a);
- k_{1c}: plastic strain at zero stress when unloading from the monotonic compressive envelope, see Figure 5.18(b);
- k_{2c}: plastic strain at the monotonic tensile envelope when unloading from the monotonic compressive envelope, see Figure 5.18(b);
- Δk_c: plastic strain increment originated by a reloading from a CT or a CTCT unloading movement (stiffness degradation between cycles, see Figure 5.16a).

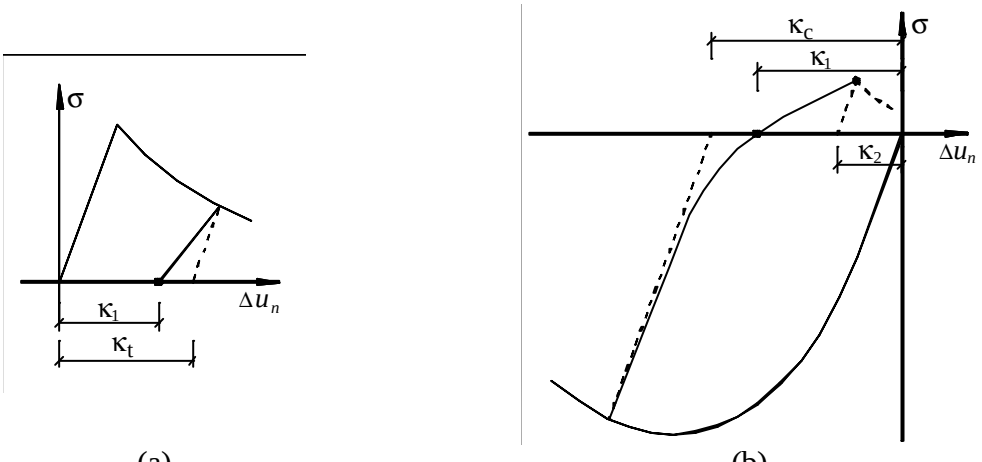

(a) (b)

Figure 5.18 – Special points at the uniaxial (s-Δu) curve: (a) tensile loading and (b) compressive loading.

Table 5.1 gives the material parameters used to simulate numerically the last three experiments presented above. These material parameters have a clear physical meaning and can be obtained from adequate uniaxial cyclic tests. The remaining parameters that fully define the selected hardening laws, which are required to observe imposed physical and mathematical conditions, were chosen to fit experimental data from the above cyclic tests and will be fixed henceforth.

Table 5.1 – Adopted material parameters for cyclic behaviour.

Numerical simulation	$\frac{k_1}{k_t}$	$\frac{k_1}{k_c}$	$\frac{k_2}{k_c}$	$\frac{\Delta k_c}{k_c}$
Gopalaratnam and Shah (1985)	0.76	—	—	—
Karsan and Jirsa (1969)	—	0.56	0.28	0.13
Reinhardt (1984)	0.73	—	—	—

5.7 Summary

The use of the Newton-Raphson method to solve non-linear equations arising from the utilization of the finite element method is briefly presented, including some advanced solution procedures, able to increase the performance of the method.

The incremental plasticity theory is reviewed and some improvements of the classical theory are described. An existing constitutive model for the monotonic behaviour of interface elements within the incremental theory of plasticity is described.

Starting from this model, a new constitutive model entirely founded on the incremental theory of plasticity able to describe the cyclic loading of interface elements is proposed. Two new auxiliary yield surfaces, similar to the monotonic ones, are introduced. Each unloading surface can only move inside the admissible stress space and towards the similar monotonic yield surface. Its motion is controlled by a mixed hardening law. Elastic unloading is assumed only for the shear component. The normal component (tension and compression) is described in a nonlinear fashion, adopting appropriate hardening laws. Afterwards, the proposed model is checked against experimental data. Four reputed experimental results available in the literature were used. Comparison between experimental and numerical results showed that the most relevant features observed in experiments are captured by the model and, therefore, it can be

considered able to represent accurately the experimental behaviour. The material parameters necessary to perform cyclic analyses are presented. Their value show clearly the need of considering non-linear material behaviour during unloading, particularly stiffness degradation. This model will be used for the analysis of full masonry structures, as described in detail in Chapter 6.

6. APPLICATIONS

The objective of this Chapter is not to perform an exhaustive use of the developed constitutive model to engineering structures but solely to assess its ability to reproduce the main features observed in experiments, in an appropriate manner, which can only be achieved if validation against reliable experimental data is done. Three different groups of masonry structures will be analysed, using the developed numerical model. The first group concerns the analysis of two stacked bond prisms, tested under cyclic loading at Universitat Politècnica de Catalunya. The second group deals with a masonry shear wall tested at Eindhoven University of Technology. Finally, the last example concerns the analysis of two masonry shear walls, tested at the Joint Research Centre (Italy) and already used by other researchers to validate cyclic numerical models. In all numerical applications presented in this Chapter, numerical results were converged for an energy norm of 1×10^{-4}.

6.1 UPC stacked bond prisms

The first example deals with two simple prisms, subjected to cyclic uniaxial compression, which have already been presented in Section 3.5. Two stacked bond prisms of five bricks each, named BP1 and BP2, were constructed and tested under cyclic loading until failure was reached. Modelling resorts to six-node zero-thickness line interface elements for the mortar joints and eight-node continuum plane stress elements for the brick units, as illustrated in Figure 6.1.

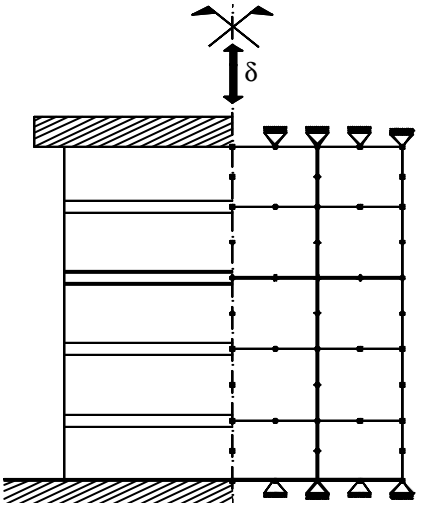

Figure 6.1 – Stacked bond prism: Geometry and modelling.

Both numerical analyses are carried out under displacement control by imposing equal vertical displacements at the top of the prisms, where horizontal movements are prevented to occur. In spite of the confinement provided by the machine platens, the slenderness ratio of 2.15 allows a predominant uniaxial behaviour at middle height.

6.1.1 Elastic parameters

The elastic properties of the bricks and mortar joints are computed using average values obtained from the experiments described in Section 3.4 and Section 3.5. The interface stiffness is derived using the expressions (CUR, 1997)

$$\begin{cases} k_n = \dfrac{E_u E_m}{h_m\left(E_u - E_m\right)} \\ k_s = \dfrac{G_u G_m}{h_m\left(G_u - G_m\right)} \end{cases} \tag{6.1}$$

in which E_u and E_m are the Young's moduli and G_u and G_m are the shear moduli of the unit and the mortar, respectively, and h_m is the mortar joint thickness. Table 6.1 summarizes the adopted elastic properties.

Table 6.1 – Elastic properties for the units and joints (BP1 and BP2).

Unit		Interface	
E [N/mm^2]	n [-]	k_n [N/mm^3]	k_s [N/mm^3]
14700	0.20	648	288

6.1.2 Inelastic parameters

In the micro-modelling strategy, usually the units are assumed to behave elastically, whereas the overall non-linear behaviour is concentrated in the interface elements (Lourenço, 1996). Consequently, in a uniaxial compressive test, the compressive strength of the joint is equal to the compressive strength of the prism. Thus, a compressive strength of 29.15 N/mm^2 is adopted for the interface elements. The parameters that characterize stiffness degradation were obtained by

inverse fitting. Table 6.2 summarizes the model parameters that characterize stiffness degradation under compressive loading, required by the numerical model.

Table 6.2 – Adopted model parameters for cyclic behaviour.

$\frac{k_1}{k_c}$	$\frac{k_2}{k_c}$	$\frac{\Delta k_c}{k_c}$
0.71	0.05	0.02

Since the specimens BP1 and BP2 were made with the same materials, both analyses are carried out using the same elastic and inelastic model parameters.

6.1.3 Discussion of the results

The finite element model described above is submitted to two different numerical displacement-controlled tests, defined in such a way that comparisons with experiments are possible. The numerical results obtained following this procedure, together with the experimental results, established in terms of axial load-displacement diagrams and evolution of the total energy, are shown in Figure 6.2 and Figure 6.3 for the prisms BP1 and BP2, respectively.

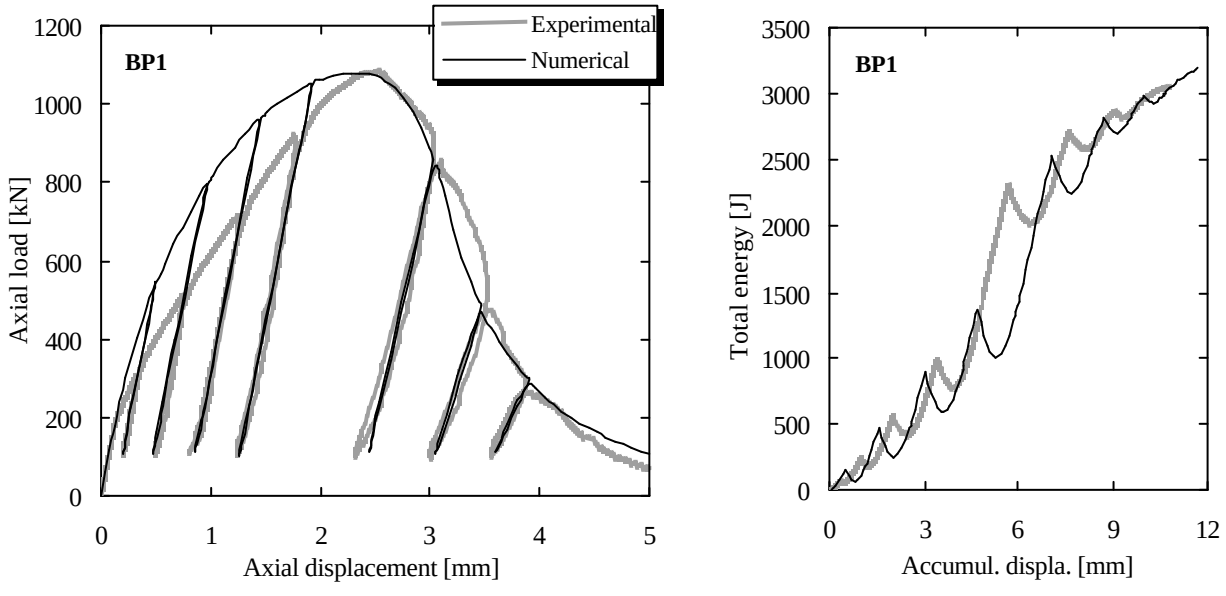

(a) (b)

Figure 6.2 – BP1: comparison between experimental and numerical results in terms of (a) axial load-displacement diagram and (b) total energy evolution.

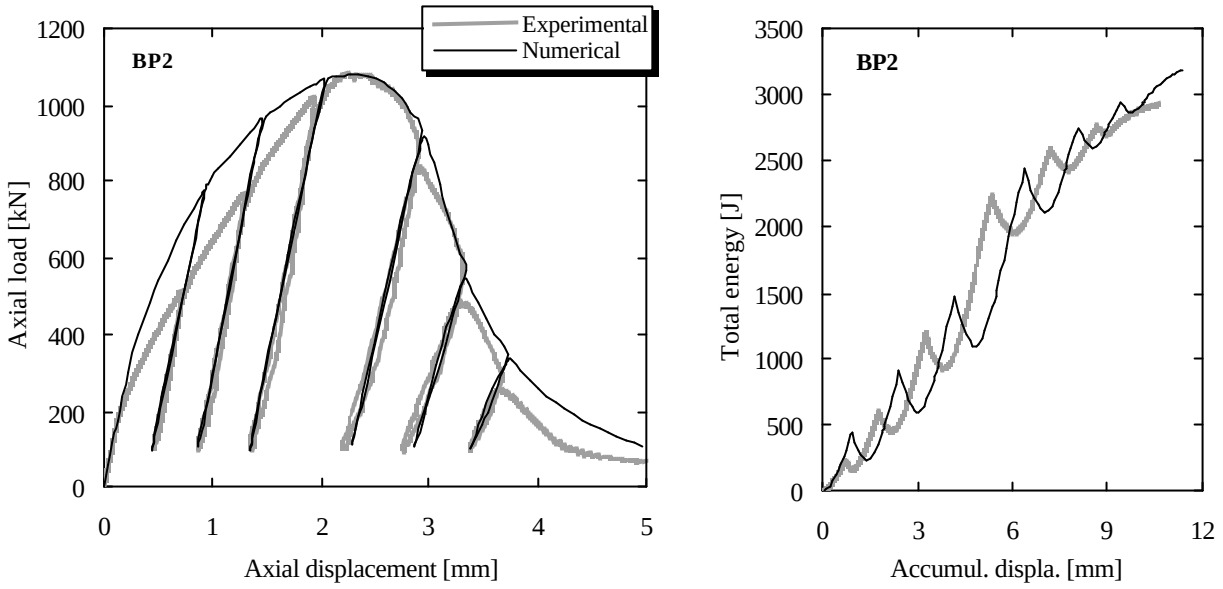

(a) (b)

Figure 6.3 – BP2: comparison between experimental and numerical results in terms of (a) axial load-displacement diagram and (b) total energy evolution.

The analysis of Figure 6.2(a) and Figure 6.3(a) indicates that the global load–displacement response is well reproduced by the model, although hardening behaviour in the pre-peak branch could have been better simulated if a different hardening law had been used. This purpose will not be pursued here, since the main objective is to evaluate the ability of the proposed model to reproduce the features observed in experiments involving cyclic loading and not to fit closely the monotonic axial load-displacement curve.

The dissipated energy is also an important issue when dealing with cyclic loading. The comparisons exhibited in Figure 6.2(b) and Figure 6.3(b) between experimental and numerical results show that a good agreement can be found, aside from the lag originated by differences in the hardening branch of the axial load-displacement diagram.

Table 6.3 exhibits the numerical Young's moduli of the prisms measured initially (elastic value) and measured at each one of the reloading branches, by means of linear least square regressions. It was found that BP1 and BP2 exhibit reloading Young's moduli values very close to each other, essentially because unloading was initiated at similar stress levels. Experimental Young's moduli, presented in Table 3.22, are also reproduced in Table 6.3 for a better comparison. In reference directly to cyclic behaviour, the comparison between numerical and experimental results has shown that stiffness degradation is well captured by the model.

Table 6.3 – Numerical Young's moduli: elastic value and values measured at each reloading branch (the experimental values are also presented for a better comparison).

Brick prism	*E* [GPa]							
	E0	rb1	rb2	rb3	rb4	rb5	rb6	rb7
BP1 (num)	11.1	10.8	10.8	10.7	10.4	9.0	7.0	4.8
BP2 (num)	11.1	10.7	10.7	10.4	9.2	7.1	4.9	—
BP1 (exp)	—	10.58	10.82	10.13	10.83	7.86	6.68	4.16
BP2 (exp)	—	10.84	11.16	11.07	7.91	5.66	4.40	—

The experimental failure modes of the prisms, see Section 3.5 for a review, pointed out that failure was essentially due to splitting of the bricks instead of crushing of the mortar, as reported by others researchers, e.g. McNary and Abrams (1985) and Binda *et al.* (1996b). This seems to be in contradiction with the assumption of elastic behaviour of the units. But, as stated in Chapter 5, these numerical results must be seen as phenomenological approaches to the observed experimental results and, in this context, the adopted modelling strategy has shown to be quite efficient in reproducing the overall observed behaviour. Furthermore, better results concerning the monotonic behaviour could have been achieved if a different hardening law had been chosen.

6.2 TUE masonry shear wall

In this section a masonry shear wall tested at the University of Eindhoven, within the scope of the CUR project (CUR, 1997), is numerically tested in a cyclic fashion. Since the wall was experimentally tested under monotonic loading, no comparisons can be established between the experiments and the numerical cyclic results to be attained here. Therefore, the main purposes of this numerical experiment are directly concerned with the application of the developed constitutive model to an existing masonry structure in order to investigate features related to cyclic behaviour, as stiffness degradation, energy dissipation and failure patterns.

6.2.1 Experimental set-up

Within the scope of the CUR project, Raijmakers and Vermeltfoort (1992) and Vermeltfoort and Raijmakers (1993) have tested several masonry shear walls, either with or without central openings. The walls were characterized by a height/width ratio of one, with dimensions of 1000×990 mm^2, as represented in Figure 6.4. The walls were made of wire-cut solid clay bricks with dimensions $210 \times 52 \times 10$ mm^3 and 10 mm thick mortar, prepared with a volumetric cement:lime:sand ratio of 1:2:9. The shear walls were built with 18 courses, from which only 16 were considered active, since the 2 extreme courses were clamped in steel beams.

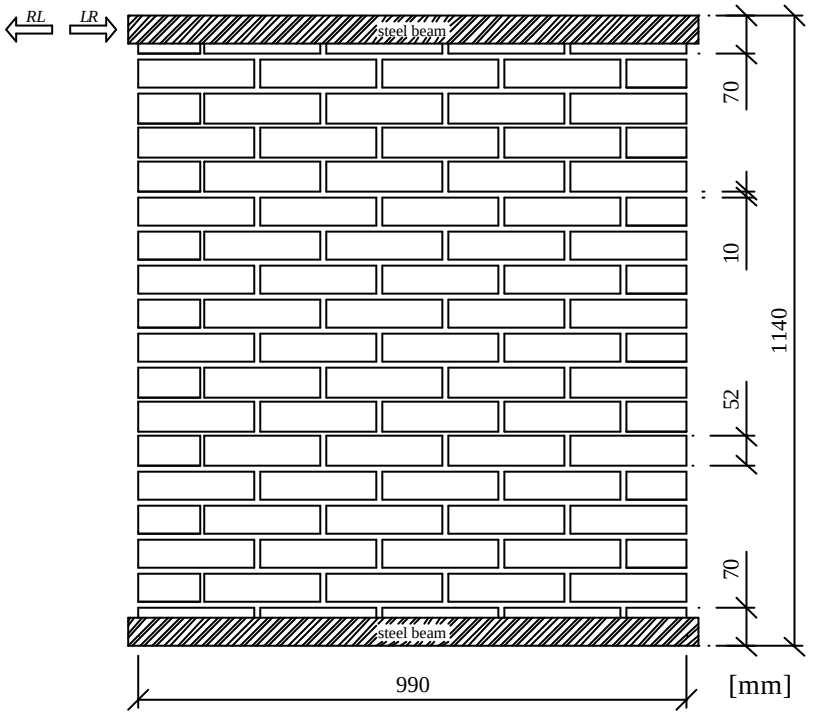

Figure 6.4 – Geometry of the tested masonry shear walls.

During testing, different vertical uniform loads were initially applied to the walls. Afterwards, for each level of vertical load, a horizontal displacement was imposed at the top steel beam, keeping the top and bottom steel beams horizontal and preventing any vertical movement of the top steel beam. For the purpose of investigating the cyclic behaviour, a wall without any opening and submitted to a vertical uniform load of 121.2 N/mm is considered here, which corresponds to an average compressive stress value of 1.21 N/mm^2. In what follows, the wall to be tested is denoted as TUE wall.

6.2.2 Numerical modelling

In the developed finite element model, units were modelled considering eight-node plane stress elements while mortar joints are represented by six-node zero-thickness line interface elements, as illustrated in Figure 6.5. Potential vertical cracks in the middle of the units are not included here since their consideration usually leads to sudden load falls in the load–displacement diagram, which is associated with numerical cracking in the middle of the unit. As a result, their inclusion generally affects the robustness of the numerical model.

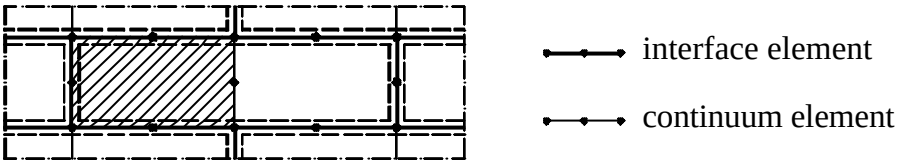

Figure 6.5 – Finite element model of the TUE wall: six-node zero-thickness line interface elements and eight-node continuum plane stress elements.

The model parameters necessary for modelling are adopted from Lourenço (1996), where this wall has been numerically tested under monotonic loading. Table 6.4 and Table 6.5 summarize the elastic and inelastic parameters necessary for a complete monotonic study.

Table 6.4 – Elastic properties for the units and joints (TUE wall).

Unit		Joint	
E [N/mm^2]	n [-]	k_n [N/mm^3]	k_s [N/mm^3]
16700	0.15	110	50

Table 6.5 – “Monotonic” inelastic properties for the joints (TUE wall).

Tension		Shear				Compression	
f_t [N/mm^2]	G_f^I [Nmm/mm^2]	c [N/mm^2]	tanϕ	tanψ	G_f^{II} [Nmm/mm^2]	f_c [N/mm^2]	G_f^{III} [Nmm/mm^2]
0.16	0.012	0.224	0.75	0.0	0.050	11.5	13.7

With respect to the parameters that control cyclic behaviour, since no experimental data concerning cyclic behaviour is available, an accurate definition of these parameters was not possible and, therefore, it was decided to base the choice of these parameters on the values introduced in Chapter 5. The adopted values are shown in Table 6.6.

Table 6.6 – "Cyclic" inelastic properties for the joints (TUE wall).

Tension	Tension - compression		Compression
$\frac{k_1}{k_t}$	$\frac{k_1}{k_c}$	$\frac{k_2}{k_c}$	$\frac{\Delta k_c}{k_c}$
0.60	0.75	0.50	0.0

The parameter C_{ss} that controls the contribution of the shear stress to compressive failure was set equal to zero. The reason of this choice is directly related to the intended robustness of the numerical model. It was verified that this assumption increases the robustness of the constitutive model, specially under load reversal and, at the same time, it is not expected to influence noticeably the accuracy of the structural response for lower compressive stress states, since only few material points are expected to have their stress state affected.

Monotonic behaviour

The finite element model of the TUE wall is submitted to increasing imposed displacements at the top steel beam, both in the left-right (*LR*) direction and in the right-left (*RL*) direction. The monotonic behaviour of the TUE wall is presented in Figure 6.6 (*LR* direction) and Figure 6.7 (*RL* direction), in terms of horizontal load-displacement diagram and deformed pattern. It was decided to stop numerical analyses after reaching peak load since the main goal is to investigate specific issues related to cyclic behaviour.

As it can be inferred from the analysis of Figure 6.6 and Figure 6.7, for displacements greater than 2 mm the horizontal load-displacement response is highly depending on the horizontal loading direction, although deformed patterns are rather resembling in qualitative terms. The geometrically asymmetric wall is due to the fact that the first course does not contain an integer number of bricks (it starts with a entire brick and finishes with a half brick) together with an even number of courses. As expected, the lower load capacity occurs when the top and bottom halves bricks are in compression (loading in the *RL* direction). Taking this issue into account, it

is likely that the wall exhibits asymmetry when loaded in a cyclic fashion, and that the cyclic behaviour deviates from the monotonic behaviour.

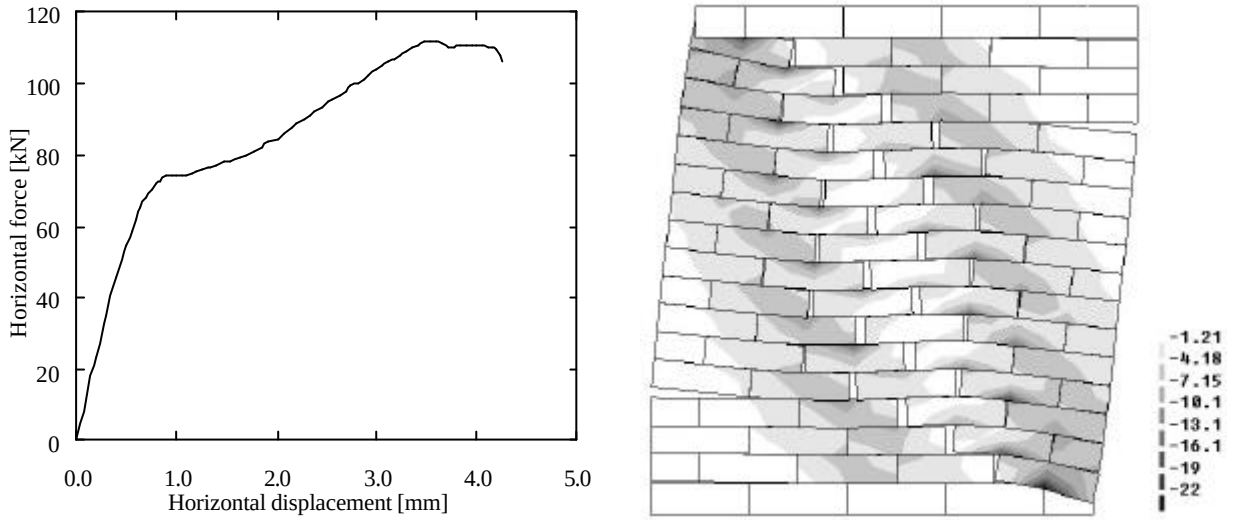

(a) (b)

Figure 6.6 – TUE wall: (a) monotonic horizontal load-displacement diagram (*LR* direction); (b) principal compressive stresses [N/mm^2] depicted on the incremental deformed mesh at the end of analysis.

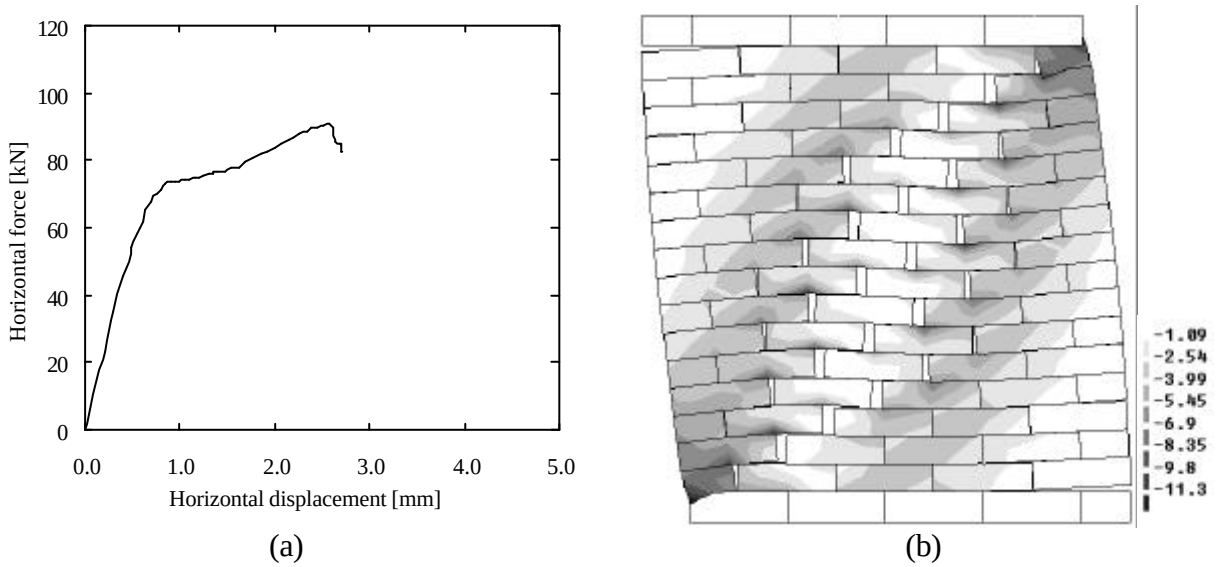

(a) (b)

Figure 6.7 – TUE wall: (a) monotonic horizontal load-displacement diagram (*RL* direction); (b) principal compressive stresses [N/mm^2] depicted on the incremental deformed mesh at the end of analysis.

Figure 6.6(b) and Figure 6.7(b) show clearly that, independently of the loading direction, failure is originated by the progress of diagonal stepped cracks. If cracking of the units had been

allowed, diagonal cracking would have been more concentrated (Lourenço, 1996). It is perceptible that the development of diagonal cracks leads to the formation of two distinct struts, one at each side of the diagonal line while minor internal forces between the two sides of the diagonal are transmitted by shearing of the bed joints. At the supports, the high compressive stress leads to masonry crushing.

Cyclic behaviour: Analysis I

In order to investigate the cyclic behaviour of the TUE wall, it was decided to submitted initially the structure to a set of loading–unloading cycles by imposing increasing horizontal displacements at the top steel beam, where unloading is performed at +1.0 mm, +2.0 mm, +3.0 mm and +4.0 mm, until a zero horizontal force value is achieved. The global horizontal load-displacement diagram, obtained following the described procedure, is shown in Figure 6.8, where the evolution of the total energy is also given.

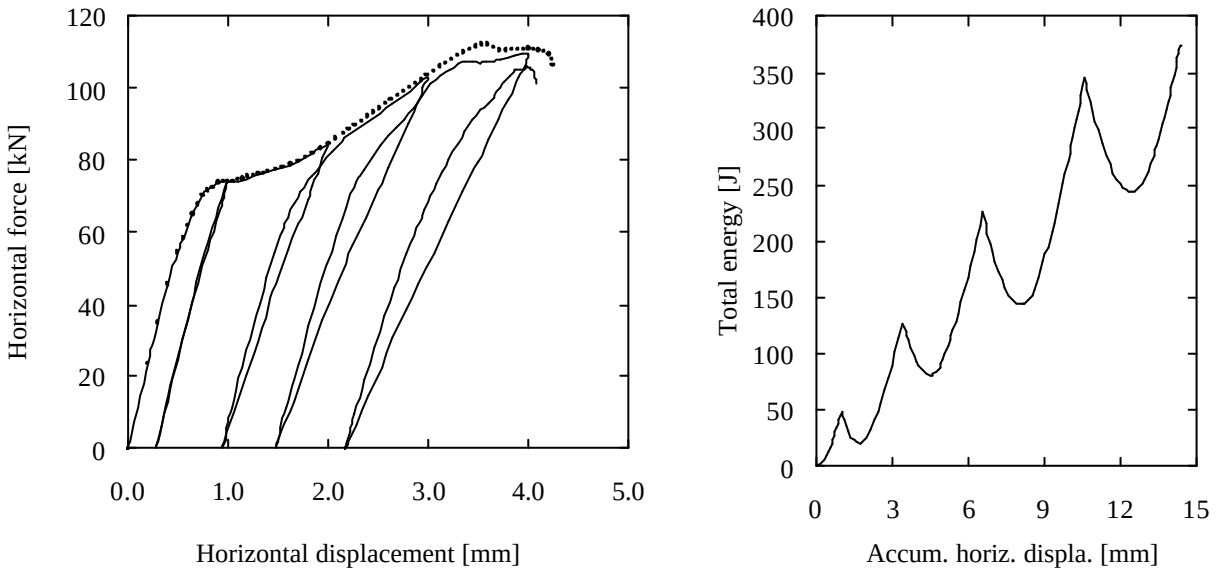

Figure 6.8 – TUE wall (analysis I): cyclic horizontal load-displacement diagram (*LR* direction), where the dotted line represents the monotonic curve; (b) total energy evolution.

Figure 6.8(a) shows that the cyclic horizontal load–displacement diagram follows closely the monotonic one aside from the final branch, where failure occurs for a smaller horizontal displacement. Unloading is performed in a quite linear fashion, while reloading presents initially high stiffness (but lower than the elastic stiffness), due to closure of diagonal cracks, with

combined mode I and mode II behaviour, and then is followed by a progressive decrease of stiffness (reopening). From Figure 6.8(a) it is also possible to notice important stiffness degradation between cycles. Since unloading is almost linear, a comparison between the elastic stiffness and the values measured in the unloading branches is rather straightforward. Table 6.7 presents the ratios between the stiffness of the unloading branches (ub), measured by means of linear least square regressions, and the elastic stiffness. Stiffness degradation increases with the imposed lateral displacements and at +4.0 mm is about half of the elastic value.

Table 6.7 – Stiffness ratio of the unloading branches.

E/E_0			
ub1	ub2	ub3	ub4
0.87	0.67	0.57	0.51

The sequence of the unloading–reloading cycles originates a structural response characterized by a light strength degradation (around 4%) as well as noticeable stiffness degradation, see Figure 6.8(a). From the same figure it can also be observed that the energy dissipated in an unloading–reloading cycle is increased from cycle to cycle, see also Figure 6.8(b). This seems to indicate that masonry shear walls with diagonal zigzag cracks possess an appropriate seismic behaviour with respect to energy dissipation. Phenomenological correct, these features are essentially dependent on the chosen shape of the hardening laws, defined in Chapter 5, and secondarily on the model parameters, defined in Table 6.6. Figure 6.9 illustrates the incremental deformed meshes with the principal compressive stresses depicted on them, for imposed horizontal displacements in correspondence with Figure 6.8(a). In spite of the cyclic horizontal displacements imposed to the wall, the deformed pattern that eventually characterizes the failure mode is quite similar to the ones found in the monotonic analyses. This fact can be concluded by comparing Figure 6.6(b) and Figure 6.7(b) with Figure 6.9(d). Initially, the structural response is characterized by the formation of a single, large, compressive strut, as evidenced in Figure 6.9(a). During unloading to zero force, cracked head joints are partially closed and bed joints slide in the opposite direction. As happened in both monotonic analyses described before, the evolution of the diagonal cracks clearly lead to the development of two struts, one at each side of the diagonal line. The softening behaviour that appears after peak load is caused by compressive crushing of the lower toe of the wall, which eventually leads to failure.

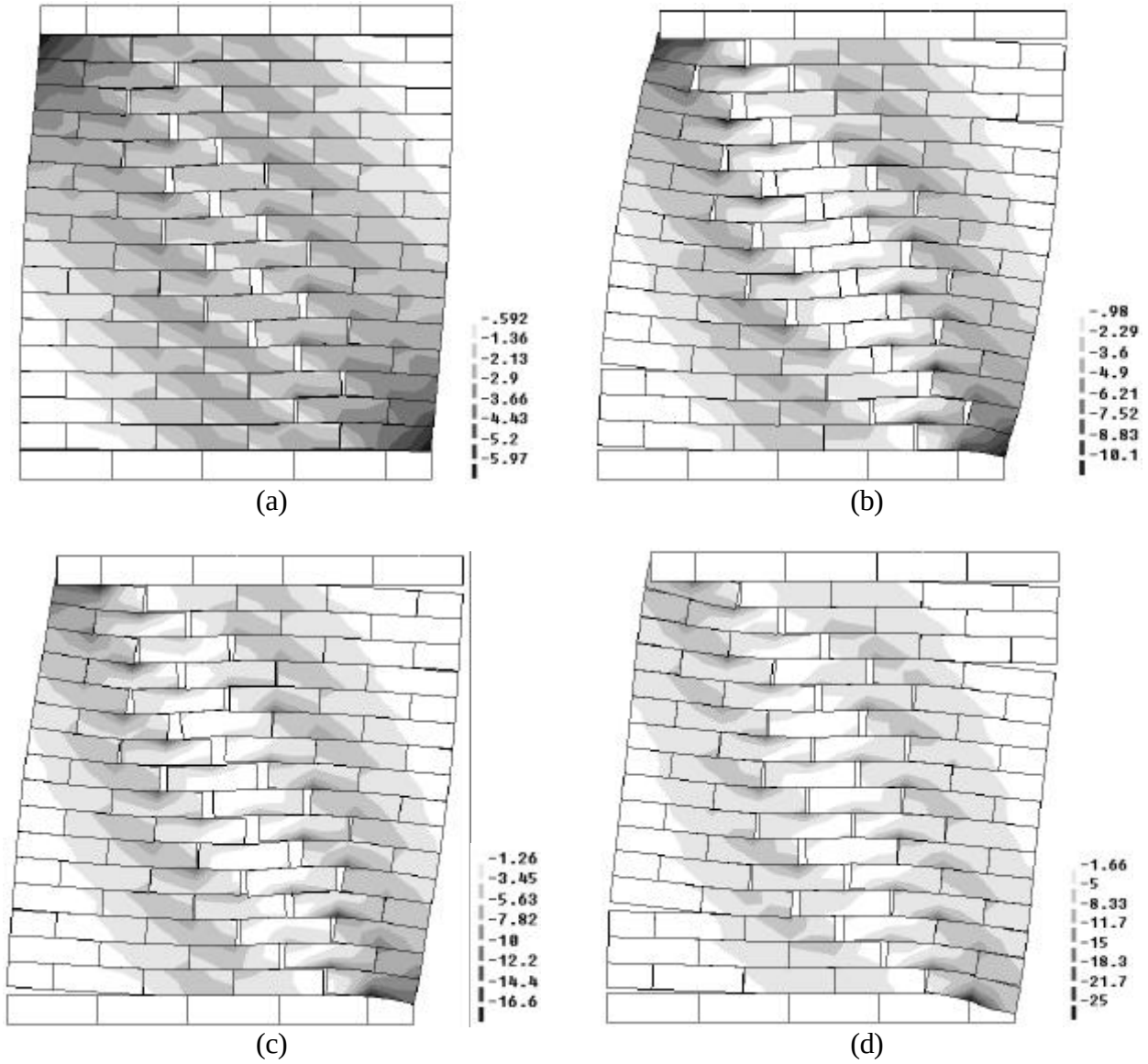

Figure 6.9 – TUE wall (analysis I): Principal compressive stresses [N/mm^2] depicted on the incremental deformed mesh for a horizontal displacement equal to [mm]: (a) +1.0; (b) +2.0; (c) +3.0; (d) +4.0.

Cyclic behaviour: Analysis II

The behaviour of the same TUE submitted to an increasing cyclic displacement-controlled test including total load reversal is now analyzed. Subsequently to the application of the vertical uniform load of 121.2 N/mm (average compressive stress value of 1.21 N/mm^2), as done before, the displacement law illustrated in Figure 6.10 is imposed at the top steel beam. Taking into account the monotonic structural response illustrated in Figure 6.7, it is expect that failure occurs before the end of the imposition of the displacement law.

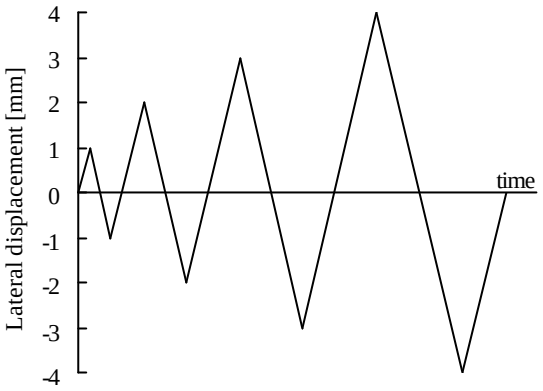

Figure 6.10 – Imposed lateral displacements to TUE wall (analysis II).

The numerical results, in terms of horizontal load-displacement diagram and total energy, are represented in Figure 6.11. From the figure it can observed that, aside from the descending branch leading to failure, the structure shows a relatively symmetric behaviour, in terms of the load-displacement curve, in spite of the geometric unit asymmetry.

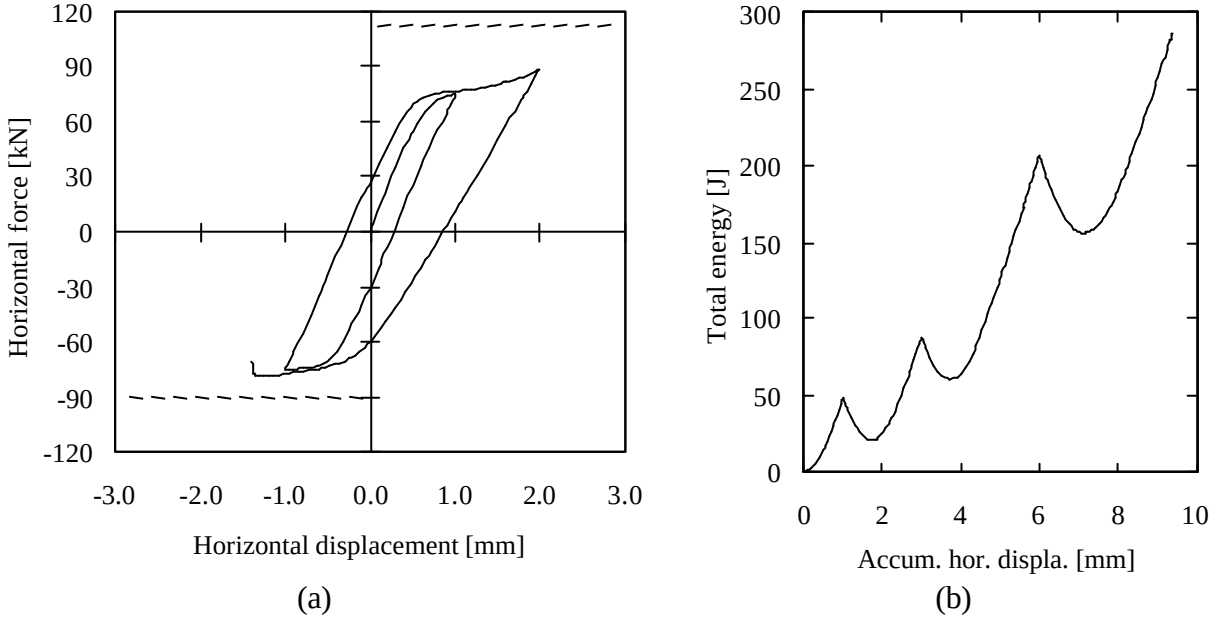

Figure 6.11 – TUE wall (analysis II): cyclic horizontal load-displacement diagram (the dashed lines represent the maximum monotonic loads); (b) total energy evolution.

The observation of symmetric response is further supported by the information displayed in Table 6.8, where horizontal loads and stiffness ratios of the load reversal points are given. As observed in *Analysis I,* unloading/reloading branches are linear in a great extension.

Table 6.8 – Characterization of the load reversal points in terms of horizontal load and unloading stiffness ratio.

Displacement [mm]	Horizontal load [kN]	Unloading stiffness ratio
+1.0	74.1	0.88
-1.0	75.3	0.89
+2.0	88.5	0.66
-1.3	78.7	—

The similarity of the structural response in both directions is due to the fact that displacements corresponding to the beginning of unloading are smaller than 2 mm, that corresponds to the limit from which the monotonic diagrams start to show clear differences between themselves. It is also stressed that the asymmetry is only in the micro-structure (units) and not in the macro-structure (wall). However, the geometric asymmetry of the wall is most likely the main cause leading to failure in the *RL* direction. Moreover, if the imposed displacement had initially been applied in the *RL* direction, probably the wall would have failed in the *RL* direction, as in this example, due to the geometric asymmetry.

Both maximum horizontal loads obtained in this analysis, either in the *LR* direction (88,5 kN) or in the *RL* direction (78,7 kN), are lower than the maximum values achieved in the monotonic analyses (112.0 kN in the *LR* direction and 90.8 kN in the *RL* direction). With reference to the *LR* direction, if the wall had not collapsed during the last *RL* movement, possibly a horizontal load higher than 88.5 kN would have been attained in the following *LR* movement (+3.0 mm). However, a maximum cyclic horizontal load, obtained during the last *RL* movement, lower than the maximum monotonic horizontal load (*RL* direction), reflects an important loss of strength (≈13%), which may be related with the diagonal cracking.

Figure 6.12 shows the incremental deformed meshes together with the principal compressive stresses, for values of the horizontal displacement corresponding to the initiation of the unloading branches. Initial visible damage appears in the middle of the wall and is characterized by the formation of cracks, both in head joints and in bed joints. When a load reversal is initiated, a closure of the cracked head joints is observed and new head joints start to crack or to reopen. The typical deformed pattern, characterized by the development of two major

compressive struts and already discussed at the time when monotonic results were presented, is once more found for cyclic loading, characterizing the structural response in both directions.

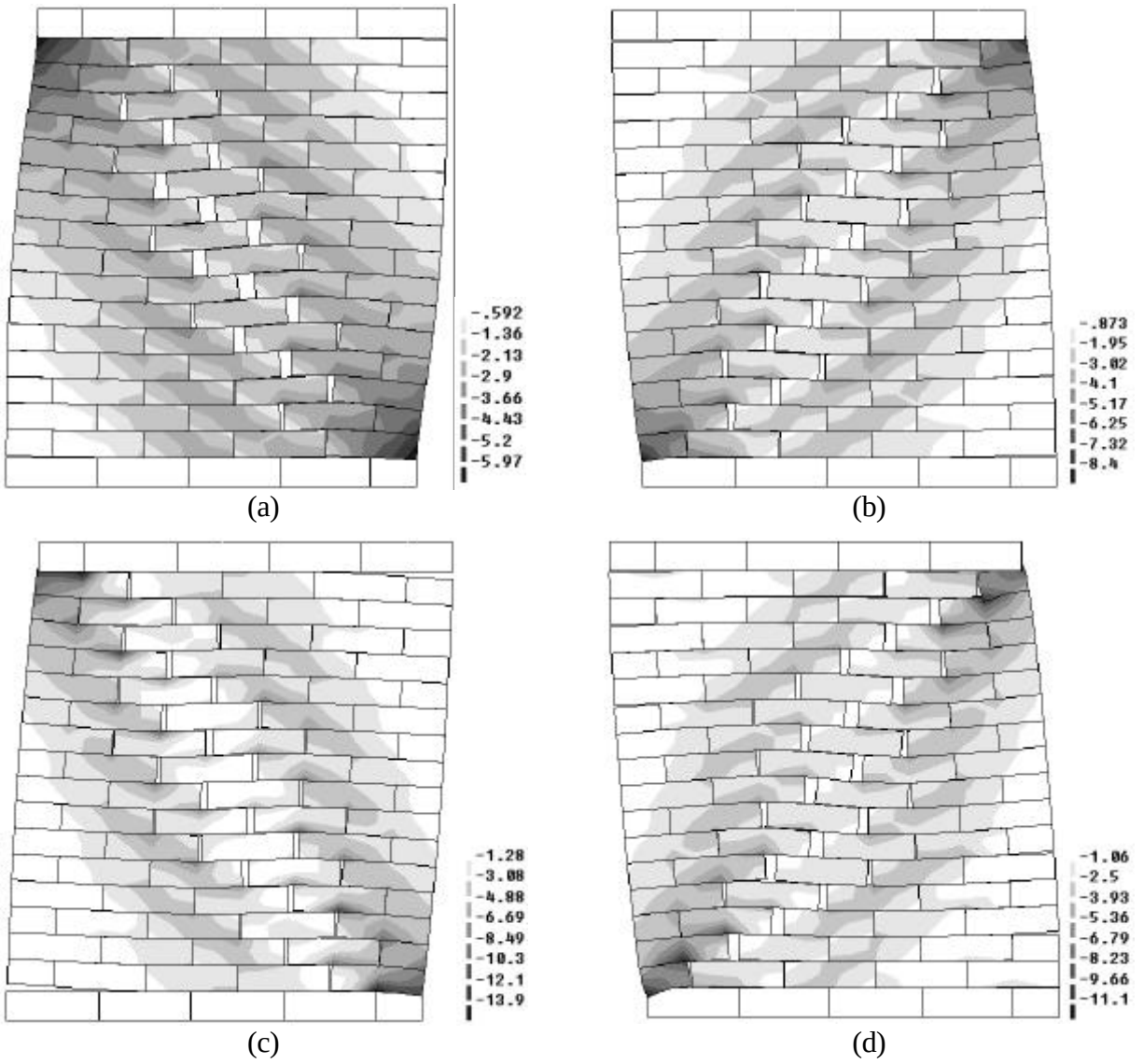

Figure 6.12 – TUE wall (analysis II): Principal compressive stresses [N/mm^2] depicted on the incremental deformed mesh for a horizontal displacement equal to [mm]: (a) +1.0; (b) –1.0; (c) +2.0; (d) -1.4 (failure initiation).

The present numerical analysis was stopped when softening behaviour was clearly detected. In spite of that, the analysis could have been continued under load control and using the arc-length method, an advanced solution procedure mentioned in Chapter 5, which exerts an indirect displacement control over the most active interface elements, that is to say interface elements submitted to the higher compressive stresses.

6.3 JRC masonry shear walls

The need for a realistic assessment of the seismic vulnerability of existing masonry buildings has led the National Research Council of Italy (CNR) to develop a comprehensive research program concerning old masonry structures. The large number of constructions built before the existence of appropriate seismic codes associated with the lack of knowledge about the material properties can be seen as the main reasons for this need, see Calvi *et al.* (1992). Generally, these (three-dimensional) structures are subject to complex loading conditions. However, the modelling of single components is preferred to understand the fundamental mechanics involved. Actually, a good understanding of how old masonry structures behave is a key aspect if structural interventions are intended to be designed or if a safety assessment is sought. Since masonry shear walls are the main reaction systems in most old masonry buildings, their study as structural components of more complex structures assumes a great importance to understand the behaviour of masonry structures.

6.3.1 Experimental set-up

Two types of masonry walls were chosen for being representative of the building prototype tested at Pavia University (Calvi *et al.*, 1992) within the framework of the research program promoted by CNR. The two walls were made of 250×120×55 mm^3 brick units and hydraulic lime mortar (the same materials as those used to construct the building prototype) arranged in two-wythes thickness English bond pattern with the same width of 1000 mm, the same thickness of 250 mm, the same joint thickness of 10 mm, but different heights, see Figure 6.13. The higher wall (HW) presented a height/width ratio of 2.0 whereas the lower wall (LW) presented a ratio of 1.35. The tests were performed at the Joint Research Centre (JRC), Ispra, Italy (Anthoine *et al.*, 1995). Henceforth, these walls are here referred as the JRC walls.

The experimental results have shown that the different height/width ratio implies quite important changes in the wall's overall behaviour. These changes are most certainly related to the activation of different mechanisms of non-linearity, namely cracking of the joints, frictional sliding along the joints, tensile and shear rupture of the units and compressive failure of masonry.

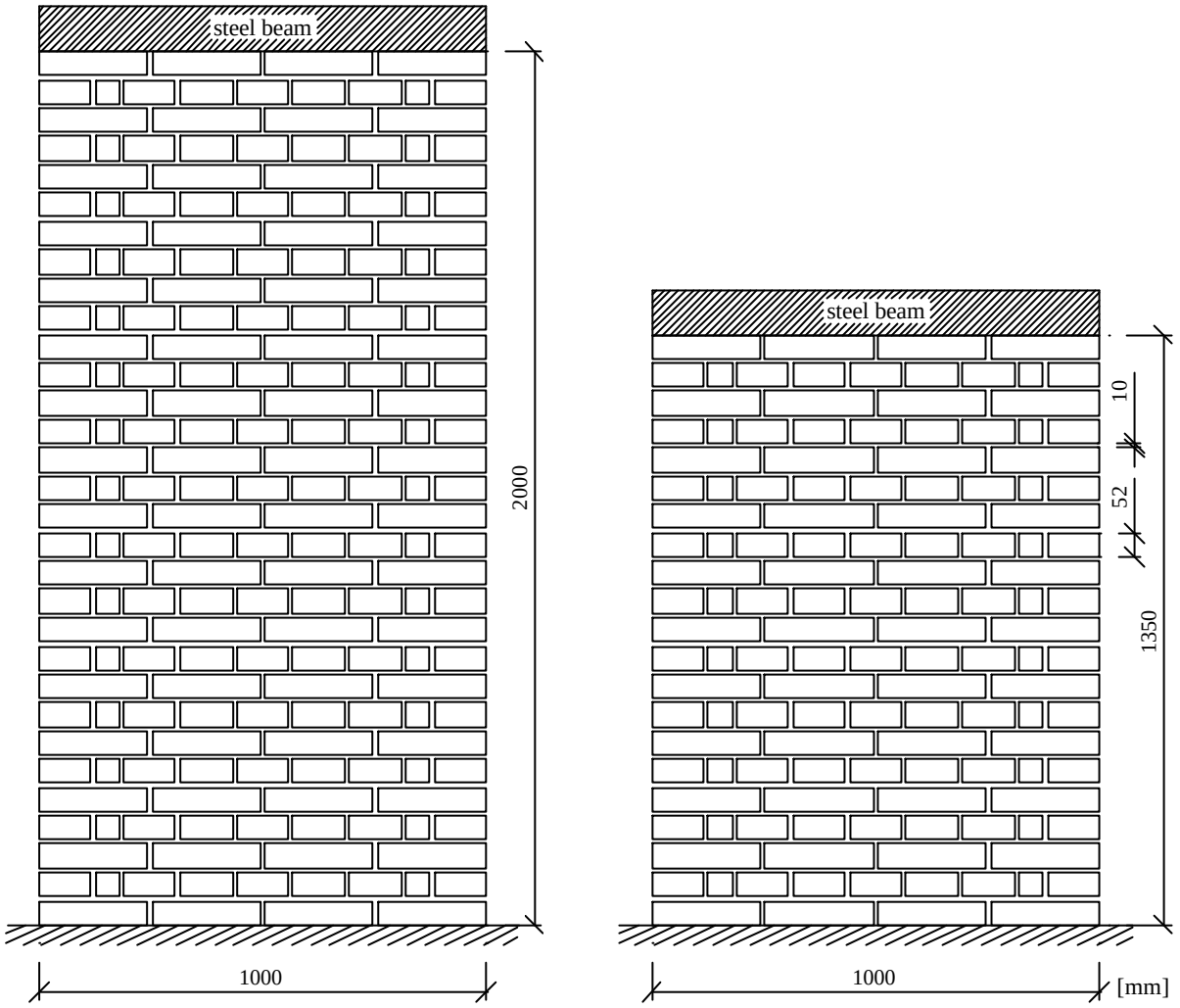

Figure 6.13 – Unreinforced masonry shear walls: (a) high wall (HW); (b) low wall (LW).

Load and boundary conditions were chosen in order to reproduce as well as possible the real conditions experienced by the walls during a seismic occurrence. In this way, a uniform vertical compressive load was initially applied. Afterwards, a quasi-static cyclic horizontal displacement was imposed to the steel beam, at the top of the wall. The experimental set-up was such that the steel beam was prevented to rotate, so allowing the same vertical and horizontal displacements to all points of the beam (Anthoine *et al.*, 1995). Both JRC walls were initially subject to a uniform vertical load of 150 kN, resulting in an average normal stress of 0.6 N/mm^2. Keeping this vertical load constant, increasing alternated in-plane horizontal displacements were imposed to each wall, which are schematically illustrated in Figure 6.14. In both experiments, two cycles were performed at each amplitude, with the exception of the low wall for which three cycles were done, for a given amplitude.

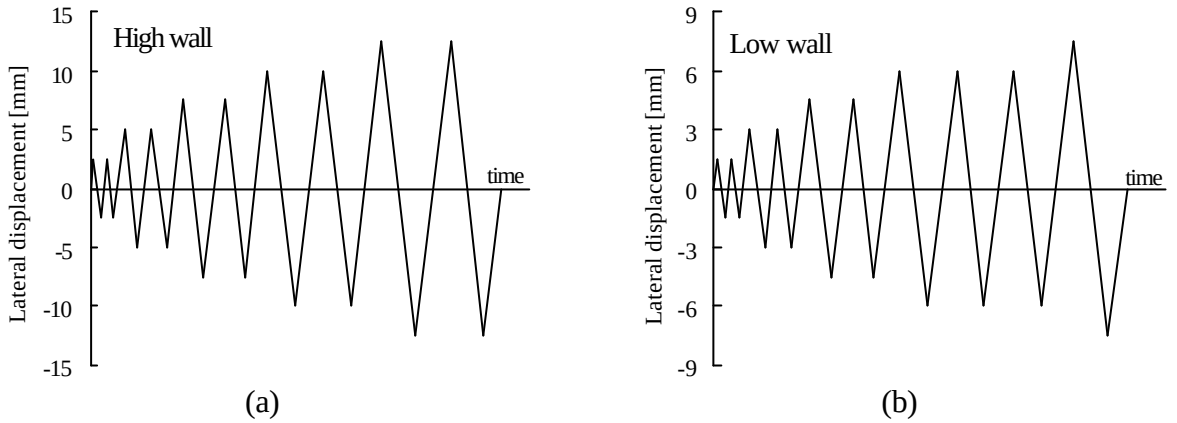

Figure 6.14 – Imposed lateral displacements in experiments: (a) high wall; (b) low wall.

6.3.2 Numerical modelling

In the finite element model developed for the analysis of these masonry walls, units are modelled through eight-node plane stress elements while mortar joints are represented by six-node zero-thickness line interface elements, as illustrated in Figure 6.15. Potential vertical cracks in the units are again not included in the model.

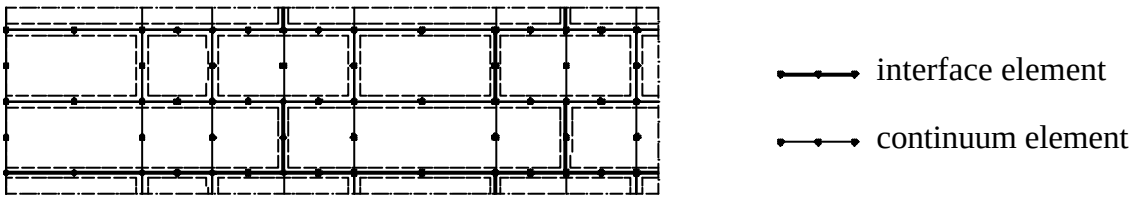

Figure 6.15 – Finite element model: six-node zero-thickness line interface elements and eight-node continuum plane stress elements.

The choice of the appropriate model parameters values necessary to numerical modelling is most of the times a quite difficult task. If, on the one hand, masonry experimental results are characterized by a wide scatter, on the other hand, reliable experimental data suitable for calibrating numerical models is, most of the times, scarce or even inexistent. Along with the construction of the construction of the building prototype and the JRC walls, the research program promoted by CNR included an experimental research to characterize those materials, see reports by Binda *et al.* (1995a, 1995b). As expected, most of the experiments showed a large scatter in the results. Therefore, it was decided that the required model parameters would be based on average experimental values. The adopted elastic and inelastic parameters are defined in Table 6.9, Table 6.10 and Table 6.11. The parameter C_{ss} is assumed to be equal to zero. With

respect to the inelastic parameters which characterize cyclic behaviour, no suitable experimental data was available. Hence, the chosen values are equal to the values used in the analysis of the TUE wall. Such scattering in the results would probably allow a close fitting of the experimental results in terms of the global load-displacement diagram. However, such attempt will not be followed here.

Table 6.9 – Elastic properties for the units and joints (JRC walls).

Unit		Joint	
E [N/mm^2]	n [-]	k_n [N/mm^3]	k_s [N/mm^3]
2500	0.15	48	21

Table 6.10 – "Monotonic" inelastic properties for the joints (JRC walls).

Tension		Shear				Compression	
f_t [N/mm^2]	G_f^I [Nmm/mm^2]	c [N/mm^2]	tanϕ	tanψ	G_f^{II} [Nmm/mm^2]	f_c [N/mm^2]	G_f^{III} [Nmm/mm^2]
0.15	0.020	0.35	0.60	0.0	0.050	5.0	5.0

Table 6.11 – "Cyclic" inelastic properties for the joints (JRC walls)

Tension	Tension - compression		Compression
$\frac{k_1}{k_t}$	$\frac{k_1}{k_c}$	$\frac{k_2}{k_c}$	$\frac{\Delta k_c}{k_c}$
0.60	0.75	0.50	0.10

High wall (HW)

In order to get an idea about the overall structural behaviour, a monotonic analysis is initially carried out. The results are shown in Figure 6.16, in terms of horizontal load-displacement diagram and incremental deformed mesh, together with the contour of the principal compressive stresses. The structural behaviour is mainly characterized by the opening of the top and bottom bed joints, in close resemblance with a rigid body movement.

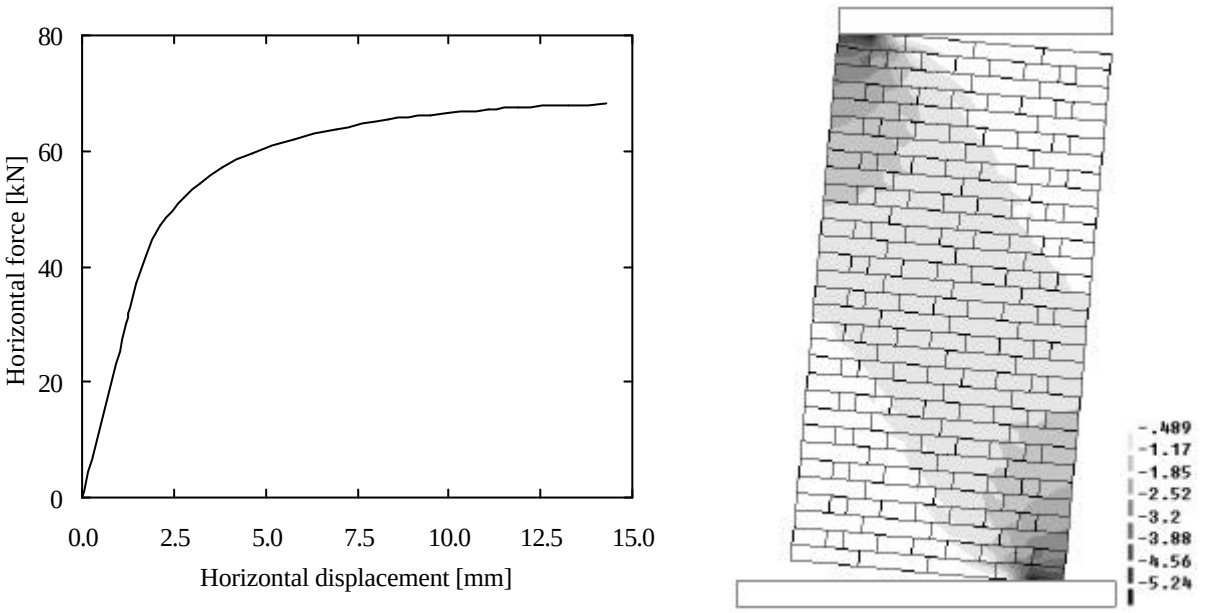

(a) (b)

Figure 6.16 – HW: (a) monotonic horizontal load-displacement diagram; (b) principal compressive stresses [N/mm^2] depicted on the incremental deformed mesh.

After the monotonic analysis, a cyclic analysis is performed. Alternated lateral displacements, in accordance with Figure 6.14(a), are imposed at the level of the top steel beam. The cycle of ±12.5 mm is only performed once, since the response mechanism is well identified and failure is not expected to occur on that cycle. Figure 6.17 presents the numerical results in terms of horizontal load-displacement diagram and total energy evolution of the system. The experimental results are illustrated in Figure 6.18, in terms of the same quantities, so that a comparison can be easily done (see also Anthoine *et al.*, 1995). Moreover, for a better understanding of the cyclic behaviour, Figure 6.19 represents the principal compressive stresses represented on the incremental deformed meshes, for lateral displacements of ±2.5 mm, ±7.5 mm and ±12.5 mm.

The numerical response indicates clearly that the high wall submitted to alternate horizontal displacements simply rocks in both ways. The highly non-linear shape of the load–displacement curve is essentially due to the opening and subsequent closure, under load reversal, of the top and bottom bed joints, which is evidenced by Figure 6.19. Similar deformed patterns, involving the opening of extreme bed joints, were observed during the experimental test (Anthoine *et al.*, 1995).

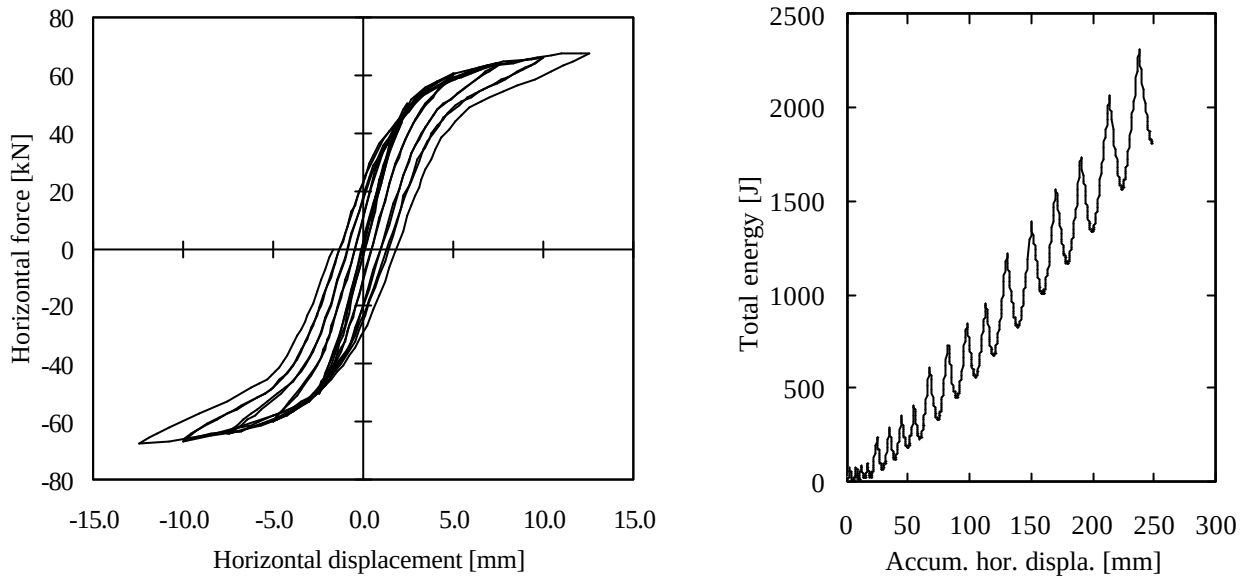

(a) (b)

Figure 6.17 – High wall: cyclic numerical results in terms of (a) horizontal load-displacement diagram and (b) total energy evolution.

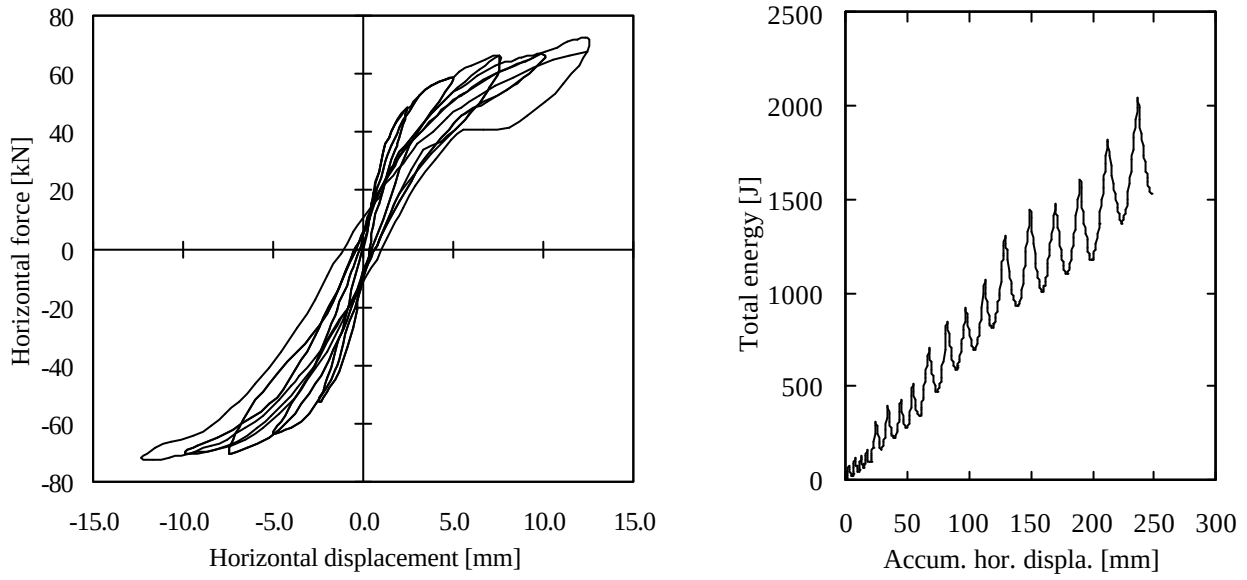

(a) (b)

Figure 6.18 – High wall: cyclic experimental results in terms of (a) horizontal load-displacement diagram and (b) total energy evolution (Anthoine *et al.*, 1995).

Numerical results show that the cyclic behaviour of the wall is essentially controlled by the opening and closure of the extreme bed joints, where damage is mainly concentrated. The model also shows low energy dissipation, which is a consequence of the non-linear mechanism activated (opening-closure of bed joints).

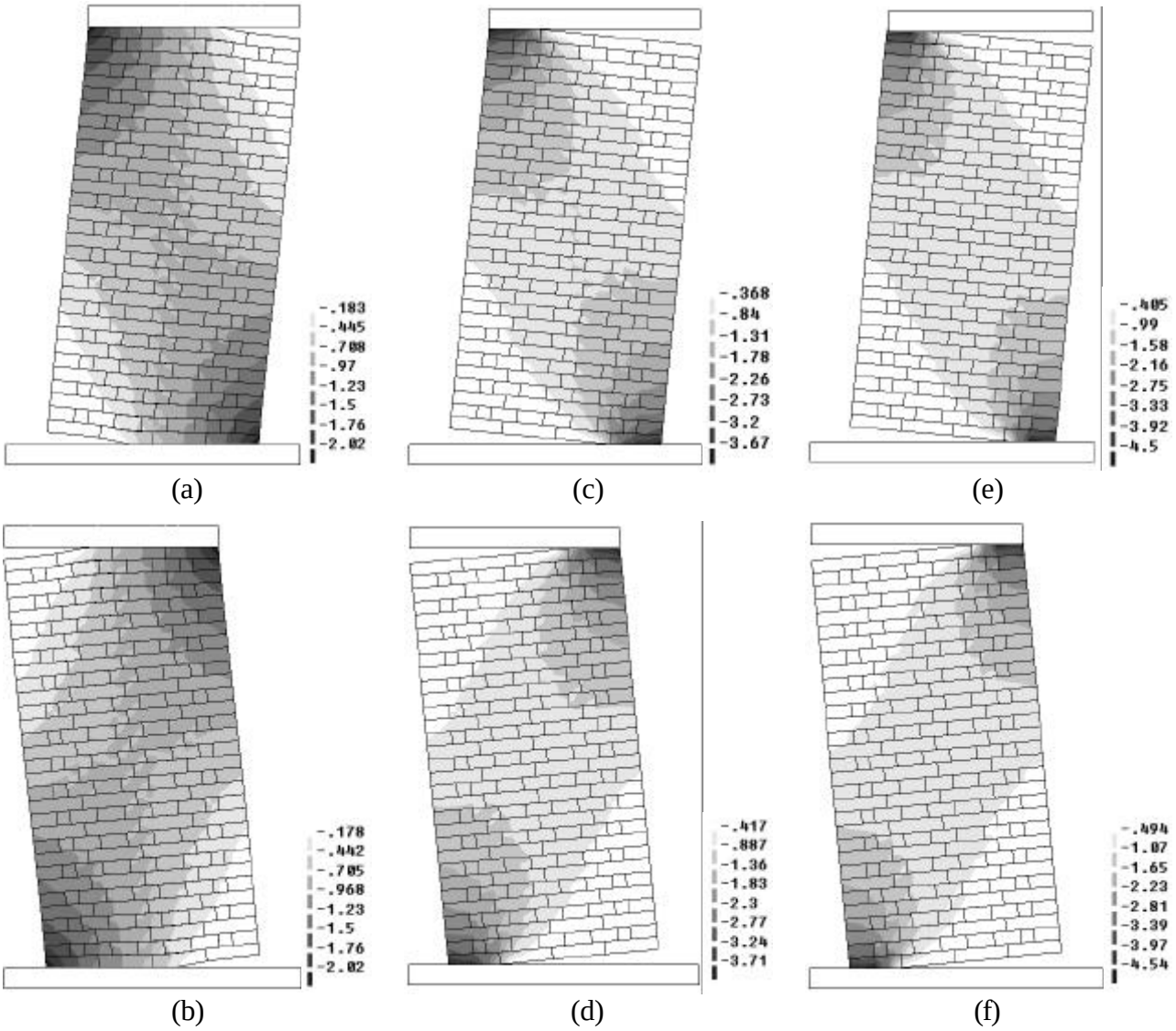

Figure 6.19 – High wall: Principal compressive stresses [N/mm^2] depicted on the incremental deformed mesh for a horizontal displacement equal to [mm]: (a) +2.5; (b) –2.5; (c) +7.5; (d) –7.5; (e) +12.5; (f) –12.5.

It was observed that at the end of the numerical test, the masonry wall seemed to be in good condition. It is believe that even if the second cycle of ±12.5 mm had been imposed, failure of the wall would have not been achieved. This fact is in accordance with the experiment. Actually, the wall was not destroyed at the end of the experimental test, which allowed it to be tested once more, this time applying a larger vertical load.

The analysis of Figure 6.17, Figure 6.18 and Figure 6.19 shows that the constitutive model is able to reproduce with accuracy the experimental cyclic response of the high wall, both in terms of maximum load (F_{exp} = 72 kN and F_{num} = 67.6 kN), global load-displacement diagram,

hystereses cycles and total energy evolution and in terms of deformed mesh, which allows to conclude that good agreement is found between the numerical and experimental results.

Low wall (LW)

In what follows, the structural response of the low wall is analyzed. For that, the same finite element model as well as the same model parameters are used in this analysis. A previous monotonic analysis is performed in order to outline the wall's behaviour. The results are shown in Figure 6.20, in terms of horizontal load-displacement diagram and incremental deformed mesh, together with the contour of the principal compressive stresses, after peak load has been reached.

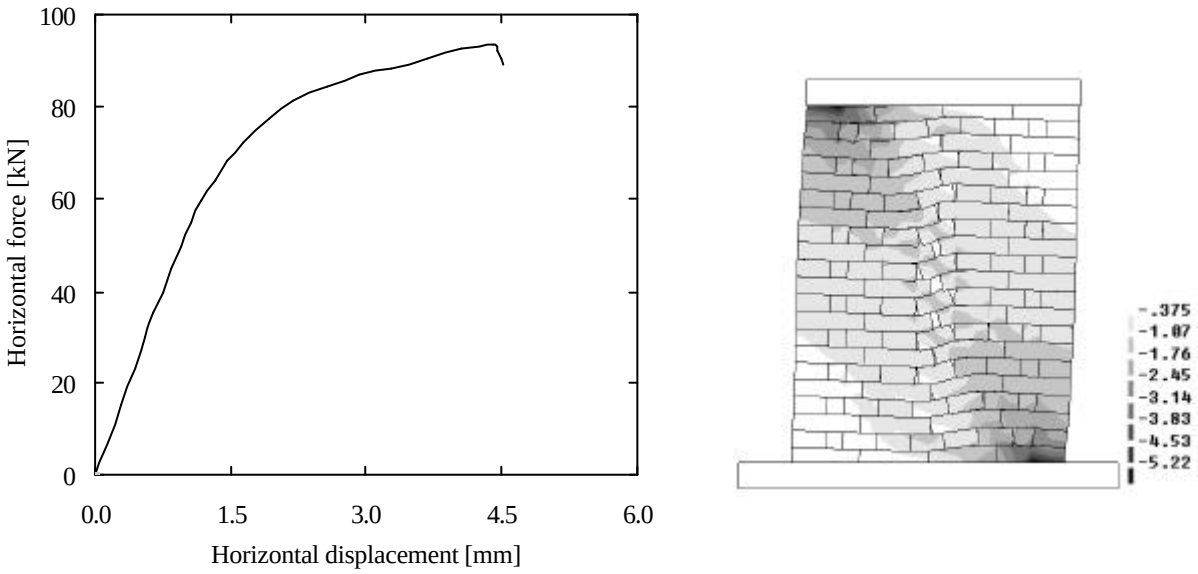

(a) (b)

Figure 6.20 – Low wall: (a) monotonic horizontal load-displacement diagram; (b) principal compressive stresses [N/mm^2] depicted on the incremental deformed mesh.

The numerical results show that the maximum horizontal load is overestimated (the experimental results are shown in Figure 6.24), in spite of the incremental deformed mesh being in accordance with the experimental crack pattern and failure mode. These preliminary results indicate that the walls behave in a distinct manner, due to a different height/width ratio, for which different inelastic mechanisms are activated. In the low wall, failure is initiated at the central part of the wall, where vertical cracks along head joints are clearly noticeable. These differences in the structural behaviour were observed in the experiments (Anthoine *et al.*, 1995).

Afterwards, the displacement law illustrated in Figure 6.14(b) is imposed to the low wall, in order to characterize its cyclic response. The numerical results are shown in Figure 6.21. It was observed that, for a displacement close to +4.1 mm, the steel beam started to slide along the top tier of bricks. Since this mechanism has not been observed in the experiment, it was decided to stop the analysis.

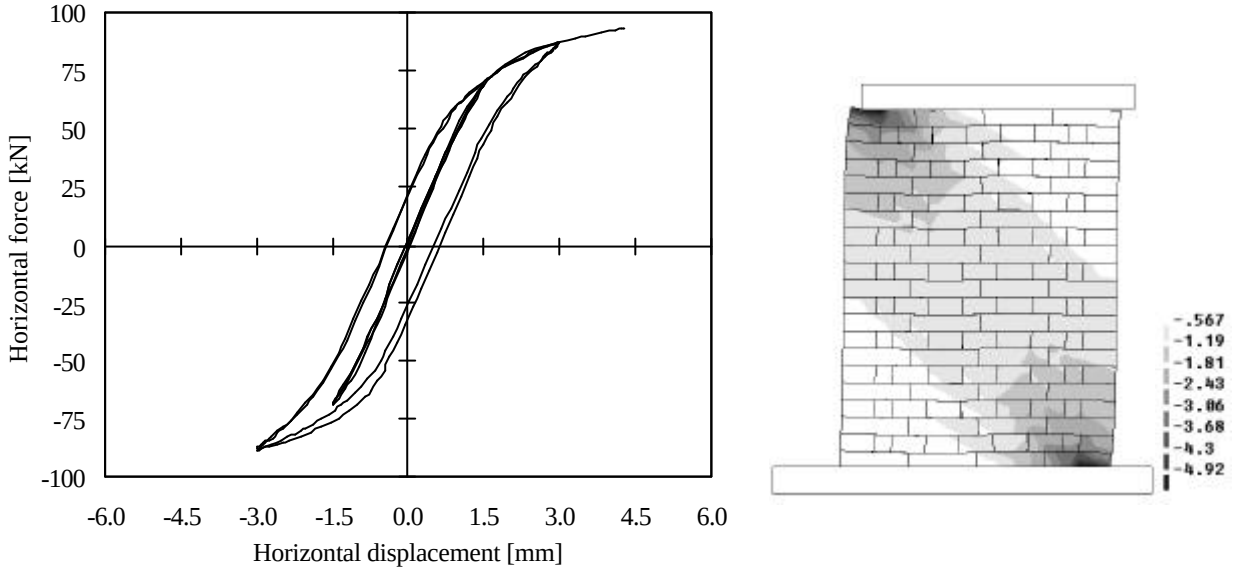

(a) (b)

Figure 6.21 – Low wall: (a) cyclic horizontal load-displacement diagram; (b) principal compressive stresses [N/mm^2] depicted on the incremental deformed mesh, for a displacement equal to +4.1 mm.

The unexpected sliding of the steel beam along the bricks raises two main questions with respect to both walls, but particularly to the low wall:

- Are the boundary conditions experienced by the walls well simulated?
- Are the chosen model parameters values the most adequate?

In relation to the first question, all the available information related to boundary conditions (Anthoine *et al.*, 1995; Gambarotta and Lagomarsino, 1997a) is rigorously followed and implemented in the present finite element model. If sliding was not prevented to happen in the experiments, then the sliding observed numerically may be related with some inappropriate model parameter value, which lead unavoidably to the second question. The definition of the model parameters values in the context of historic masonry structures is always a complex task, essentially motivated by the lack of appropriate experimental data or, when it is available, by the

important scatter present on it. With respect to this issue, with basis on the wide scatter presented in available experiments, it was decided to adopt average values, as already referred. Possibly, the adoption of other than the average values for the model parameters would lead to a better fitting of the experiments. Since no further information is available and considering that no sliding of the steel beam was detected in experiments, it is decided to perform again the analysis of the low wall, now considering perfect shear bond between the last course of bricks and the steel beam. As usually, the study was started by analyzing the monotonic behaviour of the wall. The structural response is shown in Figure 6.22, in terms of horizontal load-displacement diagram and incremental deformed mesh, with the principal compressive stresses represented on it. The wall's behaviour is quite similar to the one illustrated in Figure 6.20, which means basically that sliding of the steel beam did not occur in the first run under monotonic loading, being due to cyclic loading. On the other hand, it is believed that the overestimation of the peak load can be surpassed if a lower value of the compressive strength is adopted. But this objective is not pursued here.

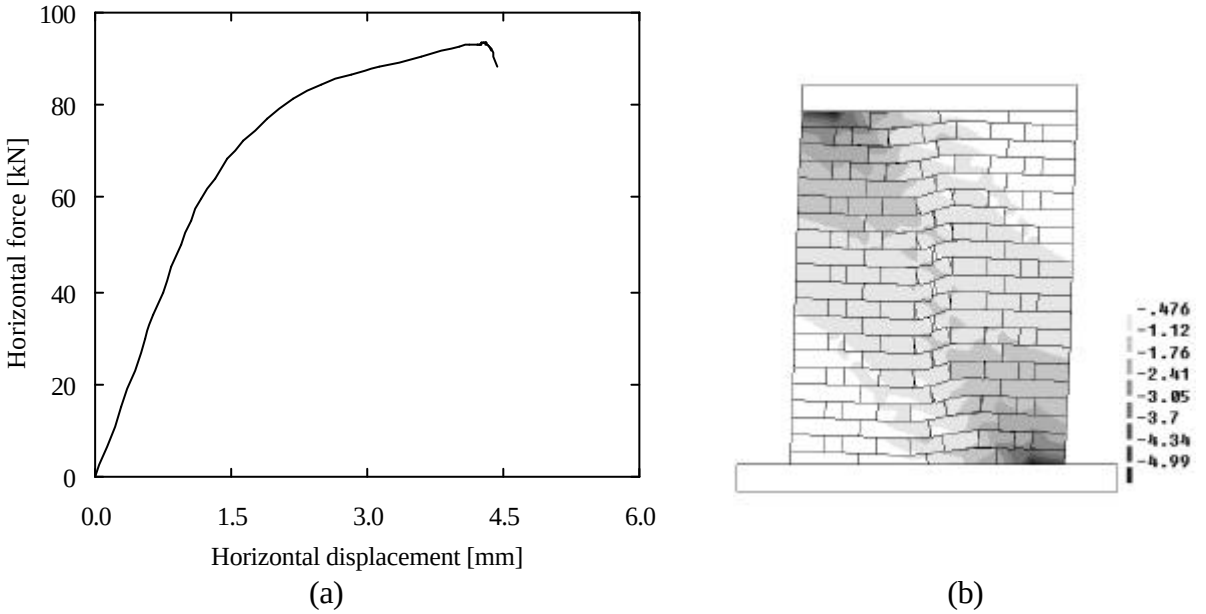

(a) (b)

Figure 6.22 – Low wall: (a) monotonic horizontal load-displacement diagram (run 2); (b) principal compressive stresses [N/mm^2] depicted on the incremental deformed mesh.

The cyclic analysis is done by imposing the prescribing horizontal displacements to the top of the wall, subsequently to the application of the vertical load. Figure 6.23 characterizes the structural response in terms of the cyclic horizontal load-displacement diagram and incremental

deformed mesh with the principal compressive stresses depicted on it, as usual. The experimental results are illustrated in Figure 6.24, in terms of the same quantities.

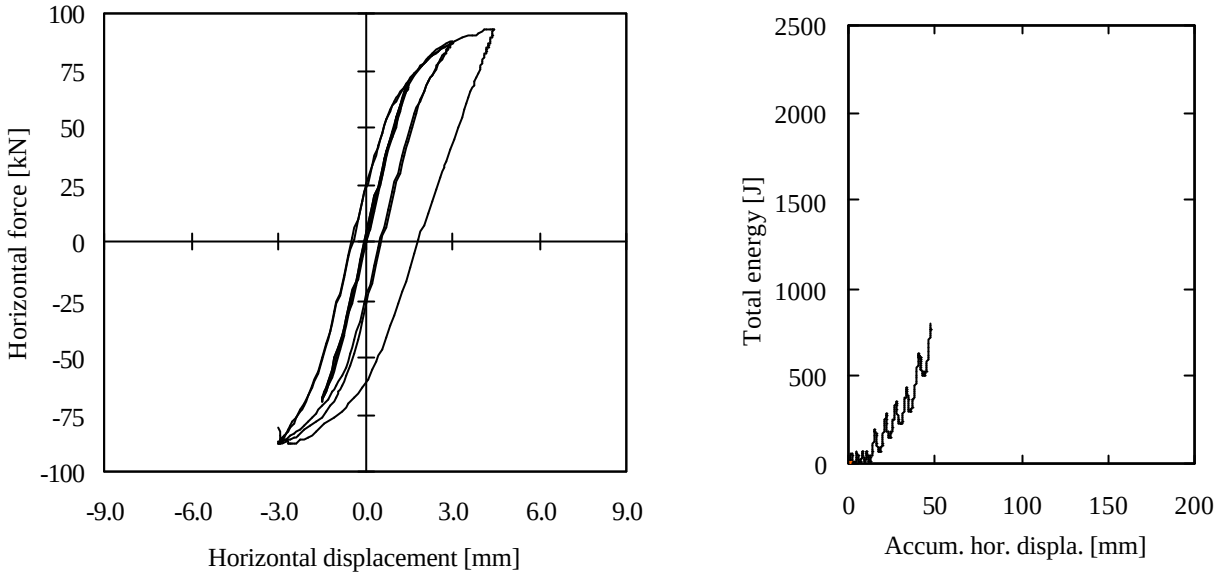

(a) (b)

Figure 6.23 – Low wall: cyclic numerical results in terms of (a) horizontal load-displacement diagram and (b) total energy evolution.

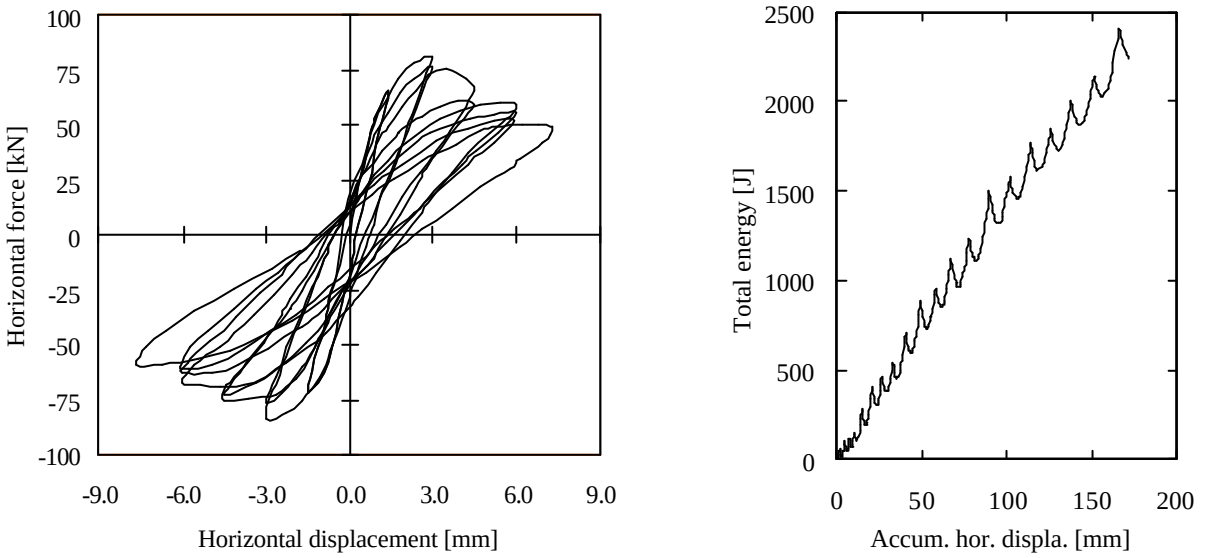

(a) (b)

Figure 6.24 – Low wall: cyclic experimental results in terms of (a) horizontal load-displacement diagram and (b) total energy evolution (Anthoine *et al.*, 1995).

In addition, Figure 6.25 shows the principal compressive stresses represented on the incremental deformed meshes, for lateral displacements of ±1.5 mm, ±3.0 mm, +4.5 mm and –2.9 mm.

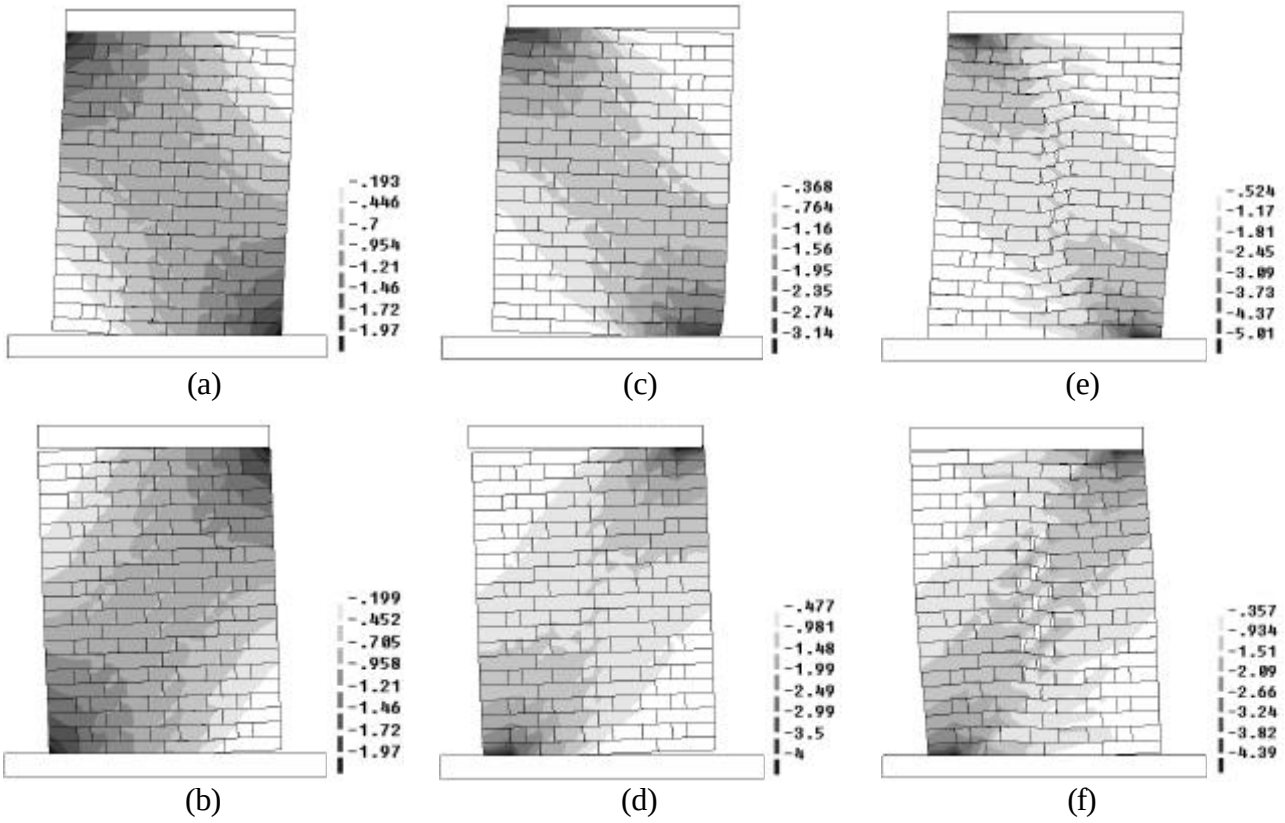

Figure 6.25 – Low wall: Principal compressive stresses [N/mm^2] depicted on the incremental deformed mesh for a horizontal displacement equal to [mm]: (a) +1.5; (b) –1.5; (c) +3.0; (d) –3.0; (e) +4.5; (f) –2.91 (failure initiation).

For the cycles of small amplitude (±1.5 mm and ±3.0 mm) damage is essentially due to the opening–closure at the corners, as it can be confirmed by analyzing the shape of the unloading branches of the load–displacement diagram and the deformed meshes from Figure 6.25. For higher displacements, the deformed pattern is characterized by the development of cracks in the head joints of the central region of the wall. The changing of the main inelastic mechanism is clearly visible from the shape of the unloading branch started at a displacement of +4.5 mm. Unloading and subsequent reloading causes damage in the same area, leading to the formation of a kind of vertical crack, only interrupted by the units, that are not allowed to crack. This kind of alignment of vertical cracks is the main cause leading to failure initiation, see Figure 6.25(f). This type of deformed pattern was also observed in the experiment. In spite of that, only a part of the numerical load-displacement diagram has been obtained, due to failure initiation for a displacement close to –2.91 mm.

It is known that some physical problems are sensitive to small variations in data parameters. This sensibility of the structural response to the input data is certainly increased with non-linear

constitutive models. Therefore, a sensibility analysis should be carried out in order to evaluate the sensibility of the structural response to the variation of most important parameters for this example, as cohesion, compressive strength and compressive facture energy. Also, more information concerning the establishment of the experimental boundary conditions is needed.

Another important feature is related with the representativeness of the experimental result from just one test. Taking into account the large scatter that characterizes masonry in general, at least two experiments of each wall should had been performed. This aspect assumes special relevance because the main objective of the numerical analyses is to capture the most relevant features observed in the experiments and not to fit closely the load-displacement diagram of a given wall.

6.4 Summary

The performance of the developed constitutive model has been investigated against three groups of masonry structures. The numerical results have shown that the model is able to reproduce the main features that characterize cyclic behaviour, where the main inelastic mechanisms as cracking of the joints, frictional sliding along the joints and compressive failure of masonry were involved. During the analysis of the TUE wall, different structural responses were found in opposite directions of horizontal loading. The reasons for such differences are related with the asymmetrical geometry of the masonry shear wall. The cyclic analysis performed on the wall exposed the main structural cyclic characteristics, as stiffness degradation and energy dissipation. With basis on the results, it is recommended that structures intended to be analysed cyclically should possess a symmetrical geometry configuration. Furthermore, the validation of the constitutive model against experimental data has been carried out. The simulation of the UPC prisms has been successfully achieved, where numeric results followed closely the experimental ones. The analysis of the JRC walls has been only partially succeeded. The simulation of the high wall has been totally fulfilled, where the dominant joint opening-closure mode was well captured by the mode. Important differences concerning the structural behaviour, failure mode and dissipated energy were found between the TUE wall and the JRC wall (high wall). Such satisfactory results have not been possible to attain for the low wall. Failure started earlier than in the experiment, although the obtained failure mode was similar to the experimental one.

The large importance of an accurate modelling of the boundary conditions has been emphasized and the difficulty of an appropriate definition of the model parameters has also been shown. This

difficulty arises mainly due to the inexistence of appropriate experimental data. Aside from any other information, a definition based simply on average values has been addressed.

Finally, a more refined finite element mesh (each unit modeled with 4×2 elements instead of 2×1 elements) would most likely increase the insight into the response of the wall specially in the softening regime, since during the possible collapse of a given integration point, less amount of energy would be released and, therefore, a more soft post-peak diagram would be achieved.

7. CONCLUDING REMARKS

The study of historical masonry structures demands a combined experimental and numerical research program in order to obtain an adequate material characterization, which is used both to supply data to numerical models and to validate the respective numerical results. This approach is followed in the present study. An advanced material characterization, based on complex deformation-controlled tests, was carried out and the experimental data obtained in this fashion was used both for the calibration of the constitutive model and for the validation of the numerical simulations. Characteristic features associated with the structural behaviour under cyclic loading were used to develop a cyclic constitutive model, based on a phenomenological approach. The material discontinuity introduced by the existence of the joints makes the use of interface elements within a finite element formulation an appropriate option to model masonry structures, which is followed in this study.

Experimental research

Within an experimental research program undertaken by Universidade do Minho, aiming at the mechanical characterization of historical masonry building materials, experimental deformation-controlled tests were carried out at Universitat Politècnica de Catalunya and at Universidade do Minho, consisting of specimens and assemblages made of stone (sandstone) and bricks, tested under monotonic and cyclic compressive and shear loading. Also dry stone masonry walls were tested under simultaneous compressive and shear loading.

The stone specimens tested under compressive loading were characterized by high peak strength values and by a very pronounced fragile softening behaviour. When measuring the Young's modulus in the specimens, no relevant differences were found between LVDTs measurements and strain gauges measurements. The comparison between the experimental results derived from the stone specimens and from the dry stone assemblages showed that the Young's modulus computed for the stone specimens and for the stone prisms presented very similar average values. On the other hand, a considerable decrease of peak strength occurred when shifting from stone specimens to masonry, in terms of average values. It seemed that both the wide scatter presented by the experimental results concerning stone specimens and the horizontal

discontinuity between the stone pieces is likely to result in stress concentrations in a few contact points, which originated the failure of the stone prisms for lower load values than the stone specimens. The shear stress-relative shear displacement diagrams from the direct shear tests performed on dry stone joints were characterized by a marked elasto-plastic behaviour. During the cyclic loading, neither stiffness degradation nor hardening behaviour between cycles was noticeable.

Also brick specimens, entirely prismatic and made of three aligned cylinders, were tested under compressive loading. Again, the results showed a manifest brittle behaviour. With reference to the Young's modulus and peak strength values, no significant differences were found between the prismatic and cylindrical specimens. In addition, four stacked bond prisms made of five bricks each, were constructed and tested under cyclic loading. The average strength value of the prisms was much higher when compared to single mortar specimens, but less than the average strength of the bricks tested separately.

The brittle behaviour exhibited both by stone and brick specimens, has shown that post-peak regime cannot be captured using an ordinary axial displacement control. A more advanced control technique, such as circumferential control, has to be used. With reference to the stone cylindrical specimens, it was shown that a reduction of the height/diameter ratio, from 2.4 to 2.0, led to a more stable post-peak behaviour. Therefore, based in these results, it is recommended its adoption in future work. However, it is noted that ratios lower than 2.0 might not ensure a uniaxial stress state at the center of the specimen. The experimental results concerning specimens and prisms have shown that the intrinsic variability of the mechanical properties of natural stone and clay brick masonry is a rather significant issue that should be taken into account when dealing with historical building materials.

Seven dry jointed stone masonry walls were built. Combined vertical and horizontal loading was applied for different vertical compressive loads. A variable stiffness of the walls was found. Moreover, it was observed that vertical stiffness increased with the compressive stress, which is a phenomenon that has not been addressed by other authors. Initially, the horizontal load-displacement diagrams of the walls exhibited large stiffness and elastic behaviour was observed almost up to 30% of the peak load. Afterwards, continuous stiffness degradation occurred under increasing horizontal deformation. The second part of the diagrams was characterized by an oscillation of the horizontal load. It was observed that the failure patterns were correlated with the amount of compressive loading. For lower confining stress levels, failure occurred by

rotation and sliding of part of the wall whereas for higher vertical loads cracking was noticeable. A linear relation between average compressive stresses and average ultimate shear stresses seems to be a good approximation to experiments, as it is usually prescribed by the codes of practice. The numerical modelling of the stone walls allowed to follow the load history and to understand the main phenomena related with their structural behaviour. Both collapse loads and evolution of the deformed meshes were in accordance with experimental results.

Numerical modelling

Based on an existing constitutive model for the monotonic analysis of interface elements, formulated within the framework of plasticity theory, a new constitutive model entirely established on the basis of the incremental theory of plasticity and able to describe the cyclic loading of interface elements was developed in this study. The cyclic behaviour is based in the introduction of two new auxiliary (unloading) yield surfaces, similar to the monotonic ones. Each unloading surface is allowed to move only inside the admissible stress space and always towards the similar monotonic yield surface. Its motion is controlled by a mixed hardening law. The hypothesis of elastic unloading is assumed only for the shear component. Therefore, the normal component is described in a nonlinear fashion, adopting suitable hardening laws based on phenomenological experimental results.

The performance of the developed constitutive model is assessed by comparisons against experimental results available in the literature, both at the element level and at the structural level. Comparison between experimental and numerical results showed that the most relevant features observed in experiments, as opening-closure and shear sliding of the joints, stiffness degradation, strength degradation and energy dissipation, are well captured by the model, which enables its use for the analysis and study of masonry structures under cyclic loading. In addition, it is shown that the material behaviour during unloading should be considered in a non-linear fashion.

Suggestions for future work

The objectives defined in the introduction of this study were successfully achieved. In particular, the mechanical characterization of historical masonry materials (stone and brick) under cyclic loading was carried out, and a constitutive model for the analysis of masonry structures (micro-level) under cyclic loading was successfully developed.

The testing of dry stone masonry under combined normal and cyclic shear loading is a challenging issue, since almost no data is currently available. The attainment of experimental results under cyclic loading is rather important both to understand the complex behaviour of the dry stone walls and to validate numerical results.

Further applications of the numerical model are required for studying the influence of the material parameters in the structural behaviour. Also, the usage of the proposed formulation for macro-level models is suggested. Finally, the incorporation of fatigue, deterioration and creep in these complex models remains a true challenge.

REFERENCES

ALMEIDA, C., 2000. Análise do comportamento da igreja do Mosteiro da Serra do Pilar sob a acção dos sismos. MSc Thesis, Faculdade de Engenharia da Universidade do Porto, Porto, Portugal.

ALMEIDA, J.C., LOURENÇO, P.B., BARROS, J.A., 2002. Characterization of brick and brick-mortar interface under uniaxial tension. F. Santos *et al.*(eds.): Proc. 7th Int. Seminar on Structural Masonry, Belo Horizonte, Brasil, pp. 67-76.

ANTHOINE, A., 1997. Homogenisation of periodic masonry: Plane stress, generalised plane strain or 3D modelling? Communications in Numerical Methods in Engineering, 13, pp. 319-326.

ANTHOINE, A.; MAGONETTE, G.; MAGENES, G., 1995. Shear-compression testing and analysis of brick masonry walls. G. Duma (ed.): Proc. 10th European Conference on Earthquake Engineering, 3, pp. 1657-1662.

ASTM, 1999. Standard test method for elastic moduli of intact rock core specimens in uniaxial compression. Annual Book of ASTM Standards, Section 4, Vol. 04.08, D 3148-96.

ATKINSON, R.H.; AMADEI, B.P.; SAEB, S.; STURE, S., 1989. Response of masonry bed joints in direct shear. J. Struct. Eng., ASCE, 115(9), pp. 2276-2296.

BARTOLI, G; CHIARUGI, A.; GUSELLA, V., 1996. Monitoring systems on historic buildings: The Brunelleschi dome. J. Struct. Eng., ASCE, 122(6), pp. 663-673.

BATHE, K.-J., 1996. Finite element procedures. Prentice-Hall, New Jersey, USA.

BERTO, L.; SAETTA, A.; SCOTTA, R.; VITALIANI, R., 2002. Orthotropic damage model for masonry structures. Int. J. Num. Meth. Engrg. (to appear).

BINDA, L; TIRABOSCHI, C.; MIRABELLA ROBERTI, G.; BARONIO, G.; CARDANI, G., 1996a. Measuring masonry material properties: detailed results from an extensive experimental research, Part I: Tests on masonry components. Report 5.1, Politecnico di Milano.

BINDA, L; TIRABOSCHI, C.; MIRABELLA ROBERTI, G.; BARONIO, G.; CARDANI, G., 1996b. Measuring masonry material properties: detailed results from an extensive experimental research, Part II: Tests on masonry specimens. Report 5.1, Politecnico di Milano.

BØVING, K.G., 1989. NDE Handbook. Butterworths, London.

BRENCICH, A.; LAGOMARSINO, S., 1998. A macroelement dynamic model for masonry shear walls. G. Pande *et al.* (eds): Computer Methods in Structural Masonry - 4, pp. 67-75.

CACHIM, P.B., 1999. Experimental and numerical analysizs of the behaviour of structural concrete under fatigue loading with applications to concrete pavements. Ph.D. Dissertation, Faculdade de Engenharia da Universidade do Porto, Porto, Portugal.

CALVI, G.M.; MAGENES, G.; MAGENES, G.; PAVESE, A., 1992. Experimental and numerical investigation on a brick masonry building prototype - Report 1.1 - Design of the experimental tests. D.M.S report, Università di Pavia.

CEN, 1995. Eurocode 6: Design of masonry structures. ENV 1996-1-1:1995, CEN, Brussels, Belgium.

CHEN, W.F., 1982. Plasticity in reinforced concrete. Mc. Graw Hill. New York, USA.

CHEN, W.F.; MIZUNO, E., 1990. Non-linear analysis in soil mechanics. Theory and implementation. Elsevier, Amsterdam.

COMBESCURE, D; PEGON, P., 1996. A plasticity-based masonry model reproducing the compressive strength degradation under cyclic loading. Special Publication Nº I.96.70, JRC, Ispra, Italy.

COMITÉ EURO-INTERNATIONAL DU BÉTON, 1990. CEB-FIP Model Code 1990. Bulletin d'information 195/196, Lausanne, Switzerland.

COOK, N.G.W., 1965. The failure of rock. Int. J. Rock Mechanics and Mining Sciences, 2(4), pp.389-404.

CRISFIELD, M.A., 1981. A fast incremental/iterative solution procedure that handles snap-through. Computers and Structures, 13, pp. 55-62.

CRISFIELD, M.A., 1991. Non-linear finite element analysis of solids and structures. Volume 1: Essentials. John Wiley & Sons, London, UK.

CROCI, G., 1997. The Colosseum: Safety evaluation and preliminary criteria of intervention. P. Roca *et al.* (eds): Structural Analysis of Historical Constructions. CIMNE, Barcelona, pp. 154-165.

CROCI, G., 1998. The conservation and structural restoration of the architectural heritage. Computational Mechanics Publications, Shouthampton, UK.

CUNDALL, P.A., 1971. A computer model for simulating progressive large scale movements in blocky rock systems. Proc. of the Symposium of the International Society of Rock Mechanics, Vol. 1, paper nº II-8, Nancy, France.

CUNDALL, P.A.; HART, R.D., 1992. Numerical modeling of discontinua. Engineering Computations, 9, pp. 101-113.

CUR, 1997. J.G. Rots (ed): Structural masonry: An experimental/numerical basis for practical design rules. Balkema, Rotterdam.

DAFALIAS, Y.F., 1986. Bounding surface plasticity. I: Matematical foundation and hypoplasticity. J. Eng. Mech., ASCE, 112(9), pp. 966-987.

DAFALIAS, Y.F.; POPOV, E.P., 1975. A model of nonlinearly hardening materials for complex loading. Acta Mech., 21, pp. 173-192.

De BORST. R.; FEENSTRA, P.H., 1990. Studies in anisotropic plasticity with reference to the Hill criterion. Int. J. Num. Meth. Engrg., 29, pp. 315-336.

DHANASEKAR, M.; PAGE, A.W.; KLEEMAN, P.W., 1985. The failure of brick masonry under biaxial stresses. Proc. Instn. Civ. Engrs., Part 2, 79, pp. 295-313.

DOEBLING, S.W.; FARRAR, C.R.; PRIME, M.B.; SHEVITZ, D.W., 1996. Damage identification and health monitoring of structural and mechanical systems from changes in their vibration characteristics: A literature review. Research report LA-13070-MS, ESA-EA Los Alamos National Laboratory, Los Alamos, USA.

DRYSDALE, R.G.; HAMID, A.A.; BAKER, L.R., 1999. Masonry structures. Behaviour and design. The Masonry Society, Boulder, Colorado, USA.

FAIRHURST, C.E.; HUDSON, J.A., 1999. Draft ISRM suggested method for the complete stress-strain curve for intact rock in uniaxial compression. Int. J. Rock Mech. and Mining Sciences, 36, pp.279-289.

FANELLI, M.; PAVESE, A., 1993. Diagnosis of masonry towers by dynamic identification. Structural Preservation IABSE Symposium, Rome, Italy.

FARDIS, M. N.; ALIBE, B.; TASSOULAS, J. L., 1983. Monotonic and cyclic constitutive law for concrete. J. Eng. Mech., ASCE, 109(2), pp. 516-536.

FEENSTRA, P.; DE BORST, R., 1992. The Rankine plasticity model for concrete cracking. Computational Plasticity. Fundamentals and Applications, Barcelona, Spain, pp. 657-668.

FEENSTRA, P.H., 1993. Computational aspects of biaxial stress in plain and reinforced concrete. Ph.D. Dissertation, Delft University of Technology, Delft, The Netherlands.

GAMBAROTTA, L.; LAGOMARSINO, S., 1997a. Damage models for the seismic response of brick masonry shear walls. Part I: the mortar joint model and its applications. Earthquake Eng. Struct. Dyn., 26, pp. 423-439.

GAMBAROTTA, L.; LAGOMARSINO, S., 1997b. Damage models for the seismic response of brick masonry shear walls. Part II: the continuum model and its applications. Earthquake Eng. Struct. Dyn., 26, pp. 441-462.

GHABOUSSI, J.; BARBOSA, R., 1990. Three-dimensional discrete element method for granular materials. Int. J. Num. Anal. Meth. Geomech., 14, pp. 451-472.

GILBERT, M.; MELBOURNE, C., 1994. Rigid-block analysis of masonry structures. The Structural Engineer, 72, nº 21.

GIUFFRÈ, A., 1993. Sicurezza e conservazione dei centri storici in area sismica, il caso Ortigia. Editori Laterza, Bari.

GOODMAN, R.E.; TAYLOR, R.L.; BREKKE, T.L., 1968. A model for the mechanics of jointed rock. J. Soil Mech. Found. Div., ASCE, 94(3), pp. 637-659.

GOPALARATNAM, V.S.; SHAH, S.P., 1985. Softening response of plain concrete in direct tension. ACI Journal, 82, pp. 310-323.

HANSEN, N.R.; SCHREYER, H.L., 1994. A thermodynamically consistent framework for theories of elastoplasticity coupled with damage. Int. J. Solids Structures, 31(4), pp. 469-484.

HASHIGUCHI, K., 1989. Subloading surface model in unconventional plasticity. Int. J. Solids Structures, 25(8), pp. 917-945.

HEYMAN, J., 1995. The stone skeleton. Cambridge University Press, Cambridge, UK.

HEYMAN, J., 1998. Mechanical behaviour of arches and vaults. P. Roca *et al.* (eds): Structural Analysis of Historical Constructions II. CIMNE, Barcelona, pp. 1-6.

HENDRY, A.W.; SINHA, B.P.; DAVIS, S.R., 1981. An introduction to loading bearing brickwork design. Ellis Horwood, England.

HILSDORF, H.K., 1969. Investigation into the failure mechanisms of brick masonry loaded in axial compression. F.H. Johnson (ed): Designing, engineering and constructing with masonry products. Gulf Publishing Company, Houston, Texas, pp. 34-41.

HODGE, P.G. Jr., 1957. Discussion [of Prager (1956)]. J. Appl. Mech., 23, pp. 482-484.

HOHBERG, J.-M., 1992. A joint element for the non-linear dynamic analysis arch dams. Report nº 186, Institute of Structural Enginerring, ETH Zurich, Zurich, Switzerland.

HORDIJK, D.A., 1991. Local approach to fatigue of concrete. Ph.D. Dissertation, Delft University of Technology, Delft, The Netherlands.

IWAN, W.D., 1967. On a class of models for the yielding behaviour of continuous and composite systems. J. Appl. Mech, 34, pp. 612-6617.

JEFFERSON, A.D.; MILLS, N.R., 1998. Fracture and shear properties of concrete construction joints from core samples. Materials and Structures, 31, pp. 595-601.

JUKES, P.; RIDDINGTON, J.R., 1997. A review of masonry joint shear strength test methods. Masonry International, 11(2), pp. 37-41.

JUKES, P.; RIDDINGTON, J.R., 1998. A review of masonry tensile bond strength test methods. Masonry International, 12(2), pp. 51-57.

KACHANOV, L.M., 1958. Time of rupture process under creep conditions (in Russian). Izvestia Akademii Nauk, Otd Tech Nauk, USSR, 8, pp. 26-31.

KACHANOV, L.M., 1986. Introduction to the theory of damage. Martinus Nijhoff Publishers, Dordrecht, the Netherlands.

KARSAN, I.D.; JIRSA, O., 1969. Behaviour of concrete under compressive loadings. J. Struct. Div., ASCE, 95, pp. 2543-2563.

KOITER, W.T., 1953. Stress-strain relations, uniqueness and variational theorems for elastic-plastic materials with a singular yield surface. Q. Appl. Math., 11(3), pp. 350-354.

KOITER, W.T., 1960. General theorems for elastic-plastic solids. Progress in solid mechanics 1, pp. 167-221.

KREIG, R.D., 1975. A practical two surface plasticity theory. J. Appl. Mech. Trans., ASME, 42(3), pp. 641-646.

LANGENBACH, R., 1994. Architectural issues in the seismic rehabilitation of masonry buildings. D. Abrams and G. Calvi (eds): US-Italy workshop on guidelines for seismic evaluation and rehabilitation of unreinforced masonry buildings. Technical report NCEER-94-0021.

LEMAITRE J.; CABOCHE, J.L., 1985. Mécanique des materiaux solides. Dunod, Paris.

LEMOS, J.V., 1995. Assessment of the ultimate load of a masonry arch using discrete elements. G.N. Pande and J. Middleton (eds): Computer Methods in Structural Masonry - 3. Books and Journals Int., pp. 294-302.

LEMOS, J.V., 1998a. Discrete element modeling of the seismic behavior of stone masonry arches. G. Pande *et al.* (eds): Computer Methods in Structural Masonry - 4, E&FN Spon, London, pp. 220-227.

LEMOS, J.V., 1998b. Numerical models for seismic analysis of monuments. Proc. of Monuments-98 Workshop on Seismic Performance of Monuments, Lisbon, pp. K19-K36.

LI, C.; PRIKRYL, R.; NORDLUND, E., 1998. The stress-strain behaviour of rock material related to fracture under compression. Engineering Geology, 49, pp. 293-302.

LIVESLEY, R.K., 1978. Limit analysis of structures formed from rigid blocks. Int. J. Num. Meth. Engrg., 12, pp. 1853-1871.

LOFTI, H.R.; SHING, P.B., 1994. Interface model applied to fracture of masonry structures. J. Struct. Eng., ASCE, 120(1), pp. 63-80.

LOURENÇO, P.B., 1994. Analysis of masonry structures with interface elements. Theory and applications. Report Nº 03.21.22.0.01, Delft University of Technology, Delft, The Netherlands.

LOURENÇO, P.B., 1996. Computational strategies for masonry structures. Ph.D. Dissertation, Delft University of Technology, Delft, The Netherlands.

LOURENÇO, P.B.; ROTS J.G., 1997. A multi-surface interface model for the analysis of masonry structures. J. Eng. Mech., ASCE, 123(7), pp. 660-668.

LOURENÇO, P.B., 1998. Experimental and numerical issues in the modelling of the mechanical behavior of masonry. P. Roca *et al.* (eds): Structural Analysis of Historical Constructions II. CIMNE, Barcelona, pp. 57-91.

LOURENÇO, P.B.; ROTS, J.G.; BLAAUWENDRAAD, J., 1998. Continuum model for masonry: Parameter estimation and validation. J. Struct. Eng., ASCE, 124(6), pp. 642-652.

LOURENÇO, P.B., 2002. Computations on historic masonry structures. Prog. Struct. Engng. Mater., 4, pp. 301-319.

LUBLINER, J., 1990. Plasticity theory. Macmillan Company, New York, USA.

MACCHI, G., 1992. Structural diagnosis and rehabilitation of historical buildings. Cuadernos INTEMAC, nº7.

MACCHI, G., 1997. General methodology. The combined use of experimental and numerical techniques inside a single study. P. Roca *et al.* (eds): Structural Analysis of Historical Constructions. CIMNE, Barcelona, pp. 10-23.

MACCHI, G., 1998. Problems related to the original conception - the case of Pavia Cathedral. P. Roca *et al.* (eds): Structural Analysis of Historical Constructions II. CIMNE, Barcelona, pp. 39-56.

MACCHI, G., 2001. Diagnosis of the façade of St. Peter's Basilica in Rome. P.B. Lourenço and P. Roca (eds): Historical Constructions. Universidade do Minho, Guimarães, pp. 309-317.

MANN, W.; MÜLLER, H., 1982. Failure of shear-stressed masonry - an enlarged theory, tests and application to shear walls. Proc. British Ceramic Society, 30, pp. 223-235.

MAUGIN, G.A., 1992. The thermomechanics of plasticity and fracture. Cambridge University Press, Cambridge.

MAZARS, J.; PIJAUDIER-CABOT, G., 1989. Continuum damage theory - application to concrete. J. Eng. Mech., ASCE, 115(2), pp. 345-365.

McNARY, W.S.; ABRAMS, D.P., 1985. Mechanics of masonry in compression. J. Struct. Eng., ASCE, 111(4), pp. 857-870.

MELBOURNE, C.; GILBERT, M., 2001. Modelling masonry arch bridges. J.W. Bull (eds): Computational Modelling of Masonry, Brickwork and Blockwork Structures. Saxe-Coburg Publications, UK.

MOLA, F.; VITALIANI, R., 1997. Analysis, diagnosis and preservation of ancient monuments: The St. Mark's Basilica in Venice. P. Roca *et al.* (eds): Structural Analysis of Historical Constructions. CIMNE, Barcelona, pp. 166-188.

MOLINS, C.; ROCA, P., 1997. Capacity of masonry arches and spatial frames. J. Struct. Eng., ASCE, 124(6), pp. 653-663.

MOSTELLER, F.; ROURKE, R.E.K., 1973. Sturdy statistics (nonparametrics and order statistics. Addison-Wesley, Reading, Massachusetts, USA (Appendix A).

MRÓZ, Z., 1967. On the description of anisotropic hardening. J. Mech. Phys. Solids, 15, pp. 163-175.

MRÓZ, Z.; NORRIS, V. A.; ZIENKIEWICZ, O. C., 1978. An anisotropic hardening model for soils and its application to cyclic loading. Int. J. Num. Anal. Meth. Geomech., 2, pp. 203-221.

MÜHLHAUS, H.B., 1993. Continuum models for layered soil and blocky rock. Comprehensive Rock Engineering, Vol. 2. Pergamon Press.

NEMAT-NASSER, S.; HORI, M, 1993. Micro-mechanics: overall properties of heterogeneous materials: North-Holland series in applied mathematics and mechanics, Elsevier, Amsterdam.

NEVILLE, A.M., 1995. Properties of concrete. Pitman Publishing, London.

NGO, D.; SCORDELIS A.C., 1967. Finite element analysis of reinforced concrete beams. J. Amer. Concr. Inst., 64(3), pp.152-163.

ODQVIST, F.K.G., 1933. Die Verfestigung von flusseisenahnlichen Korpern. Ein Beitrag zur Plastizitiitstheorie, Zeit. angew. Math. und Mech., 13, 360-3.

OLIVEIRA, D.V., 2000. Experimental characterization of stone and brick masonry. Report 00-DEC/E-4, Universidade do Minho, Guimarães, Portugal.

ORDUÑA, A.; LOURENÇO, P.B., 2002. Cap model for limit analysis and strengthening of masonry structures. J. Struct. Eng., ASCE (to appear).

ORTIZ, M; POPOV, E.P., 1985. Accuracy and stability of integration algorithms for elastoplastic constitutive equations. Int. J. Num. Meth. Engrg., 28, pp. 1561-1576.

OWEN, D.R.J.; HILTON, E., 1980. Finite elements in plasticity: theory and practice. Pineridge Press Ltd. Swansea, UK.

PAGE, A.W., 1978. Finite element model for masonry. J. Struct. Div., ASCE, 104(8), pp. 1267-1285.

PAGE, A.W., 1981. The biaxial compressive strength of brick masonry. Proc. Instn. Civ. Engrs., Part 2, 71, pp. 893-906.

PAGE, A.W., 1983. The strength of brick masonry under biaxial compression-tension. Int. J. Masonry Constr., 3(1), pp. 26-31.

PAGE, A.W., SAMARASINGHE, W.; HENDRY, A.W., 1980. The failure of masonry shear walls. Int. J. Masonry Constr., 1(2), pp. 52-57.

PAGNONI, T., 1994. Seismic analysis of masonry and block structures with the discrete element method. Proc. 10th European Conference on Earthquake Engineering, Vol. 3, pp. 1674-1694.

PAN, Y.-W., 1991. Generalized nonassociative multisurface approach for granular materials. J. Geotech. Eng., ASCE, 117(5), pp. 1336-1353.

PANDE, G.N.; LIANG, J.X.; MIDDLETON J., 1989. Equivalent elastic moduli for unit masonry. Computers and Geotechnics, 8, pp. 243-265.

PAPA. E.; 1996. A unilateral damage model for masonry based on a homogenisation procedure. Mech. of Cohesive-Frictional Materials, 1, pp. 349-366.

PASTOR, M; ZIENKIEWICZ, O.C.; CHAN, A.H.C., 1990. Generalized plasticity and the modelling of soil behaviour. Int. J. Num. Anal. Meth. Geomech., 14, pp. 151-190.

PEGON, P.; PINTO, A.V., 1996. Seismic study of monumental structures - structural analysis, modelling and definition of experimental model. Report EUR 16387 EN, JRC, Ispra, Italy.

PRAGER W., 1955. The theory of plasticity: A survey of recent achievements. Proc. Inst. Mech. Eng. (London), 169, pp. 41-57.

RAIJMAKERS, T.M.J.; VERMELTFOORT, A.T., 1992. Deformation controlled tests in masonry shear walls (in Dutch). Report B-92-1156, TNO-Bow, Delft, The Netherlands.

RAMM, E., 1981. Strategies for tracing the non-linear responses near limit points. W. Wunderlich, E. Stein and J.-K. Bathe (eds): Non-linear Finite Element Analysis in Structural Mechanics, pp. 63-89.

RAMOS, L.F., 2002. Análise experimental e numérica de estruturas históricas de alvenaria. MSc Thesis, Universidade do Minho, Guimarães, Portugal.

REINHARDT, H.W., 1984. Fracture mechanics of an elastic softening material like concrete. Heron, 29(2), pp. 3-41.

RIKS, E., 1979. An incremental approach to the solution of snapping and buckling problems. Int. J. Solids Structures, 15, pp. 529-551.

RILEM, 1994a. Technical recommendations for the testing and use of constructions materials: LUMA1 - Compressive strength of masonry units. Chapman & Hall, UK.

RILEM, 1994b. Technical recommendations for the testing and use of constructions materials: LUMB1 - Compressive strength of small walls and prisms. Chapman & Hall, UK.

ROCA, P.; PELLEGRINI, L.; OÑATE, E.; HANGUNU, A., 1998. Analysis of the structure of Gothic cathedrals: Application to Barcelona cathedral. P. Roca *et al.* (eds): Structural Analysis of Historical Constructions II. CIMNE, Barcelona, pp. 231-258.

ROCA, P.; OLIVEIRA, D.; LOURENÇO, P.; CAROL, I., 2001. Mechanical response of dry joint masonry. G. Arun and N. Seçkin (eds): 2nd International Congress on Studies in Ancient Structures, Yildiz Technical University, Istanbul, pp. 571-579.

ROCHA, M., 1981. Mecânica das rochas. Laboratório Nacional de Engenharia Civil, Lisboa.

ROSSI, P.P., 1982. Analysis of mechanical characteristics of brick masonry tested by means of nondestructive in situ tests. Proc. 6th Int. Brick Masonry Conference, Rome, Italy.

ROSSI, P.P., 1997. Possibilities of the experimental techniques for the structural analysis of historical constructions. P. Roca *et al.* (eds): Structural Analysis of Historical Constructions. CIMNE, Barcelona, pp. 24-46.

ROSSI, P.P.; ROSSI, C., 1998. Surveillance and monitoring of ancient structures: recent developments. P. Roca *et al.* (eds): Structural Analysis of Historical Constructions II. CIMNE, Barcelona, pp. 163-178.

ROTS, J.G., 1991. Numerical simulation of cracking in structural masonry. Heron, 36(2), pp. 49-63.

SCHELLEKENS, J.; DE BORST, R., 1993. On the numerical integration of interface elements. Int. J. Num. Meth. Engrg., 36, pp. 43-66.

SIMO, J.C.; HUGHES, T.J.R., 1998. Computational Inelasticity. Springer-Verlag, New York, USA.

SIMO, J.C.; KENNEDY, J.G.; GOVINDJEE, S., 1988. Non-smooth multisurface plasticity and viscoplasticity. Loading/unloading conditions and numerical algorithms. Int. J. Num. Meth. Engrg., 26, pp. 2161-2185.

SIMO, J.C.; TAYLOR, R.L., 1985. Consistent tangent operators for rate-independent elastoplasticity. Comput. Meth. Appl. Mech Engrg. 48, pp. 101-118.

SINCRAIAN, G.E., 2001. Seismic behaviour of blocky masonry structures. A discrete element method approach. Ph.D. Dissertation, IST, Lisbon, Portugal.

STANKOWSKI, T.; RUNESSON, K.; STURE, S., 1993. Fracture and slip of interfaces in cementitious composites. I: characteristics. J. Eng. Mech., ASCE, 119(2), pp. 292-314.

SUPRENANT, B.A.; SHULLER, M.P., 1994. Nondestructive evaluation & testing of masonry structures. Aberdeen Group.

Van der PLUIJM, R., 1993. Shear behaviour of bed joints. A.A. Hamid and H.G. Harris (eds): Proc. 6th North American Masonry Conference. Vol. 1, pp. 125-136.

Van der PLUIJM, R., 1997. Non-linear behaviour of masonry under tension. Heron, 42(1), pp. 25-54.

Van MIER, J.G.M., 1984. Strain-softening of concrete under multiaxial loading conditions. Ph.D. Dissertation. Eindhoven University of Technology, Eindhoven, The Netherlands.

VERMELTFOORT, A.T., 1997. Effects of the width and boundary conditions on the mechanical properties of masonry prisms under compression. Proc. 11th Int. Brick/Block Masonry Conference, Shangai, pp. 181-190.

VERMELTFOORT, A.T.; RAIJMAKERS, T.M.J., 1993. Deformation controlled tests in masonry shear walls, part 2 (in Dutch). Report TUE/BKO/93.08, Eindhoven University of Technology, Eindhoven, The Netherlands.

VONK, R.A., 1992. Softening of concrete loaded in compression. Ph.D. Dissertation. Eindhoven University of Technology, Eindhoven, The Netherlands.

WAWERSIK, W.R., 1968. Detailed analysis of rock failure in laboratory compression tests. Ph.D. Dissertation, University of Minnesota.

WAWERSIK, W.R.; FAIRHURST, C., 1970. A study of brittle rock fracture in laboratory compression experiments. Int. J. Rock Mech. Mining Sciences, 7, pp. 561-575.

ZIENKIEWICZ, O.C.; LEUNG, K.H.; PASTOR, M, 1985. Simple model for transient soil loading in earthquake analysis. I: Basic model and its application. Int. J. Num. Anal. Meth. Geomech., 9, pp. 453-476.

ZIENKIEWICZ, O.C.; MRÓZ, Z., 1984. Generalized plasticity formulation and applications to geomechanics. C.S. Desai and R.H. Gallager (eds): Mechanics of Engineering Materials, Wiley, pp. 655-679.

ZIENKIEWICZ, O.C.; TAYLOR, R.L., 1991. The finite element method. 4th edition, Volume 2: Solid and fluid mechanics, dynamics and non-linearity. Mc-Graw Hill, London, UK.

ZIGLER, H., 1959. A modification of Prager's hardening rule. Appl. Math., 17, pp. 55-65.

ZUCCHINI, A.; LOURENÇO, P.B., 2002. A micromechanical model for the homogenisation of masonry. Int. J. Solids Structures, 39(12), pp. 3233-3255.

APPENDIX A: DRY STONE MASONRY WALL TESTS

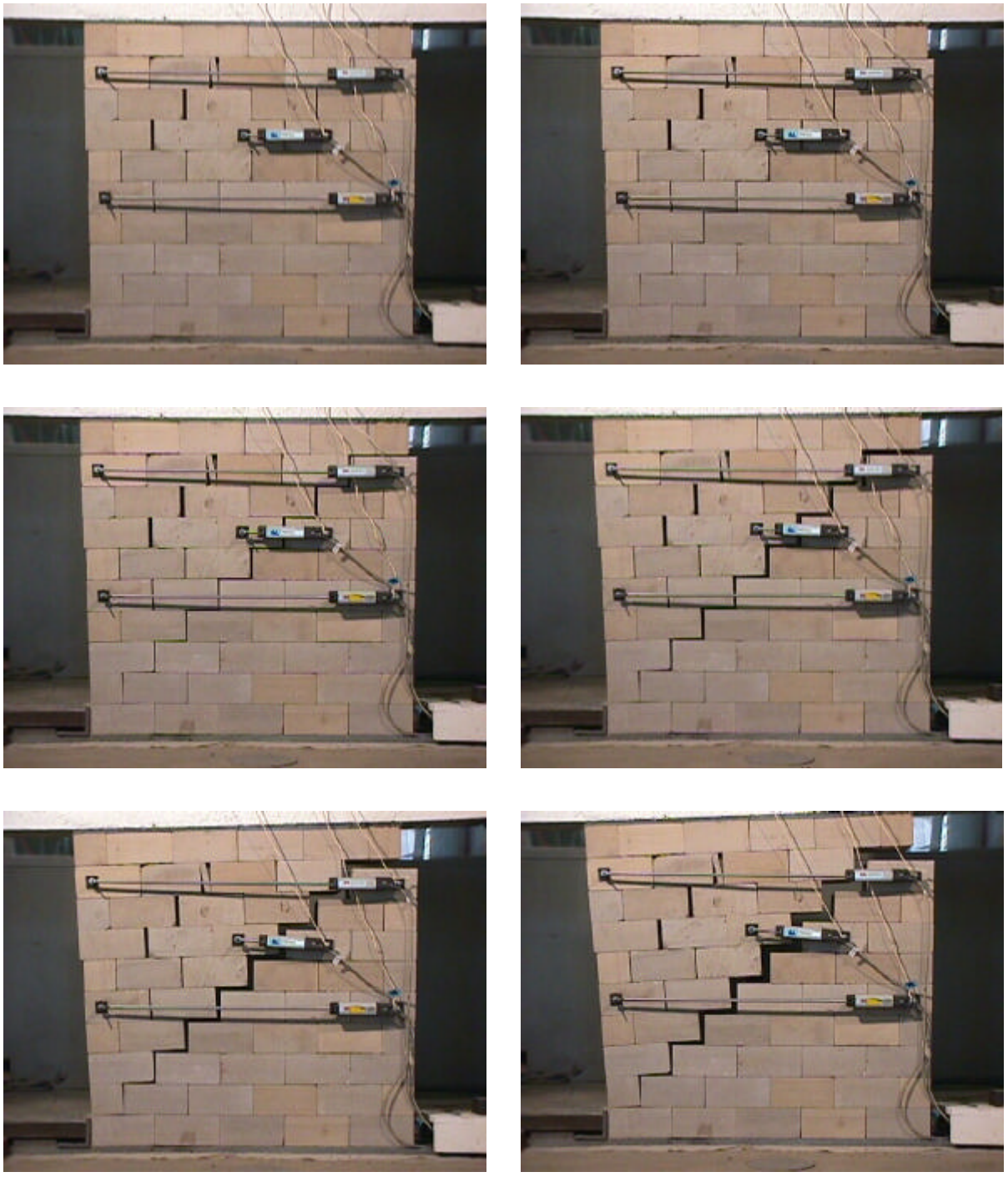

Pictures of the SW30.1 stone wall test

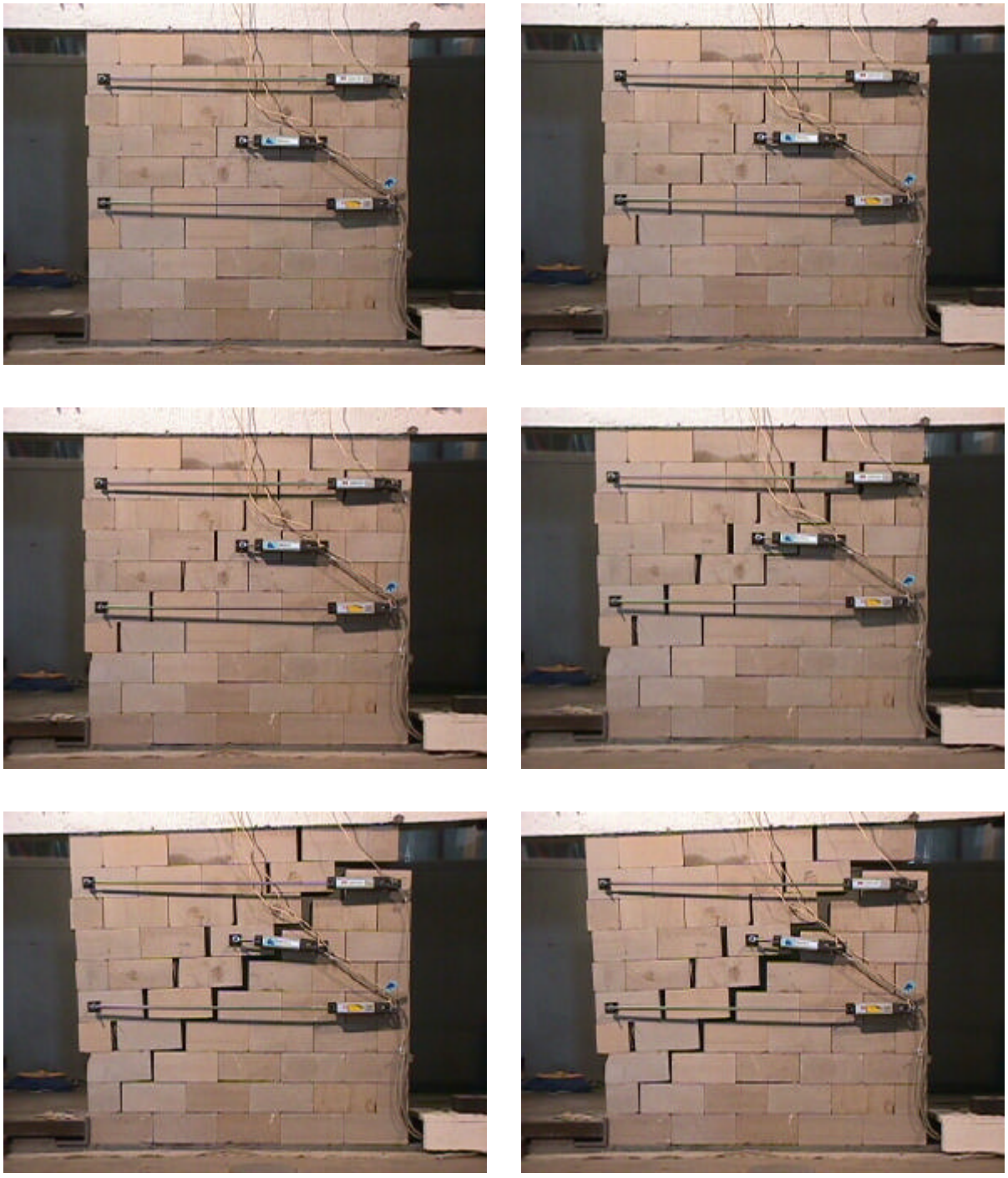

Pictures of the SW30.2 stone wall test.

Pictures of the SW100.1 stone wall test.

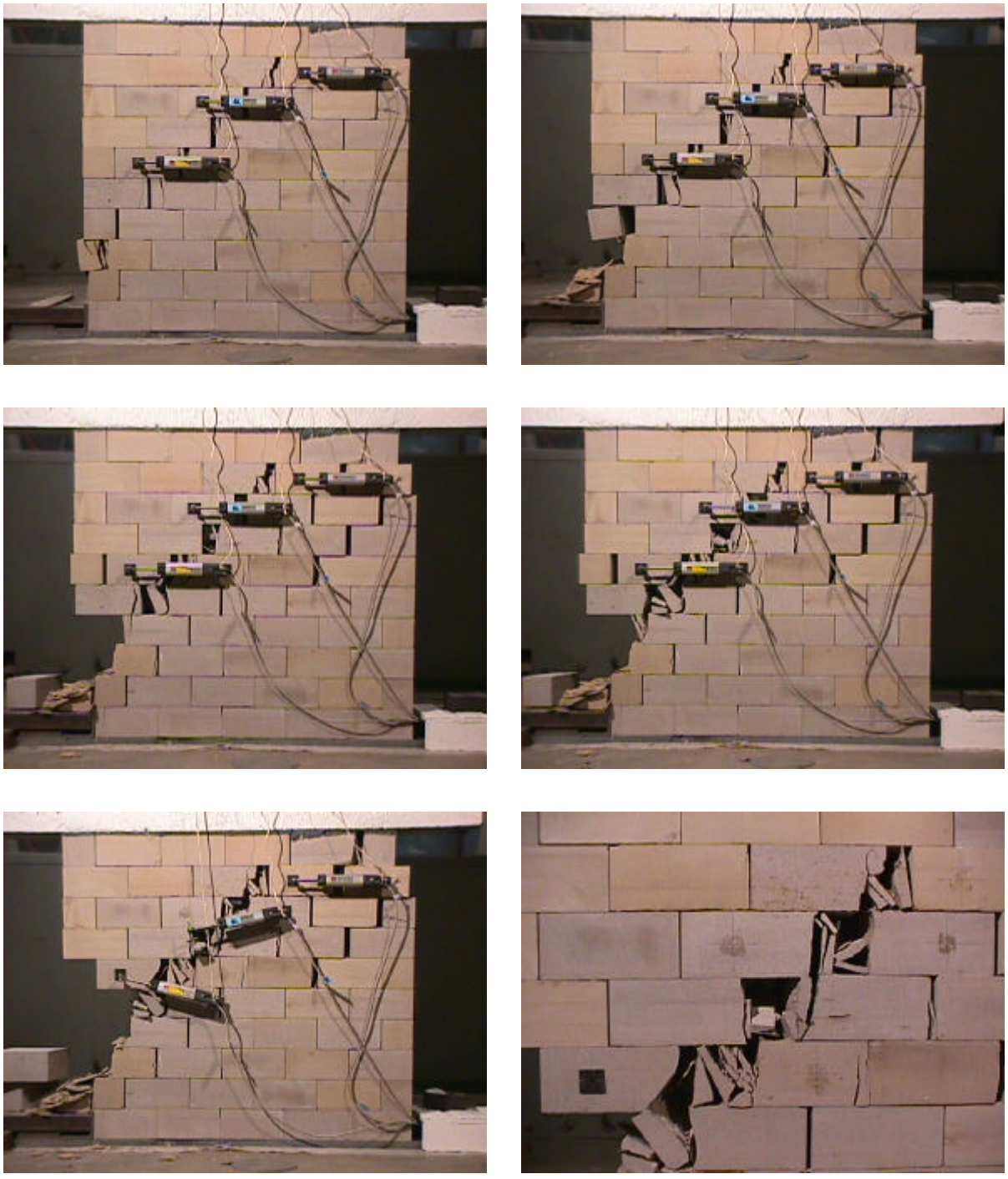

Pictures of the SW100.2 stone wall test.

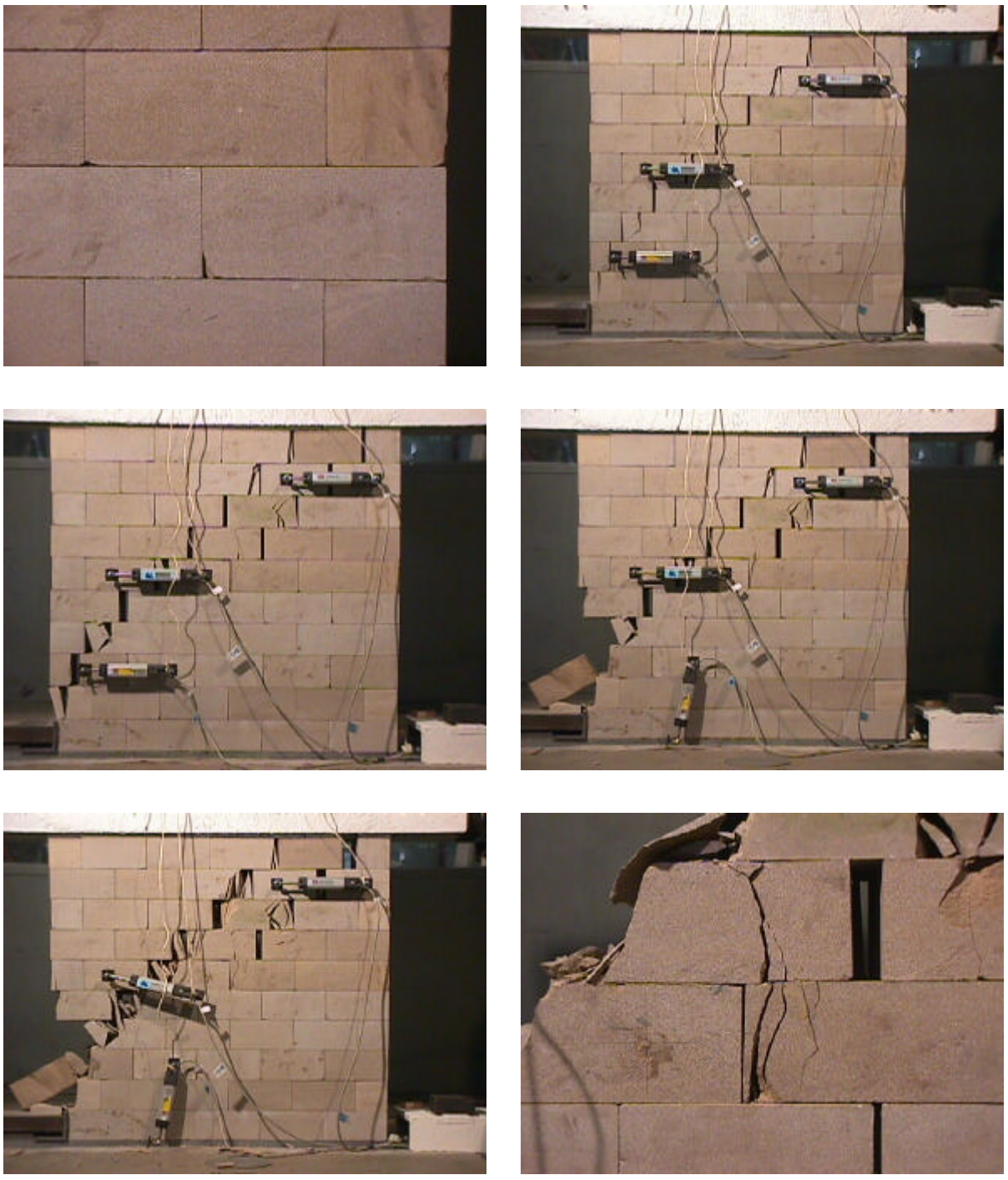

Pictures of the SW200.1 stone wall test.

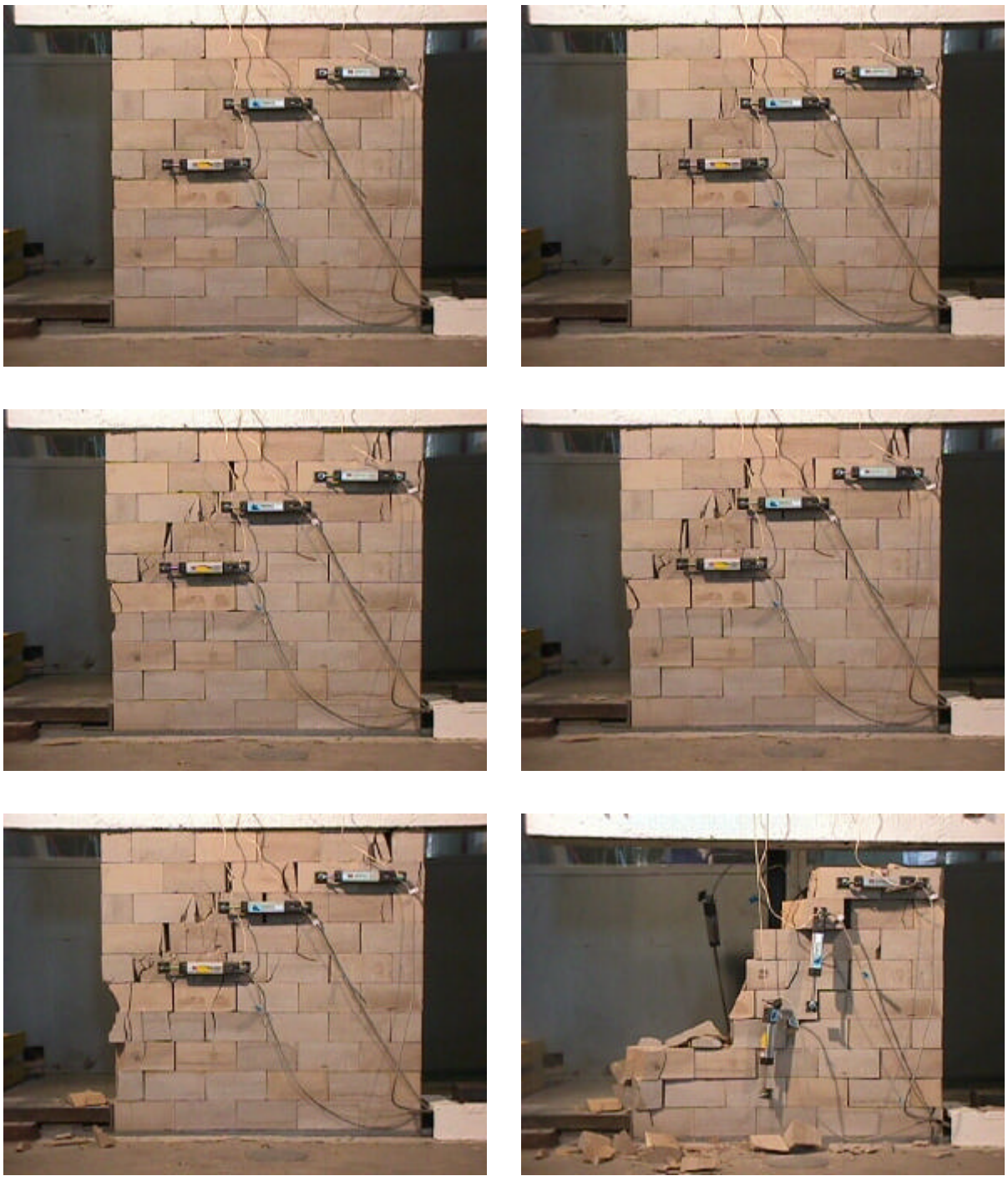

Pictures of the SW200.2 stone wall test.

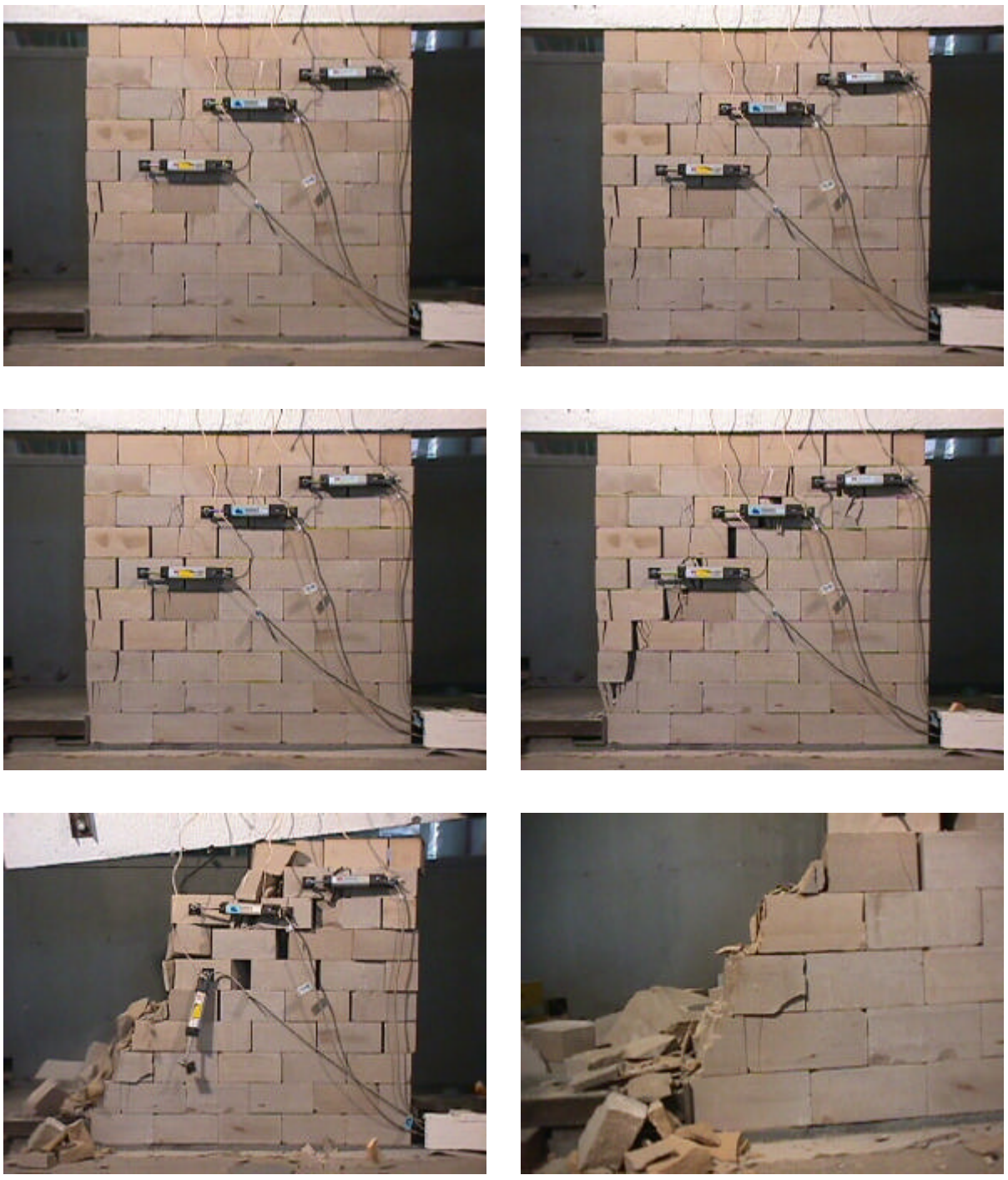

Pictures of the SW250.1 stone wall test.